VIBRATION-BASED DAMAGE DETECTON OF SIMPLE BRIDGE SUPERSTRUCTURES

A thesis Submitted to the College of

Graduate Studies and Research

in Partial Fulfillment of the requirements

for the Degree of Doctor of Philosophy

in the Department of Civil and Geological Engineering

University of Saskatchewan

Saskatoon

By

Zhengjie Zhou

PERMISSION TO USE

In presenting this thesis in partial fulfillment of the requirements for a Postgraduate degree from the University of Saskatchewan, I agree that the Libraries of this University may make it freely available for inspection. I further agree that permission for copying this thesis in any manner, in whole or in part, for scholarly purposes may be granted by the professors who supervised my thesis work or, in their absence, by the Head of the Department or the Dean of the College in which my thesis work was done. It is understood that any copying or publication or use of this thesis or parts thereof for financial gain shall not be allowed without my written permission. It is also understood that due recognition shall be given to me and to the University of Saskatchewan in any scholarly use which may be made of any material in my thesis.

Requests for permission to copy or to make other use of material in this thesis in whole or part should be addressed to:

Head of the Department of Civil and Geological Engineering

University of Saskatchewan

57 Campus Drive

Saskatoon, Saskatchewan, S7N 5A9

ABSTRACT

This thesis addresses the experimental and numerical study of vibration-based damage detection (VBDD) techniques in structural health monitoring (SHM) of bridge superstructures. The primary goal of SHM is to ascertain the condition or "health" of a structure so that decisions can be made with regard to the need for remediation. VBDD techniques are global non-destructive evaluation (NDE) techniques. The principle of VBDD techniques is to detect damage using changes in the dynamic characteristics of a structure caused by the damage. The advantage of VBDD techniques over local NDE techniques is that VBDD techniques can assess the condition of an entire structure at once and are not limited to accessible components.

Well controlled laboratory experiments on a half-scale, simply supported steel-free bridge deck and two full-scale, simply supported prestressed concrete girders demonstrated that small scale damage at different locations can be reliably detected and located by VBDD techniques using a relatively small number of sensors (accelerometers or strain gauges) and considering changes to only the fundamental mode of vibration. The resolution of damage localization, defined as the length of the window within which damage could be located when the technique predicts it to be located at a particular point, was 70% of measurement point spacing for the deck and 82% for the girders, provided the damage was not located too close to a simple support.

To establish the potential of VBDD techniques in the absence of experimental uncertainty, eigenvalue analyses using finite element models of the deck and the girders were undertaken to investigate ability of five VBDD methods to predict the longitudinal

location of damage. It was found that when mode shapes were well-defined with a large number of measurement points, the damage location could be determined with great accuracy using any of the five VBDD techniques investigated. The resolution of longitudinal localization of damage was 40 to 80% of the spacing between measurement points when small numbers of measurement points were used, provided the damage was not located too close to a simple support.

The experimental study successfully detected small scale damage under forced resonant harmonic excitation but failed in detecting damage under forced random excitation, although the use of random sources of excitation is more practical in field testing. Transient dynamic analyses on the finite element model of the steel-free bridge deck were performed to investigate the implications of using random forced vibrations to characterize mode shapes to be used to detect damage. It was found that the probability of successful damage localization depends upon the severity of the damage, the number of trials used to obtain the average mode shape, the location of damage relative to the nearest sensor, the distance between the damage and the support, and the magnitude of measurement errors. A method based on the repeatability of measured mode shapes is proposed to calculate the probability of successful damage detection and localization.

In summary, results of this research demonstrate that VBDD techniques are a promising tool for structural health monitoring of bridge superstructures. However, although these methods have been shown to be capable of effectively detecting small scale damage under well controlled conditions, a significant amount of challenging work remains to be done before they can be applied to real structures.

ACKNOWLEDGEMENTS

I wish to express my profound gratitude to my supervisors: Professor Leon Wegner and Professor Bruce Sparling. Throughout the duration of the present study, they have given me invaluable guidance, criticism, suggestions, and encouragement. Their enthusiasm and expertise were immersed into any little progress on my research work. For all of this, I will always be greatly appreciative.

Also, I would like to extend my appreciation to other members of my Advisory Committee: Professor M. Hosain, Professor M. Boulfiza, Professor G. Watson and Professor J. Peng for their examination and advice in the whole process.

The financial support from the ISIS Canada Network of Centres of Excellence is greatly appreciated.

A special thanks goes to Mr. Dale Pavier, Mr. Alan Duffy, Structural Laboratory technicians, and Mr. Doug Bitner, Mechanical Laboratory technician, for their constant assistance in the experimental work for this thesis.

Finally, I thank my wife, Tao who looked after our son Jonathan, my parents who looked after my younger daughter Julie, my wife's parents who looked after our older daughter Yi during my Ph.D. study. Without their understanding, encouragement and support, as a father of three young kids, I could not have completed my Ph.D. program.

DEDICATION

This thesis is dedicated to:

Tao

Yi, Julie and Jonathan

TABLE OF CONTENTS

LIST OF TABLES

LIST OF FIGURES

NOMENCLATURE

D_{ij} difference between $\Delta\bar{\phi}_i$ at location *i* and $\Delta\bar{\phi}_j$ at location *j*

C_{ij} normalized covariance between the change in mode shape at location *i* and *j*

$[C]$ Rayleigh damping matrix of a system

F flexibility matrix of a structure in undamaged state

F^* flexibility matrix of a structure in damage state

ΔF change in flexibility matrix

f uniform load flexibility

f'' uniform flexibility curvature

f_{detect} probability of successfully locating damage

$H(\omega)$ frequency response function

$[K]$ stiffness matrix of a system

$[M]$ mass matrix of a system

m_{ij} mean value of D_{ij}

S_{dij} standard deviation of D_{ij}

S_j standard deviations of the mode shape coordinates ϕ_j

S_j^* standard deviations of the mode shape coordinates ϕ_j^*

$\bar{S}_j$ standard deviations of the mean of the mode shape coordinates $\bar{\phi}_j$

$\bar{S}_j^*$ standard deviations of the mean of the mode shape coordinates $\bar{\phi}_j^*$

$S_{\Delta j}$ standard deviation of $\Delta\overline{\phi}_j$

Z_j normalized damage index at location j

β_j damage index at location j

β_{ji} damage index based on the change in modal strain energy at location j for the i^{th} mode

β_{MAC} ratio of $\tilde{\Delta}_{MAC}$ over $\overline{\Delta}_{MAC}$

Δ_{MAC} change in mode shape assurance criteria

$\overline{\Delta}_{MAC}$ mean value of Δ_{MAC}

$\tilde{\Delta}_{MAC}$ standard deviation of Δ_{MAC}

ε the strain at certain point of a structure

ϕ_i unit-mass normalized mode shape vectors for the ith mode of a beam in the undamaged state

ϕ_i^* unit-mass normalized mode shape vectors for the ith mode of a beam in the damaged state

$\Delta\phi_i$ change of the unit-mass normalized mode shape vectors for the ith mode of a beam in the damaged state

ϕ_i'' curvature vectors for the ith mode of a beam in the undamaged state

$\phi_i''^*$ curvature vectors for the ith mode of a beam in the damaged state

$\Delta\phi_i''$ change of the curvature vectors for the ith mode of a beam in the damaged state

ϕ_{ji} unit-mass normalized modal displacement at point j corresponding to the i^{th} mode

ϕ''_{ji} curvature at point j corresponding to the i^{th} mode

$\bar{\phi}_j$ mean value for the mode shape with different trials at location j in undamage state

$\bar{\phi}_j^*$ mean value for the mode shape with different trials at location j in damage state

$\Delta\bar{\phi}_j$ change of the mean of the mode shape at location j

κ the curvature at certain point of a structure

μ_β mean of damage indices for all locations

σ_β standard deviation of damage indices for all locations

ω_i angular natural frequency of the i^{th} mode

ξ damping ratio of a system

LIST OF ABBREVIATIONS

SHM	Structural health monitoring
NDE	Non-destructive evaluation
VBDD	Vibration-based damage detection
VBDI	Vibration-based damage identification
FFT	Fast Fourier transform
DFT	Discrete Fourier transform
MAC	Modal assurance criterion
COMAC	Co-ordinate modal assurance criterion
FRF	Frequency response function FRF

CHAPTER 1. INTRODUCTION

1.1 BACKGROUND

The primary goal of structural health monitoring (SHM) is to ascertain the condition or "health" of a structure so that decisions can be made with regard to the need for remediation. The amount of research relating to structural health monitoring of bridges has increased significantly in the past decades since a large number of bridges all over the world are in urgent need of condition assessment.

Mufti (2001) states that "In Canada, more than 40% of the bridges currently in use were built over 30 years ago. A significant number of these structures are in urgent need of strengthening, rehabilitation or replacement." In the United States, of the 570,000 existing highway bridges, about 187,000 bridges were classified as deficient in 1997, and an estimated 5,000 additional bridges were becoming deficient each year (Chase and Washer 1997). The majority of these bridges were built prior to 1970 and their conditions have yet to be fully assessed. Japan currently has over 140,000 existing bridges (Fujino and Abe 2001). Of these, most of the railway bridges were built prior to 1970, and over 50% of roadway bridges were built prior to 1980. Many of these bridges are in need of extensive maintenance.

Since it cannot be measured directly, structural health must be inferred from empirical data derived from the structure. Notwithstanding the unclear relationship between the empirical data and the actual condition (i.e. its load-carrying capacity and

reliability), the types of data that may be used for this purpose and the methods available to acquire those data are numerous. The method most commonly employed is visual inspection. While regarded as indispensable by transportation authorities, the reliability of visual inspections alone has been found to be remarkably low (FHWA 2001), leading many to acknowledge the need for additional methods to ascertain structural health.

Other SHM techniques include local non-destructive evaluation (NDE) methods and global damage detection methods. Many of these techniques are capable of detecting damage at an early stage, before the damage is visible and when mitigation measures may be less extensive and less costly. The large number of local NDE methods have been summarized in several references (Cartz 1995, Chong et al. 2001, Raj et al. 2002, Uomoto 2000). NDE techniques include chain drags, half-cell potential readings, radiography (including X-ray and gamma ray), ultrasonics, liquid penetrants, magnetic particles, eddy currents, and acoustic emissions. While each technique has its own strengths, the main advantage of local NDE methods as a group lies in the fact that they can be used to detect, locate, and/or characterize defects quite precisely. However, NDE methods are generally capable of interrogating only small areas at a time, so that the inspection of a large structure can be costly and time consuming. In addition, the region to be inspected must be accessible.

Global SHM methods, on the other hand, use changes in the overall response of a structure as indicators of damage. Global methods include static field tests (e.g. Jenkins et al. 1997, Bakht and Csagoly 1980), semi-static field tests (e.g. Schulz et al. 1995), and vibration-based methods (Doebling et al. 1996). These methods are capable of assessing the condition of an entire structure at once and are not limited to accessible components. Consequently, they can be performed relatively quickly once an appropriate system of

sensors has been installed. In many cases, they can also be set up for remote monitoring. To date, however, the ability of global techniques to locate and quantify the extent of damage is largely unproven unless applied to very simple structures.

One set of global SHM techniques receiving increasing attention in recent years is vibration-based damage detection (VBDD). The underlying principle for VBDD methods is relatively straightforward: since the dynamic characteristics of a structure (notably natural frequencies, mode shapes, and damping properties) are functions of its physical properties (e.g. material properties, geometrical configuration, distribution of mass, and support conditions), any changes to these physical properties caused by damage will be reflected in changes to the dynamic characteristics. VBDD methods therefore rely on accurate measurements of modal parameters, typically at both some baseline state (preferably pristine) and periodically during the operating life of the structure. Measured changes in these parameters are then used to detect, locate, and quantify damage.

A number of researchers have explored the use of vibration-based damage detection techniques, also sometimes referred to as vibration-based damage identification (VBDI) techniques, for assessing the condition of bridges and other types of structures (Doebling et al. 1996, 1998). VBDD techniques have been particularly successful when applied to rotating machinery (Shives and Mertaugh 1986, Farrar and Duffey 1999), but have also been successfully applied to well-defined aerospace or mechanical systems (West 1982; Hunt et al. 1990; Chang 1997, 1999) and simple structures such as beams or trusses (Pandey and Biswas 1994). The application of VBDD methods to civil engineering structures such as bridges has been complicated by a combination of factors, including the relatively large size of these structures, the inherently greater uncertainties in

material properties, support conditions, and connectivity of components, and variability in loading and environmental conditions. Nonetheless, a number of efforts have been made to apply VBDD techniques to real bridge structures over the last decade (Toksoy and Aktan 1994, Farrar et al. 1994, Jauregui and Farrar 1996, Zhang and Aktan 1998, Peeters 2000, Catbas and Aktan 2002, Ventura et al. 2002, Kim and Stubbs 2003). These studies have shown that the techniques can be used to detect the presence, location, and occasionally severity of damage on bridge structures. However, they typically address a small number of relatively severe damage scenarios and their findings often serve to further underscore the complexities associated with applying VBDD techniques to bridges.

After a thorough literature review of the development and application of VBDD techniques, Doebling et al. (1996) point out the critical issues for future research in damage identification and health monitoring:

> "One issue of primary importance is the dependence on prior analytical models and/or prior test data for the detection and location of damage. Many algorithms presume access to a detailed FEM (finite element model) of the structure, while others presume that a data set from the undamaged structure is available. Often, the lack of availability of this type of data can make a method impractical for certain applications. While it is doubtful that all dependence on prior models and data can be eliminated, certain steps can and should be taken to minimize the dependence on such information.
>
> The number and location of measurement sensors is another important issue that has not been addressed to any significant extent in the current literature. Many techniques that appear to work well in example cases actually perform poorly when subjected to the measurement constraints imposed by actual testing. Techniques that are to be seriously considered for implementation in the field should demonstrate that they can perform well under the limitations of a small number of measurement locations, and under the constraint that these locations be selected a *priori*.
>
> An issue that is a point of controversy among many researchers is the general level of sensitivity that modal parameters have to small flaws in a structure. Much of the evidence on both sides of this disagreement is anecdotal because it is only demonstrated for specific structures or systems and not proven in a fundamental sense. This issue is important for the

development of health-monitoring techniques because the user of such methods needs to have confidence that the damage will be recognized while the structure still has sufficient integrity to allow repair. A related issue is the discernment of changes in the modal properties resulting from damage from those resulting from statistical variations in the measurements: a high level of uncertainty in the measurements will prevent the detection of small levels of damage."

Despite the challenges, the development of reliable VBDD methods for constructed facilities has the potential for great benefit and cost savings to infrastructure owners. It is therefore important that their capabilities and limits be explored more fully, with particular consideration given to the practical case of early, small-scale damage scenarios and the use of relatively few sensors.

1.2 OBJECTIVES

The primary objective of this project is to investigate the capability of VBDD techniques to detect and locate small scale damage in bridge superstructures using a relatively small number of sensors.

Since this is a relatively new field, there remain a large number of questions related to the practical implementation of VBDD methods. The issues addressed specifically in this research are presented below:

- Damage in a structure needs to be detected at an early stage in order to reduce the cost of maintenance, but the change of dynamic characteristics of structures is relatively insensitive to small scale damage. The question therefore remains as to whether VBDD methods are sensitive enough to detect and locate small scale damage.

- Many different kinds of excitation methods can be used for dynamic testing. For example, ambient vibration, impact loading, random forced excitation and harmonic forced vibration can all be used to excite a dynamic response. As every type of excitation has its own advantages, this study assessed the relative influence of random and harmonic forced vibration on the measurement of mode shapes of structures and on the application of VBDD methods.
- Since building a reliable finite element model of a structure is costly and time-consuming, the ability of model-independent VBDD methods to detect and locate damage was studied.
- Intuitively, it may be expected that the higher modes would be more sensitive to damage due to their higher strain energy gradients, but that the accuracy with which these modes can be measured would be lower as a result of lower vibration amplitudes; in addition, due to their increased curvature, it is also evident that a higher number of measurement points would be required to properly define the higher mode shapes. With that in mind, the suitability of various modes for use in VBDD applications was assessed, along with the feasibility of using only the fundamental mode to detect and locate small scale damage.
- The influence of the structural type on the application of VBDD methods was evaluated, including innovative structures like steel-free bridge decks.
- There are many different kinds of sensors that can be used to acquire data during dynamic testing, such as accelerometers and electrical resistance strain gauges. Although electrical resistance strain gauges are probably the least expensive of

all sensors, their performance in detecting small scale damage is unclear due to low signal to noise ratios. Therefore, the effect that the noise inherent in the signals acquired by these sensors has on the measurement accuracy of dynamic tests was investigated.

- The influence of the number of sensors used, along with their spacing and location relative to the damage, was studied for the case of low level damage.
- Similarly, the influence of damage location, particularly damage near supports, was considered.
- The limitations of various VBDD methods proposed in the literature, the resolutions with which damage may be located by each one, and their robustness was studied.
- Finally, the use of various established criteria, such as the modal assurance criterion (MAC) to identify damage was investigated.

1.3 SCOPE AND METHODOLOGY

The basic premise of vibration-based damage detection techniques (VBDD) is the use of changes in dynamic properties (notably damping ratio, natural frequency and mode shape) of a structure caused by damage to detect and locate damage. For this project, the change in natural frequencies and mode shapes were the principal measures used to detect damage. As a result, the first step of VBDD was to accurately determine the change of mode shapes or natural frequencies; the second step was then to use these changes to reliably detect the damage.

Both experimental and numerical studies were undertaken in this project. The objective of the experimental studies was to investigate the possibility of using VBDD

techniques to detect small scale damage with a small number of sensors. The numerical studies were composed of two parts: eigenvalue analyses and transient dynamic analyses, both undertaken using finite element models. The primary purpose of the eigenvalue analyses was to evaluate the capabilities of the damage detection methods in the absence of excitation and measurement uncertainties. The primary purpose of the transient dynamic analyses was to investigate the possibility of using VBDD techniques to detect small scale damage using random forced vibration as the source of excitation in the presence of measurement uncertainties. Fig. 1.1 provides a graphical overview of the framework of this study.

The raw vibration data from both the experimental and the transient dynamic numerical analyses were obtained in the time domain. Signal processing was used to obtain the required mode shapes and natural frequencies. The details of signal processing are described in Chapter 3.

Experiments were carried under well controlled conditions in the Structural Laboratory in the College of Engineering at the University of Saskatchewan. No field testing was performed as part of this thesis. The laboratory specimens included a six-metre long half-scale steel-free bridge deck, and two twelve-metre long full-scale prestressed concrete box girders removed from an abandoned bridge. In all cases, damage was simulated by removing small square blocks of concrete from the top surface of the specimens.

For the experimental studies, a hydraulic shaker was used to generate the white noise random excitation for the purpose of identifying natural frequencies and resonant harmonic excitation for accurate measurement of mode shapes. In addition, ambient vibration, sand bag drops and hammer induced impacts were also used to excite a

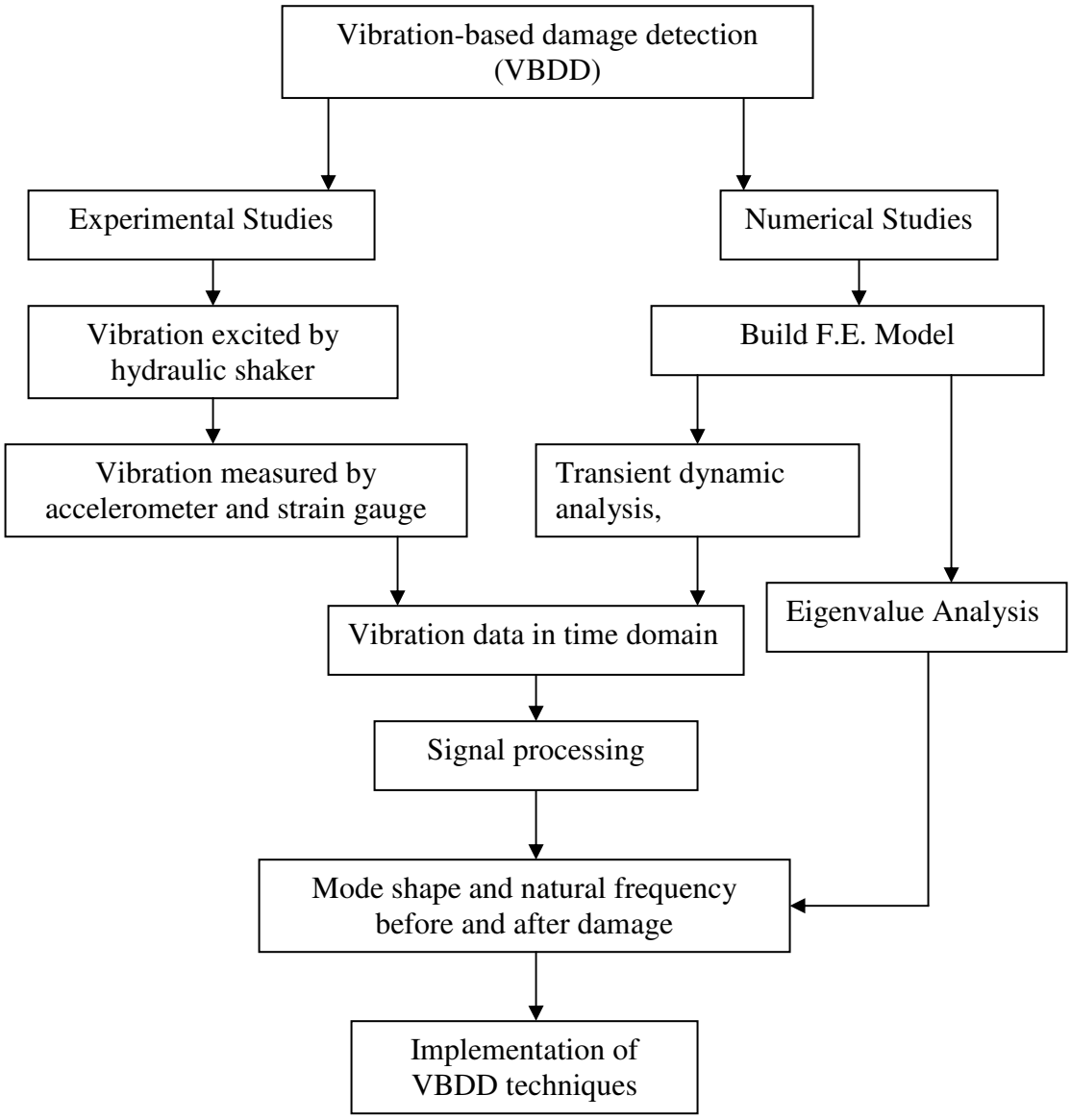

Fig. 1.1. The framework of the VBDD study

dynamic response for comparison. Accelerometers and electrical resistance strain gauges were used to measure the vibration response.

Five different VBDD methods proposed by others were investigated in this thesis. All of these methods are non-model based; that is, no finite element model was required

for the application of these methods. Instead, they relied only on changes in the measured natural frequencies and mode shapes.

A well known classification for damage identification methods, presented by Rytter (1993), defines four levels of structural health monitoring:

- Level 1 - Damage detection: determination that damage is present in the structure;
- Level 2 - Damage localization: determination of the geometric location of the damage;
- Level 3 - Quantification of the severity of the damage; and
- Level 4 - Prediction of the remaining service life of the structure

This thesis only focuses on Level 1 and Level 2 damage detection.

1.4 LAYOUT OF THESIS

This thesis consists of experimental and numerical studies of VBDD techniques. The experimental studies focused on using harmonic vibration to detect small levels of damage on a half-scale steel-free bridge deck (Chapter 4) and on full-scale prestressed concrete girders (Chapters 5 and 6). Finite element model-based eigenvalue analyses were used to investigate the capabilities of VBDD methods in the absence of experimental uncertainties (Chapters 4, 5, and 6). Numerical transient dynamic analysis was used to investigate the feasibility of using random vibration to detect damage (Chapter 7).

The contents of the different chapters in the thesis are described below.

Chapter 1 covers the background of structural health monitoring of civil engineering infrastructure, and the objectives, scope, methodology, and layout of this thesis.

In Chapter 2, a literature review of vibration-based damage detection methods, signal processing and data analysis techniques is presented.

Chapter 3 introduces the general procedures and setups for the vibration-based damage detection experiments on a steel-free bridge deck and two prestressed concrete girders in the structural laboratory. The signal processing program for transforming time-domain signals to frequency domain results and filtering the noise in the signals is also presented.

Chapter 4 describes the experimental and numerical studies related to the steel-free bridge deck system. Topics dealt within this chapter include building and calibration of the finite element model of the deck, eigenvalue analysis using the finite element model, and investigation of different damage states using numerical model. Also covered are the measurement of vibration of the experimental model using strain gauges and accelerometers, implementation of five different VBDD methods using both the numerical and experimental test data, and a proposed transverse location estimation procedure. Finally, the results of numerical and experimental studies are presented and discussed, and the performances of the five different VBDD methods are compared.

In Chapter 5, the conclusions from Chapter 4 are verified using a full-scale prestressed concrete box girder. Similar in format to Chapter 4, this chapter includes descriptions of building and calibration of the finite element model of the girder, eigenvalue analysis using the finite element model, investigation different damage states on the numerical model, the measurement of vibration of the laboratory model using

strain gauges and accelerometers, implementation of five different VBDD methods using both the numerical and experimental test data, and a transverse location estimation procedure. The chapter concludes with a discussion and comparison of the results of numerical and experimental studies, and a comparison of the performance of the five different VBDD methods.

Chapter 6 describes a study investigating the detection of multiple damage states on a prestressed concrete girder (i.e. the existence of more than one previously undetected damage locations). The specimen, instrumentation and test procedures are similar to those described in Chapter 5, except that this study investigated the capability of the VBDD techniques for detection of multiple damage states.

Chapter 7 focuses on using random vibration to detect damage. A transient dynamic analysis using the finite element model of the steel-free bridge deck is described. Issues considered included the influences of the severity of damage, the number of trials used to characterize mode shapes, the location of damage relative to the nearest sensor, the distance between damage and support, and measurement errors on the probability of successful damage detection.

Finally, Chapter 8, presents conclusions and recommendations for future research.

CHAPTER 2. LITERATURE REVIEW

2.1 OVERVIEW

The objective of this project was to investigate the capability of vibration-based damage detection (VBDD) techniques to detect and locate small scale damage in bridge superstructures using a relatively small number of sensors. VBDD is not a new research topic; many VBDD methods have been developed, but these methods have yet to be successfully applied to real, large civil engineering structures.

Presented in this chapter are reviews of the state-of-the-art in VBDD methods, classification of these methods according to the dynamic characteristics and the procedures used to detect damage, identification of the principles and implementation procedures of each method, and a discussion of the advantages, requirements and limitations of these methods. The application of VBDD methods to rotating machinery is then discussed and contrasted with the application of the same techniques to civil infrastructure. VBDD has enjoyed a great success when applied to rotating machinery, but has yet to show robust application to civil engineering infrastructure.

Signal processing is a basic and important step for the implementation of VBDD methods, and successful implementation often relies on the quality of signal processing. Therefore, this chapter reviews the signal processing methods most often used in VBDD.

Finally, the five VBDD methods applied in subsequent chapters of this thesis are presented, along with a justification for their selection.

2.2 VBDD TECHNIQUES

2.2.1 Overview

Over the past forty years, numerous damage indices, derived from damage induced changes to modal parameters, have been proposed. Detailed reviews of these have been provided by Doebling et al. (1996, 1998).

In this thesis, VBDD techniques are grouped based on specific measured dynamic properties. The various VBDD categories are described below.

2.2.2 Methods based on natural frequency shifts

The amount of literature related to damage detection using shifts in natural frequency is quite large (Loland and Dodds 1976, Cawley and Adams 1979, Salawu 1997 and Doebling et at. 1996). The observation that changes in structural properties should cause corresponding changes in vibration frequencies was, in fact, the impetus for using modal methods for damage identification and structural health monitoring. The simplicity of this approach makes it attractive as a means of damage detection. However, frequency shifts have proven to be relatively insensitive to damage; even worse, natural frequencies are very sensitive to changes in temperature and other environmental conditions.

The group of methods based on frequency change can be further subdivided into two categories: Category-1 methods are limited to Level 1 damage identification, while Category-2 are typically used for Level 2 and Level 3 damage identification.

Category-1 methods have been developed for many years. As early as 1976, Loland and Dodds (1976) used changes in the resonant frequencies and response spectra to identify damage in offshore oil platforms. Changes in resonant frequencies of 3% over time were observed and attributed to changes to the mass of the decks and to changes in the tide level. Frequency changes of 10% to 15% were observed when a structural modification was implemented that resembled a structural failure near the waterline. Thus, the authors concluded that change in natural frequency and the response spectrum could be used to monitor structural integrity.

However, Fox's numerical and experimental study (1992) of a beam yielded a different conclusion. In this study, it was found that changes in the resonant frequencies were a poor indicator of damage in a beam caused by a saw cut. In the experimental data, resonant frequencies were actually observed to increase slightly for some modes after the damage had been induced. These increases were attributed to inaccuracies in the methods used to estimate the resonant frequencies.

Kim and Stubbs (2003) investigated the bridge over the Rio Grand River on U.S. Interstate Highway 40, New Mexico. It was found that measured natural frequencies of the first three modes slightly increased when two separate small scale damage states were induced. The increases were attributed to changes in ambient temperature. After the introduction of two large scale damage states, however, the natural frequencies of the first three modes decreased compared with the undamaged state. It was concluded that the effect of temperature on dynamic properties appeared to be a significant barrier to the application of natural frequency-based damage detection methods to real civil engineering structures.

Based on simultaneous vibration and environment measurements on the Z-24 highway bridge in Switzerland, Steenackers and Guillaume (2005) proposed a method to establish the correlation between variations in temperatures and the resulting resonant frequency variations. The authors concluded that it is possible to distinguish changes in modal parameters due to damage from changes caused by temperature or other environmental variations.

Nasser et al. (2005) presented a simplified expression for defining the effect of temperature on modal parameters of interest. An explanation was provided as to how the temperature influences the flexural stiffness of a structure, and thus the modal parameters. Finally, they modified their damage detection tests for handling the measured temperature as a nuisance parameter. Applying statistical testing methods, they monitored deviations in the modal parameters while rejecting the temperature effect.

Category-2 frequency change based methods, which includes Level 2 or Level 3 damage identification, are used to estimate various damage parameters, such as crack length and/or location, from frequency shifts.

Cawley and Adams (1979) developed a damage identification technique based on changes in the natural frequency. Using experimentally derived natural frequencies and a numerically generated sensitivity matrix, the method predicted the location and magnitude of damage in plate structures. Results were presented from tests on an aluminium plate and a cross-ply carbon-fibre-reinforced polymer (CFRP) plate. Excellent agreement was shown between the predicted and actual damage sites; in addition, a useful indication of the magnitude of the defect was obtained.

It has to be noted, however, that the tests were carried out in a constant-temperature enclosure, which kept the structure being tested at $25 \pm 1^{o}C$ in order to be sufficiently stable to enable accurate frequency changes to be recorded. The test on the rectangular aluminium plate identified the natural frequencies of six modes with a resolution of 0.04%. The test on the trapezoidal cross-ply CFRP plate identified the natural frequencies of 10 modes with a resolution of 0.05%. In any attempt to apply this method to civil engineering structures, it must be recognized that it is very difficult to define so many modes with the same level of precision in a field test.

Many other Category-2 frequency change based methods were introduced in the literature reviews of Doebling et al. (1996 and 1998). All of them were model-based, typically relying on the use of finite element models. The requirement for an accurate model may be a drawback for these types of methods, especially for complicated structures.

A thorough review of the literature on structural damage detection through changes in eigenfrequencies is given by Salawu (1997). The major advantage of using only eigenfrequencies in the damage assessment of structures is that they are readily acquired, providing for an inexpensive structural assessment technique. However, special care is needed to filter out the influence of the environmental conditions such as temperature on the stiffness of the structure and the influence of temperature on boundary conditions.

A further drawback of techniques using only eigenfrequencies is that unrealistic damage patterns are sometimes found. These methods typically cannot distinguish between damage at symmetrical locations in a symmetric structure; in addition, the number of measured eigenfrequencies is generally lower than the number of unknown

model parameters, resulting in a non-unique solution. Therefore, mode shapes are often also considered within the damage assessment process.

2.2.3 Methods based on damping

The history of using damping for damage assessment is as long as that of using natural frequency shifts, although there is very much less literature related to the use of damping. The relative scarcity of literature about damping-based damage detection can be attributed to both the lack of accuracy in determining damping ratios from system identification techniques and the apparent lack of consistent correlation between the system damping and damage.

Adams et al. (1975) found that, with fibre-reinforced plastics, a state of damage could be detected by a reduction in the dynamic stiffness and an increase in damping, whether this damage was localized, as in a crack, or distributed through the bulk of the specimen as in the case of many micro cracks.

However, Casas and Aparicio (1994) did a test on partially cracked concrete beams and found that there was no clear relationship between crack growth and increase in damping. In fact, in the test performed, a cracked beam was found to possess values of damping slightly lower than those for an uncracked beam.

Also, Farrar and Jauregui (1998a) found that the damping in a steel plate girder bridge did not consistently increase or decrease with an increase in the level of damage.

Tests before and after structural repairs to a reinforced concrete bridge were conducted by Salawu and Williams (1995). No clear trend in damping value could be detected.

2.2.4 Methods based on change of mode shapes

(a) Direct change in mode shape

Several studies have indicated that changes in mode shape can be used to detect the presence and location of damage.

Single-number measures of mode shape changes have been proposed to detect damage. A common single-number measure is the Modal Assurance Criterion (MAC) (Ewins, 2000). The MAC value of two modes ϕ and ϕ^* (e.g. a mode shape in the undamaged and damaged states, respectively) is defined as:

$$MAC = \frac{\left|\sum_{j=1}^{n} \phi_j \phi_j^*\right|^2}{\sum_{j}^{n} \phi_j^2 \sum_{j}^{n} \phi_j^{*2}} \qquad [2.1]$$

with n equal to the degrees of freedom defining the mode shape. The MAC value therefore indicates the degree of correlation between two modes and varies from 0 to 1, with 0 representing the case where there is no correlation and 1 for the case with perfect correlation. The deviation from 1 for a MAC value derived from a comparison of two mode shape measurements on a given structure can be interpreted as an indication of damage in the structure. Allemang (2002) gives an overview of the use of MAC values and other related assurance criteria for the correlation between two modes.

Srinivasan and Kot (1992) found that changes in mode shapes were a more sensitive indicator of damage than changes in resonant frequencies for a shell structure. These changes were quantified using changes in the MAC values comparing the damaged and undamaged mode shapes.

The Co-ordinate Modal Assurance Criterion (COMAC) is differentiated from the MAC definition as it gives local information, as well as combining information from different modes. The COMAC at modal co-ordinate *j* using *m* modes is defined as (West 1984):

$$COMAC_j = \frac{\left|\sum_{i=1}^{m} \phi_{j,i} \phi_{j,i}^*\right|^2}{\sum_{i=1}^{m} \phi_{j,i}^2 \sum_{i=1}^{m} \phi_{j,i}^{*\,2}} \qquad [2.2]$$

If the modal displacements at co-ordinate *j* from two sets of measurements are identical, the COMAC value equals 1 for this co-ordinate. The smallest COMAC value at any point indicates the most likely location of damage.

Salawu and Williams (1995) found that the MAC values could be used to indicate which mode was benefiting most by structural repairs. Also, the COMAC values were found to give good indications of the presence and location of the repairs. In these tests, two of the three repaired points were correctly identified; however, two spurious locations were also identified. The success of damage localization using MAC and COMAC values was found to depend on whether or not the modes and measurement locations used in the analysis adequately reflected the damage. Thus, it was concluded that it was not possible to identify all the damaged areas, as demonstrated by the fact that one affected point was not properly identified.

Fox (1992) demonstrated that single-number measures of mode shapes such as the MAC were relatively insensitive to damage in a beam damaged by a saw cut. Graphical comparisons of the relative change in mode shapes proved to be the best way of

detecting the damage location when only resonant frequencies and mode shapes were examined.

The most straightforward way of using mode shapes is one which simply considers the difference between the damaged and undamaged unit-norm normalized mode shapes. Since damage is expected to cause a localized decrease in stiffness, the greatest change in mode shape displacement is expected to occur at the location of damage.

The definition of unit-norm normalized mode shape has to be introduced for understanding the change of mode shape method. For a free vibration system, the dynamic equilibrium equations can be written in the following format:

$$[m]\{\ddot{y}\}+[k]\{y\}=\{0\} \qquad [2.3]$$

where $[m]$ and $[k]$ are the system mass matrix and stiffness matrix, respectively, and $\{y\}$and $\{\ddot{y}\}$ are the displacement vector and acceleration vector of the system, respectively. The displacement vector $\{y\}$ associated with a specific mode of vibration can be expressed as follows:

$$\{y\}=\{\phi\}\sin(\omega t) \qquad [2.4]$$

where $\{\phi\}$ is a mode shape of the system, ω is the angular natural frequency associated with that mode shape, and *t* is time. Thus,

$$\{\ddot{y}\}=\omega^2\{y\}\sin(\omega t) \qquad [2.5]$$

Substituting Eq. 2.4 and Eq. 2.5 into Eq. 2.3, one obtains a set of simultaneous homogeneous algebraic equations as follows:

$$\left([k]-\omega^2[m]\right)\{\phi\}=\{0\} \qquad [2.6]$$

Solving this equation produces its i^{th} eigenvalue, $\omega_{io}^{\ 2}$, and its i^{th} eigenvector, $\{\phi_{io}\}$. The total number of eigenvalues and eigenvectors equals the rank of the stiffness matrix and mass matrix, i.e., the number of the degrees of freedom.

The amplitude of mode shape $\{\phi_{io}\}$ is always indeterminate. In a practical dynamic test, the amplitude of mode shapes is also indeterminate, but the shape of the mode, i.e., the ratio between different measurement points is determinate. For the purpose of graphical comparisons of the relative change in mode shapes, mode shapes must be normalized in order to compare the mode shapes before and after damage. Many different ways can be used to normalize mode shapes. For example, one of the elements in the eigenvector may act as a benchmark point, and then the values of the remaining elements can be determined. The drawback of this normalization method is that the change of mode shape at the damage location will be zero if the benchmark point is chosen at the damage location.

Another method is to use the mass matrix to normalize mode shapes using the following equation:

$$\phi_i^T [m] \phi_i = 1, \text{ and } \phi_i = \alpha \phi_{io} \qquad [2.7]$$

where ϕ_i is referred as to the i^{th} normalized mode shape, and α is a constant scalar. In order to apply this method, the mass matrix has to be known, which may be a time consuming and/or difficult process. However, most bridge structures consist of simply supported beams or continuous beams of uniform cross-section. In this case, the mass matrix can be simplified to the diagonal form of $[m] = m_u I$, where m_u is a constant scalar, and I is a diagonal identity matrix. Assuming that $m_u = 1$, then $[m] = I$. The normalization procedure then becomes much simpler:

$$\phi_i^T \phi_i = 1 \text{, or } (\alpha\phi_{io})^T (\alpha\phi_{io}) = 1 \quad [2.8]$$

Then

$$\alpha = \frac{1}{\sqrt{\phi_{io}^T \phi_{io}}} \quad [2.9]$$

The unit-norm normalized mode shape can then be calculated as follows:

$$\phi_i = \frac{\phi_{io}}{\sqrt{\phi_{io}^T \phi_{io}}} \quad [2.10]$$

Once the mode shapes have been suitably normalized, the change in mode shape can be expressed as:

$$\Delta\phi_i = \left|\phi_i^*\right| - \left|\phi_i\right|, \quad [2.11]$$

where ϕ_i and ϕ_i^* represent the i^{th} unit-norm normalized mode shapes before and after damage, respectively.

(b) Change in mode shape curvature

An alternative to using mode shapes directly to obtain information about changes in vibration characteristics is the use of mode shape derivatives, such as curvature (i.e. the second derivative of the mode shape with respect to position). It is first noted that for beams, the curvature κ, and bending strain ε, are directly related by

$$\varepsilon = \frac{y}{R} = \kappa \cdot y \quad [2.12]$$

where *R* is the radius of curvature, and *y* is the perpendicular distance from the point in question to the neutral axis. Practical issues related to the direct measurement of strain or the computation of strain from displacements or accelerations are discussed by some researchers (Pandey et al. 1991, Chance et al. 1994, Salawu and Williams 1994).

The use of mode shape curvatures for damage detection was introduced by Pandey et al. (1991). Assume that the i^{th} unit-norm normalized mode shapes for a structure in its original (baseline) and damaged states are known and are denoted by the vectors $\boldsymbol{\phi}_i$ and $\boldsymbol{\phi}_i^*$, respectively. The curvature vectors associated with these mode shapes are then given by $\boldsymbol{\phi}''_i$ and $\boldsymbol{\phi}''^*_i$, where the double prime notation represents the second spatial derivative. In that case, the increase in mode shape curvature associated with damage is calculated by

$$\Delta\boldsymbol{\phi}''_i = |\boldsymbol{\phi}''^*_i - \boldsymbol{\phi}''_i| , \qquad [2.13]$$

where evaluation of absolute values is carried out at the vector element, rather than the vector, level. Large positive peaks within the $\Delta\boldsymbol{\phi}''_i$ vector are indicative of the location of damage.

As an alternative to Eq. 2.13, Eq. 2.13a was suggested to locate damage in this study.

$$\Delta\boldsymbol{\phi}''_i = |\boldsymbol{\phi}''^*_i| - |\boldsymbol{\phi}''_i| \qquad [2.13a]$$

For a comparison of Eq. 2.13 and Eq.2.13a, the distributions obtained when two separated damage states were present on a prestressed concrete girder using the fundamental mode by Eq. 2.13 and Eq. 2.13a are plotted in Fig. 2.1 and Fig. 2.2, respectively. In Figs. 2.1 (a), (b), and (c), (corresponding to the use of 79, 15, and 7 measurement points were, respectively), more than two positive peaks are apparent, and the second highest peak does not necessarily correspond to the second damage state, making it impossible to determine the number of damage states. However, only two positive peaks appear in Figs. 2.2 (a), (b), and (c), with the two peaks clearly indicating the two damage states.

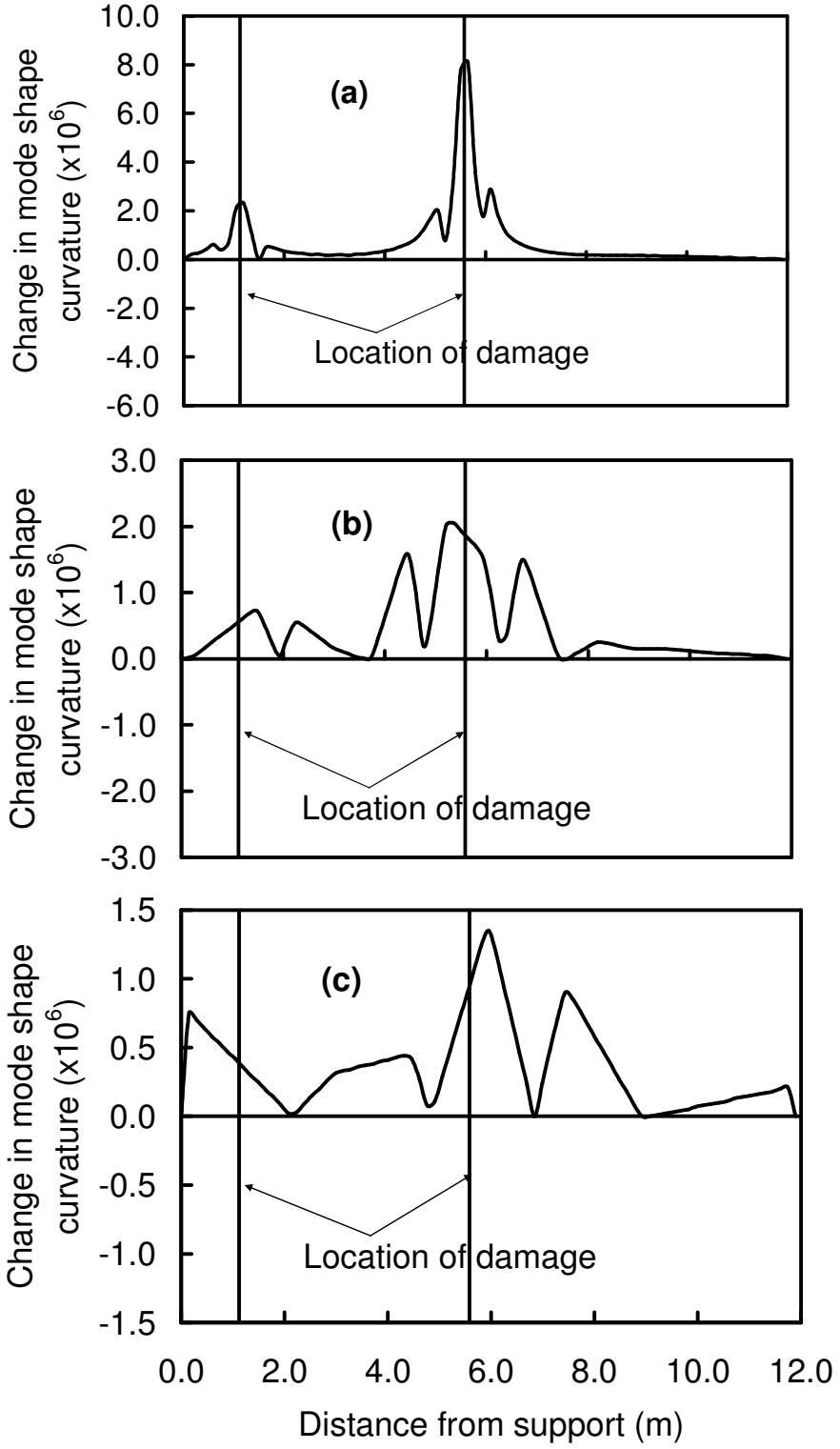

Figure 2.1. Localization of damage using Eq. 2.13 when (a) 79 measurement points, (b) 15 measurement points, and (c) 7 measurement points were used.

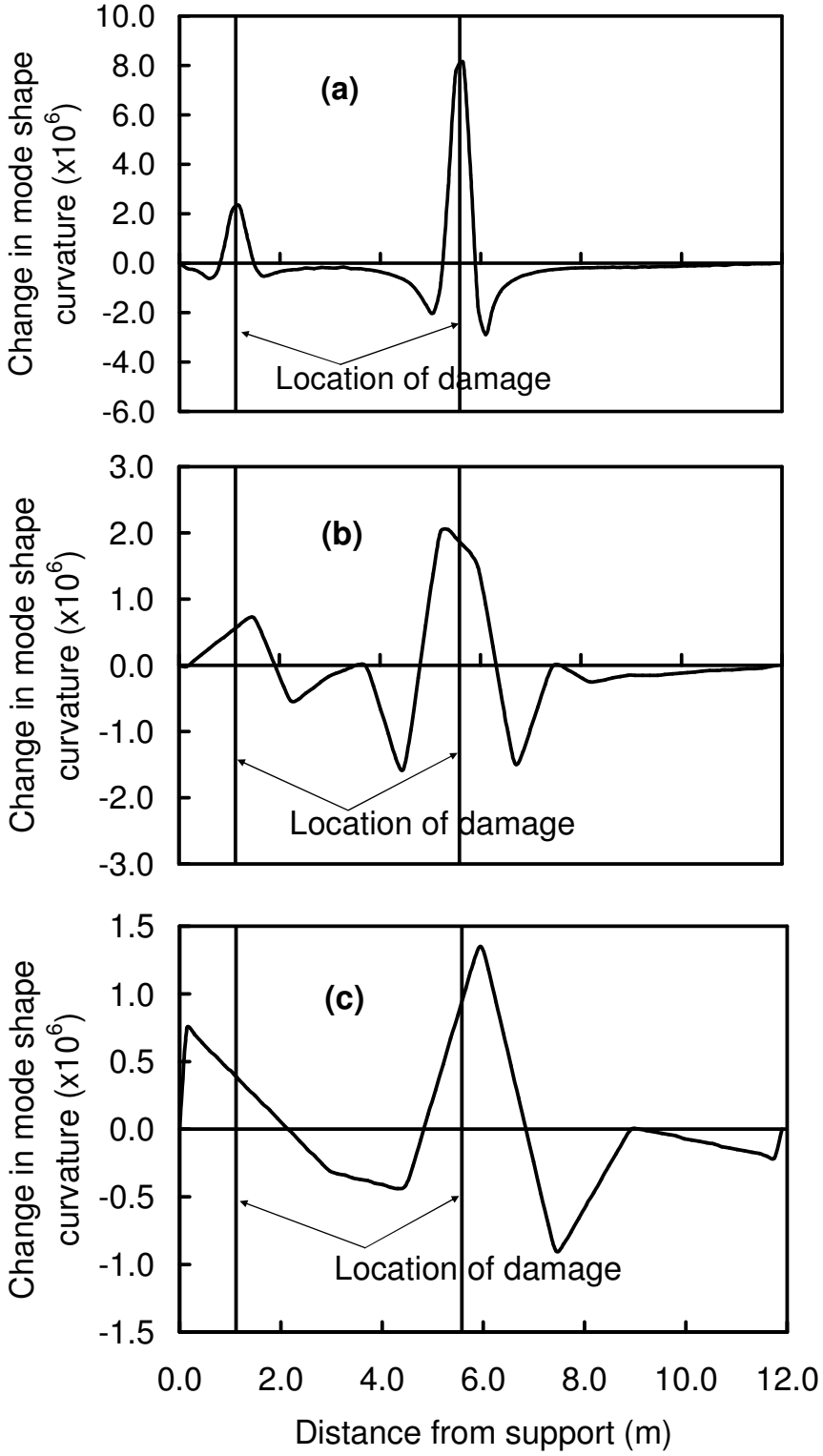

Figure 2.2. Localization of damage using Eq. 2.13a when (a) 79 measurement points, (b) 15 measurement points, and (c) 7 measurement points were used.

If multiple modes are used, the sum of differences in curvature may be employed as a damage indicator as follows:

$$\Delta\boldsymbol{\phi}'' = \sum_{i=1}^{n} \Delta\boldsymbol{\phi}''_i, \qquad [2.14]$$

where n is the number of modes used.

In practice, analytical expressions for mode shapes are not known; rather, mode shapes are defined by measured or calculated values at a finite number of discrete locations on the structure. If that is the case, mode shape curvature vectors can be computed using the central difference approximation for the second derivative, given by

$$\phi''_{ji} = \frac{\phi_{(j+1)i} - 2\phi_{ji} + \phi_{(j-1)i}}{h^2}, \qquad [2.15]$$

where ϕ''_{ji} is the curvature at point j corresponding to the i^{th} mode (i.e. the j^{th} element of the vector $\boldsymbol{\phi}''_i$), ϕ_{ji} is the displacement at point j corresponding to the i^{th} mode (i.e. the j^{th} element of the vector $\boldsymbol{\phi}_i$), and h is the average distance between discrete points in the $\boldsymbol{\phi}_i$ vector.

In their investigations, Pandey et al. (1991) made use of finite element models of simply supported and cantilever beams. They found that the modal curvature was a far more sensitive damage indicator than the MAC or COMAC values. They also suggested obtaining the experimental curvature mode shapes directly by measuring strains instead of displacements or accelerations.

Salawu and Williams (1994) employed a mode shape curvature measure computed using a central difference approximation. They compared the performance of this method to a direct change in mode shape method. They demonstrated that the curvature change did not typically give a good indication of damage using experimental data. They

pointed out that the most important factor was the selection of modes to be used in the analysis. In addition, if the methods (mode shape curvature and mode shape relative difference) were to be applied to a large structure, it would be necessary to measure the response at a sufficient number of points, possibly in a grid-like format, in order to reasonably refine the identification.

Chance et al. (1994) found that numerically calculating curvature from mode shapes resulted in unacceptable errors. Instead, they used measured strain to calculate curvature directly, which dramatically improved results.

(c) Change of modal strain energy (damage index method)

The use of change in modal strain energy (MSE) to detect structural damage has been employed in several studies. The concept of the method was introduced by Stubbs et al. (1992). They developed a method based on the decrease in modal strain energy caused by damage in a region located between two structural degrees of freedom, as derived from the curvature of the measured mode shapes. This method is referred to in the literature as the damage index method.

For a structure that can be represented as a beam, the damage index β_{ji} based on the change in modal strain energy at location *j* for the i^{th} mode can be expressed as follows:

$$\beta_{ji} = \frac{\left(\int_a^b \left[\phi_i''^*(x)\right]^2 dx + \int_0^L \left[\phi_i''^*(x)\right]^2 dx \right)}{\left(\int_a^b \left[\phi_i''(x)\right]^2 dx + \int_0^L \left[\phi_i''(x)\right]^2 dx \right)} \times \frac{\int_0^L \left[\phi_i''(x)\right]^2 dx}{\int_0^L \left[\phi_i''^*(x)\right]^2 dx} = \frac{NUM_{ji}}{DEN_{ji}}, \qquad [2.16]$$

where $\phi_i''(x)$ and $\phi_i''^*(x)$ are continuous mode shape curvature functions for the i^{th} mode in terms of distance, *x*, along the beam, corresponding to the undamaged and damaged structures, respectively, based on the second derivatives of continuous displacement

mode shape functions, $\phi_i(x)$ and $\phi_i^*(x)$. In addition, L is the length of the beam, and a and b are the limits of a segment of the beam over which the damage is being evaluated. In discrete form, assuming that the spacing between points in the mode shape vectors is uniform, calculation of the damage index is carried out by

$$\beta_{ji} = \frac{\left(\phi''^{*}_{ji}\right)^2 + \sum_{k=1}^{m}\left(\phi''^{*}_{ki}\right)^2}{\left(\phi''_{ji}\right)^2 + \sum_{k=1}^{m}\left(\phi''_{ki}\right)^2} \times \frac{\sum_{k=1}^{m}\left(\phi''_{ki}\right)^2}{\sum_{k=1}^{m}\left(\phi''^{*}_{ki}\right)^2} = \frac{NUM_{ji}}{DEN_{ji}}, \qquad [2.17]$$

in which all the variables have been defined previously. If more than one mode is used, a single index for each location, *j*, is formed by

$$\beta_j = \frac{\sum_{i=1}^{n} NUM_{ji}}{\sum_{i=1}^{n} DEN_{ji}} \qquad [2.18]$$

Assuming that the set of damage indices for the structure represents a sample population of a normally distributed random variable, a normalized damage indicator Z_j for a given location may be calculated as follows:

$$Z_j = (\beta_j - \mu_\beta)/\sigma_\beta, \qquad [2.19]$$

where μ_β and σ_β are the mean and standard deviation of damage indices for all locations, respectively. Damage indices falling two or more standard deviations from the mean value (i.e. $Z_j \geq 2$) are deemed to be indicative of a possible damage location (Stubbs et al. 1995).

Stubbs and Kim (1995) and Kim and Stubbs (2003) applied this method to a steel bridge. In these studies, damage was successfully localized using the three lowest vibration modes.

Again, Kim and Stubbs (1995) applied this approach to a model plate girder. It was observed that damage could be located confidently with a relatively small localization error and a relatively small false-negative (i.e., missing detection of true damage locations) error; however, a relatively large incidence of false-positive (i.e., prediction of locations that are not damaged) errors was observed.

Chen et al. (1999) used a two-dimensional strain energy distribution to detect damage on an aluminium plate and a composite plate subjected to different damage scenarios. The method was shown to be effective for damage detection on plates.

2.2.5 Methods based on flexibility of a structure

Another category of damage identification methods makes use of the dynamically measured flexibility matrix to estimate changes in the static behaviour of a structure. The flexibility matrix is defined as the inverse of the stiffness matrix; it reflects the relationship between the applied static force and the resulting structural displacement. In the flexibility matrix, therefore, each column represents a set of nodal displacements of the structure due to a unit force applied at one of the degrees of freedom (DOF). Both change in flexibility method and change in uniform flexibility curvature method belong to this category of methods.

(a) Change in flexibility method

The flexibility matrix of a structure in its undamaged and damaged states, denoted by $\boldsymbol{F}$ and $\boldsymbol{F}^*$ respectively, may be estimated from a few of the lower vibration modes as follows (Pandey and Biswas 1994):

$$\mathbf{F} \approx \sum_{i=1}^{n} \frac{1}{\omega_i^2} \boldsymbol{\phi}_i \boldsymbol{\phi}_i^T \ , \qquad [2.20]$$

$$\mathbf{F}^* \approx \sum_{i=1}^{n} \frac{1}{\omega_i^{*2}} \boldsymbol{\phi}_i^* \boldsymbol{\phi}_i^{*T} \ , \qquad [2.21]$$

where ω_i is the angular frequency of the i^{th} mode, n is the number of measured modes, $\boldsymbol{\phi}_i$ are the unit-norm normalized mode shapes, as above, and asterisks signify properties of the damaged structure. The change in flexibility caused by damage can be obtained from the difference between the respective matrices:

$$\boldsymbol{\Delta}\mathbf{F} = \mathbf{F}^* - \mathbf{F} \, , \qquad [2.22]$$

where $\boldsymbol{\Delta F}$ is the change in flexibility matrix. If, for the j^{th} column of this matrix, $\bar{\delta}_j$ represents the maximum of the absolute values of elements in that column, then

$$\bar{\delta}_j = \max\left|\Delta F_{ij}\right|, \ i = 1 \ldots m, \qquad [2.23]$$

where ΔF_{ij} are elements of $\boldsymbol{\Delta F}$, and m is the number of points at which the mode shape is defined. The parameter $\bar{\delta}_j$ is taken to be a measure of the change of flexibility at point j. The largest value of $\bar{\delta}_j$ is therefore indicative of the most probable location where the change in physical properties (i.e. damage) is located.

Pandey and Biswas (1994) applied the change in flexibility method to several numerical examples and to an actual spliced beam. The success of the proposed method with the experimental data suggested the practical applicability of this method on full-scale structures. A numerical study indicated that this method worked best when damage was located at a section where high bending moments occur. It was found that the flexibility matrix was only very slightly affected by high-frequency modes and, hence, could be accurately estimated from a few low frequency modes. Another advantage of measuring only the lower modes is that one does not have to be concerned about non-linearity, which can be a problem for higher frequencies for some structures.

(b) Change in uniform flexibility curvature method

Zhang and Aktan (1995) found that the change in the curvature of the uniform load surface (i.e. the deformed shape of the structure when subjected to a uniform load), calculated using the uniform load flexibilities, as defined below, was a sensitive indicator of local damage. They stated that changes in the uniform load surface are appropriate to identify uniform deterioration.

The j^{th} column of the flexibility matrix $\boldsymbol{F}$ calculated by Eq. [2.20] corresponds to the deflected shape assumed by the structure when a unit load is applied at the j^{th} degree of freedom. The sum of corresponding elements of all columns of the flexibility matrix therefore produces a vector representing the deflected shape if a unit load is applied at each degree of freedom simultaneously. This shape is referred to as the uniform load flexibility, and is represented here by the vector $\boldsymbol{f}$.

Elements of the uniform flexibility curvature vector, $\boldsymbol{f''}$, may be calculated from $\boldsymbol{f}$, again using the central difference approximation

$$f_j'' = \frac{f_{j+1} - 2f_j + f_{j-1}}{h^2}, \qquad [2.24]$$

where h is the average distance between measurement locations.

The absolute increase value of the curvature at location j can be evaluated as

$$\Delta f_j'' = \left| f_j''^* - f_j'' \right| \qquad [2.25]$$

where the asterisk indicates the damaged state. The largest positive value of $\boldsymbol{\Delta f''}$ was taken to be indicative of the location of damage.

Again, as an alternative to Eq. 2.25, Eq. 2.25a was suggested to locate damage in this study.

$$\Delta f_j'' = \left| f_j''^* \right| - \left| f_j'' \right| \qquad [2.25a]$$

The reason that used Eq. 2.25a as an alternative to Eq. 2.25 in this study is the same as that described in the previous section for Eq. 2.13a as an alternative to Eq. 2.13.

(c) Other flexibility-based methods

There are also some similar methods based on the change of flexibility of structures reported in the literature, the principle of these methods are same, their procedures have some difference.

Aktan et al. (1994) proposed the use of modal flexibility as a "condition index" to indicate the relative integrity of a bridge. This technique was applied to two bridges for which the modal flexibility derived from dynamic tests were verified by correlating with the static deflections induced by a set of truck-load tests. It was found that modal flexibility was a reliable tool for condition assessment. In addition, they calibrated three-dimensional analytical models of the bridges to experimental data, then used the calibrated models as a basis for condition assessment in the absence of baseline experimental data.

Toksoy and Aktan (1994) computed the measured flexibility of a bridge and examined the cross-sectional deflection profiles with and without a baseline data set. It was found that anomalies in the deflection profile could indicate damage even without a baseline data set.

Mayes (1995) used the flexibility synthesized using the results of the modal test of a bridge to locate damage. The method required experimental frequency response function data measured at discrete locations along the major bridge load paths. For bridge damage applications, the algorithm was found to be most effective when applied to static

flexibility shapes estimated using a truncated set of six mode shapes rather than from individual mode shapes. The algorithm compared “before damage” and “after damage” data to locate physical areas where significant stiffness changes had occurred. Damage was correctly located in the two most significant damage cases using this technique.

2.2.6 Methods based on model updating

Another class of damage identification techniques is based on the modification of structural model parameters in a numerical model, such as stiffness, mass, or damping, to match as closely as possible the measured static and/or dynamic response. Alternative updating techniques can be formulated based on the choice of the objective function to be minimised, on the constraint conditions of the problem and on the numerical scheme used to solve the minimisation problem.

Model based techniques for damage assessment require the development of a numerical model (in most cases a finite element model (FEM)) of the structure. In FEM updating, an optimization problem is established in which differences between experimental and numerical modal data have to be minimised by adjusting uncertain model parameters. The numerical model has to correspond as closely as possible to the real structure in order to detect, localize and quantify the damage on the basis of the tuned model.

The core of the solution procedure is the minimisation of the residual between the experimental and analytical modal properties that describe the dynamics of the structure. Furthermore, it is necessary to choose the appropriate updating parameters. Examples of updating parameters include the (spring) stiffness of supports, bending and torsional stiffness of individual beam elements, and parameters involving mathematical expressions that describe the damage over several elements (damage functions).

Another aspect in the minimisation process is the composition of the residual. Apart from the resonance frequencies, the residual can contain modal displacements, modal curvatures and nearly any dynamic characteristic of the system: frequency response functions, elements of the Modal Assurance Criterion (MAC) matrix, elements of the orthogonality matrices, etc. Different terms in the residual are often weighted to express the reliability of the measured dynamic parameters of the system, and constraints on the updating parameters are often imposed.

The advantage of model updating damage identification methods is that one can use them to estimate the severity of damage (Level 3 methods); some of these methods can also be used to detect damage without the baseline of an undamaged state. Many papers about this class of methods have been published, as described below; however, limited success has been demonstrated to date. Therefore, this remains a very challenging research topic.

Hajela and Soeiro (1990) presented two optimization methods to detect structural damage, an output error approach and an equation error approach. Both of these methods were tested on a fifteen-bar planar truss and a two-bar planar truss. Damage was successfully detected on the numerical model (no physical model was investigated).

Zimmerman and Kaouk (1992) implemented a subspace rotation algorithm, a model updating method, for damage detection. The algorithm makes use of the original finite element model and a subset of derived eigenvalues and eigenvectors. This technique was successfully applied to determine the damage location and damage extent of a six bay truss (no physical model was tested).

Beck and Katafygiotis (1992a, b) described a method for detecting significant changes in stiffness distribution through continual updating of a structural model using

vibration measurements. A Bayesian probabilistic formulation was used to treat uncertainties which arose from measurement noise, modelling errors, and an inherent non-uniqueness common to this type of inverse problem. Two different structural models were considered using numerically generated dynamic data: a six-story planar shear building model, and a finite element model of a two-span bridge. The damage probabilities of these two structures were computed by this method (again, no physical model was used).

Fares and Maloof (1997) developed a probabilistic framework to detect and identify anomalies such as damage in structures. The framework presented related the sensitivity of the measurements to damage, the rate of false detection or identification, error levels and the capability of detecting and identifying particular damage configurations. The application was used to detect and identify cracks extending part-way through a plate using surface strain measurements (only a numerical model was considered).

Zimmerman and Smith (1992) performed some dynamic testing on a physical model, and used the measured data to refine a finite element model. Damage was then induced in the finite element model. Using the subspace rotation algorithm, damage in the numerical model was successfully detected and identified.

Zimmerman and Kaouk (1994) presented the basic minimum rank perturbation theory. This approach was motivated by the observation that damage will tend to be concentrated in a few structural members, rather than distributed throughout a large number of structural members. Thus, the perturbation matrices will tend to be of small rank. The method was successfully used to detect the damage on a eight-bay truss, in which damage was induced by removing specified members.

Amin Abdel Zeher (2002) experimentally demonstrated that a member removed from a truss can be detected using model updating-based methods.

Hu et al. (2001) described a model updating method that employed a special subspace rotation algorithm. They successfully located the damage and identified the magnitude of the damage on an aluminium beam with two fixed ends. However, it should be noted that the saw-cut damage was very significant, extending through half of the cross-section.

Casas and Aparcio (1994) presented a method for identifying the cracked portions of concrete beams by using a non-linear, least squares method to identify the equivalent moments of inertia for beam elements in a finite element model. The method was based on minimizing the error between measured eigenfrequencies and modal amplitudes and those calculated using a finite element model. In this study, damage was successfully identified on a physical model. Once again, though, the damage was quite severe, causing shifts in the fundamental natural frequency of 15%.

In summary, this class of methods is very attractive due to their ability to estimate the severity of damage and to detect damage without the baseline of an undamaged state, but it is still in a developmental stage. At this point, model updating methods have not been successfully used to detect small scale damage on a physical model, even in an ideal laboratory environment. Another potential drawback for this class of methods is the requirement for a numerical model.

2.2.7 Neural network methods

In recent years the interest in using neural networks to estimate and predict the extent and location of damage in complex structures has been increasing. Neural networks have been promoted as universal function approximators for functions of

arbitrary complexity. The most common neural network in use is the multilayer perceptron (MLP) trained by back-propagation (Wu et al. 1992). The so-called "backprop" neural network is a system of cascaded sigmoid functions where the sum of weighted and biased outputs of one layer is used as the inputs to next layer. A sigmoid function is the solution to a first order differential equation. Once an architecture for given network is chosen, the actual function represented by the neural network is encoded by the weights and biases. The backpropagation learning algorithm is a technique for adjusting the weights and biases by minimizing the error between the predicted and measured outputs.

Wu et al. (1992) used a backprop neural network to identify damage in a three-story building modelled as a two-dimensional "shear building" driven by earthquake excitation. The damage was introduced by reducing the stiffness of a specified member by 50% to 70%. The neural network was used to identify the level of damage in each of the members using the Fourier transform of acceleration data. Acceleration spectrum data from 0 Hz to 20 Hz were used as network inputs. The first attempt relied on using only acceleration data from the top floor (third floor). The neural network was only able to identify third floor damage with any accuracy. A second network was implemented that used acceleration data from the first and second floors as inputs. This network was able to diagnose damage on the first floor and third floors but was still unable to predict damage to the second floor with any accuracy. The latter method relied on a complete knowledge of the time histories of two of the three DOF.

Doebling et al. (1996) provided a thorough literature review of neural network-based damage identification methods. In that literature, it was found that damage was typically modelled by a linear process; specifically, most studies used changing member shape

and/or cross-sectional area to describe damage. Therefore, the considered cases did not produce a non-linear dynamic system, which may be expected in a real damaged structure.

Masri et al. (1993, 2000) developed a procedure based on the use of an artificial neural network for the identification of damage in nonlinear dynamic systems and applied the method to a damped Duffing oscillator under deterministic excitation. The ability of the neural network was invoked to predict the response of the same nonlinear oscillator under stochastic excitations of differing magnitudes. It was shown that neural networks can provide a high-fidelity mathematical model of nonlinear systems encountered in the applied mechanics fields.

Masri et al. (1996) successfully used a neural network-based approach to detect relatively small changes in structural parameters, even when the vibration measurements were polluted by noise.

As compared with other damage detection methods, the identification of damage using neural networks is still in its infancy. Most of the studies on this topic have assumed a detailed knowledge of the mechanical structure, including the complete mass and stiffness matrices. A few published methods performed an identification of system parameters based on measured data so that detailed knowledge of the structure was not required a priori. Further research about practical application of this class of methods is required.

2.3 CONTRASTING THE APPLICATION OF VBDD METHODS TO ROTATING MACHINERY AND CIVIL STRUCTURES

A particular application of vibration-based damage detection that has perhaps enjoyed the greatest success is that of damage detection in rotating machinery. In contrast, these methods have yet to show robust application to civil engineering infrastructure. Farrar and Duffey (1999) state that:

> …the application of vibration-based damage detection to rotating machinery has made the transition from a research topic to successful implementation by practicing engineers. In contrast, vibration-based damage detection in large structures, such as bridges, has been studied for many years, but this application has in most cases, not progressed beyond the research phase.

By comparing and contrasting rotating machinery and civil engineering infrastructure applications, it is hoped that some insight will be gained into the limitations of VBDD techniques applied to civil engineering infrastructure and how to improve these techniques for this application.

Roth and Pandit (1999) reported on some recent progress in generalized failure prediction indices capable of monitoring the condition of a wide variety of manufacturing equipment. These methods could be broken down into the following categories: time-domain methods, transform-domain methods, and time-frequency methods. Briefly, frequency-domain methods characterize changes in machine vibrations over a given time window; in particular, these methods have been applied to roller bearings, as roller bearings typically fail by localized defects caused by fatigue cracking and the associated removal of a piece of material on one of the contact surfaces of the bearing. Time domain and time-frequency methods have been shown to have

application to non-stationary faults, such as those associated with machines that exhibit different phenomena in different phases of the machine cycle.

The main difference between rotating machinery and large civil engineering infrastructure may be summarized as follows:

(a) Rotating machinery usually has well-known homogeneous material properties, support conditions and connectivity of components, whereas large civil engineering structures have inherently greater uncertainties in material properties, support conditions, and connectivity of components.

(b) Rotating machinery is often situated in a relatively protected environment and operates under relatively constant conditions, whereas civil engineering infrastructure experiences a greater variability in environmental and operational conditions.

(c) Civil engineering infrastructure is generally composed of one-of-a-kind items with little or no data available regarding the behaviour of the damaged structure. In contrast, rotating machinery is often available in large inventories with response data available for both the undamaged and damaged systems. It is therefore much easier to build databases of damage-sensitive features from these inventories.

(d) One common point in practical health monitoring applications is that measured vibration inputs are generally not applied to either rotating machinery or civil engineering infrastructure. However, rotating machinery typically exhibits response to a harmonic-like input, while the traffic and wind excitations for civil infrastructure tend to produce inputs that are assumed to be random in nature.

(e) Because the approximate location of damage is generally known for rotating machinery, vibration test equipment can consist of a single sensor and a single channel FFT analyzer only. Monitoring of civil engineering infrastructure, on the other hand, normally must be performed with a relatively large number of sensors distributed over a relatively large spatial region. For damage identification on a highway bridge, for example 30 to 50 data acquisition channels represents a relatively sparsely instrumented bridge.

(f) A well developed database of features corresponding to various types of damage has been developed by researchers studying rotating machinery. Many of these features are qualitative in nature and have been developed by comparing vibration signatures from undamaged systems to signatures from systems with known types, locations and levels of damage. Many of the features observed in the vibration signatures of rotating machinery result from nonlinear behaviour exhibited by the damaged system. Features used to identify damage in civil engineering infrastructures, on the other hand, are most often derived from linear modal properties such as resonant frequencies and mode shapes. These features must be identified before and after damage and require a distributed system of sensors for adequate definition. Few studies report the development of damage-sensitive features for civil engineering infrastructures based on nonlinear response characteristics.

In short, the application of vibration-based damage detection to large civil engineering structures is much more challenging than that associated with rotating machinery. Researchers in the vibration-based damage detection field as applied to civil infrastructure evidently have a long way to go, but could learn from experiences of the

rotating machinery researchers. At the same time, new methods for civil engineering infrastructure are required because the conditions encountered with civil infrastructure are significantly different from those related to rotating machinery. At this stage, much of the basic research in the civil engineering field has yet to be done before research on the more complex issues can be carried out.

2.4. SIGNAL PROCESSING

Signal processing can be classified as time domain analysis of a signal, frequency domain analysis of a signal and time-frequency domain analysis of a signal. For the purpose of damage detection in structures, changes to natural frequencies, mode shapes and damping ratios are used to identify damage, so frequency domain and time-frequency domain analyses of signals are often used. These will be discussed in this section.

2.4.1. Frequency domain analysis of a signal

2.4.1.1. Discrete Fourier Transform (DFT) and Fast Fourier Transform (FFT)

The basic premise of VBDD is to use changes to the dynamic properties (notably natural frequencies, mode shapes, and damping ratios) of a structure caused by damage to identify the damage. However, the acquired signals of vibration are typically obtained in the time domain. It is much more convenient to identify the dynamic properties of a structure from a frequency response spectrum than directly from time-domain data. Therefore, a Fourier transform is required to convert the signal from the time-domain to the frequency-domain.

The vibration responses of a structure are continuous in time, but the raw data recorded in a computer through a data acquisition system are sampled at discrete intervals. Therefore, a discrete Fourier transform (DFT) is required.

A DFT is a discrete approximation of the Fourier integral, which is the analog counterpart of the DFT. The fast Fourier transform (FFT) is an algorithm for computing the DFT. The major advantage of the FFT is the speed with which it analyzes large numbers of waveform samples. By making use of periodicities in the sinusoidal functions that are multiplied to do the transforms, the FFT greatly reduces the amount of calculation required. Ramirez (1985) gave the details of the implementation of the FFT.

2.4.1.2. Peak-Picking method (PP)

For civil engineering, the simplest approach to estimate the modal parameters of a structure subjected to a random vibration is the so-called Peak-Picking (PP) method. The method is named after the key step of the method: the identification of the natural frequencies as the peaks of a Fourier response spectrum plot. It is the most widely used method in civil engineering, probably due to its simplicity. The theoretical justification of the method is given in the following paragraphs:

For the forced vibration of a single degree of freedom system, the Fourier transform of the displacement of the system, $X(\omega)$, can be evaluated as follows (Clough and Penzien 1975):

$$X(\omega) = H(\omega)P(\omega) \qquad [2.26]$$

where ω is the frequency of excitation, $P(\omega)$ is the Fourier transform of the excitation force, and $H(\omega)$ is the complex dynamic amplification factor of the system. $H(\omega)$ can be evaluated as follows:

$$H(\omega) = \frac{1}{1-\left(\frac{\omega}{\omega_o}\right)^2 + 2\xi\left(\frac{\omega}{\omega_o}\right)*i} \qquad [2.27]$$

where ω_o is the natural frequency of the system, and ξ is the damping ratio of the system.

The magnitude of $H(\omega)$ is

$$\left|H(\omega)\right| = \frac{1}{\sqrt{\left[1-\left(\frac{\omega}{\omega_o}\right)^2\right]^2 + \left[2\xi\left(\frac{\omega}{\omega_o}\right)\right]^2}} \qquad [2.28]$$

The dynamic amplification factor magnitude vs. frequency ratio is shown in Fig. 2.3. The peak in the dynamic amplification factor curves occur when $\frac{\omega}{\omega_o} = \sqrt{1-2\xi^2}$, at which point the dynamic amplification factor is given by

$$\left|H(\omega)\right|_{\max} = \frac{1}{2\xi\sqrt{1-\xi^2}} \approx \frac{1}{2\xi} \qquad [2.29]$$

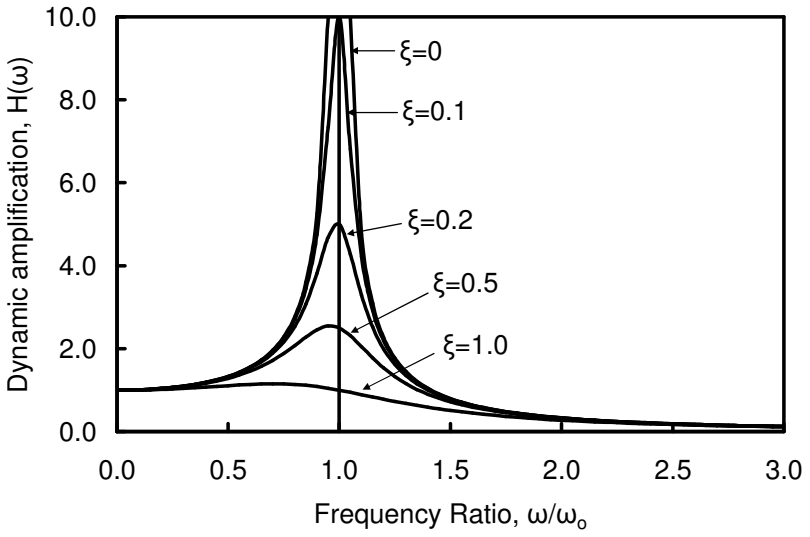

Figure 2.3. Dynamic amplification factor vs. frequency ratio.

For steel structures and concrete structures in civil engineering, the range of damping ratios is usually between 0.5% and 2%; therefore, at the peak, $\omega = (0.999987 \sim 0.998) * \omega_o$, meaning that the location of the peak in the dynamic amplification factor curve is very close to the natural frequency of the system.

However, the dynamic amplification factor in a field test is typically unknown; instead, the response of the system is measured using some form of dynamic test. Fortunately, as indicated by Eq. 2.26, the Fourier transform of the displacement of the system (i.e. the response of the system) is equal to the product of the Fourier transform of the excitation and the dynamic amplification factor. Fig. 2.4 shows the relationship between the excitating force, dynamic amplification factor and response of the system; as demonstrated in Fig. 2.4a, random excitation has been assumed for this example. The response of the system shown in Fig. 2.4c is affected by both the dynamic amplification factor and the frequency content of the exciting force. Because of variation in the forcing spectrum, therefore, the highest peak of the response of the system will not necessarily coincide with the highest peak of the dynamic amplification factor.

By definition, however, a white noise random excitation features a nearly horizontal spectrum, as shown in Fig. 2.5a. In that case, the response spectrum shown in Fig. 2.5c is very similar to the dynamic amplification factor curve provided in Fig. 2.5b. Therefore the peak-picking method can be more readily used to predict the natural frequency of a system when a white noise random excitation is used in a dynamic test. In practical dynamic testing, pure white noise cannot be attained, meaning that the frequency content of the force will vary from test to test, producing potential variations in identified natural frequencies.

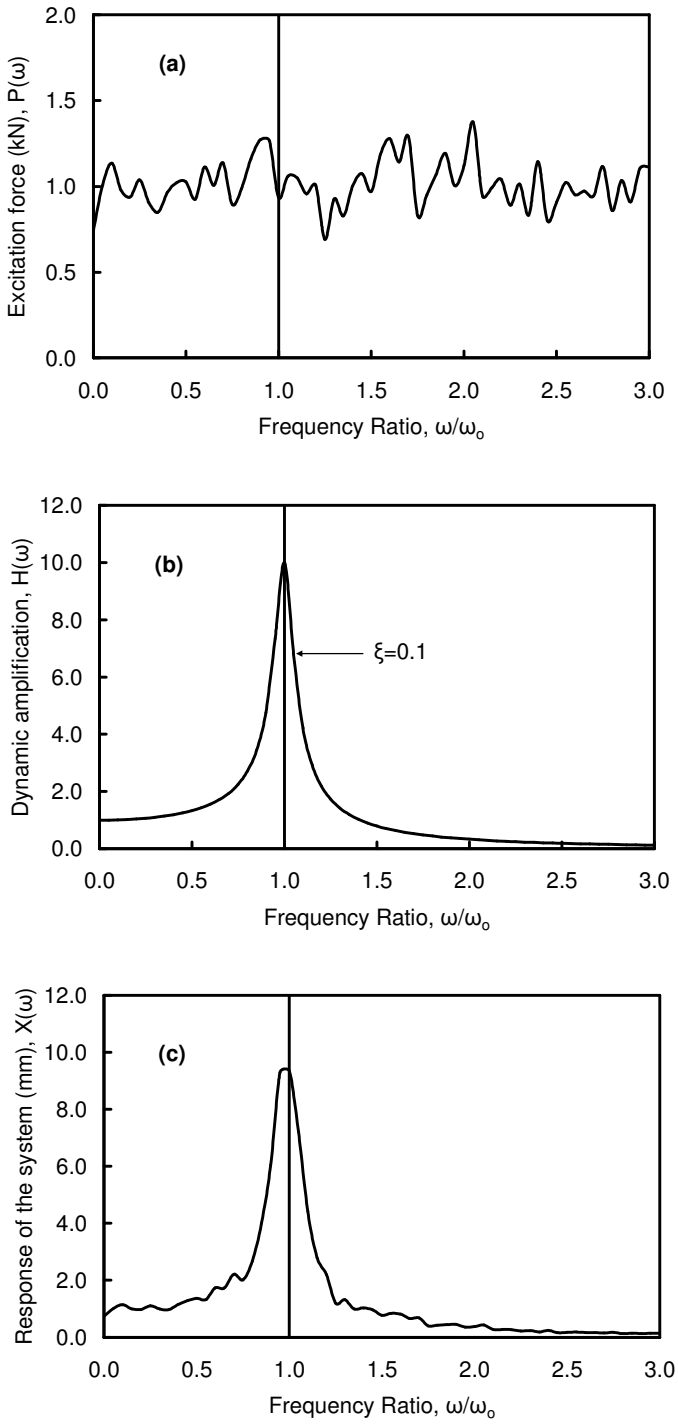

Figure 2.4. The relationship between excitation force, dynamic amplification factor and response of the system: (a) spectrum of exciting force; (b) dynamic amplification factor function; and (c) spectrum of system response.

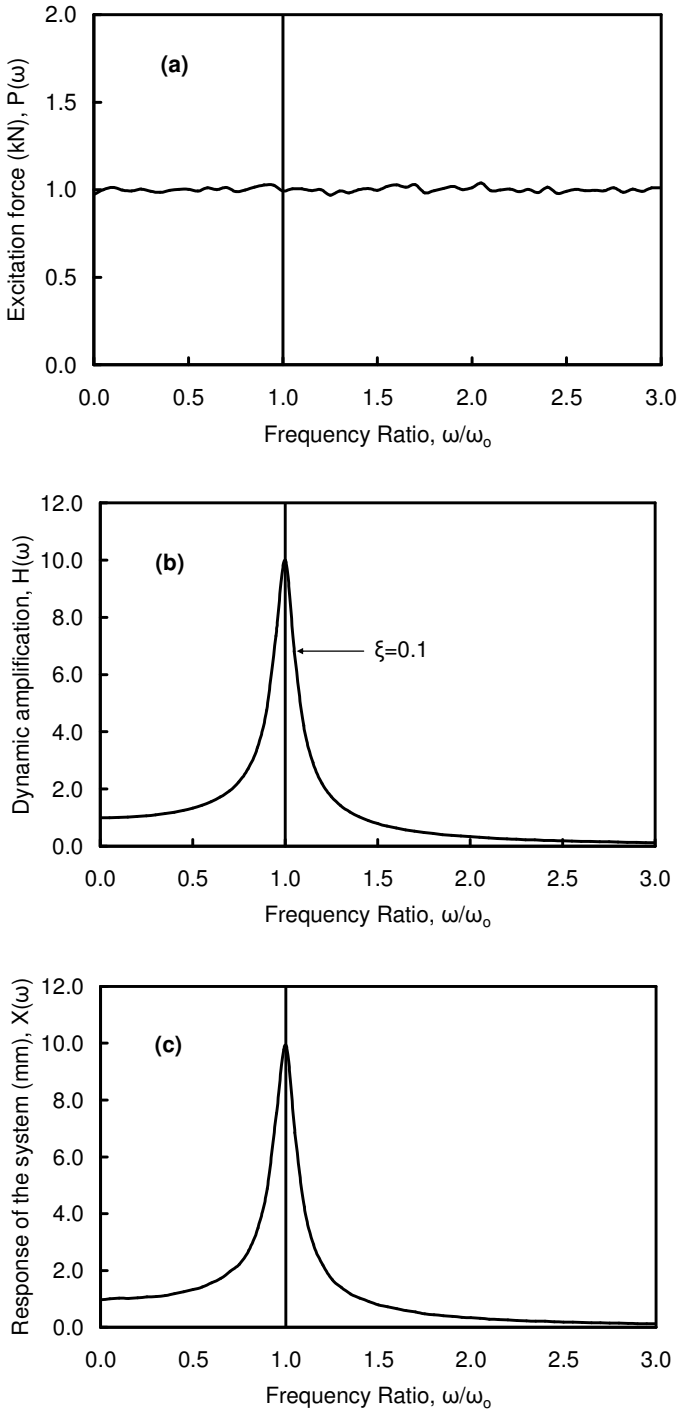

Figure 2.5. Using a white noise random excitation to identify the natural frequency of a system: (a) spectrum of exciting force; (b) dynamic amplification factor function; and (c) spectrum of system response.

For bridge-like structures, although they represent multiple degree of freedom systems, the modes of interests are often well separated. Different peaks in the frequency response function (FRF) of the system therefore correspond to distinct natural frequencies. As a result, the peak-picking method can be used more reliably to identify dynamic characteristics in this kind of structure.

There are also other methods, such as Stochastic-Subspace Identification methods (Peeters 2000) and Complex Mode Indication Function (CMIF) methods, as alternatives to the PP method for civil engineering applications (Shih et al. 1988, Brincker et al. 2000). These methods can be used to identify the modes of complex system; but they are not discussed here since they have no advantage over the PP method for simply supported beams and slabs, which were the focus of this study.

2.4.2. Time-frequency domain analysis of a signal

Random processes can be classified as stationary processes and non-stationary processes. If the statistical properties of a random process are independent of time, this random process is said to be stationary; otherwise, it is non-stationary.

PP and CMIF methods are based on the traditional Fourier transform (FT). However, a FT cannot describe the time dependency of signals and cannot capture the evolutionary characteristics that are commonly observed in signals measured from naturally excited structures. In other words, FT is only suitable for stationary signals.

The wavelet transform (WT) is an extension of the traditional FT with an adjustable window location and size. An arbitrary function can be expressed as a series expansion in which each term is one of the basis wavelets multiplied by its magnitude. The Fourier-based analyses use global sine and cosine functions as bases; however, the basis wavelets are local functions, each of which is defined by two parameters: its scale

(relating to frequency) and its position (relating to time). The use of local functions allows time-frequency resolution changes simultaneously; therefore, non-stationary data can be represented by multi-resolution. Due to this time-frequency multi-resolution property, the WT has recently been demonstrated as a promising tool for damage assessment of machinery and structures.

For example, a WT–based method was developed by Kitada (1998) for the identification of nonlinear structural dynamic systems. Wang and Deng (1999) developed a WT-based technique for analyzing spatially distributed structural response signals. They found that the response perturbations due to structural damage were discernable from wavelet components. Hou et al. (2000) used a simple structural model with multiple breakable springs subjected to harmonic excitation and showed that the WT could successfully be used to identify both abrupt and cumulative damage. These are only some simple examples of the use of WT methods, there are also many other application examples of WT methods reported in the literature.

2.5 SELECTION OF FIVE VBDD METHODS FOR THIS THESIS

Five VBDD methods are investigated in this thesis, including the change in mode shape method, the mode shape curvature method (Pandey et al. 1991), the change in flexibility method (Pandey and Biswas 1994), the damage index method (Stubbs and Kim 1995) and the change in uniform flexibility curvature method (Zhang and Aktan 1995). The advantage of these five methods is that they do not require the use of a finite element model; three of the methods rely solely on the change of mode shapes (or their spatial derivatives), while the remaining two rely on changes of both mode shapes and

natural frequencies. These methods can be used to detect and locate damage but cannot, at present, be used to determine the severity of damage.

Methods only based on natural frequency shifts were not chosen for this project because natural frequencies are much more sensitive to environmental factors such as temperature changes than to damage; also, these methods typically cannot distinguish between damage at symmetrical locations in a symmetric structure.

Neither model updating based methods nor neural network methods were chosen for this project because both are model-based methods. Building a finite element model is both costly and time consuming; in addition, calibrating a finite element model using test data is challenging, and not likely to be performed by practicing engineers for a large inventory of relatively small bridge structures. Adjusting a finite element model to match dynamic test results does not necessarily produce the best model, because many unknown factors can be used to calibrate a model and it is difficult to identify which factors should be used. In addition, the procedure of calibration is indeterminate.

Methods based on damping were not chosen for this project because of both the difficulty in accurately determining damping ratios from system identification techniques and the apparent lack of consistent correlation between the system damping and damage (Section 2.2.2).

CHAPTER 3. DESCRIPTION OF EXPERIMENTAL PROGRAM

3.1 INTRODUCTION

This project is composed of experimental and numerical studies of vibration-based damage detection techniques (VBDD). This chapter focuses on a description of the experimental study.

The advantage of an experimental study of VBDD is that experimental results can be expected to be closer to those obtained from a practical application of VBDD techniques. On the other hand, an experimental study is more challenging than a numerical study because it is influenced by uncertainties associated with measurement, excitation, material properties and support conditions (including support friction); it is very difficult to isolate or control the impact of each type of uncertainty on the test results.

Over the past forty years, numerous experiments have been undertaken to investigate VBDD techniques. However, many of these experiments were carried out using small scale specimens, such as small steel or aluminium plates, because the support conditions and excitation were easier to control and material properties were more homogeneous for small scale specimens. Although some researchers have applied VBDD techniques to real bridges, they have typically addressed a small number of relatively severe damage scenarios. In spite of this, their findings often served to underscore the complexities associated with applying VBDD techniques to large, complicated structures. These

experiments left many unanswered questions. For example, it has yet to be demonstrated whether small scale damage in large scale structures can be reliably detected and located by VBDD methods, whether a small number of sensors is sufficient to detect and locate damage with a reasonable degree of accuracy, what the influence of different types of excitation is on the measurement of the dynamic characteristics of a structure and on the application of VBDD methods, or what the influence of the type of structure is on the application of VBDD methods. Also, although electrical resistance strain gauges are very inexpensive compared to accelerometers, it is unclear whether they can be used to measure dynamic properties with sufficient accuracy. Therefore, the objective of the experimental program was to investigate these unknowns, and, thus, to advance the possibility of the practical application of VBDD technologies to bridges.

In the experimental program, the measured mode shapes and natural frequencies of a structure before and after damage were used to detect the damage. This chapter describes the types of specimens, different means of excitation, measurement sensors, induced damage, signal processing, implementation of the selected VBDD methods, and experimental procedures. The specific procedures and experimental results for individual sets of experiments are presented, interpreted and discussed in Chapters 4, 5 and 6.

3.2 EXPERIMENTAL SETUP AND PROCEDURES

The basic principle of VBDD techniques is to use changes in dynamic properties to identify damage in a structure. The procedure followed in this study was to measure the dynamic characteristics of the undamaged and progressively damaged specimen using

an array of sensors, and use changes in the dynamic characteristics to detect and locate the damage. The description of the experimental setup is divided into four parts: the specimens, creation of damage, methods of excitation, and measurement equipment.

3.2.1. Specimens

The specimens used in these experiments included a simply supported, six-metre long, half-scale steel-free bridge deck and two simply supported, twelve-metre long, full-scale prestressed concrete girders removed from an abandoned bridge.

The steel-free bridge deck is an innovative structure; the details and the advantages of this type of deck are described in Section 4.2. Because of its innovative nature, this type of structure requires reliable and efficient methods to monitor its condition in order to provide a level of confidence in its proper performance. While VBDD methods show great promise for structural health monitoring, the application of VBDD methods to a steel-free bridge deck has not been reported.

Prestressed concrete girders are frequently used in bridge construction; however, a reliable and efficient assessment method for the deterioration and damage of prestressed concrete girders is not yet available. The experiments on the full-scale prestressed concrete bridge girders were thought to simulate real conditions more closely, and were deemed necessary, in case scaling effects influenced the response of the half-scale bridge deck.

All tests were carried out in the Structures Laboratory of the Civil and Geological Engineering Department of the University of Saskatchewan.

3.2.2. Damage simulation

In VBDD experiments to date, the most often induced types of damage appear to be overload-crack damage and saw-cut damage. In these experiments, the damage was

simulated by removing a small square block of concrete from the top surface of a specimen; this can be considered to be a saw-cut type of damage.

Using saw-cut damage has some advantages. First, saw-cut damage can be located precisely in a small area, making the localization by VBDD methods more readily evaluated. On the other hand, overload-crack damage typically consists of many cracks that cover a large area, perhaps more than a quarter span for a simply-supported beam. In that case, it is very difficult to say exactly where the damage is located, making it difficult to evaluate the damage locating abilities of VBDD methods. Secondly, the severity of saw cut damage can be more easily controlled and quantified in that the reduction of stiffness caused by saw-cut damage can be calculated accurately. Thirdly, multiple saw-cut damage sites do not affect each other, so that a large number of saw-cut damage cases can be induced on one specimen, either simultaneously or in succession. Finally, saw-cut damage can be used to simulate the deterioration of reinforced concrete bridges, particularly when the deterioration results in spalling of the concrete from the bridge girder or deck.

It should be noted that research considering overload-crack damage also has its advantages and applications. However, that type of damage was thought to be less suitable for the investigation performed here.

The size and location of damage states induced in these experiments are defined in detail in Sections 4.4.1, 5.3.1, and 6.3.1, respectively.

3.2.3 Excitation of vibration

Excitation is a critical issue in dynamic experiments, especially in the investigation of VBDD methods, because the method of excitation significantly affects the accuracy of dynamic test results (measured natural frequencies and mode shapes of the system).

In these experiments, many different excitation methods were evaluated, including harmonic and white noise random vibration generated by a hydraulic shaker, vibration induced by the ambient motion of the laboratory floor, sand bag drop impact, and impact produced by a hammer strike.

Harmonic loading, also called pure sinusoidal loading, may be characterized by a single frequency. If the frequency of harmonic load coincides with one of the natural frequencies of the system, a resonant response will occur, producing a large constant amplitude vibration which can be used to obtain a consistent mode shape measurement.

On the other hand, random loading features components at a multitude of frequencies, producing a continuous spectrum over a range of frequencies. As a special case of a random process, the spectrum of a white noise random signal is a constant for all frequencies. From random vibration theory (Clough and Penzien 1975), the power spectrum density function of the applied force is multiplied by frequency response function to obtain the displacement response power spectrum of a linear system. Since the power spectrum density function of the white noise random force is constant, the shape of displacement response spectrum is the same as that of the system's frequency response function, with only the amplitude being different (see Fig. 2.5). Thus the displacement response spectrum can be used to accurately identify the natural frequencies of the system, as discussed in Section 2.4.1.2.

In these experiments, a hydraulic shaker was used as the source of both forced harmonic and random excitation. It was mounted on the top surface of the specimen as shown in Fig. 3.1. The device consisted of a hydraulic actuator mounted vertically in the centre of a steel frame, with a 36 kg weight attached to the bottom end of the actuator. Threaded inserts were embedded into the specimen to accommodate the secure

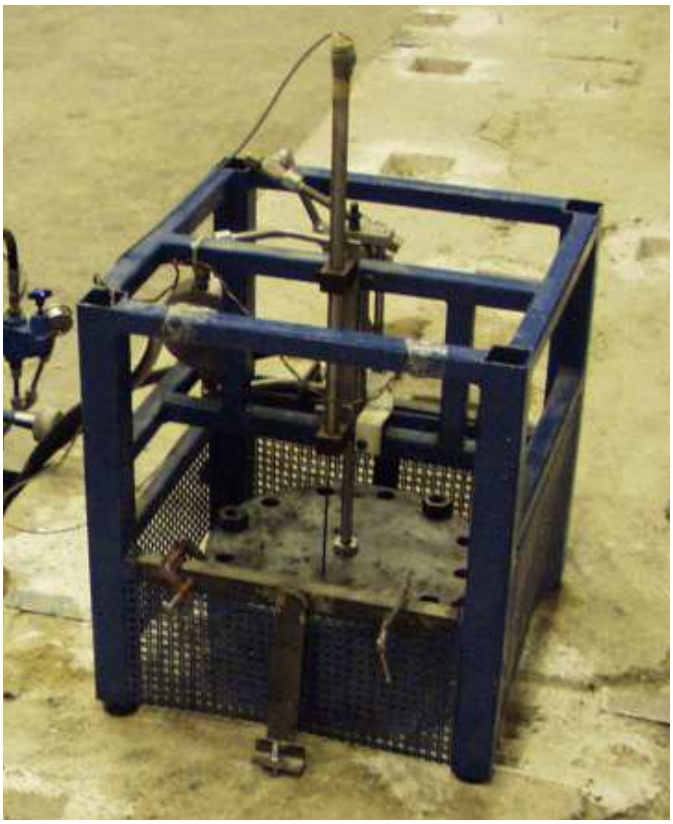

Fig. 3.1. The hydraulic shaker used to excite harmonic and random vibrations in the experiments.

attachment of the shaker frame. The location of the shaker was varied depending on the vibration mode that was required for a specific test. The control signal for the shaker, which determined the time history of the applied load, was generated using LabView™ software (LabView 2000) implemented on a personal computer. Based on preliminary test results, the most effective test procedure was found to entail the use of white noise random loads to first identify the system natural frequencies, followed by the application of resonant loads to measure mode shapes.

Ambient vibration of the laboratory floor was also used to identify the fundamental natural frequencies of the specimens, even though the levels of ambient vibration were

very weak in the structural laboratory. As discussed below, both high sensitivity accelerometers and conventional electrical resistance strain gauges were used to measure the response of the specimens. When ambient vibrations in the laboratory were used to excite a dynamic response, the accelerometers worked well, but strain gauges failed to identify the natural frequencies because of the low signal-noise ratio experienced by the strain gauges. The advantage of ambient vibration was that it was convenient and could be done without the addition of any mass to the structure; the disadvantage was that the amplitude of ambient vibration was very small, making accurate measurement of mode shapes more difficult. Also, ambient vibration is significantly affected by building use and environmental factors.

Impact loading excited by either dropping a sand bag on the top surface of the specimen or striking the specimen with a hammer was carried out repeatedly; however, neither the measured natural frequencies nor the measured mode shapes were found to be consistent with this form of excitation. Therefore, these forms of impact loading could not be used to identify the damage in these experiments, although they were easy to impart.

3.2.4 Setup of measurement sensors

The measurement of the vibration response of specimens was conducted in two ways, each of which used data acquired from a different set of sensors. Conventional metallic foil electrical resistance strain gauges were used as the first type of sensor, while accelerometers were used for the second. The model was also instrumented with linear displacement transducers, but these were not used in sufficient numbers to allow this data to be used in the application of damage detection techniques. In this thesis, only the conventional metallic foil strain gauges and accelerometers are described in detail.

3.2.4.1 Conventional metallic foil strain gauges

For the first way of measuring the vibration response, conventional 120 ohm foil strain gauges, oriented to measure longitudinal strain, were bonded to each girder web of the steel-free bridge deck specimen, as shown in Fig. 3.2 (a), or bonded on the vertical side of a prestressed concrete girder, as shown in Fig. 3.2 (b), in vertically aligned groups of three at selected locations along the length of the girders.

The use of vertically aligned strain gauges to obtain the curvature of a beam relies on the assumption that planes perpendicular to the axis of the beam still remain plane after

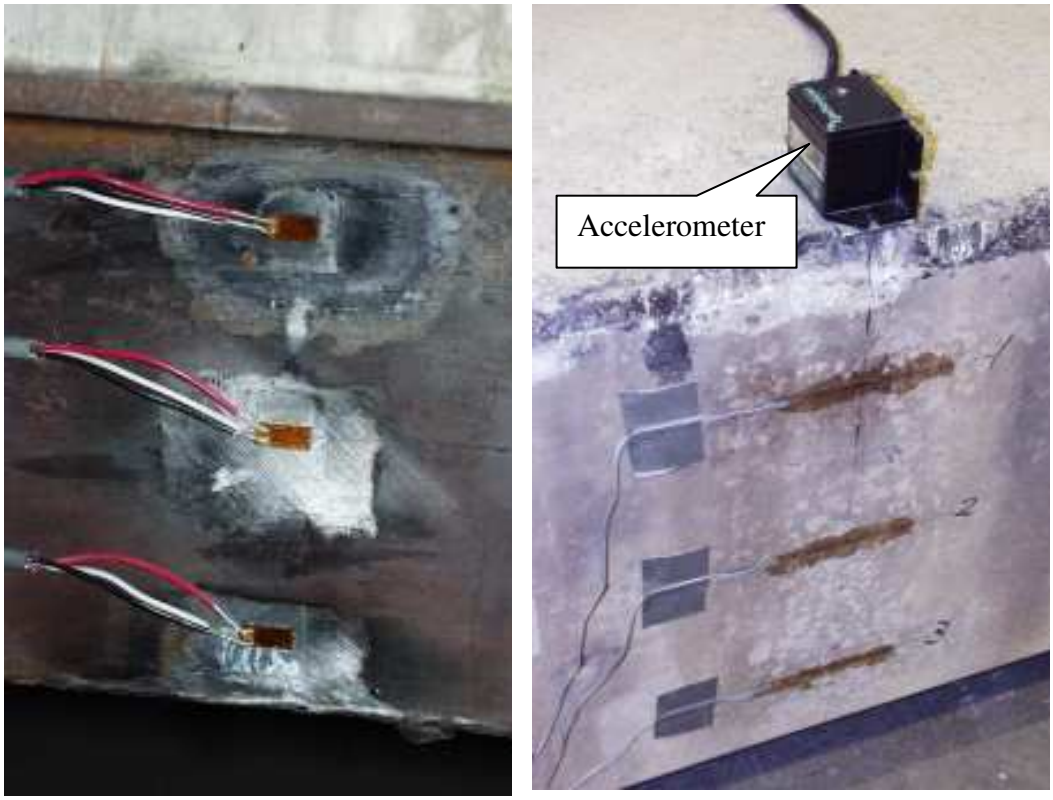

Fig. 3.2. Installation of sensors: (a) strain gauges bonded on the girder web of the steel-free bridge deck; (b) strain gauges bonded on the vertical side and the accelerometer mounted on the top surface of the prestressed concrete girder.

flexural deformation. Based on this assumption, the curvature κ of the beam for small deformations may be expressed as

$$\kappa = \frac{d\varepsilon}{dY} = \tan\theta \approx \theta \qquad [3\text{-}1]$$

where ε is the measured strain at some vertical location Y (see Fig. 3.3). To attenuate the influence of random measurement errors in the strain, the instantaneous curvature for each vertical line of gauges was estimated from the slope of the best-fit line through the three measured strain values found using a linear regression analysis.

After the time histories of the beam curvature were obtained at the gauge locations corresponding curvature distributions along the beam could be calculated for use in applying VBDD methods. Details are discussed in Section 3.4.

Two different lengths of strain gauges were used for these experiments. The strain gauges bonded to the steel girders of the steel-free bridge deck were model CEA-06-

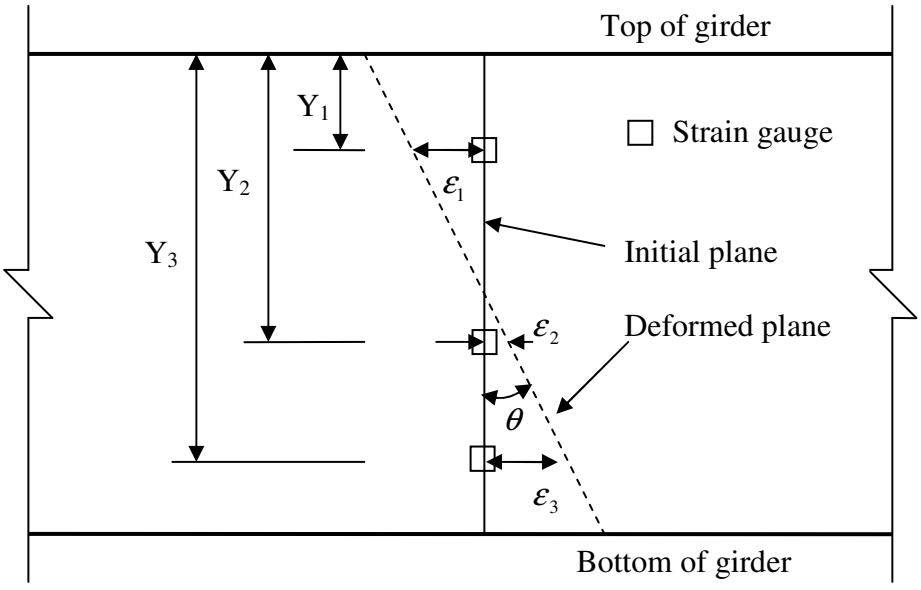

Figure 3.3. Setup of the strain gauges on the vertical side of a girder.

250UN-120, supplied by Micro-Measurements Division, Measurements Group, Inc. (Raleigh, North Carolina) and featured a gauge length of 10 mm. Those bonded to prestressed concrete girders had a 90 mm gauge length, a model number of PL-90-11, and were made by Tokyo Sokki Kenkjujo Co., Ltd. (Tokyo, Japan). The length of the strain gauges on the prestressed concrete girders was selected to be three times the maximum aggregate size to help average potential stress concentration due to the presence of aggregate near the surface and surface cracks due to flexure and shrinkage.

3.2.4.2 Accelerometers

The second type of vibration response measurement featured the use of several accelerometers, each configured for a maximum range of ±0.5g and a precision of 0.00025g. The accelerometer used were model EpiSensor ES-U, made by Kinemetrics Inc. (Pasadena, CA). A typical accelerometer is shown in Fig. 3.2 (b), illustrating how they were bonded to the top surface of specimen along each longitudinal edge of a specimen to measure vertical acceleration. In all cases, accelerometers were evenly spaced in the longitudinal direction; specifics regarding sensor locations for the various tests are provided in Chapters 4, 5 and 6.

Regardless of the type of specimen tested, separate tests were performed with the accelerometers first installed along one longitudinal edge and then along the other. The measured mode shapes along each side were tracked and normalized (scaled) independently.

To improve the repeatability of mode shape measurements, thereby improving the sensitivity of the damage detection techniques, it was found necessary to calibrate the accelerometers relative to each other prior to conducting each individual test. This was done by stacking all the accelerometers one on top of the other and subjecting them to a

vertical sinusoidal vibration. To ensure consistency, differences in the measured accelerations were minimized using the following iterative procedure. For each successive trial, the amplitudes of all accelerometers were averaged, and the ratio of amplitude of each accelerometer to the average amplitude was calculated; the updated calibration factor for each accelerometer was then determined based on this amplitude ratio. The calibration trials were repeated until the adjustment ratios for all accelerometers were greater than 0.9999 or less than 1.0001. This level of consistency was found to be adequate for detecting damage of the scale investigated in this thesis.

3.2.5 Measurement of vibration

As noted in Section 2.5, some of the VBDD methods used in this project relied only on the change of mode shape to detect damage, while others relied on both the change of natural frequencies and mode shapes. In these experiments, natural frequencies were identified by first measuring the response of the system to a random vibration; the mode shapes were then accurately measured using a harmonic vibration (for justification, see Section 2.2.3). Data were acquired using a 12-bit data acquisition system (National Instruments SCXI 1001, LabView^{TM} 6i) at sampling rates as noted below.

Natural frequencies were identified from the average of ten normalized frequency response spectra obtained from tests during which data were acquired at 150 samples per second for a period of 220 seconds. For the specimens considered in these experiments, the natural frequencies of the first three modes were found to be between 7 Hz and 50 Hz; therefore, a sampling rate of 150 samples per second (3 times the highest natural frequency of interest) was deemed appropriate for natural frequency identification. At this sampling rate taken over a period of 220 seconds, the resolution of the frequency response spectrum was 0.0046 Hz. It should be noted that the incremental change in

natural frequency caused by inducing a single state of damage of the size selected for these experiments was generally observed to be smaller than this frequency resolution (0.0046 Hz). However, the total accumulated change caused by a number of successive damage states was found to be measurable. Therefore, when required for VBDD calculations, natural frequencies at each intermediate damage state between the baseline (undamaged) and final damage states were estimated by assuming an equal change caused by each subsequent state of damage.

Theoretically, a longer test period produces a higher resolution in the frequency response spectrum. Practically, the error (or fluctuation) associated with each measurement limited the accuracy with which the frequencies could be differentiated. It was therefore found to be of little value to use an excessively long test period to obtain a high resolution of the frequency response spectrum.

Both ambient vibration and random vibration generated by a shaker using white noise random signals were used to identify the natural frequencies. The ambient environmental excitation typically resulted in a measurable response for only the fundamental mode. The shaker-generated random excitation, on the other hand, produced a higher amplitude response and excited higher modes, but resulted in a slightly lower measured fundamental frequency. The small discrepancies in measured natural frequencies can attributed, in part, to slight nonlinearities and second order effects in the systems. One disadvantage of using the hydraulic shaker, though, was the limited time that it could be run continuously (approximately 10 minutes) due to concerns about overheating.

The normalized frequency response spectrum was obtained by dividing the amplitude for each frequency increment of the spectrum by the root mean square (rms) of the spectrum.

After natural frequencies had been identified, a sinusoidal excitation was applied by the shaker at each of the selected natural frequencies in turn to accurately measure the corresponding mode shapes. Preliminary studies indicated that harmonic excitation produced more reliable mode shapes than random excitation. During this procedure, each set of data was acquired at 300 samples per second for 21 seconds. For mode shape measurement, a shorter sampling period was selected since a higher resolution of the frequency response spectrum was not required. A higher sampling rate, though, was adopted to avoid any signal contamination due to aliasing.

The average of ten unit-norm normalized mode shape measurements (see Section 2.2.3) was calculated for use by VBDD techniques. Only the fundamental mode was used for damage detection because the measurement accuracy of the second and third modes was much lower than that of the first mode. However, the first three modes were used for calibration of the finite element (FE) models described in subsequent sections.

3.3 SIGNAL PROCESSING METHODS

The objective of the experiments was to make use of measured mode shapes and natural frequencies to detect damage by VBDD techniques. However, the raw data from accelerometers and strain gauges acquired using a data acquisition system are recorded in the form of changes of voltage with respect to the test time for each channel. These data must first be converted to acceleration and strain values, after which a Fast Fourier Transform (FFT) (Ramirez 1985) must be used to convert these discrete time-domain

acceleration and strain signals to frequency response spectra. Mode shapes and natural frequencies can then be obtained from the frequency response spectra.

Theoretically, changes in the output voltages from accelerometers and strain gauges are caused only by the vibration of the specimen. In reality, environmental electro-magnetic noise and the fluctuation and drift inherent in a measurement device can also cause voltage changes. The effects of drift may be eliminated by frequent calibration, as described earlier. Other unexpected random changes of voltage are referred to noise, which can cause errors in the measured mode shapes and natural frequencies. VBDD methods rely on high quality and reliable measured mode shapes and natural frequencies because small scale damage only causes very small changes to mode shapes and natural frequencies. Large measurement errors can overshadow the changes of mode shapes and natural frequencies caused by small scale damage and make it impossible for VBDD methods to work successfully. Fortunately, the noise can be minimized by some special techniques referred to as “filtering”.

The objective of signal processing in this study was to convert the time-domain raw vibration data to frequency-domain data, while also filtering out the random measurement errors to obtain reliable mode shapes and natural frequencies. A flow chart illustrating the signal processing procedures adopted for the current study is shown in Fig. 3.4.

First, a data conditioning program was employed to perform preliminary data processing. Functions performed as part of data conditioning included the removal of the initial average baseline output (DC component), separation of data from different instrumentation types into separate files, and the conversion of measured strain gauge voltages and accelerometer readings to the appropriate physical measurements.

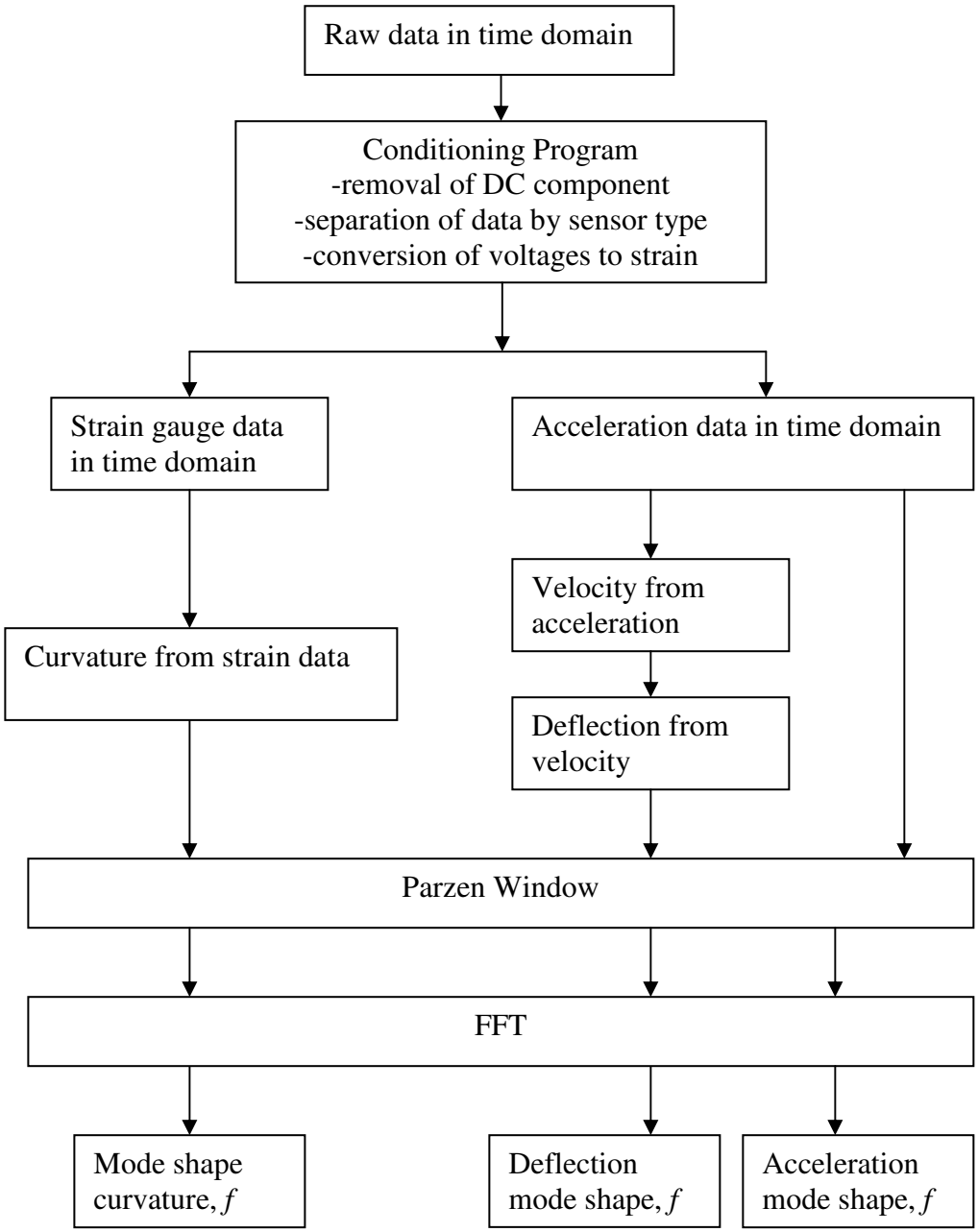

Fig. 3.4. The flow chart of signal processing (f denotes for the natural frequency).

3.3.1 Parzen Window

In the current study, time-domain data were scaled using a Parzen window function (Ramirez 1985) before applying an FFT to reduce "leakage" in the resulting spectrum. Inherent in a Fourier transform is the assumption that the signal being analysed is periodic and continuously repeated. If the sampled time history does not represent an integer number of full harmonic cycles, however, the connection between two adjacent segments of the assumed infinite signal may not be smooth, as shown in Fig.3.5(a). This will manifest itself in the resulting spectrum as range of spurious higher harmonic components required to produce the apparent sudden changes in the signal.

One method of removing the spurious harmonics caused by the end effects is to

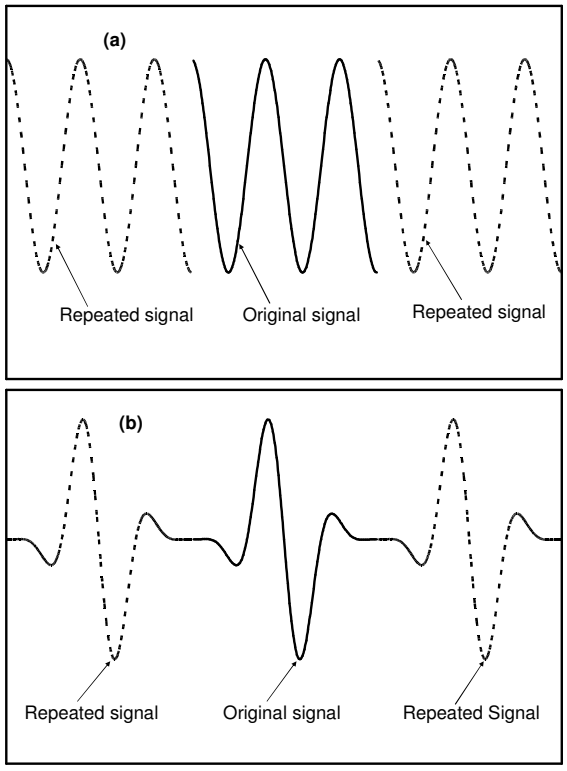

Figure 3.5. (a) A discontinuous periodic signal assumed by a Fourier transform, (b) The same signal after a Parzen Window has been applied.

ensure that the signal decreases smoothly to zero at both the start and finish of the measured signal. This is achieved by multiplying the original signal by a 'window' function which attenuates at the ends to eliminate the discontinuities, as indicated in Fig. 3.6. The result of applying a Parzen window to the signal in Fig. 3.5. (a) is the smooth function shownin Fig. 3.5 (b).

There are many different kinds of window functions available, including the Parzen Window, Rectangular Window, Bartlett Window, Welch Window, Hann and Hamming Window, Blackman Window, Lanczos Window, Gaussian Window and Kaiser Window (Ramirez 1985). Each one has its own advantages and limitations.

In order to understand why the Parzen Window was selected, it is important to understand how the performance of different windows is measured. As an example, the rectangular window is a square pulse; its frequency domain magnitude is shown in Fig. 3.7. The amplitude of the highest side lobe of a window can be expressed in decibels referenced to the major lobe peak. For the rectangular window, the amplitude of the highest side lobe is -13.2 dB (Ramirez 1985). In general, as the side lobes decrease, the ability to distinguish adjacent frequency components of unequal amplitudes increases. The highest side lobe of the Parzen Window is -53.2 dB (Ramirez 1985), which is the lowest among all windows listed. Therefore, the Parzen Window was used in the current study.

The Parzen Window can be expressed as follows:

$$f_t = 2(1-t)^3 \qquad \text{if } t \le 0.25 \text{, or } t \ge 0.75 \qquad [3.2a]$$

$$f_t = 1-6t^2+6t^3 \qquad \text{if } 0.25 \le t \le 0.75 \qquad [3.2b]$$

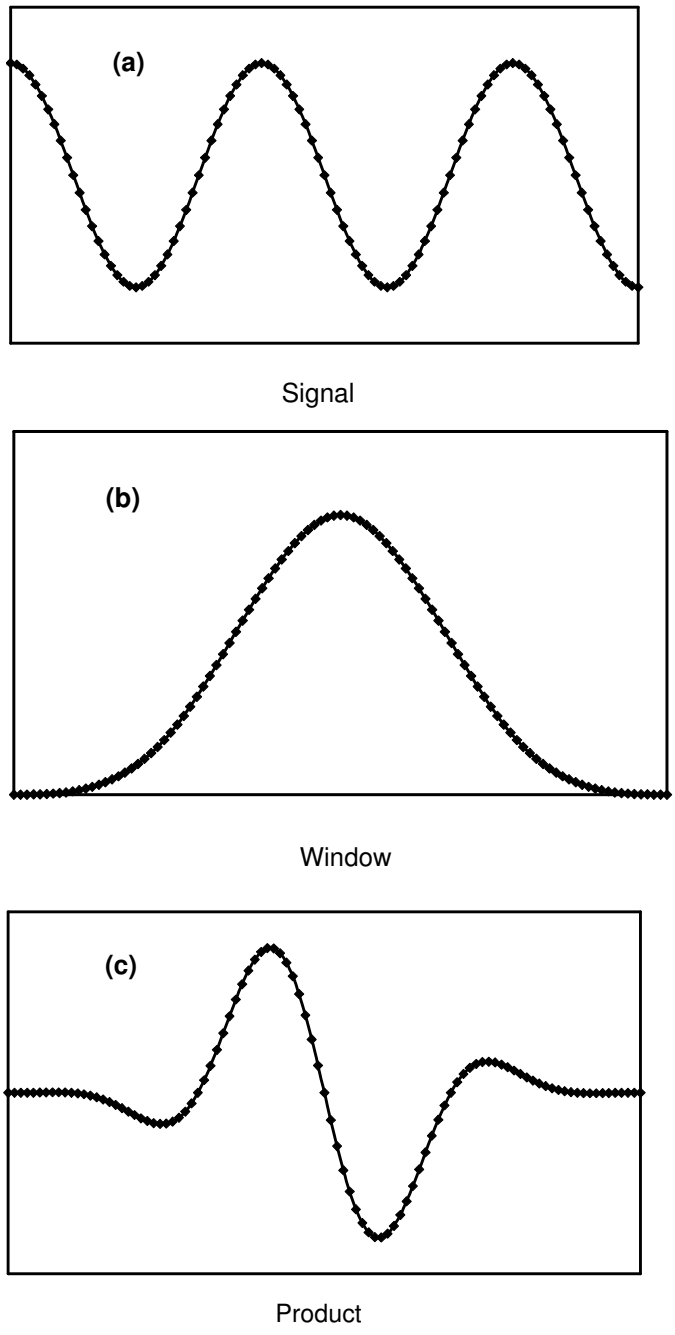

Figure 3.6. Window effects. The original signal (a) is multiplied by the window function (b) to give the product (c) which avoids sudden transitions at the ends.

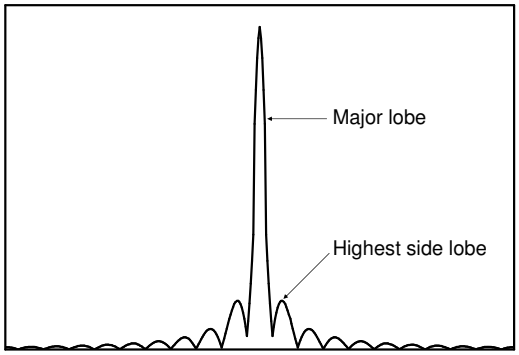

Figure 3.7. The frequency domain magnitude of a rectangular window.

where $t = \left| \frac{2i}{N-1} - 1 \right|$, i is sequence number of the sample, N is the total number of samples in the signal, and f_t is the window value corresponding to the i^{th} sample. In order that the Parzen window not alter the energy in the original signal, the window value has to be normalized. This is accomplished using the following procedure. Before the FFT is applied, the time-domain vibration raw data y_t is multiplied by its weight W_t

$$W_t = f_t * \sqrt{\frac{N-1}{\sum_{t=0}^{1} f_t^2}} \qquad [3.3]$$

After the FFT is applied, the spectrum of the windowed signal is multiplied by the following correction factor:

$$f_c = \sqrt{\frac{\sum_{t=0}^{1} y_t^2}{\sum_{t=0}^{1} y_t^2 W_t^2}} \qquad [3.4]$$

3.3.2 Processing of strain gauge data

For the strain gauge data, the instantaneous strain profile along a vertical cross section at each set of vertically aligned gauges was obtained at each instant of time by fitting a least-squares regression line through the three individual strain measurements. This linear profile was used to calculate the instantaneous bending curvature at that location (see Section 2.2.4.1 and Fig. 3.3). The curvature-time series was converted to spectrum data for the curvatures by applying an FFT analysis. The curvatures associated with the fundamental mode at the measurement points were used to calculate the change of curvature vector, $\Delta\phi''$, for use with the mode shape curvature method (see Section 2.2.3).

In addition, the instantaneous deflection at each measurement location was calculated by integrating the appropriate areas under the curvature diagram. The deflection-time series was used to obtain spectrum data for the deflections and obtain the deflection mode shape. Theoretically, the deflection mode shape derived from strain gauge data can be used in conjunction with all five VBDD methods described in Section 2.5; however, it was found that the process of integrating curvatures to derive deflections resulted in a lower degree of accuracy than was possible using accelerometer data. As a result, the deflection mode shapes based on strain gauge data resulted in an unacceptable level of accuracy for detecting small scale damage in the experimental study. Therefore, all deflection mode shape values referred to in subsequent discussions were derived from accelerometers, rather than from strain gauges.

3.3.3 Processing of accelerometer data

For the use of accelerometer data, two options were considered; one was to produce the spatial distribution of modal acceleration from the acceleration-time series directly, while the second was to produce the conventional mode shape from the displacement-time series. To distinguish these two modal response patterns, the former is referred to as 'acceleration mode shape', while the latter is referred to as 'deflection mode shape' in this thesis.

In order to obtain a deflection mode shape from acceleration data, vertical displacements at each accelerometer location were obtained by integrating the acceleration signal twice with respect to elapsed time to obtain first velocity and then displacement. Prior to performing the first integration, a second order recursive high pass filter was applied to the acceleration signal to remove baseline drift (Proakis 1992). In addition, the second order recursive filter was also subsequently applied to both the resulting velocity and displacement signals to remove the remaining baseline drift in these signals. Furthermore, linear regression (Younger 1979) was used to identify and remove an observed linear trend in the displacement signal; the details of this procedure are described in Appendix A.

Theoretically, the acceleration mode shape should be exactly proportional to the deflection mode shape due to the fact that the amplitude of acceleration A_a at any location of a system experiencing harmonic vibration is proportional to the amplitude of the deflection A_d at the same location, as indicated in the following equation:

$$A_a \propto A_d (2\pi f)^2 \quad \text{or} \quad A_d \propto A_a / (2\pi f)^2 \qquad [3.5]$$

where f is the natural frequency. In actuality, some differences were observed due to the different levels of signal processing involved, and the resulting effect on the embedded measurement errors.

For the first mode, the deflection mode shape usually resulted in better repeatability, due in part to the fact that the noise was attenuated by integration over time and by the filters employed. For the second and third modes, however, the deflection mode shape produced poorer repeatability than the acceleration mode shape because the magnitudes of the deflections of the second and third modes were found to be much smaller than those of the first mode, resulting in a very low signal-noise ratio. In contrast, the magnitudes of the accelerations associated with the second and third modes were found to be equal or even higher than those of the first mode due to the frequency-squared factor apparent in Eq. 3.6.

3.4 IMPLEMENTATION OF DAMAGE DETECTION METHODS

The basis of the five VBDD methods in the current study was to directly or indirectly use the change of mode shape to locate damage (see Sections 2.2 and 2.5). The damage indices investigated here included the change of mode shape, the change of mode shape curvature, the change of flexibility, and others. The highest peak of each damage index when plotted along the span length of a specimen is expected to occur at the longitudinal location of damage. Practically, however, there are only a very limited number of measurement points available. In this study, only five to seven measurement points were employed along each side of a specimen. Of course, the damage could be located between two adjacent measurement points instead of exactly at the location of a

measurement point, meaning that the highest peak should occur between the two measurement points when the damage is located between them. In order to determine the location of damage is such a case, it is necessary to estimate the values of a mode shape between the measurement points. Interpolation was therefore employed to build a smooth curve passing through given measurement points in an attempt to improve the precision of VBDD results.

For the current study, two different interpolation techniques were used. One was conventional cubic spline interpolation as implemented in MathCAD Professional (2000), while the other was cubic Bezier spline interpolation as implemented in Microsoft Office Excel (2003). These two interpolation methods produced curves that were both doubly differentiable over their entire length, as required for calculating curvatures, and free of discontinuities in slope and curvatures.

Conventional cubic spline interpolation allows one to pass a curve through a set of points in such a way that the first and second derivatives of the curve are continuous across each point. In addition, continuity of the third derivative at the first and last interior data points were also enforced.

Cubic Bezier spline interpolation (Mortenson 1997) is more complicated than conventional cubic spline interpolation. Artificial control points are used to control the curvature of the curve such that each segment of the Cubic Bezier spline is very close to a straight line and each peak of the curve is very close to the nearest given points. Therefore, a cubic Bezier spline does not have the disadvantage exhibited by the conventional cubic spline which may produce unexpected or undesirable perturbations and inflections.

For example, Fig. 3.8 shows the distributions of change of mode shape curvature from strain gauge data produced using the two different interpolation methods. The highest peak indicates the predicted location of damage. The cubic Bezier spline successfully located the damage, while the conventional cubic spline failed because an artificial peak occurred close to the east support of the beam.

A preliminary study indicated that the distribution of the change of mode shape curvature derived from strain gauge data was very irregular, with many peaks and reversals in curvature even when only a single damage state was induced on a simply supported beam. This was attributed to the large measurement uncertainties in the strain gauge data due, in part, to environmental electro-magnetic noise. Use of a conventional cubic spline often resulted in undesirable perturbations of the strain gauge data; therefore, a cubic Bezier spline was adopted throughout for use with strain gauge data to

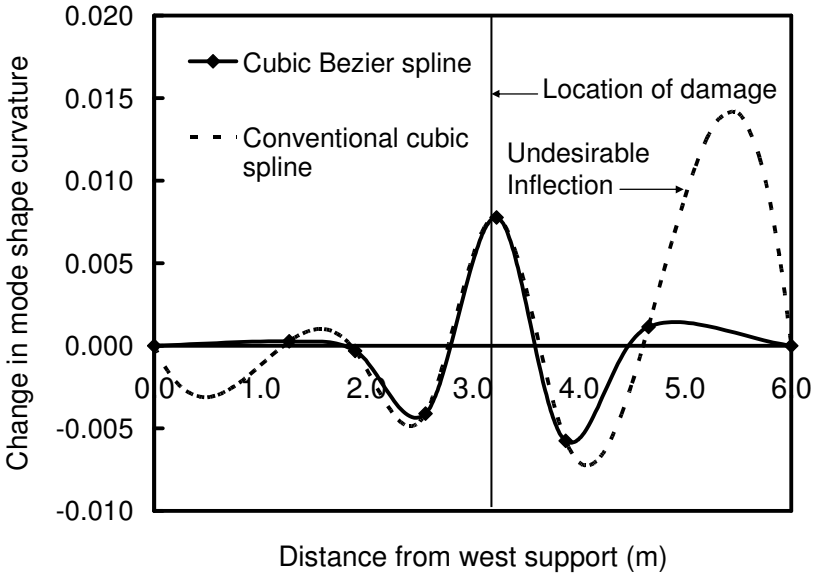

Figure 3.8. Change in mode shape curvature calculated using different interpolation methods.

detect damage.

On the other hand, the curve produced by a cubic Bezier spline is not really smooth, so it is not suitable to produce a smooth curve like a sine wave. Fig. 3.9 compares the two interpolation techniques when applied to a sine wave defined by a small number of measured points. Obviously, the conventional cubic spline curve is very close to the original curve, with its highest peak also very close to that of the original curve. However, in this case, the cubic Bezier spline curve deviates significantly from the original curve in places; significantly for VBDD application, its highest peak is also far away from the highest peak of the original curve. Since a preliminary study indicated that the distribution of the change of mode shapes from accelerometer data was typically smooth, the conventional cubic spline was used to interpolate the mode shape curves obtained from accelerometer data.

After obtaining the values at intermediate points on the mode shapes or mode shape

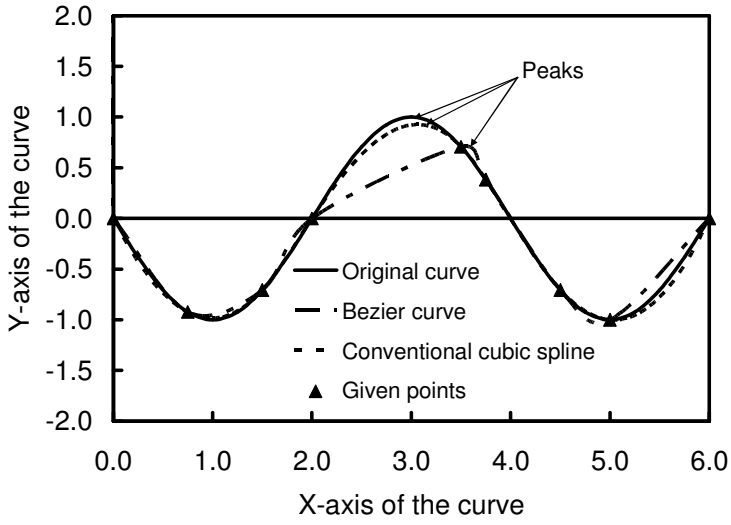

Figure 3.9. Comparison between Bezier cubic spline and conventional cubic spline when applied to a sine wave defined by a small number of points.

curvatures through interpolation, the mode shape vectors from accelerometers or mode shape curvature vectors from strain gauge data were unit-norm normalized prior to applying the damage detection techniques. The objective and procedure of unit-norm normalization has been given in Section 2.2.3.

When accelerometer data was used to obtain mode shape curvatures, the mode shape curvatures were computed using the central difference approximation for the second derivative, given by

$$\phi''_{ji} = \frac{\phi_{(j+1)i} - 2\phi_{ji} + \phi_{(j-1)i}}{h^2}, \qquad [3.7]$$

where ϕ''_{ji} is the curvature at point j corresponding to the i^{th} mode (i.e. the j^{th} element of the vector $\boldsymbol{\phi}''_i$), ϕ_{ji} is the displacement at point j corresponding to the i^{th} mode (i.e. the j^{th} element of the vector $\boldsymbol{\phi}_i$), and h is the average distance between discrete points in the $\boldsymbol{\phi}_i$ vector.

The central difference approximation for the second derivative was also used to convert the flexibility to flexibility curvature for use by the change of uniform flexibility curvature method (Section 2.2.5).

The procedure used to implement the five VBDD methods on MathCAD is described in Appendix B.

CHAPTER 4. DAMAGE DETECTION ON A STEEL-FREE BRIDGE DECK

4.1 INTRODUCTION

This chapter describes a study undertaken to ascertain the theoretical and practical potential of five VBDD techniques, described in Chapter 2, for detecting and locating low levels of damage on a bridge deck using a small number of sensors. First, the bridge deck system used as a basis for the study is described; numerical and laboratory-based experimental studies are then presented. These studies form the initial stages of a larger, systematic research program designed to address VBDD issues of increasing complexity in a progressive and incremental manner. As such, many of the complexities associated with applying VBDD techniques to constructed facilities in the field are not addressed by these initial studies. The purpose of this investigation was limited to determining theoretical and practical limitations of the techniques when applied to a bridge deck under well-controlled conditions. Studies extending the techniques to field structures are currently underway by other students in this research group.

4.2 SYSTEM DESCRIPTION

The system used as the basis for both the numerical and experimental aspects of the study was a half-scale laboratory model of a two-girder, simple-span, slab-on-girder bridge deck. The deck slab was constructed using the steel-free design technique

developed by Mufti et al. (1993) and first applied in the construction of the Salmon River Bridge in Nova Scotia, Canada (Newhook and Mufti 1996, Bakht and Mufti 1998). In this type of construction, the slab is completely devoid of reinforcing steel and relies upon compressive arching action within the deck to transmit concentrated wheel loads to the girders.

Fig. 4.1 shows the configuration of the system. The concrete deck slab was 75 mm thick at the centre and tapered transversely to 113 mm thick at the girders. It was supported by two structural WT girders spaced at 1.5 m and spanning 6.0 m; shear studs were used to make the system fully composite. The use of WT sections created a

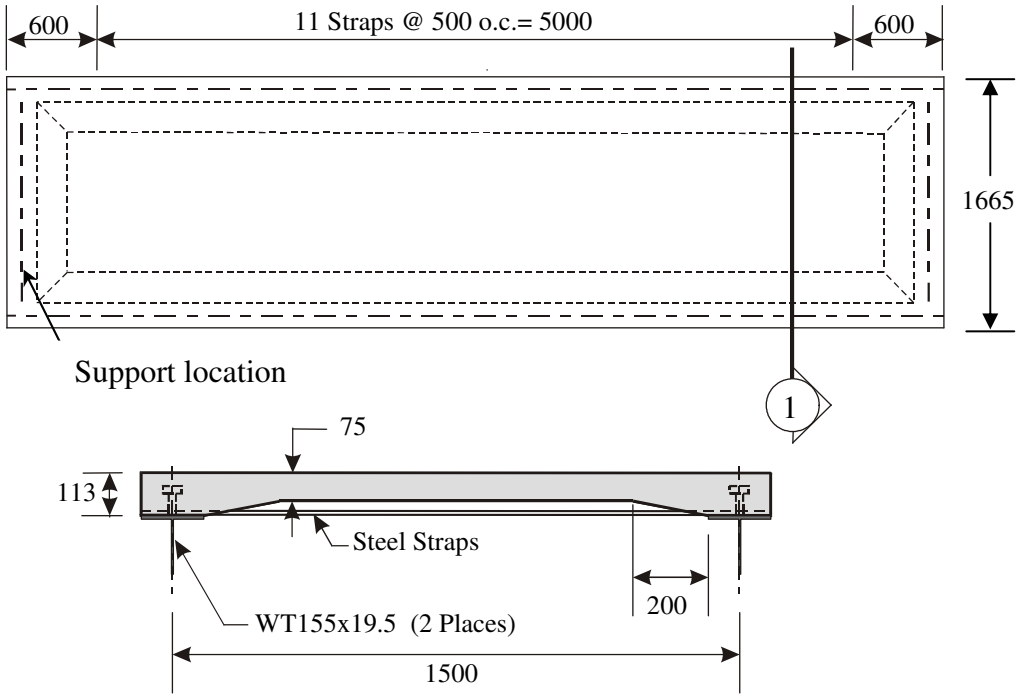

Figure 4.1. The slab-on-girder bridge deck model used for the study (dimensions in mm).

relatively flexible system, resulting in larger amplitude vibrations more conducive to measuring the dynamic response. To provide the lateral restraint required for the development of internal arching forces, the upper flanges of the girders were tied together using transversely oriented steel straps spaced at 500 mm longitudinally and connected to the deck above the girders by means of shear studs welded to the straps.

4.3 NUMERICAL STUDY

4.3.1 Description of Numerical Study

The numerical study was initiated after the laboratory model had been constructed (to allow calibration of the numerical model); however, the majority of the numerical work was completed prior to conducting the experimental study described in Section 4.4. The primary purpose of the numerical study was to evaluate the capabilities of the damage detection methods in the absence of experimental uncertainties. This permitted an assessment of the feasibility of proceeding with the experimental study, and aided in its design. In addition, one of the principal objectives of the numerical study was to determine whether a small number of measurement points could characterize the mode shapes with sufficient accuracy to permit reliable detection and localization of small-scale damage. This issue is particularly important since a structure can reasonably be instrumented at only a relatively small number of locations, and "techniques that are seriously considered for implementation in the field should demonstrate that they can perform well under the limitations of a small number of measurement locations, and under the constraint that these locations be selected a priori" (Doebling et al. 1996).

The commercial finite element (FE) analysis package ANSYS (2003) was used to perform eigenvalue analyses to generate the natural frequencies and mode shapes of the system. Although the undamaged system was symmetrical both longitudinally and transversely, the investigation of unsymmetrical damage states precluded the use of symmetry boundary conditions to reduce the size of the model.

The concrete slab was divided into 8-node 3-dimensional isoparametric brick elements: 62 elements longitudinally, 17 elements transversely, and three (in the 75 mm thick areas) or four elements (elsewhere) through the slab thickness as shown in Fig. 4.2. The girders were modelled using 2-node, 3-dimensional linear beam elements that were located along the centroidal axes of the WT sections. In order to accurately calibrate the model to the physical system, it was necessary to represent the composite connection of the slab to the girders by modelling the shear studs as 2-node 3-dimensional beam elements. The flexural stiffness of the studs was varied to calibrate the natural frequencies of the model to those of the physical system. Between stud locations, vertically oriented compression-only rigid truss elements (defined with extremely large axial stiffness) connected girder nodes to nodes on the bottom surface of the slab. The transverse steel straps were modelled using linear truss elements.

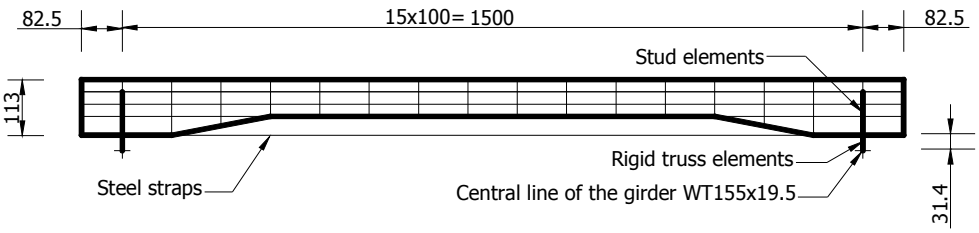

Figure 4.2. Transverse cross section of the finite element model of the deck (dimensions in mm).

Constraint boundary conditions were imposed at the four girder support nodes located along the central line of the girder, preventing displacement in the vertical direction. In addition, one of these nodes was restrained in both the longitudinal and transverse directions, a second in the longitudinal direction, and a third in the transverse direction, thus preventing rigid body movement of the system. Elastic and section properties of the physical components were applied as model parameters. The material properties used in the FE model are shown in Table 4.1. No spatial variation in material properties was assumed.

The model was calibrated to the first three natural frequencies and mode shapes of the undamaged physical system by adjusting the flexural stiffness of the studs, as mentioned above. The mode shapes of the first three modes generated by the FE model are shown in Fig.4.3. Both the first and third modes are flexural modes, while the second mode is a torsional mode with the two girder lines vibrating in opposite directions. It should be noted that while all mode shapes of the deck are three-dimensional surfaces, as shown in Fig.4.3, only portions of the mode shape defined along girders were used in this study to detect damage, simulating the measurement locations used for the experimental study. Therefore, mode shapes referred to in subsequent discussions are those along either of the two girders are therefore curves rather than surfaces.

As demonstrated in Table 4.2, the maximum relative difference between predicted

Table 4.1. Material properties of the steel-free bridge deck used in FE model

Material properties	*Young's modulus (GPa)*	*Density (kg / m^3)*	*Poisson's ratio*
Concrete	26.6	2400	0.3
Steel	200	7850	0.3

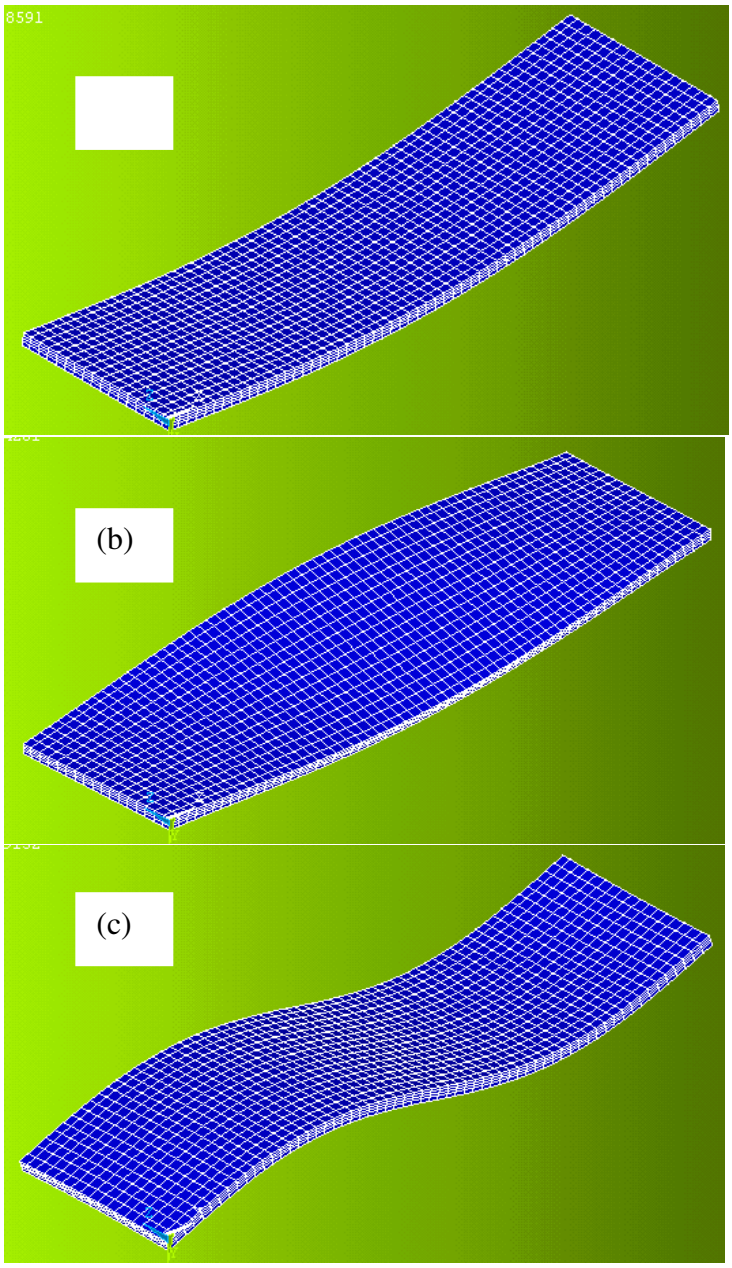

Figure 4.3. The first three mode shapes of the steel-free bridge deck generated by FE model: (a) first mode, (b) second mode, and (c) third mode

and measured natural frequencies was only 3.5%. In addition, the modal assurance criteria (MAC) comparing the numerical and measured mode shapes for the first three modes exceeded 0.998 in all cases. As defined in Eq. 2.1, a MAC value of 1.0 would

indicate perfect correlation between the corresponding measured and numerical mode shapes. Only the mode shape values at five measurement points on each girder were used for calculating the MAC; also, the MAC values provided in Table 4.2 correspond to the average of the MAC values obtained along both of the girders.

Once the model had been calibrated, damage to the deck slab was simulated by eliminating a single element, with dimensions of 100 x 100 mm in plan by 25 mm thick, from the top surface of the slab. Such damage may be representative of deterioration of the surface of the concrete. The discrete nature of this simulated damage also made it possible to investigate the potential precision of VBDD techniques in the localisation of small scale damage. A total of 39 damage cases were simulated, each one representing a different damage location. The locations of these damage cases are shown in Fig. 4.4. For the first series of 30 damage cases, the transverse location of damage remained constant, being positioned near one of the girders, while the longitudinal location of the removed element was varied in 0.1 m increments between 0.05 and 2.95 m from one support, as measured to the centre of the element. For second series of damage cases, the longitudinal location of damage remained constant at 2.35 m from one support, while the transverse location was varied in 0.1 m increments from -0.04 to 0.75 m from one

Table 4.2. Comparison of FE and experimental natural frequencies and mode shapes for the undamaged system.

Parameter	1st Mode	2nd Mode	3rd Mode
Natural Frequencies (Hz)			
Experimental model	7.36	18.8	25.3
Finite element model	7.32	19.46	25.80
Relative error	-0.5 %	3.5 %	2.0 %
Modal Assurance Criteria:	0.9999	0.9989	0.9986

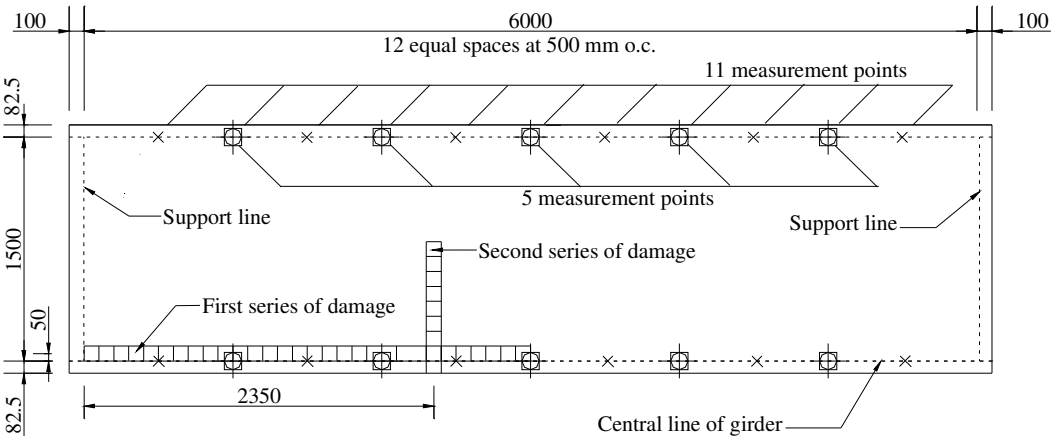

Figure 4.4. The locations of 39 damage cases and measurement points.

girder centre-line toward the second girder.

The post-processing of the FE analysis results was intended to simulate the acquisition of measured data from sensors attached to a physical system at a small number of locations. Therefore, displacement data were extracted from the FE-generated mode shapes of the system at a small number of uniformly spaced "measurement" points along each girder. Three cases were investigated: one in which five measurement points were used, one in which eleven measurement points were used, and a well-defined reference case in which 59 measurement points were used. The location of the five and eleven measurement points are indicated in Fig. 4.4. In addition to these measurement points, the mode shape deflections at supports were assumed to be zero.

Of primary interest was the performance of the damage detection techniques when only the fundamental mode shape was used, since accurate measurement of higher mode shapes is more difficult in practice. However, the use of the first three flexural mode shapes was also investigated to determine whether significant improvements could be

realized by considering higher modes in the VBDD calculations. As described above, mode shapes were defined by "measurements" at five, eleven, or 59 points, in addition to zero displacements at supports. However, in order to obtain a better estimate of mode shapes when five or eleven measurement points were used, intermediate mode shape values between measurement locations were generated using a cubic spline interpolation technique, by which cubic polynomials were used to define the mode shapes between data points. Continuity of the second derivative at data points and continuity of the third derivative at the first interior data points were enforced by the cubic spline definition routine that was employed. In this way, displacements at a total of 61 points were used to define the flexural mode shapes along girders, regardless of the number of measurement points. These mode shape vectors were unit-norm normalized to bring them to similar magnitudes prior to applying the five damage detection techniques described in Section 2.2. The unit-norm normalization process was defined in Eq. 2.10.

4.3.2 Results and Discussion

The objective of this section is to evaluate the performance of the five VBDD methods in terms of the accuracy with which they were able to predict the actual location of damage. As such, this section focuses on Level 2 damage identification (locating damage), rather than Level 1 (determining the presence of damage).

4.3.2.1 Performance of VBDD methods using well-defined mode shapes

Fig. 4.5 shows the performance of the five methods for locating a damage state located 1.75 metres from the support along the centre line of a girder. These plots were produced using only the fundamental mode shape before and after damage of the girder that was nearer to the damage and 59 measurement points along the girder. In each case, the highest positive peak corresponds to the predicted location of damage.

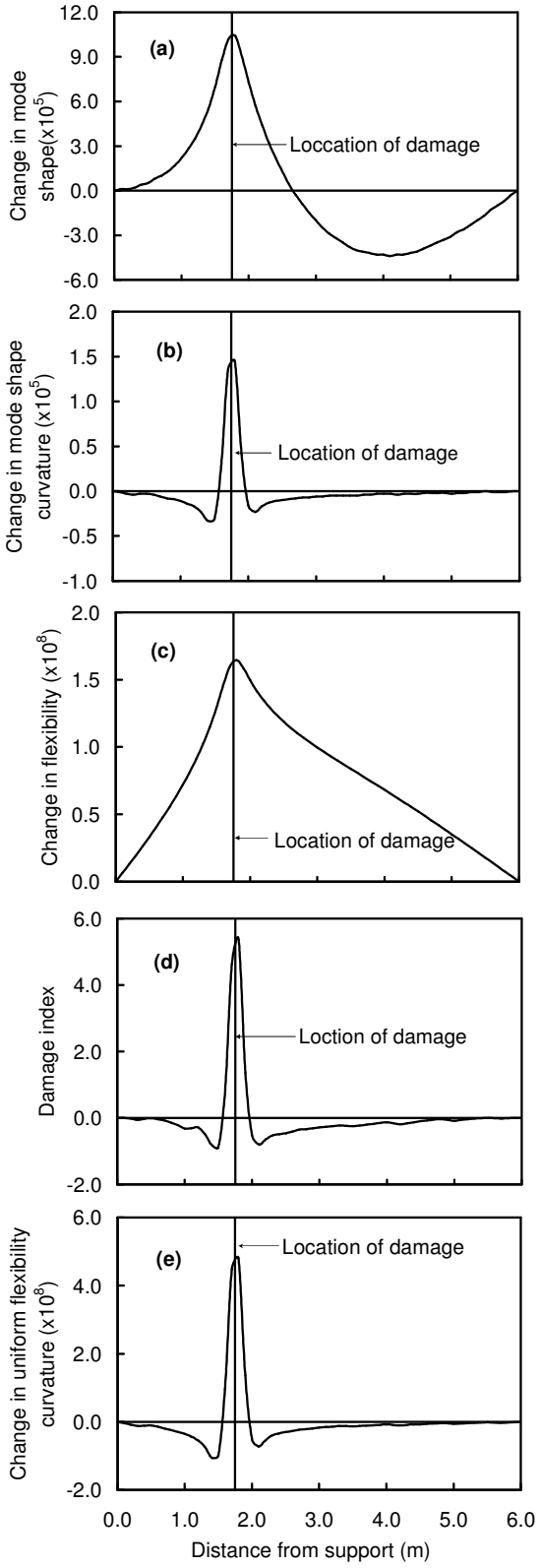

Figure 4.5. Performance of the five VBDD methods for locating the damage located at 1.75 m from support.

The change in mode shape produced by this damage case is shown in Fig. 4.5 (a). The distribution represents the difference between the unit-norm normalized mode shapes before and after damage was induced. Only one positive peak is visible, with this peak clearly and accurately indicating the location of damage. The maximum change of the mode shape was only 0.00010, which corresponds to 0.055% of the maximum value of the unit-norm normalized mode shape at mid-span, which was 0.183. Therefore, mode shape changes due to such small-scale damage require precise mode shape measurements.

The change in mode shape curvature is shown in Fig. 4.5 (b). In this case, the plotted value indicates the difference between the mode shape curvatures before and after damage was induced. Again, only one upward peak apparent in the figure; this peak is sharp, clearly and accurately indicating the location of damage. In contrast to the change in mode shape, the change in mode shape curvature is much sharper near the location of damage, but tends to decay to zero very quickly at locations far away from the damage. Therefore, the change in mode shape curvature appears to present more precise localized information, while the change in mode shape plot provides a more global indication of the presence of damage at some point on the beam.

The change in flexibility is shown in Fig. 4.5 (c); the vertical axis indicates the change in flexibility of the deck derived from the mode shapes before and after damage. All values of change of flexibility were positive. The peak correctly indicated the location of damage, although the peak is not particularly sharp.

The distribution of the damage index is shown in Fig. 4.5 (d). This distribution is very similar to that of the change in mode shape curvature shown in Fig. 4.5 (b); the difference is that the value of the damage index at the damage location (5.37) is much

larger than the value of change in mode shape curvature (0.000015) due to the fact that the damage index is a normalized value (see Section 2.2.3). This figure also supports Stubbs et al.'s finding (1995) that a value of damage index greater than 2.0 is deemed to be indicative of a possible damage location. The damage index method is the only one of the five VBDD methods investigated with an explicit criterion for establishing the existence of damage.

The change in uniform flexibility curvature is shown in Fig. 4.5 (e). The sharp upward peak clearly and accurately indicated the location of damage. Comparing Figs. 4.5 (e) and (b), it is apparent that the shapes of these two figures are almost the same, a finding that was consistent for all damage cases considered.

4.3.2.2 Influence of using a small number of measurement points

The above results, which are representative of those found for other damage locations, show that all five VBDD methods accurately predicted the longitudinal location of damage on the steel-free bridge deck when 59 measurement points were used. However, a small number of measurement points are more practical for the application of VBDD methods; therefore, the influence of the number of measurement points on the accuracy of the predicted longitudinal location of damage by these five VBDD methods is discussed next.

Fig. 4.6 shows the distributions of the five damage detection parameters calculated using the fundamental mode shapes defined by 5, 11, and 59 FE simulated measurement points when damage was located 1.75 m from the support.

Results using the change in mode shape are shown in Fig. 4.6 (a). The predicted locations of the damage were 1.8, 1.8 and 1.9 metres from the support when 59, 11, and 5 FE simulated measurement points were used, respectively. The corresponding errors

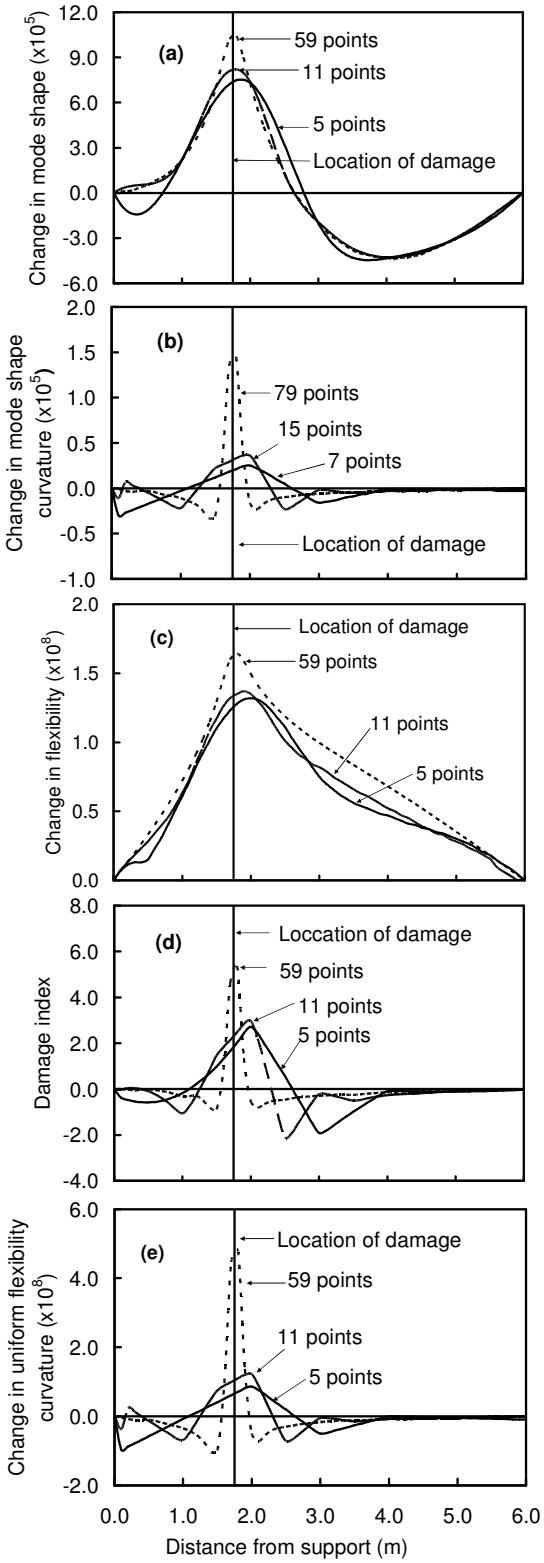

Figure 4.6. The influence of the number of measurement points on the accuracy of predicted longitudinal location of damage by five VBDD methods when damage was located 1.75 m from the support.

were therefore 0.05, 0.05 and 0.15 metres, respectively. A loss in the sharpness of the peak by using fewer measurement points was also observed, a finding that was consistent for all five VBDD methods (see Figs. 4.6 (b), (d) and (e)).

The change in flexibility is shown in Fig. 4.6 (c). The predicted locations of the damage were 1.8, 1.9 and 2.0 metres when 59, 11, and 5 FE simulated measurement points were used, respectively, with corresponding errors of 0.05, 0.15, and 0.25 metres, respectively.

The change in mode shape curvature, damage index, and change in uniform flexibility curvature are shown in Figs. 4.6 (b), (d), and (e), respectively. These three methods provided similar results, producing predicted locations of damage of 1.8, 2.0 and 2.0 metres when 59, 11, and 5 FE simulated measurement points were used, respectively, and corresponding errors of 0.05, 0.25, and 0.25 metres, respectively. It should be noted that, in these cases, the predicted locations of damage corresponded exactly to the location of the measurement point nearest to the damage, which was 2.0 metres from the support when 5 and 11 measurement points were used.

It is therefore evident that the accuracy of the predicted damage location improved as the number of measurement points increased for all five VBDD methods; in addition, the change in mode shape method performed better (i.e., more accurate damage localization) than other methods when a small number of measurement points were used. Also, the upward peaks of all five VBDD curves became sharper for the curves using 59 points; thus, the clarity of the peak improved as the number of measurement points increased.

The correlations between predicted and actual damage locations for all 30 longitudinally varying damage cases, as calculated using change in mode shape and

change in flexibility methods, are plotted in Fig. 4.7, considering only the fundamental mode. Figs. 4.7 (a), (b), and (c) indicate the correlation between predicted and actual locations of damage calculated by the change in flexibility method using 59, 11, and 5 FE simulated measurement points, respectively. Figs. 4.7 (d), (e), and (f) indicate the correlation between predicted and actual location of damage calculated by the change in mode shape method using 59, 11, and 5 FE simulated measurement points, respectively. For ease of reference, the gridlines in these plots indicate the locations of measurement points. Data points marked by solid circles indicate cases for which the predicted damage location was unambiguous, while open circles indicate that a peak in the parameter distribution plot was identified at these locations, but was not very well-defined; furthermore, one or more peaks of comparable magnitude also existed elsewhere, as illustrated in Fig. 4.8. In some cases, this could result in ambiguity with regard to identifying the location of damage, although it is believed that an experienced user would learn to correctly interpret these curves to ascertain the probable location of damage based on other characteristics of the curve. For example, a sharper upward peak is more likely to indicate the true damage location when two upward peaks of comparable magnitudes exist in the change in flexibility distribution, as shown in the plots represent 11 and 59 measurement points in Fig. 4.8.

Figs. 4.7 (a) and 4.7 (d), corresponding to cases in which 59 measurement points were used in conjunction with the change in flexibility and change in mode shape methods, respectively, show that mode shapes defined at a large number of points enable the damage to be located with great accuracy using either method.

Generally speaking, as the number of measurement points decreased, the accuracy in detecting the location of damage also decreased when using these two methods.

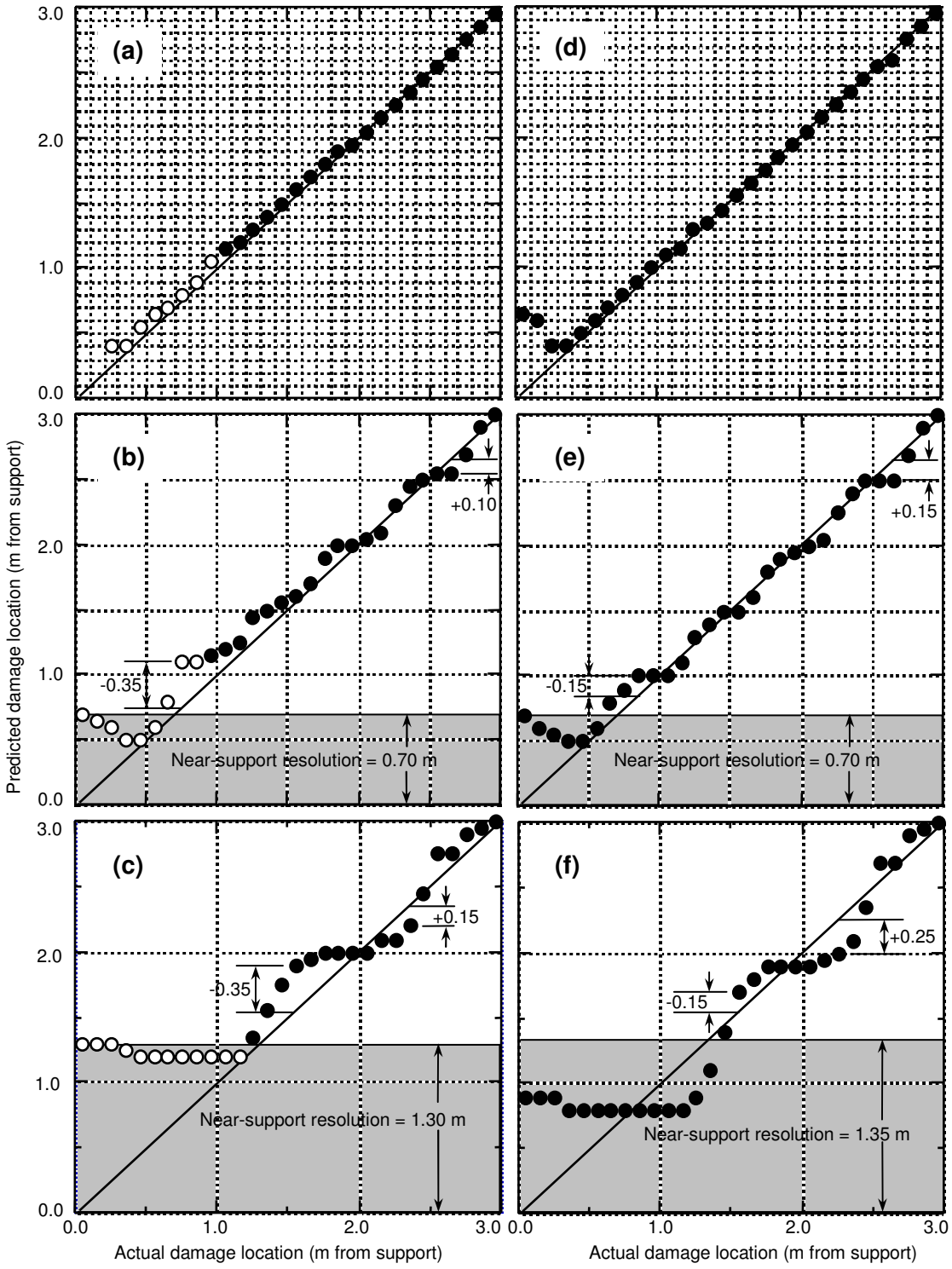

Figure 4.7. Correlation between predicted and actual longitudinal location of damage calculated by the change in flexibility method using a) 59, b) 11, and c) 5 FE simulated measurement points; and by the change in mode shape method using d) 59, e) 11, and f) 5 FE simulated measurement points.

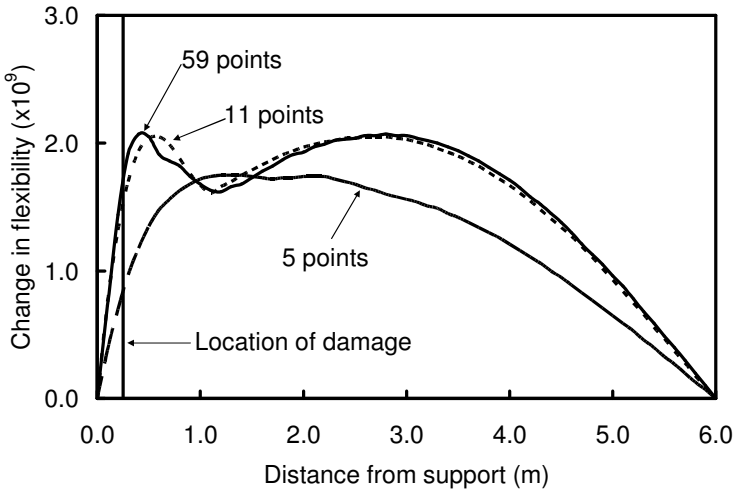

Figure 4.8. Variation of change in flexibility along girder for damage located 0.25 m from support, calculated using 5, 11, and 59 FE simulated measurement points using only the fundamental mode shapes.

However, this was not true for all cases. As long as damage was not located within the "near-support" regions (shown shaded on the graphs and defined below), the maximum error observed using the change in flexibility method with 11 measurement points (Fig. 4.7 (b)) was 0.35 m, or 70% of the distance between measurement points. When five measurement points were used (Fig. 4.7(c)), the maximum error was also 0.35 m, or 35% of the distance between measurement points. The change in mode shape method produced maximum errors of 0.15 m and 0.25 m, respectively, for these two cases (Figs. 4.7(e) and (f)).

Fig. 4.9 shows the plots of the predicted versus actual location of damage using mode shape curvature, change in uniform flexibility and damage index methods with 59, 11 and 5 simulated measurement points when only fundamental mode was used. Figs. 4.9 (a), (b), and (c) represent the results obtained from both mode shape curvature

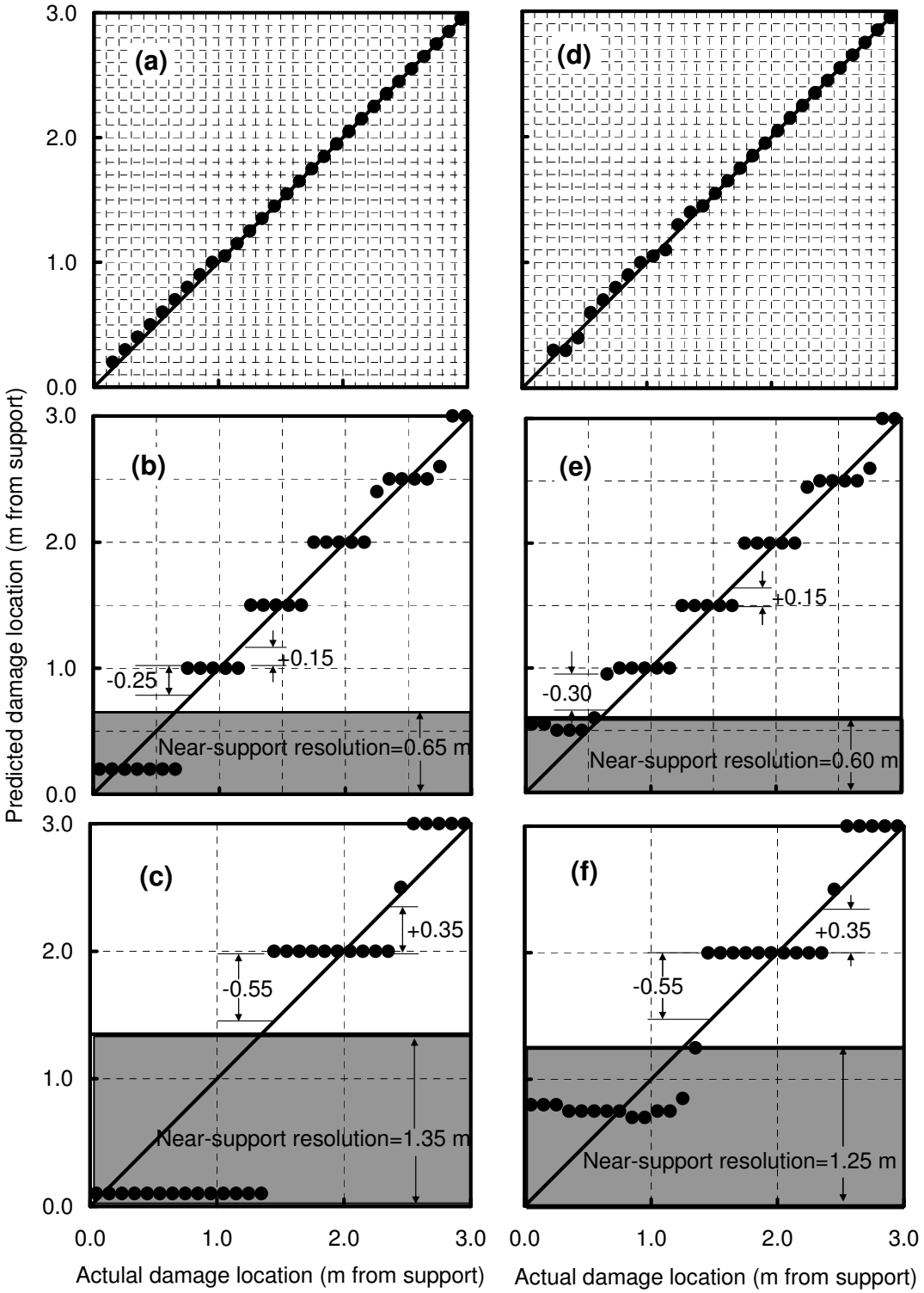

Figure 4.9. Correlation between predicted and actual longitudinal location of damage calculated by the mode shape curvature and change in uniform flexibility curvature methods using a) 59, b) 11, and c) 5 FE simulated measurement points; and by the damage index method using d) 59, e) 11, and f) 5 FE simulated measurement points.

and change in uniform flexibility curvature methods since these two methods produced identical results for all these damage cases.

Similar to Fig. 4.7 (a) and (d), Figs. 4.9 (a) and (d) represent the damage detection results using 59 simulated measurement results. Excellent results were therefore observed for all damage detection methods investigated when a large number of measurement points were used, indicating that any of the techniques are capable of detecting and locating small-scale damage with a high degree of precision if fundamental mode shapes can be defined very precisely.

The damage detection results by the mode shape curvature and change in uniform flexibility curvature methods are plotted in Fig. 4.9 (b) when 11 measurement points were used and in Fig. 4.9 (c) when 5 measurement points were used, respectively. When damage was not located within the "near-support" regions (denoted by the shaded regions on the graphs and discussed further in section 4.3.2.3), the maximum error observed using mode shape curvature and change in uniform flexibility methods with 11 measurement points (Fig. 4.9 (b)) was 0.25 m, or 50% of the distance between measurement points. When five measurement points were used (Fig. 4.9(c)), the maximum error was 0.55 m, or 55% of the distance between measurement points. The damage index method produced maximum errors of 0.30 m and 0.55 m when 11 and 5 measurement points were used, as shown in Fig. 4.9(e) and Fig. 4.9 (f), respectively. It is therefore obvious that as the number of measurement points decreased, the accuracy in detecting the location of damage also decreased for these three methods.

As suggested in Figs. 4.9 (b), (c), (e), and (f), the mode shape curvature method, the damage index method, and the change in uniform flexibility curvature method showed a pronounced tendency to predict damage to be located exactly at the nearest

measurement point. The reason for this tendency when the mode shape curvature was used directly or indirectly as the basis for VBDD is related to the use of cubic polynomials to interpolate mode shapes between measurement points, which leads to piecewise linear distributions of curvature. The reliance of the damage index and change in uniform flexibility curvature methods on different forms of mode shape curvature must also be responsible for a similar tendency with these two methods. Given this tendency, the best that can be expected from these methods is a maximum error of not less than half the spacing between measurement points. In addition, the maximum error typically occurred when damage was located furthest from measurement points (i.e. one-half the distance between measurement points). Conversely, when damage was located near a measurement point, the accuracy in locating it was very high, regardless of the number of measurement points. Again, this peculiarity is a function of the cubic spline interpolation technique. Preliminary study shows that the use of higher order interpolation methods can diminish this feature; however, higher order interpolation methods are more sensitive to the uncertainty in the mode shape measurement, preventing improved location resolution when these VBDD techniques are used in practical application. Increased vulnerability to measurement noise is believed to be the reason why the use of higher order interpolation methods in VBDD has not been reported in any of the related literature.

4.3.2.3 Influence of proximity of damage to a support

It is seen in Figs. 4.7 and 4.9 that the accuracy with which damage could be located by the VBDD techniques investigated declined when damage was located near the support, especially when a small number of measurement points were used. This result is

not unexpected since both the mode shape values and curvatures are small in the vicinity of a simple support.

This phenomenon can be understood by considering Fig. 4.8, which shows a plot of the change in flexibility parameter when damage was located 0.25 metres from the support calculated using 59, 11 and 5 measurement points. In this case, the clarity of the peaks was diminished compared to when damage was located farther from the support (Fig. 4.6); curves typically indicated that damage was present and that it was likely located near the support, but its location could not be determined with certainty due to the indistinct nature of the peaks and the presence of large values elsewhere as well. This was true even when mode shapes were precisely defined at 59 points, although in this case the identified peaks were somewhat more distinct than those when fewer points were used and were present close to the actual damage location, as reflected in Fig. 4.7 (a). When 11 measurement points were used (Fig. 4.7b), an identifiable peak was located near the actual damage location only when damage was located near the first measurement point (at 0.5 m).

4.3.2.4 Influence of numbers of modes considered

Many researchers investigating VBDD have suggested that higher modes are more sensitive to damage (Pandey et al. 1991, Pai and Young 2001); however, no conclusive evidence has been presented to support the hypothesis that higher modes improve the accuracy of damage localization. The influence of the numbers of modes considered on the accuracy of predicted damage location in the present study is discussed next.

Fig. 4.10 shows a plot of the change in flexibility method calculated using the first three flexural modes when damage was located 0.25 metres from the support and 5, 11, and 59 measurement points were used to define mode shapes. Comparing Fig. 4.10 with

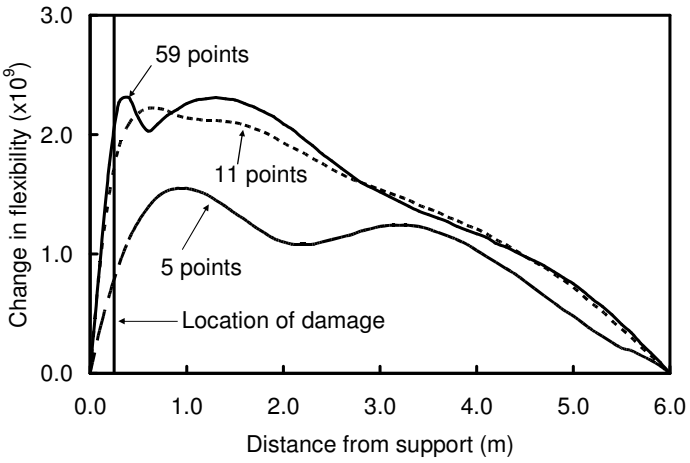

Figure 4.10. Variation of change in flexibility along girder for damage located 0.25 m from support, calculated using 5, 11, and 59 FE simulated measurement points using the first three flexural modes.

Fig. 4.8, it is seen that the use of two additional flexural modes produced slightly more distinct peaks near the support when 59 measurement points were used, but the accuracy did not improve significantly.

Fig. 4.11 shows the distribution of the change in mode shape calculated using the first three flexural modes when damage was located 2.05 metres from the support and 5, 11, and 59 measurement points were used to define mode shapes. The y-axis represents the sum of the change of each mode shape for the first three modes, as defined in Eq. 2.11. It was found that the highest peak did not necessarily occur at the location of damage regardless of the number of the measurement points when the first three flexural modes were used. In other words, it appears that the change in mode shape method should only be used with the fundamental mode.

The correlation between predicted and actual damage locations for all 30 longitudinally varying damage cases, as calculated by the change in uniform flexibility

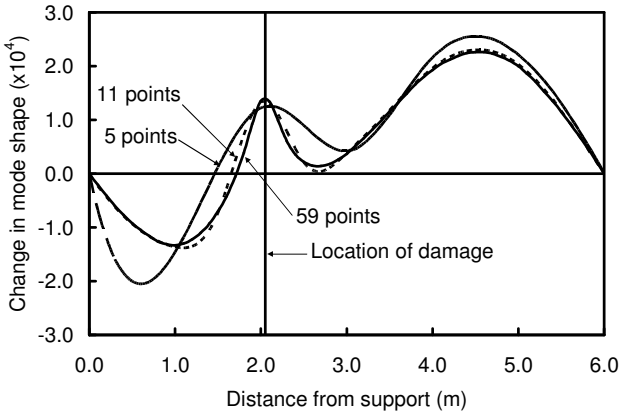

Figure 4.11. Variation of change in mode shape along girder for damage located 2.05 m from support, calculated using 5, 11, and 59 FE simulated measurement points using the first three flexural modes.

curvature method using 59, 11 and 5 measurement points is plotted in Figs. 4.12 (a), (b), and (c), respectively. Comparing with Figs. 4.9 (a), (b), and (c), it is apparent that identical results were obtained by using both the fundamental mode and the first three flexural modes regardless of the number of measurement points. This finding is attributed to the fact that the magnitude of the change in uniform flexibility curvature for higher modes is much smaller than that of the fundamental mode; in other words, the change in uniform flexibility curvature of the fundamental mode plays the key role in the sum of the change in uniform flexibility curvature for the first three modes.

The correlations between predicted and actual damage locations for all 30 longitudinally varying damage cases, as calculated by the change in flexibility method using 59, 11 and 5 FE simulated measurement points and first three flexural modes are plotted in Figs. 4.12 (d), (e) and (f). Figs. 4.12 (d), (e) and (f) illustrate that the use of two additional flexural modes produced more distinct peaks near the support, but comparison with Figs. 4.7 (a), (b) and (c) shows that the accuracy did not improve

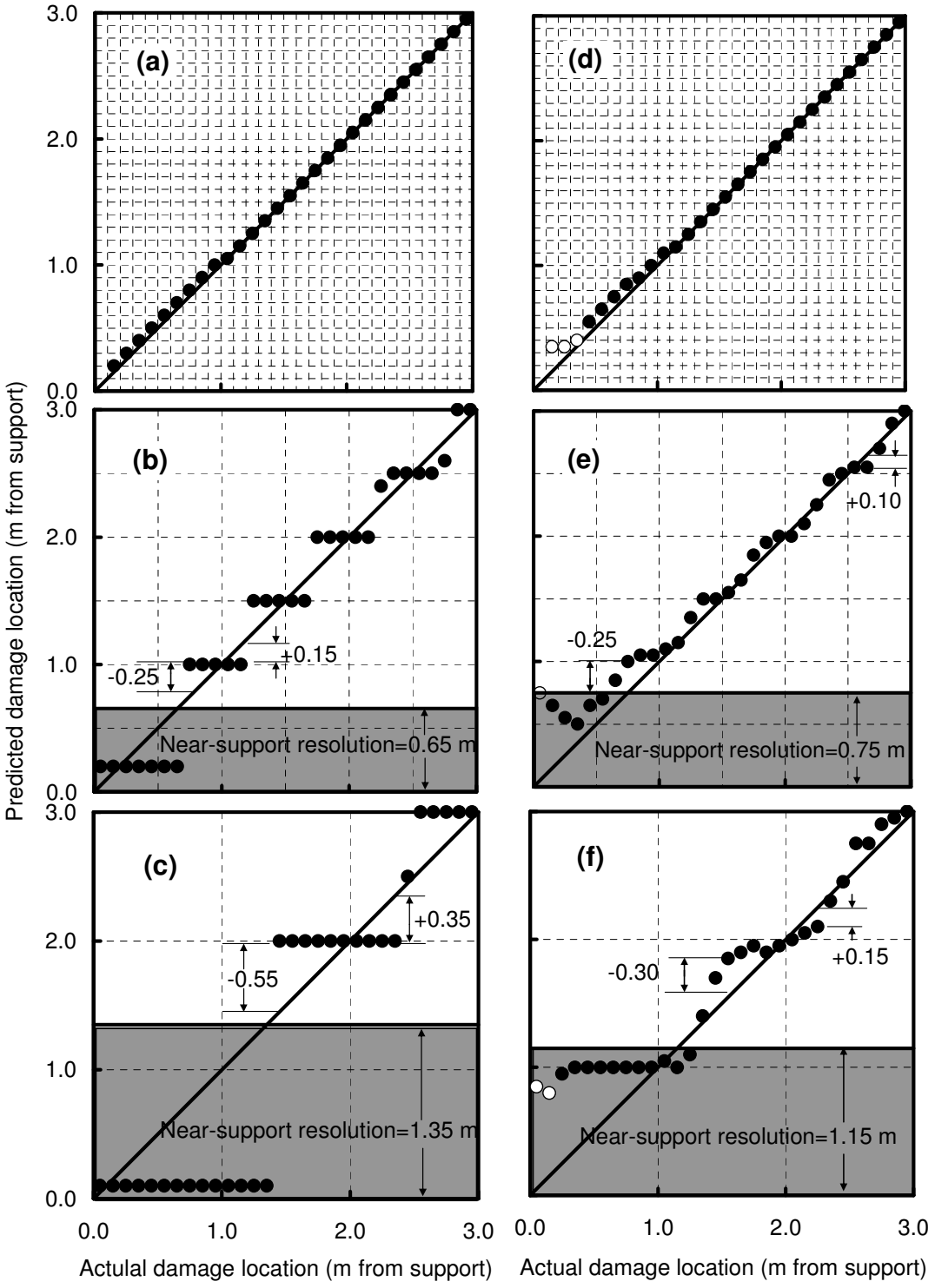

Figure 4.12. Correlation between predicted and actual longitudinal location of damage calculated by change in uniform flexibility curvature method using a) 59, b) 11, and c) 5 FE simulated measurement points; and by the change in flexibility method using d) 59, e) 11, and f) 5 FE simulated measurement points when the first three flexural modes were used.

significantly, either near the support or elsewhere. This was true in general, regardless of the number of measurement points.

The correlation between predicted and actual damage locations for these 30 damage cases, as calculated by the mode shape curvature and damage index methods using the first three flexural modes are plotted in Fig. 4.13. Comparing Fig. 4.13 (a), (b), and (c) with Figs. 4.9 (a), (b), and (c), it is seen that using the first three flexural modes did not significantly improve the accuracy of predicted damage location for the mode shape curvature method regardless of the number of the measurement points or whether the damage was located in a near-support region or non-near-support region.

Comparing Fig. 4.13 (d), (e), and (f) with Figs. 4.9 (d), (e), and (f), it is seen that the accuracy of the predicted damage location by the damage index method using the first three flexural modes decreased slightly in the near-support region and decreased significantly in non-near-support region when a small number of measurement points were used. This was attributed to the instability of the index when the reference modal strain energy was close to zero in a given region; i.e., the nodal points where the value of mode shape curvature is zero (Kim and Stubbs 2003).

In general, the use of three modes resulted in only slight improvements, at best, of the accuracy of damage localization. For the damage index method, in fact, the accuracy decreased as a small number of measurement points were used.

4.3.2.5 Comparison of VBDD techniques in terms of accuracy of damage localization

In order to facilitate comparisons of the performance of different VBDD methods in terms of their ability to localize damage, the resolution of a damage locating procedure was defined as the length of the window within which damage could actually lie when

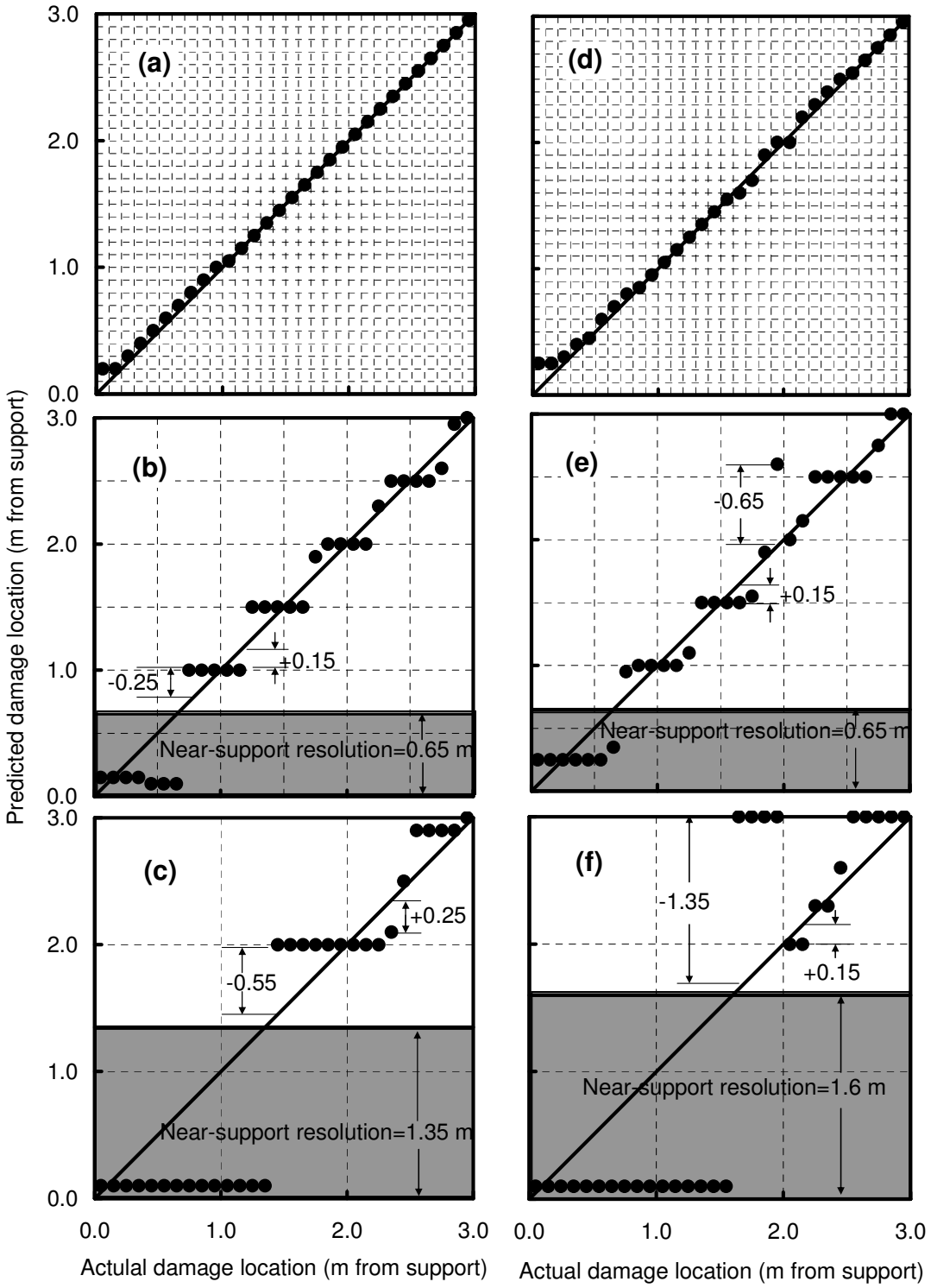

Figure 4.13. Correlation between predicted and actual longitudinal location of damage calculated by the mode shape curvature methods using a) 59, b) 11, and c) 5 FE simulated measurement points; and by the damage index method using d) 59, e) 11, and f) 5 FE simulated measurement points when the first three flexural modes were used.

the procedure predicts it to be located at a particular point. In attempting to define the resolution for different techniques, two observations are instructive. First, when the location of damage was predicted to lie within a certain characteristic distance from a support, the actual location could be anywhere within this near-support region. This characteristic distance has been termed the "near-support resolution" and is indicated in Figs. 4.7, 4.9, 4.12, and 4.13 by the shaded regions. In other words, there was no correlation between the predicted and actual location of damage when damage was predicted to lie within this support region.

For example, for the change in flexibility method using five measurement points (Fig. 4.7 (c)), the near-support resolution was 1.30 m, since any time the predicted location of damage lay within 1.30 m of the support, the actual damage location could be anywhere within this region. For the change in mode shape method using five measurement points, inspection of Fig. 4.7 (f) reveals a near-support resolution of 1.35 m.

A second observation is that when damage was located outside the near-support region, individual techniques tended to produce larger errors on either one side or the other of the actual damage location. This is illustrated in Figs. 4.7, 4.9, 4.12 and 4.13 by identifying the maximum errors when actual damage locations are closer to supports (shown as negative) and farther from supports (shown as positive) than predicted locations. For example, Figs. 4.7 (a) through 4.7 (c) show that the change in flexibility method tended to produce larger errors when the actual location lay closer to the support than the predicted location. For the case of five measurement points, when the actual location was closer to the support than the predicted location, the maximum error was 0.35 m; when the actual location was farther from the support, the maximum error was

only 0.15 m. Therefore, when damage was predicted to be located at a certain point, the actual location was known to lie within a region 0.35 m closer to the support or 0.15 m farther from the support; for this case, the damage location resolution was 0.50 m, or half the spacing between measurement points, with the resolution window skewed 70-30 toward the support. For the change in mode shape method (Fig. 4.7 (f)), the resolution was 0.40 m, skewed 62-38 away from the support.

Employing these definitions with the results shown in Figs. 4.7, 4.9, 4.12 and 4.13, Fig. 4.14 provides the damage localization resolutions achieved using all the VBDD techniques investigated, normalized by the spacing between measurement points, h. The focus of this discussion is initially on the performance using only the fundamental mode (indicated by solid bars); shaded bars correspond to the use of three flexural modes.

Figs. 4.14 (a) and (b) show that the performance of most techniques was comparable using either 5 or 11 measurement points to locate damage away from supports, achieving resolutions between $0.8h$ and $0.9h$. However, the change in mode shape method performed better than this, achieving resolutions of $0.6h$ and $0.4h$ for 11 and 5 measurement points, respectively. The change in flexibility method also performed very well, achieving a resolution of $0.5h$ when 5 points were used.

In most cases, an increase in the number of measurement points led to a proportional improvement in resolution (in absolute terms). In other words, resolution was a direct function of measurement point spacing, h. However, for the change in flexibility method, the resolution in relative terms was much better when 5 measurement points were used, which corresponded to a decline in absolute resolution of only 5 cm when the number of measurement points decreased from 11 to 5.

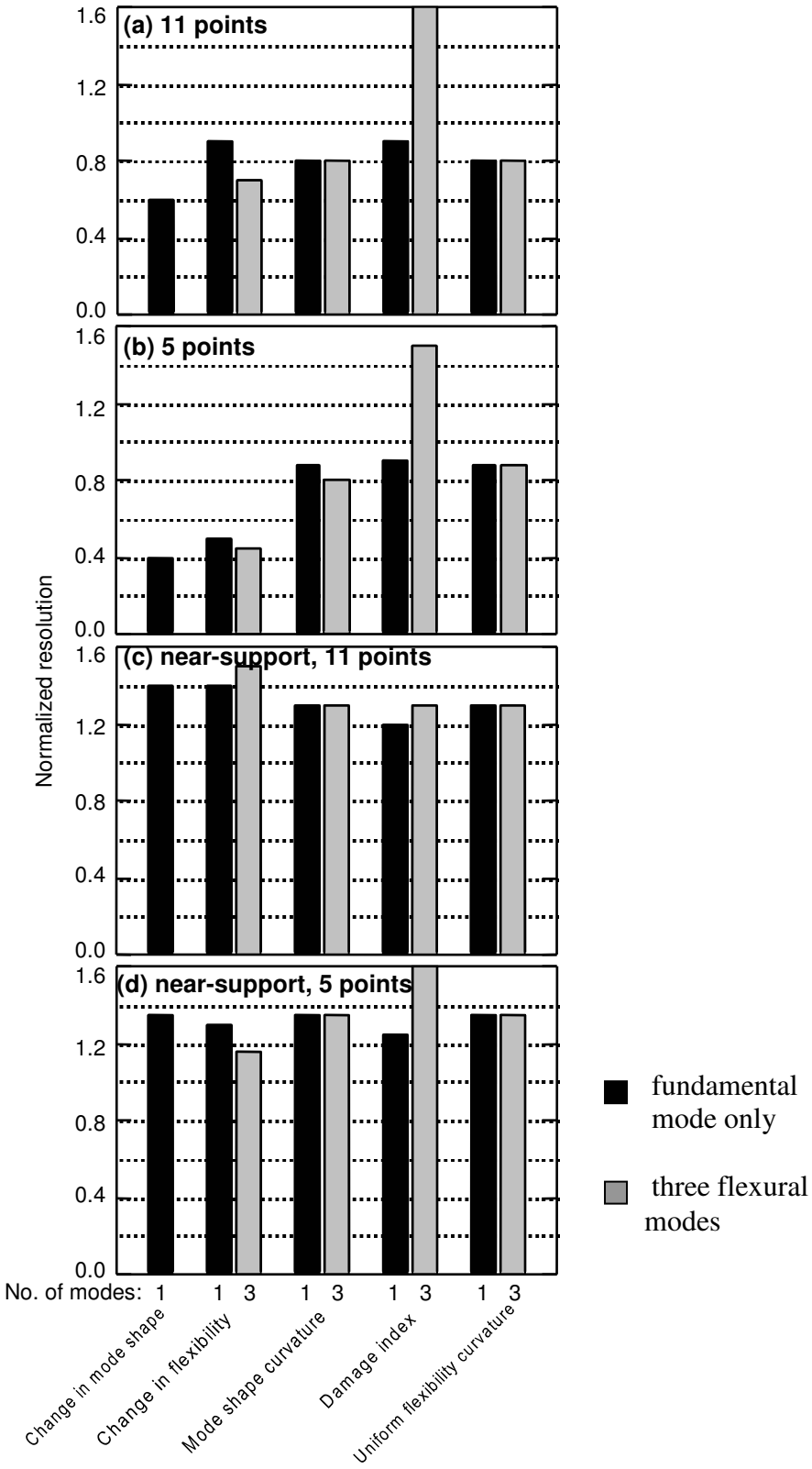

Figure 4.14. FE derived damage localization resolutions, normalized by the spacing between measurement points, using a) 11 and b) five measurement points; and near-support resolutions for c) 11 and d) five measurement points.

The near-support resolutions of most methods were also comparable, achieving values between 1.2*h* and 1.4*h* (Figs. 4.14 (c) and (d)). The use of additional modes did not improve the performance significantly.

An improved damage localization resolution was sometimes achieved by considering the intersection of overlapping resolution windows produced by different methods. For example, since the window of the change in flexibility method was skewed toward the support relative to the predicted location, while the window of the change in mode shape method was skewed away from the support, if both techniques predict damage to be located at the same point, the intersection of the two windows was smaller than either of the individual windows. When five measurement points were used, the intersection between the windows described above was 0.30 m or 0.3*h*. This combined resolution cannot be quantified precisely because different techniques typically predicted different damage locations and the relationship between these locations was not constant.

4.3.2.6 Transverse damage localization

Finally, the determination of the transverse location of damage is discussed in this section. Although a great deal of research on the application of VBDD methods on girders has been done over the past thirty years, most of this research has focused on the longitudinal location of damage. It is very rare to find research related to the determination of the transverse location of damage.

In this study, when the change in mode shape method and the fundamental mode were used to determine the longitudinal location of damage, it was found that the change in the mode shapes along the two girders were different, except when the damage was located exactly midway between the two girders. As expected, the mode shape along the

girder closer to the damage exhibited a larger change compared with the mode shape along the girder which was farther from the damage. Therefore, it was hypothesized that comparison of the mode shape changes along the two girders could provide information regarding the transverse location of damage.

Based on the above finding, a procedure was developed to estimate the transverse damage location on a two-girder slab-on-girder bridge deck using mode shape measurements along each girder, before and after damage. In this method, Δ_s is defined as the difference between the damaged and undamaged unit-norm-normalized mode shapes at the point of maximum change in mode shape (calculated by Eq. 2.11) for the girder with the smaller difference at the point of maximum change in mode shape; similarly, Δ_l is defined as the corresponding difference for the girder with the larger change of mode shape. The transverse distance, z_d, from the girder with the larger difference to the location of damage was found to be approximated by

$$z_d = \frac{\Delta_s}{|\Delta_s|} \cdot \sqrt{\frac{|\Delta_s|}{\Delta_l}} \cdot \frac{S_g}{2}, \qquad [4.1]$$

where S_g is the girder spacing. It should be noted that the form of Eq. 4.1 was adopted after many different functions of $\frac{\Delta_s}{\Delta_l}$ were investigated.

Figs. 4.15 (a), (b), and (c) show the correlations between predicted and actual transverse locations for the second series of damage states (as defined in Fig. 4.4) when 59, 11 and 5 measurement points were used, respectively. Excellent correlation is seen between predicted and actual damage locations in Fig. 4.15(a) when 59 measurement points were used, with a maximum error of less than 7% of the girder spacing. The

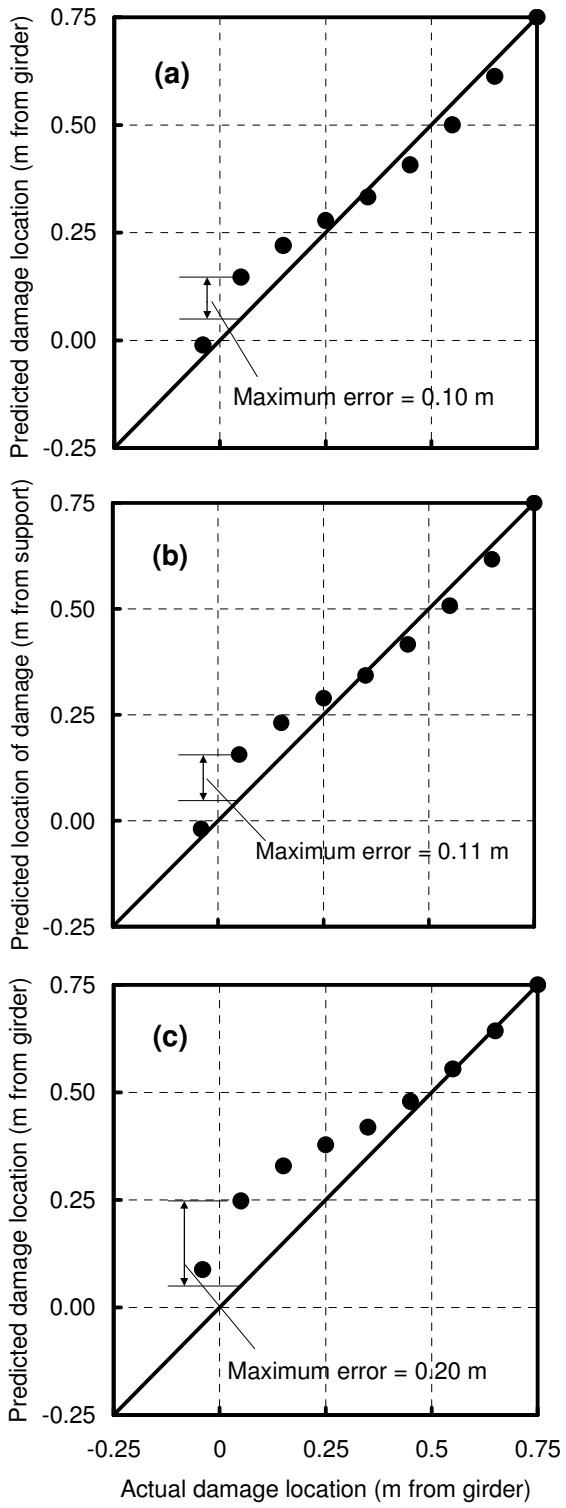

Figure 4.15. Correlation between predicted and actual transverse locations for the second series of damage states in Fig. 4.4, calculated using (a) 59, (b) 11, and (c) 5 FE simulated measurement points.

accuracy improved as damage moved closer to midway between girders, and was worst when damage was located close to one of the girders.

The results using 11 measurement points in Fig. 4.15 (b) are very similar to those using 59 measurement points. When only 5 measurement points were used, however, the maximum error was doubled to 0.20 metres, equivalent to 13.3% of the girder spacing, a result still considered to be acceptable.

4.3.2.7 Summary

In the absence of experimental uncertainty, small-scale damage was detected and located on the deck of a simple span bridge with a longitudinal resolution of approximately 40% of the spacing between five evenly spaced measurement points, and transversely with a resolution of 13.3% of the girder spacing, provided it did not occur too near a support. When damage is located near the support, the resolution and level of certainty diminished, but its presence and location could still be determined.

4.4 EXPERIMENTAL STUDY

4.4.1 Description of Experimental Study

The setup of the experiment for the steel-free bridge deck is shown in Fig. 4.16. The hydraulic shaker was mounted along the center line of the deck, while five evenly spaced accelerometers were mounted along one side of the deck.

The configuration of damage induced in the physical system was similar to that modelled numerically: small square blocks of concrete, 100 x 100 mm in plan and 25 mm deep, were physically removed from the top surface of the deck, as shown in Fig. 4.17. This was a very low level of damage for the bridge deck, corresponding to a local

Figure 4.16 Experimental set-up for the steel-free bridge deck.

Figure 4.17. Damage induced on the surface of the laboratory model.

reduction in flexural rigidity of approximately 1.57%. Damage was induced incrementally at nine different locations, as shown in Fig. 4.18, on which damage states are numbered according to the sequence in which they were introduced. The nine cases represented a wide variation in longitudinal and transverse locations to test the damage locating capability of the VBDD techniques over the full range of possible damage locations. The experimental procedure consisted of measuring the initial (undamaged) dynamic properties of the system, and then incrementally inducing a new state of damage and measuring the properties associated with each state. The "undamaged" dynamic signature for a particular damage state was taken to be that measured for the previous state of damage.

Dynamic excitation and measurement procedures were described in Chapter 3. The locations of accelerometers and strain gauges are shown in Fig. 4.18. Five evenly spaced accelerometers were used along each girder line, and six sets of unevenly spaced strain

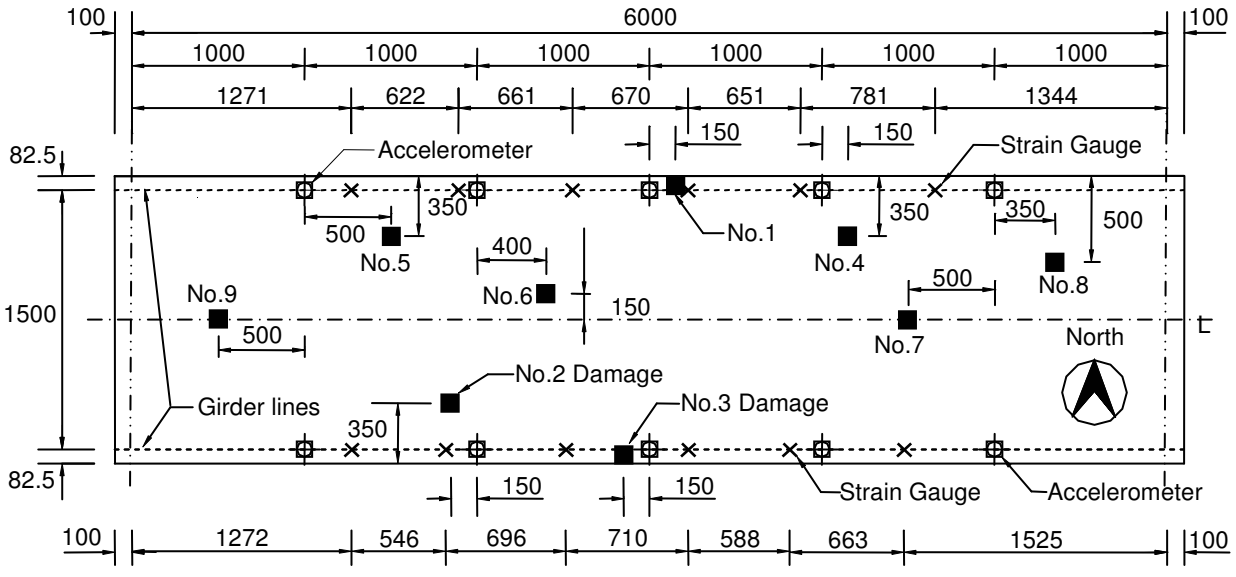

Figure 4.18. Schematic plan of deck showing locations of induced damage and sensors (dimensions in mm).

gauges were used along each girder. The five VBDD techniques described in Chapter 2 were applied using the accelerometer data. They included the mode shape curvature method, the change in flexibility method, the damage index method, the change in uniform flexibility curvature method, and the change in fundamental mode shape method.

The method proposed in Section 4.3.2.6 for determining the transverse location of damage on the deck slab of a two-girder bridge deck was also applied experimentally using the accelerometer data.

4.4.2 Results and Discussion

4.4.2.1. Strain Gauge Data

Only the mode shape curvature method was used with strain gauge data to detect damage since mode shape curvature can be obtained directly from strain gauge data. The other four VBDD methods rely on the deflection mode shapes, while the process of integrating curvatures based on strain gauge data to derive deflections resulted in an unacceptable level of accuracy for detecting small scale damage (see Section 3.3.2).

Fig. 4.19 shows representative plots of change in mode shape curvature, $\Delta\phi''_1$, calculated using flexural curvatures associated with the fundamental mode shape derived from strains measured on girder webs. The change in mode shape curvature of remaining damage cases are plotted in Figs. C.1 and C.2 of Appendix C. It should be recalled that the baseline ("undamaged") curvature for each state of damage was that associated with the previous state of damage and that curvatures were taken as the average value from ten repeated trials.

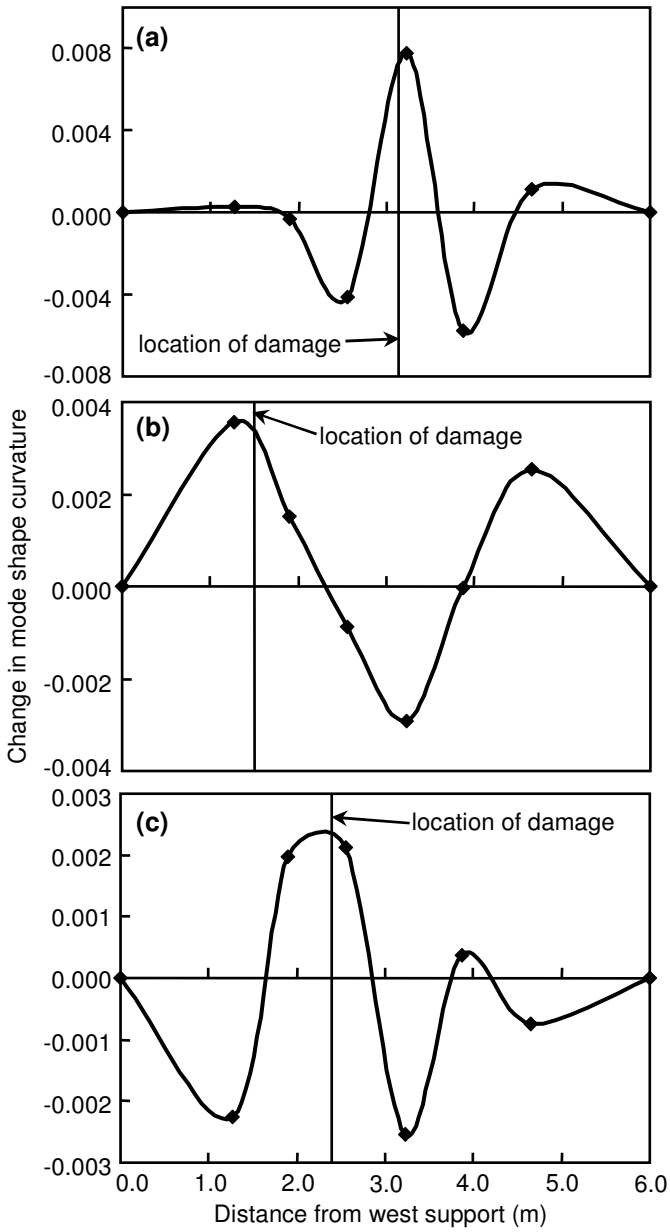

Figure 4.19. Change in mode shape curvature along the north girder, calculated using strain gauge measured curvature for a) damage case 1, b) damage case 5, and c) damage case 6, as defined in Fig. 4.18.

The highest positive peaks in these plots indicate the predicted longitudinal location of damage. No ambiguity is apparent with respect to identifying the highest positive peak, which was observed to occur near the actual location of all damage states

except damage cases 8 and 9, which were located very near the support. Note that these plots also show significant negative peaks. These correspond to reductions in mode shape curvature associated with the introduction of damage, and do not indicate a damage location. It should also be noted that only the data from the strain gauges on the girder to which the damage was closer indicated the location of damage well; the strain gauges on the opposite girder did not provide useful information for damage localization. Both damage cases 7 and 9 were located midway between the two girders; for those cases, strain gauges on the south girder did not properly indicate the damage location. It is therefore suspected that the strain gauges on south girder experienced more electrical interference since they were closer to the motor of the hydraulic pump.

The correlations between predicted and actual damage locations are shown in Fig. 4.20, with data points labelled according to the damage cases of Fig. 4.18. The gridlines shown as dotted lines correspond to the locations of measurement points on the north girder. Since south girder data were used for damage cases 2 and 3, and measurement locations differed slightly for each girder, the locations of the grids are not accurate for these damage cases.

Good agreement is noted for the first seven damage cases. The maximum absolute error was 0.30 m, attained for damage case 3, which corresponds to a relative error of approximately 42% of the spacing between measurement points at that location. Numerical study results for the mode shape curvature method indicated that the maximum relative error was 50% and 55% of the spacing between measurement points when 11 and 5 measurement points were used, as shown in Figs. 4.9 (b) and 4.9 (c), respectively. It should be noted that although 5 measurement points were used in the experiment, the average spacing between sensors near mid-span of the deck was about

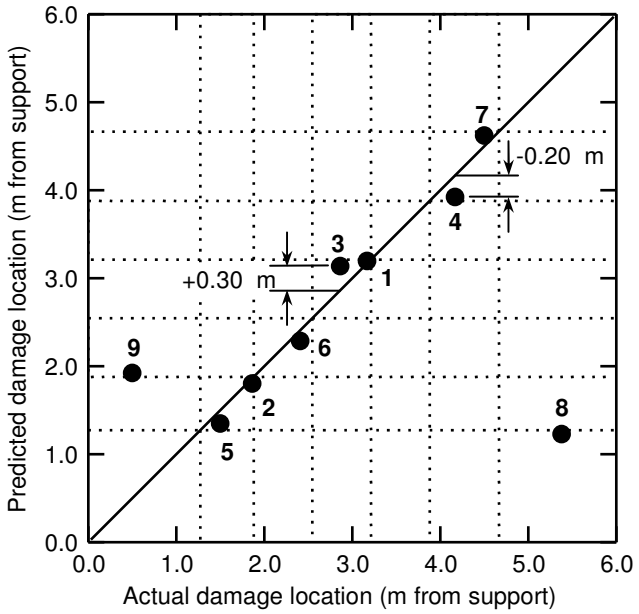

Figure 4.20. Correlation between predicted and actual longitudinal locations of damage, as calculated by the mode shape curvature method using strain gauge measured curvature (the numbers refer to damage cases defined in Fig. 4.18).

0.6 metres, which is close to the spacing between measurement points (0.5 m) when using 11 FE simulated measurement points, rather than that (1.0 m) using 5 measurement points. The maximum error achieved experimentally can be considered to be a lower bound on the actual expected maximum error because of the relatively small number of damage cases considered, and the fact that no damage cases were induced exactly midway between measurement points, where maximum errors were observed numerically.

The detection technique failed to successfully locate damage cases 8 and 9, both located relatively close to supports. In fact, the results for these two cases—particularly case 8—were misleading in that the predicted location, denoted by a clear peak, was nowhere near the actual location. Several factors are believed to have contributed to this

failure. The distance between supports and the nearest measurement points was relatively large, and the proximity of both damage cases to the nearest gauge was more than double that for any other case. In addition, curvatures, and therefore strain measurements near supports, were small. This led to smaller signal-to-noise ratios and smaller changes in curvature in these regions. Positioning a set of gauges nearer to the supports may have improved the performance of this damage locating technique for these two damage cases; however, this was not investigated. While this study focussed on a simply supported structure, it can be reasonably postulated that regions near mode shape inflection points for indeterminate structures may require special attention as well when this type of VBDD technique is used.

The proximity of damage to a measurement point was found to significantly influence the accuracy with which damage could be located. A plot of absolute error versus the longitudinal distance to the nearest gauge in Fig. 4.21 shows a high correlation (R = 0.96) between these two variables, as long as cases 8 and 9 were excluded.

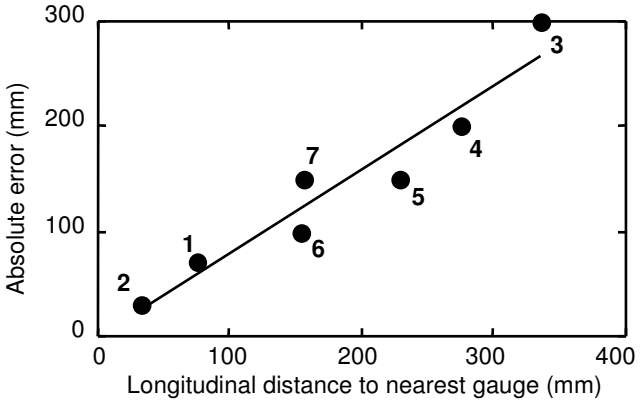

Figure 4.21. Absolute error in locating damage, as a function of longitudinal distance to the nearest strain gauge group, calculated by the mode shape curvature method using strain gauge measured curvature.

The resolution of damage localization, defined as the length of the window within which damage is known to lie when the procedure predicts it to be located at a particular point, was found to be 0.50 m (or approximately 0.68*h*, where *h* is the spacing between measurement points) when damage was not located between a support and the nearest measurement point. This accounts for the fact that the resolution window is skewed slightly away from the support. In other words, the actual location of damage was a maximum of 0.3 m (0.42*h*) farther from the support (case 3) and 0.2 m (0.26*h*) closer to the support (case 4) than the predicted location (see Fig. 4.20). Given the limited number of damage cases studied, this result must be viewed as a lower bound since the worst possible damage location may not have been considered. However, the level of resolution was slightly smaller than that achieved numerically in the absence of experimental uncertainty. Fig. 4.14 indicates that the resolution of the mode shape curvature method achieved in the numerical study was 0.8*h*, larger than the 0.68*h* resolution achieved experimentally. The inability of the method to locate damage cases 8 and 9 precluded the formation of a near-support damage localization resolution for this method.

4.4.2.2. Accelerometer Data

Fig. 4.22 shows the distributions of all five damage detection parameters corresponding to the fifth damage case, for which damage was located 1.5 m from the support; for these calculations, accelerometer data acquired at five evenly spaced accelerometers along the north girder were used (see Fig. 4.18). The highest positive peak in each plot indicates the predicted longitudinal location of damage. In these plots, parameters have been normalized relative to their maximum values to facilitate comparisons. The damage index parameter would not ordinarily be normalized, since its

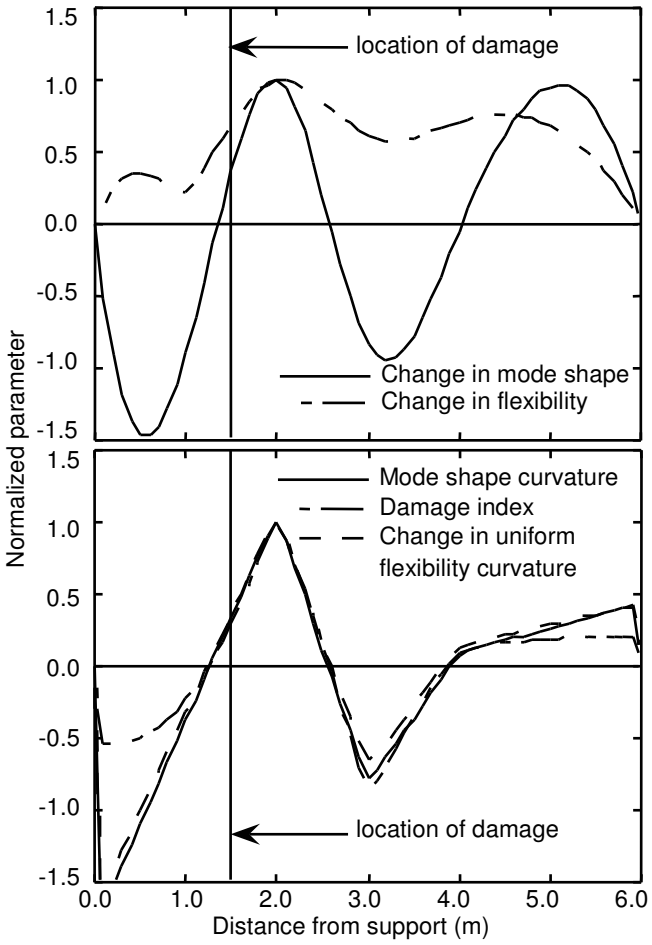

Figure 4.22. Distribution of normalized damage detection parameters, calculated along the north girder for damage case 5 by all methods.

magnitude is of significance (a threshold value of two is used to indicate damage); however, its normalization permits the plotting of all parameters on a common scale. Appendix D contains similar figures for the remaining damage cases.

The plots illustrate three features observed more generally when the entire set of results is examined. First, the highest peak occurred at or close to the same location (2.0 metres from the support in this case) for each method. Second, the predicted location coincided with the location of an accelerometer (see Fig. 4.18). Third, the mode shape curvature and change in uniform flexibility curvature methods produced virtually

identical distributions in which the parameters varied linearly between measurement points, a feature that resulted from the use of cubic polynomials to interpolate mode shape displacements between measurement points. The damage index method, which also makes use of mode shape curvatures (though not as linear functions), produced distributions which were similar to those of the two methods just mentioned, but which differed from them by taking on smaller values near the supports. As shown subsequently, this latter feature allowed the damage index method to produce a more unambiguous determination of the damage location in cases when damage was not located near a support.

One further note should be made with reference to Fig. 4.22: for this particular damage case, the change in mode shape method produced an ambiguous result since two positive peaks with similar magnitudes were observed—one near two metres and one near five metres from the support. While not characteristic of this particular method, it serves to illustrate the type of ambiguity that occurred in some cases for all methods that were used. In the correlation plots presented below, such a result is indicated by an open circle symbol at the location of the highest peak. When the lower of two peaks of similar magnitude occurred closer to the actual location of damage, the location of the lower peak was plotted and was indicated by an open square symbol with an inscribed 'x'.

The correlations between predicted and actual damage locations for all damage cases are shown in Fig. 4.23, in which gridlines correspond to the locations of accelerometers, filled circle symbols indicate the location of unambiguous peaks in the damage detection parameters, and other symbols indicate ambiguous cases as described above. All techniques are seen to have performed relatively well. Not including the near-support

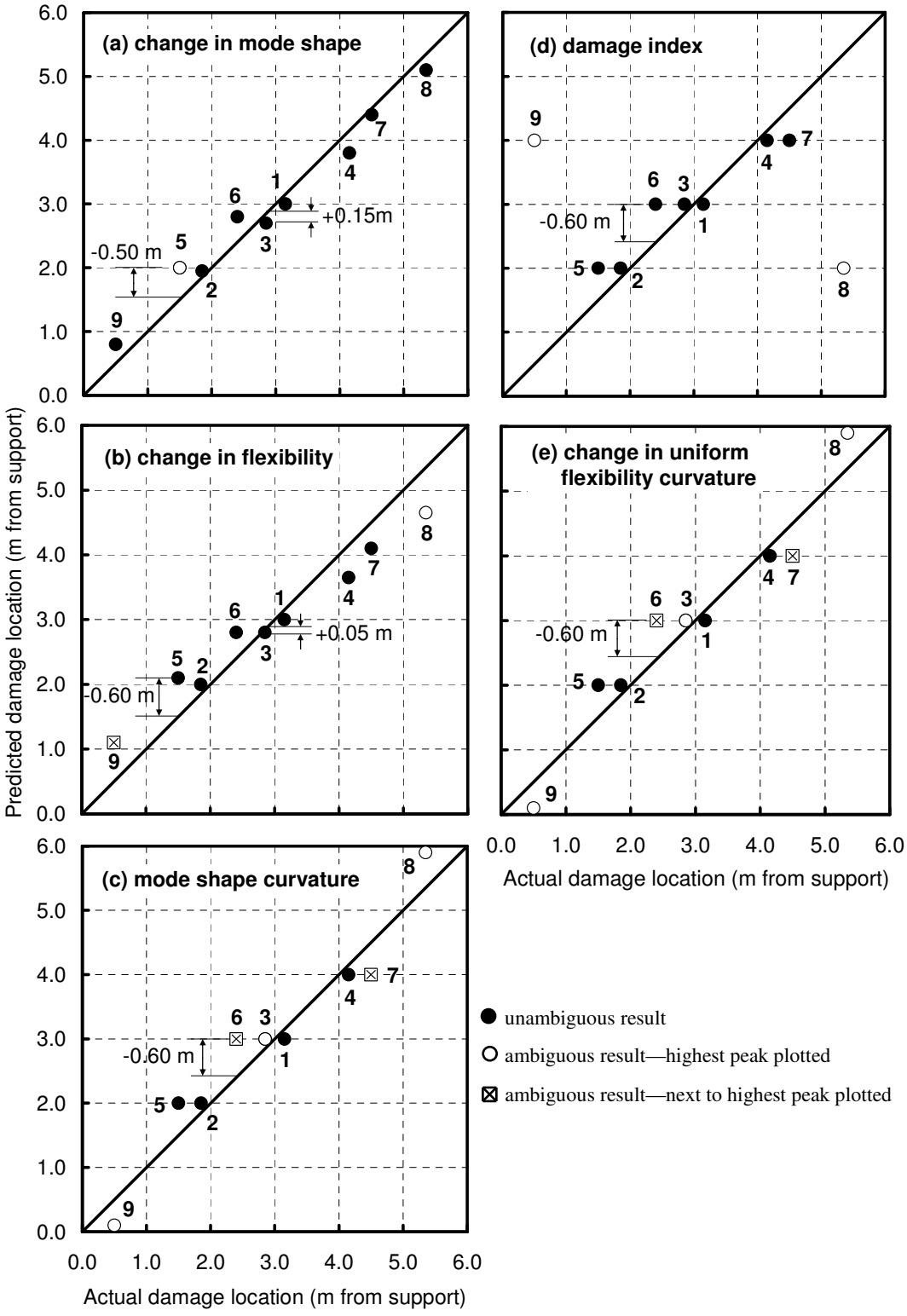

Figure 4.23. Correlation between predicted and actual longitudinal locations of damage calculated by a) change in mode shape, b) change in flexibility, c) mode shape curvature, d) damage index, and e) change in uniform flexibility curvature methods.

damage cases (8 and 9), which must be treated separately, and ignoring for the moment the fact that some results were ambiguous, the maximum observed error was 0.60 m (0.6*h*) for all methods except the change in mode shape method, for which the maximum error was 0.50 m (0.5*h*).

As already alluded to, the mode shape curvature and change in uniform flexibility curvature methods produced identical results, to the extent that identical ambiguities were also produced. Fig. 4.24 (a) shows that the distribution of the change in mode shape curvature caused by damage case 6 using the cubic spline to define the mode

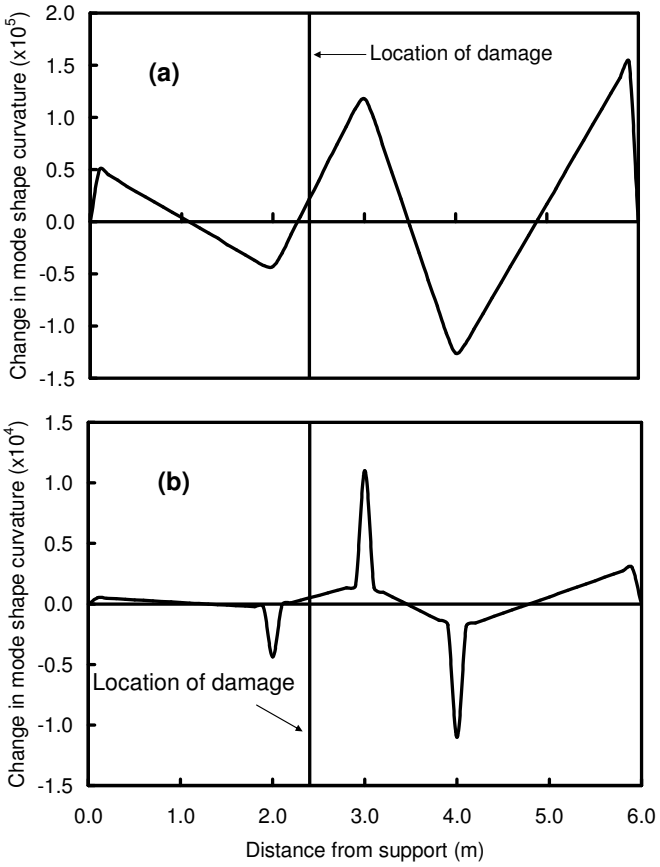

Figure 4.24. The distribution of the change in mode shape curvature caused by the damage case 6 (see Fig. 4.18): a) using a cubic spline, and (b) using a cubic polynomial interpolation function.

shape between measurement points. The second highest peak in the figure is near the location of damage, while the highest peak is near a support. These ambiguities were removed when a cubic polynomial interpolation procedure similar to the cubic spline was used to define mode shapes between measurement points, but without enforcing continuity of the second derivative (i.e. curvature) at measurement points as shown in Fig. 4.24 (b). The modified procedure resulted in spikes in mode shape curvature at measurement points which were significantly larger at predicted damage locations. While these spikes were artefacts of the interpolation technique, the resulting elimination of ambiguities suggests that each method has its own advantages and disadvantages; therefore, the combination of using different interpolation procedures could improve the clarity with which damage may be located.

Fig. 4.25 shows the correlation between predicted and actual longitudinal locations

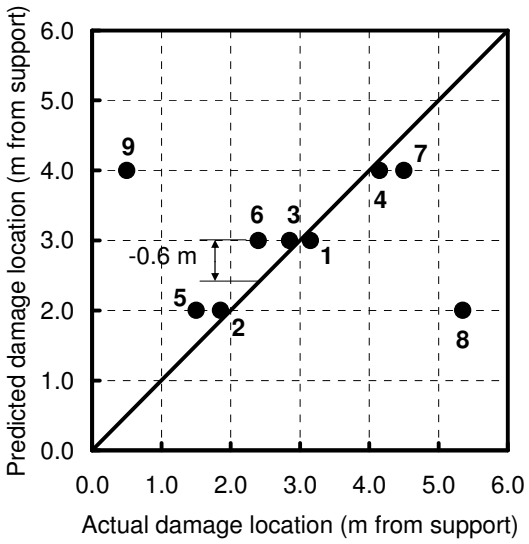

Fig. 4.25. Correlation between predicted and actual longitudinal locations of damage calculated by mode shape curvature method using a cubic polynomial interpolation function instead of a cubic spline.

of damage calculated by mode shape curvature method using a cubic polynomial interpolation instead of a cubic spline. It is apparent that the ambiguity of the localization of damage case 3, 6 and 7 was removed, but huge errors were produced in the localization of damage case 8 and 9.

The damage index method predicted damage locations that were identical to the mode shape curvature and change in uniform flexibility curvature methods, but without ambiguity, except near supports. Near supports, the reference strain energy is relatively small, resulting in the instability of the damage index parameter (Kim and Stubbs 2003). All three of these methods predicted damage to be located exactly at measurement points, as evidenced by the position of data points along horizontal gridlines. This is also an artefact of the interpolation technique used, suggesting again that refinements to interpolation procedures may be capable of eliminating this peculiarity and improving the performance of these techniques.

It was not possible to quantify the resolution of the damage locating procedures with the same level of confidence as was done using numerical results (see Section 4.3.2), since a relatively small number of cases were examined experimentally. Nonetheless, it should be observed that when damage was not located too near a support, with only two exceptions the actual damage was located closer to the nearest support than the predicted location (i.e. further from mid-span than the predicted location). It may be that this phenomenon was specific to the particular experimental system and setup used. If considered, however, the resolution window was 0.60 to 0.65 m for all methods, skewed almost entirely toward the nearest support.

Cases in which damage was predicted to be located at mid-span must be treated differently, since the predicted location was equidistant from support; therefore, the

damage could be located on either side of the predicted location. For the three curvature-based methods, this led to a mid-span resolution of approximately 1.2 m. The apparent decline in resolution near mid-span may be remedied by avoiding the use of any single method in isolation, but rather considering several methods simultaneously. For example, while any of the curvature-based parameters may only identify a 1.2 m window, centred at mid-span, within which damage could be located for case 6, either the change in mode shape or change in flexibility method could be used to indicate on which side of mid-span the damage is actually located, thereby narrowing the window to 0.60 m. If all methods predict damage to be located at mid-span (e.g. case 1), this may be taken as an indication that damage is actually located much closer to mid-span, in this case within a window of approximately 0.30 m centred on mid-span. The simultaneous use of several methods has the added benefit of removing ambiguities that might be present when a single method is applied in isolation.

4.4.2.3. Comparison between experimental and numerical studies

Comparison of Fig. 4.23 with Figs. 4.7 and 4.9 in Section 4.3.2.2 shows that the experimental results were in general agreement with those of the numerical study when five simulated measurement points were used. The experimental resolution for damage localization (0.65h) was within the range found numerically (0.4h to 0.8h, as shown in Fig. 4.14b), though it was not as good as the best resolution achieved numerically (0.4h). Thus, the presence of experimental uncertainty did not appear to have had a significant effect on the performance of the VBDD techniques under these well controlled conditions.

The direct use of curvature obtained using strain gauge measurements achieved half the maximum absolute error (0.3 m) compared with the methods that used accelerometer

measurements (0.6 m). However, the resolution of the former method (0.68*h*) was approximately equal to that of the latter, owing to the fact that the resolution window for the acceleration derived techniques was strongly skewed toward supports, while the strain derived window featured a moderate 60-40 skew away from supports. It should also be noted that higher amplitude vibrations were required to obtain strain signals with sufficiently high signal-to-noise ratios to achieve the observed level of resolution using strain gauge measurements. This may prove not to be feasible in field applications.

When damage was located between a support and the first measurement point (cases 8 and 9), Fig. 4.23 indicates that the distribution of most damage locating parameters was subject to greater ambiguity. Generally, the parameter distributions indicated that damage was likely located near the support, but its location could not be determined with certainty. The damage index method performed particularly poorly in this region, while the change in mode shape curvature method performed relatively well. As an example, Fig. 4.26 shows the detection of damage case 8 using these two methods. It is apparent that the highest peak of change in mode shape curvature was located close to the east support, near the actual damage location. However, the highest peak of damage index occurred 2 metres from the west support, far away from the actual damage location. The experimental results were generally consistent with the numerically observed near-support resolution of approximately 1.3*h* (Fig. 4.14 (d)), although the change in mode shape method appears to have performed much better than this for the two near-support cases investigated experimentally. Again, the use of several methods simultaneously seemed to improve the certainty with which damage could be located near the supports.

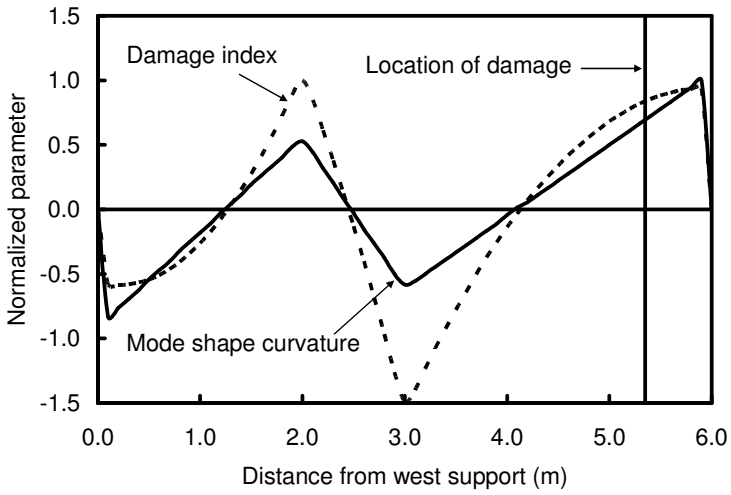

Figure 4.26. Distribution of normalized damage detection parameters, calculated along the north girder for damage case 8 by mode shape curvature and damage index methods.

4.4.2.4. Transverse Damage Localization

Fig. 4.27 shows the correlation between predicted and actual transverse locations of damage when experimental acceleration data were used. Comparison with Fig. 4.15 (c) in Section 4.3.2.6 shows that the experimental accuracy was significantly worse than that achieved numerically, with the location of damage successfully determined to lie within the bounds of the slab surface in only five of nine cases. For these five cases, a maximum error of 0.56 m was observed or 38% of girder spacing. The poor performance is thought to be due to inaccuracies in mode shape measurement, particularly along the girder farther from the damage location, for which changes in mode shape would have been smaller. It appears that greater measurement accuracy is required to determine the transverse location using the proposed method. The success of the technique numerically suggests that its performance is limited by the level of measurement uncertainty.

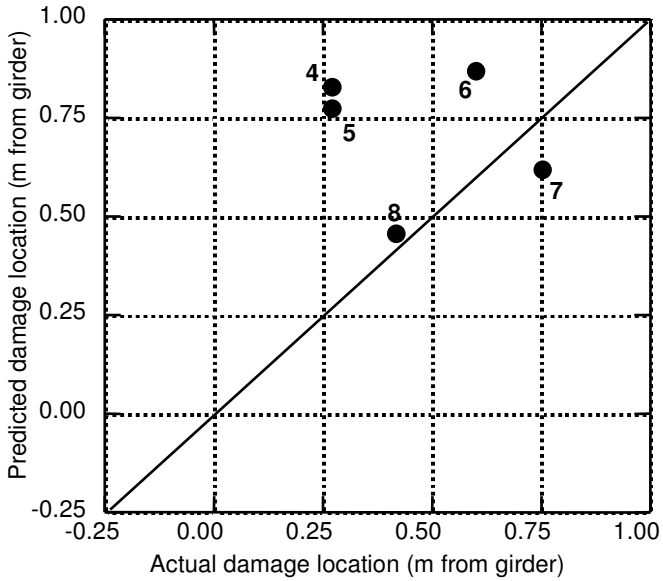

Figure 4.27. Correlation between predicted and actual transverse locations of damage, calculated using experimentally measured accelerations at five locations along each girder.

4.5 CONCLUSIONS

4.5.1 Conclusion from the Numerical Study

Using FE analysis, this study has shown that the presence of small-scale damage on the deck of a simply-supported, two-girder bridge can be detected and located with reasonable accuracy using vibration-based damage detection (VBDD) techniques which use measurements of only the fundamental mode shape before and after damage. When damage is detected, the size of the region within which it can be confidently predicted to lie—i.e. the resolution of damage localization—depends upon how accurately the mode shapes can be defined. When mode shapes are well-defined with a large number of

measurement points, the damage location can be pinpointed with great accuracy using any of the five VBDD techniques investigated.

In practice, only a relatively small number of measurement points are feasible, and damage localization resolution in this case was found to depend upon the number and spacing between measurement points. In the absence of experimental uncertainty, and provided the damage was not located too near a support, the resolution of damage localization was found to be 40 to 80% of the spacing between measurement points when five evenly spaced points were used along each girder. The best results were achieved by the change in mode shape and change in flexibility methods. In some cases, particularly when these two techniques predicted the same damage location, their simultaneous use could improve the resolution to approximately 30% of measurement point spacing by accounting for characteristic skews in the resolution windows. The use of additional modes did not improve the performance of the techniques; furthermore, an increase in the number of measurement points from 5 to 11 improved their performance only slightly.

When damage was located near a support, the resolution of damage localization was found to be approximately 30% greater than the distance from the support to the first measurement point. In addition, the proposed transverse damage localization procedure allowed damage to be located within 13% of girder spacing transversely when five measurement points were used along each girder.

Results of the numerical study appear to demonstrate excellent potential for VBDD techniques as structural health monitoring tools applied to bridge decks.

4.5.2 Conclusions from the Experimental Study

Using experiments conducted on a half-scale laboratory model, this study has shown that the presence of small-scale damage on the deck of a simply-supported, two-girder bridge could be reliably detected and located using vibration-based damage detection (VBDD) techniques that employ measurements of only the fundamental mode shape before and after damage. The location of damage could be determined with a resolution of approximately 65 to 70% of measurement point spacing when as few as five or six measurement points were distributed along each girder, unless the damage was located too near the support.

When vertical acceleration measurements were used to determine mode shapes, the reported level of resolution accounts for the fact that the resolution windows were strongly skewed toward supports—i.e. the actual location of damage was typically located closer to the supports than the predicted location. The simultaneous application of several VBDD techniques was required to remove ambiguities that any one technique produced and to narrow the resolution window when the predicted location was near mid-span. Due to the relative small number of damage cases considered in the experimental study, however, the skewed nature of the observed resolution windows may, in part, be a reflection of the damage locations relative to the sensors.

The use of strain gauges bonded to girder webs to measure mode shape curvatures was found to result in smaller errors in the predicted damage locations, but did not improve the damage localization resolution since the resolution window was not strongly skewed. Comparison of these results with those of the numerical study demonstrates that the presence of experimental uncertainty resulted in only a slight decline in damage localization resolution.

Although only a small number of near-support damage cases were studied, the resolution of damage localization near supports was found to be consistent with that achieved in the numerical study—approximately 30% greater than the distance from the support to the first interior measurement point. However, near-support damage detection and location appears to present significant challenges. Although not investigated thoroughly, closer spacing of measurement points near supports appears to be an important factor influencing the accuracy and reliability of locating damage in this region. Additional work is required to confirm this and to improve the performance of VBDD techniques near supports.

Of the five VBDD techniques investigated, the change in mode shape method, which uses simply the difference between damaged and undamaged unit-norm normalized fundamental mode shapes, appeared to perform the best. Not only did it produce the smallest errors in predicted locations, including near supports, it also tended to produce fewer ambiguous results. While the simultaneous use of several techniques is recommended, the change in mode shape method should be among the methods used.

It is believed that the levels of damage localization resolution and the characteristic skews of resolution windows observed in this study may be unique to the system investigated here. As such, eventual field application of these techniques will likely require calibration studies to determine appropriate levels of resolution and skew for a particular structure. These studies are likely to require the use of numerical models that incorporate reasonable levels of measurement uncertainty.

The proposed transverse damage localization procedure did not perform well experimentally, being able to determine the location of damage in only five of nine cases, and then with an accuracy of approximately 38% of girder spacing. Given that

the procedure was able to achieve an accuracy of 13% of girder spacing using numerically generated data, the proposed procedure appears to be much more sensitive to measurement uncertainty; therefore, additional work is required in this area.

Results of this study demonstrate that existing VBDD algorithms are adequate for detecting and locating low levels of damage on a bridge deck, at least for two-girder systems and simple support conditions. However, in order to take advantage of the potential of the algorithms, mode shapes must be known with a high level of accuracy since changes to mode shapes caused by low levels of damage are very small. Measurement methods that demonstrate a very high level of repeatability are required. In addition, it is believed that when a small number of measurement points are used, the accuracy of mode shape estimation—and therefore the performance of the VBDD algorithms—may be improved to a certain extent by refining the methods used for data manipulation prior to applying the VBDD algorithms, with particular attention paid to the interpolation methods used.

CHAPTER 5. DAMAGE DETECTION ON A PRESTRESSED CONCRETE GIRDER

5.1 INTRODUCTION

The study described in Chapter 4 demonstrated that small scale damage on a half-scale steel-free bridge deck could be reliably detected and located using VBDD techniques and only a small number of sensors, provided the damage was not located too near a simple support. However, the properties of a small scale model of a simplified structure may not necessarily reflect what may be encountered in full-size structures (for example, stiffness, natural frequencies, damping ratio, etc.). In addition, the methods that performed well on the deck model may not necessarily perform as well for girders. Therefore, full-scale girder tests were performed to determine whether the methods performed as well for a realistic structural component.

This chapter describes a study undertaken to ascertain the theoretical and practical potential of five VBDD techniques, described in Chapter 2, for detecting and locating low levels of damage on a full-scale prestressed concrete box girder using a small number of sensors. First, the bridge girder used as a basis for the study is described; then, the numerical and laboratory-based experimental studies are presented. Together with the study described in the previous chapter, these studies form the initial stages of a larger systematic research program designed to address issues of increasing complexity in a progressive and incremental manner. As such, many of the complexities associated

with applying VBDD techniques to constructed facilities in the field are not addressed by these initial studies. The purpose of this investigation was limited to determining theoretical and practical limitations of the techniques when applied to a full-scale bridge girder under well-controlled conditions.

Compared to the test on the half-scale bridge deck described in Chapter 4, the tests on the full-scale prestressed concrete box girder described in this chapter have three major differences. First, the strain gauges were installed on the side surface of the concrete girder (Fig. 3.2 (b)) instead of on steel. It is possible that the inhomogeneity and deteriorated state of the concrete may have affected the consistency of strain gauge data, even though 90-mm long strain gauges were used. Secondly, the span of the girder was 11.9 metres, much larger than that of the deck. Therefore, the curvature of the girder was expected to be much smaller than that of the deck when the amplitude of the displacement at mid-span was the same. Smaller curvatures make the signal-to-noise ratio smaller; as a result, damage detection would likely become more challenging. Thirdly, the torsional stiffness (St. Venant torsion constant) of the box girder was much larger than that of the deck; this was expected to increase the difficulty of determining the transverse location of damage.

5.2 NUMERICAL STUDY

5.2.1 Description of numerical study

The primary purpose of the numerical study was to evaluate the capabilities of the damage detection methods in the absence of excitation and measurement uncertainties. The specimen used for the investigation was a full-scale prestressed concrete box girder

removed from abandoned bridge. The girder was 12.2 metres long, spanned 11.9 metres, and had a 1216 x 508 mm cross section, as shown in Fig. 5.1. It was simply supported at its four corners.

The commercial finite element (FE) analysis package ANSYS (2003) was used to perform an eigenvalue analysis to generate the natural frequencies and mode shapes of the system. Although the undamaged system was symmetrical both longitudinally and transversely, the investigation of unsymmetrical damage states precluded the use of symmetry boundary conditions to reduce the size of the model. Fig. 5.2 shows the transverse cross section of the finite element model of the girder. The prestressed concrete box girder was divided into 8-node 3-dimensional isoparametric solid elements. A total of 84 elements were used longitudinally, with the top and bottom flanges divided into twenty-four elements transversely, and two (for the bottom plate) or three (for the top plate) elements through the thickness. The vertical webs were divided into five elements vertically and two elements through the width. The prestressing tendons were modelled using linear truss elements fully bonded at nodes.

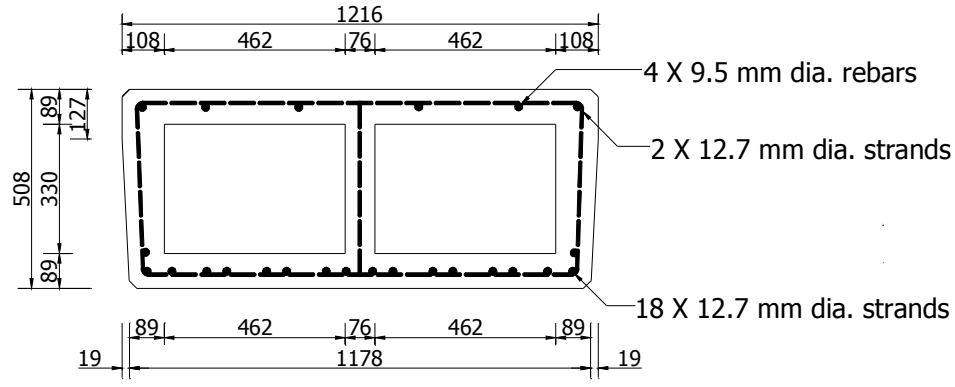

Figure 5.1. Transverse cross-section of the prestressed concrete girder used for the study. (dimensions in mm)

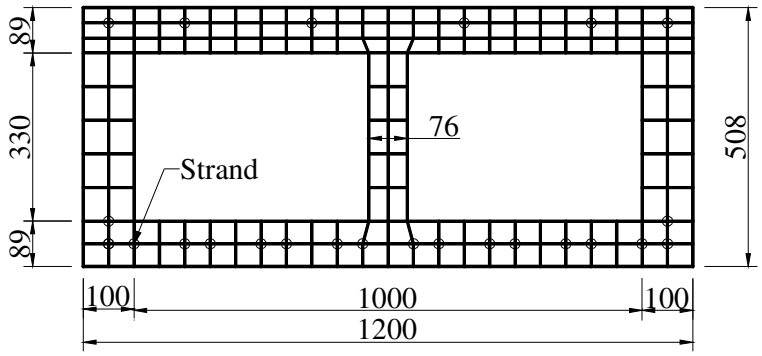

Figure. 5.2. Transverse cross section of the finite element model of the girder (dimensions in mm).

Boundary conditions were imposed at the four support nodes (150 mm from the ends, 50 mm from the sides), restraining them against movement in the vertical direction. In addition, one of these nodes was restrained in both the longitudinal and transverse directions, a second in the longitudinal direction, and a third in the transverse direction, preventing rigid body movement of the system. Elastic and section properties of the physical components were applied as model parameters. The material properties assumed for the finite element girder model are shown in Table 5.1. The Young's modulus was calculated based on the compressive strength of 34.5 MPa for the concrete, a value which was indicated on the design drawings for the girder.

The mode shapes of the first four modes of the girder generated by the FE model are shown in Fig. 5.3.

Table 5.1. Material properties of the prestressed concrete girder used in the FE model.

Material properties	*Young's modulus (GPa)*	*Density (kg/m^3)*	*Poisson's ratio*
Concrete	26.1	2400	0.3
Steel	200	7850	0.3

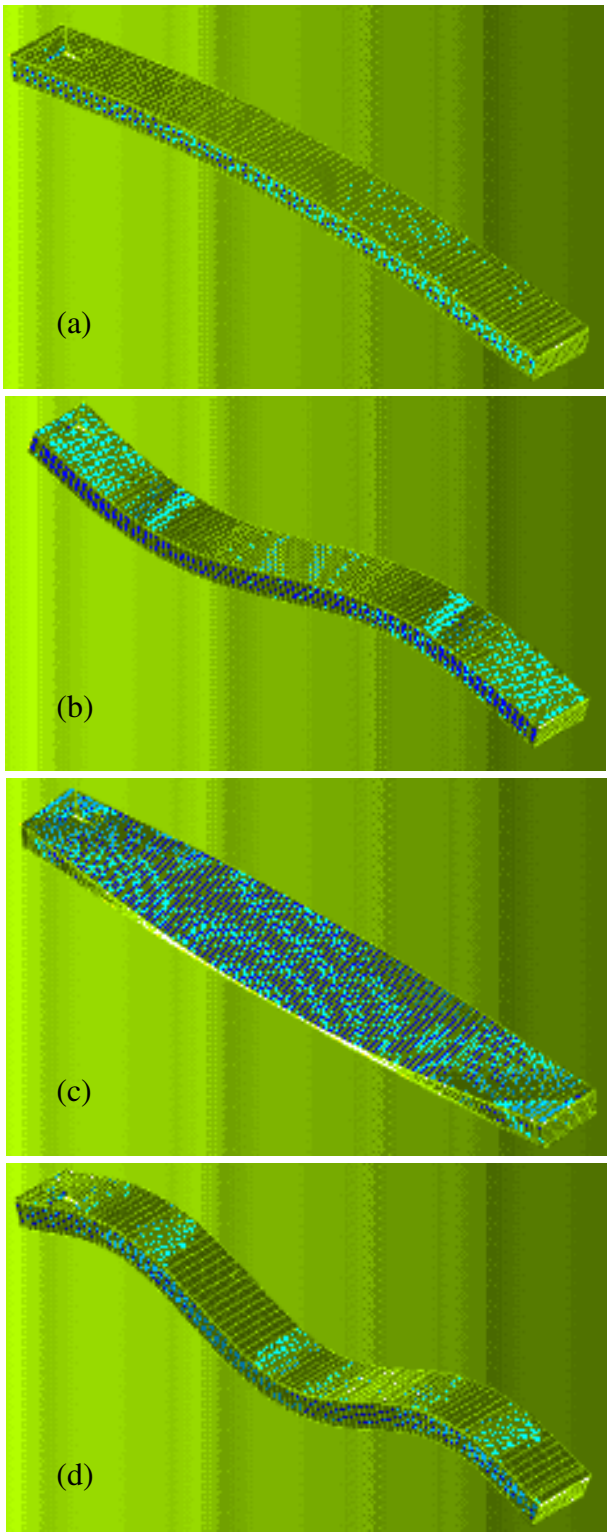

Figure 5.3. The first four mode shapes of the girder generated by FE model: (a) 1st mode [7.58 Hz], (b) 2nd mode [27.23 Hz], (c) 3rd mode [36.46 Hz], and (d) 4th mode [58.95 Hz].

The model was calibrated to the first four natural frequencies and mode shapes measured for the undamaged physical system by adjusting the Young's modulus of the concrete. Table 5.2 demonstrates that good agreement (<3.5% error) between predicted and measured natural frequencies was achieved except for the 3rd mode, which was primarily a torsional mode. Also, modal assurance criteria (MAC) values were excellent (>0.9967) for the lowest two modes, as well as quite good for the 3rd and 4th modes (>0.9865).

Once the model had been calibrated, damage to the girder was simulated by eliminating three transversely adjacent elements, each 149 mm long, 50 mm wide and 30 mm thick, from the top surface of the girder. This corresponded to a local reduction in flexural rigidity of approximately 2.49%. A total of 51 damage cases were simulated, as shown in Fig. 5.4, each one situated at a different location. For the first series of damage states (40 damage cases), the transverse location of damage was set such that the centre of damage was 0.225 m from one edge of the girder, while the longitudinal location of the centre of the three removed elements was varied between 0.074 and 5.875 m from the support at 0.149 m intervals. For the second series of damage cases,

Table 5.2. Comparison of FE and experimental natural frequencies and mode shapes for the undamaged system.

Parameter	1st Mode	2nd Mode	3rd Mode	4th Mode
Natural Frequencies (Hz)				
Experimental model	7.61	26.3	31.7	57.9
Finite element model	7.58	27.23	36.46	58.95
Relative error	-0.4%	3.5%	15.0%	1.8%
Modal Assurance Criteria:	0.9999	0.9967	0.9882	0.9865

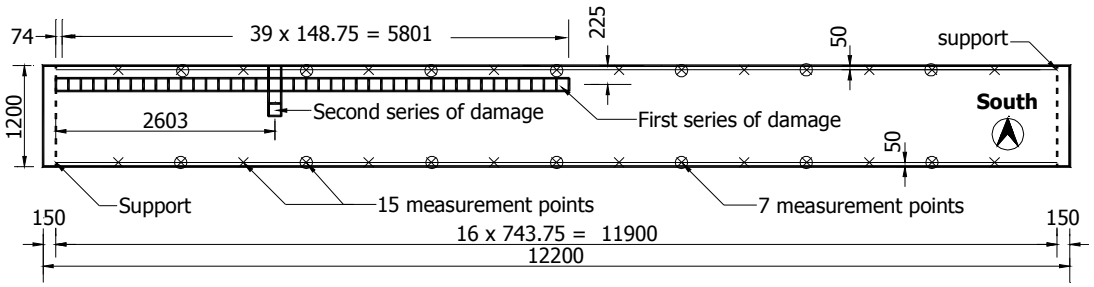

Figure 5.4. The locations of 51 damage cases and measurement points
(Dimensions in mm)

the longitudinal location of damage remained constant at 2.60 m from the support while the transverse location was varied from 0.075 to 0.575 m from one edge of the girder at 0.05 m intervals.

The FE analysis was intended to simulate the acquisition of measured data from sensors attached to a physical system at a small number of locations. Therefore, vertical displacement data were extracted from the FE-generated mode shapes of the system at a small number of uniformly spaced "measurement" points along each side of the girder. Three cases were investigated: one in which seven measurement points were used, one in which 15 measurement points were used, and a well-defined reference case in which 79 measurement points were used. In addition to these measurement points, mode shape deflections at the supports were assumed to be zero.

Of primary interest was the performance of the damage detection techniques when only the fundamental mode shape was used, since accurate measurement of higher mode shapes is more difficult in practice. However, the use of the first three flexural mode shapes was also investigated to determine whether significant improvements could be realized. As described above, mode shapes were defined by "measurements" at seven, 15, or 79 points, in addition to zero displacements at supports. However, in order to

obtain a better estimate of mode shapes when seven or fifteen measurement points were used, intermediate displacements between measurement locations were generated using the cubic spline interpolation technique described in the previous chapter, by which cubic polynomials were used to define the mode shapes between data points. In this way, displacements at a total of 81 points were used to define the flexural mode shapes along girders, regardless of the number of measurement points. These mode shape vectors were unit-norm normalized, prior to applying the damage detection techniques.

5.2.2 Results and discussion

In this section, the performance of the five VBDD methods in terms of the accuracy with which they were able to predict the actual location of damage on the prestressed concrete girder is evaluated using finite element model simulated data. The similarities and differences between the performance of these methods when applied to the steel-free bridge deck and the prestressed concrete girder are also discussed in this section.

5.2.2.1 Performance of VBDD methods using well-defined mode shapes

Fig. 5.5 shows the performance of the five VBDD methods for locating the damage when it was located 2.60 metres from the support using only the fundamental mode shape of the girder and 79 measurement points along the girder. For the points discussed below, this damage case is typical of all damage cases, except those damage cases near a support when detected by the change in flexibility method, a case that will be described later.

The change in unit-norm normalized mode shape resulting from this damage state is shown in Fig. 5.5(a). Only one upward peak is apparent in the figure; in addition, this peak clearly and accurately indicated the location of damage. The maximum change of

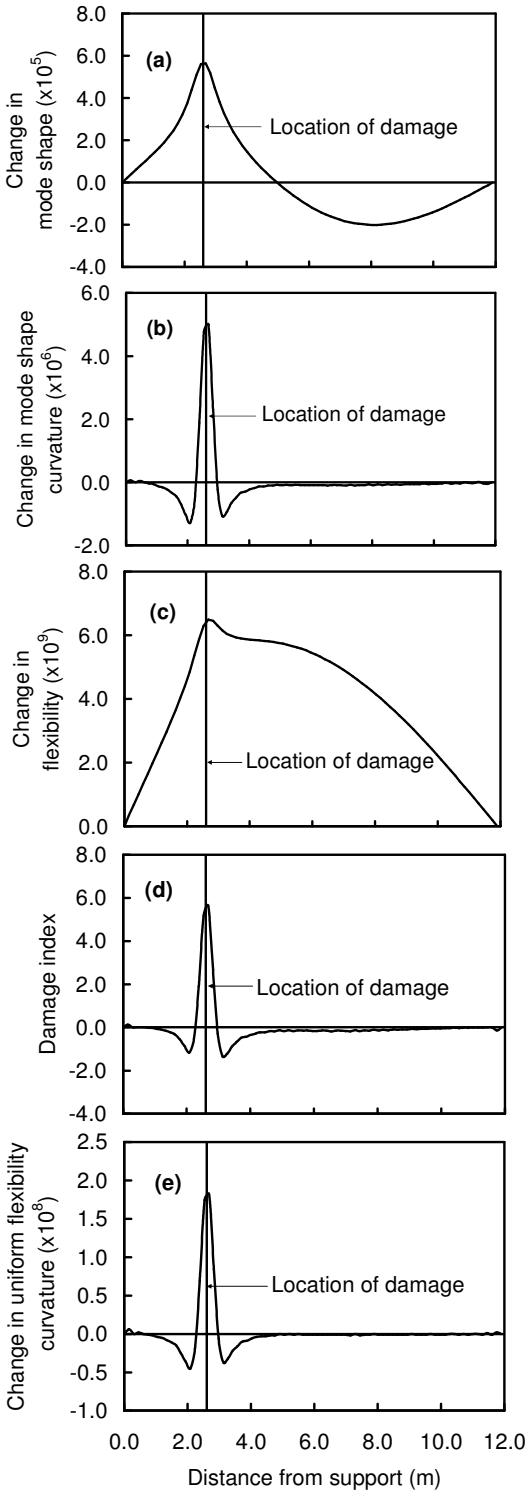

Figure 5.5. Performance of the five VBDD methods for locating the damage located at 2.60 m from support: (a) change in mode shape method, (b) mode shape curvature method, (c) change in flexibility method, (d) damage index method, and (e) change in uniform flexibility curvature method.

the mode shape was 0.000056, which corresponded to 0.035% of the maximum value of the undamaged unit-norm normalized mode shape at mid-span (0.158).

The change in mode shape curvature is shown in Fig. 5.5(b). Again, only one upward peak occurred, clearly and accurately indicating the location of damage. In contrast to the change in mode shape, the peak in the change in mode shape curvature was much sharper near the location of damage, but tended to decay to zero very quickly at locations far away from the damage. Therefore, the change in mode shape curvature appeared to present more precise localized information, while the change in mode shape provided more widely distributed global information.

The change in flexibility resulting from the damage is shown in Fig. 5.5(c), with all the change of flexibility values being positive. While the upward peak accurately indicated the location of damage, the peak was not sharply defined.

The damage index distribution is shown in Fig. 5.5(d). This figure is very similar to Fig. 5.5(b) (change in mode shape curvature), with the primary difference being that the value of the damage index at the damage location was equal to 5.63, which was much larger than that of the change in mode shape curvature (0.000005). It must be remembered, though, that the damage index is a normalized parameter (see Section 2.2.3). This figure also verifies Stubbs et al.'s finding (1995) that a value of the damage index greater than 2.0 is indicative of a possible damage location. As stated previously, the damage index method is the only one of the five VBDD methods investigated to provide a threshold value to indicate the presence of damage.

The change in uniform flexibility curvature is shown in Fig. 5.5(e). The sharp upward peak clearly and accurately indicated the location of damage. Comparing Fig. 5.5(e) and 5.5(b), it is obvious that the shapes of these two figures are almost the same.

Comparing Fig. 5.5 with Fig. 4.5, it is evident that the distributions of the VBDD parameters are very similar for both the scaled model deck and prestressed girder. For the damage index method, even the maximum values of the damage index were very close for the two systems (5.63 for the girder, and 5.37 for the deck). However, for the other four VBDD methods, the maximum value of each parameter for the girder was one-third to one-half that obtained for the deck. These differences could be caused by the differences in the number of measurement points and the types of the structures, since more measurement points result in smaller value of unit-norm normalized mode shape and different types of structures will exhibit different dynamic behaviours. In addition, the location and magnitude of damage differed for the two systems. The curvature change of the girder being lower than that of the deck is also due to the longer span of the girder.

5.2.2.2 Influence of using a small number of measurement points

All five VBDD methods were able to accurately predict the longitudinal location of damage on the prestressed concrete girder when 79 measurement points were used. However, a small number of measurement points is more practical for the application of VBDD methods; therefore, the influence of the number of measurement points on the accuracy of the predicted longitudinal location of damage by these five VBDD methods is discussed next.

Fig. 5.6 shows the distributions of the five damage detection parameters calculated using the fundamental mode shapes defined by 7, 15, and 79 FE simulated measurement points when damage was located 2.60 m from the support. Again, detection of this damage case is typical for all damage cases except those damage cases near a support and detected by the change in flexibility method, a case that will be presented later.

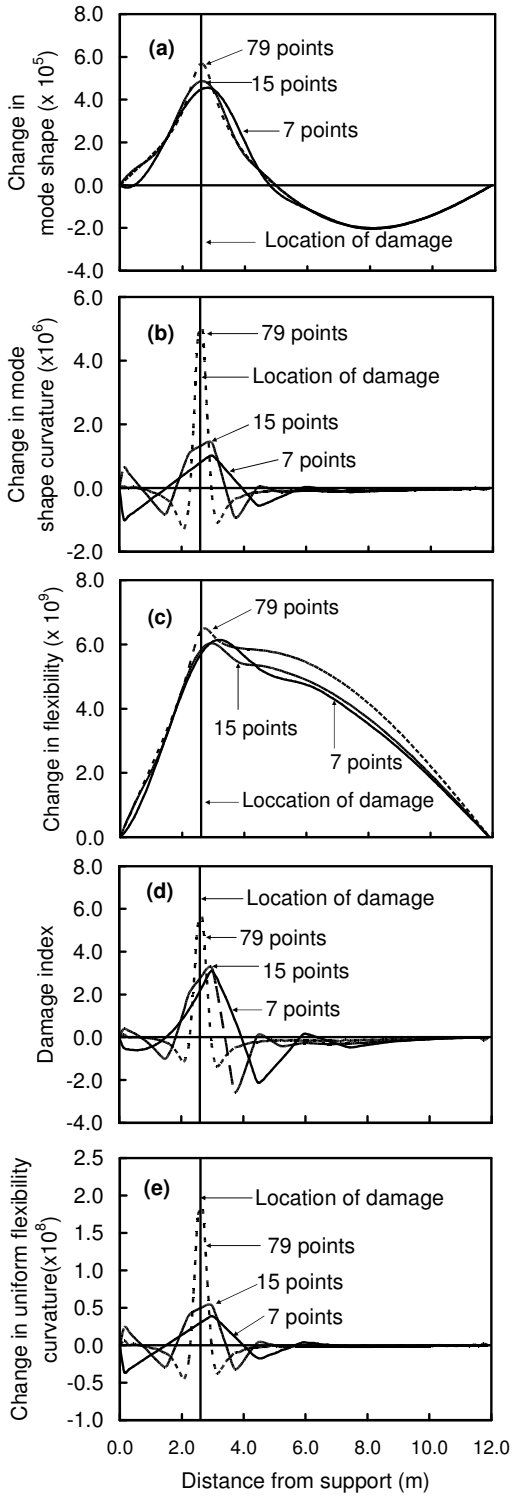

Figure 5.6. Performance of the five VBDD methods for locating the damage located at 2.60 m from support using 79, 15 and 7 measurement points: (a) change in mode shape method, (b) mode shape curvature method, (c) change in flexibility method, (d) damage index method, and (e) change in uniform flexibility curvature method.

The change in mode shape is shown in Fig. 5.6(a). The predicted locations of the damage were 2.68, 2.68 and 2.83 metres when 79, 15, and 7 FE simulated measurement points were used, respectively. The corresponding errors were 0.08, 0.08 and 0.23 metres, respectively.

The change in flexibility is shown in Fig. 5.6(c). In this case, the predicted locations of the damage were 2.68, 2.98 and 3.20 metres when 79, 15, and 7 FE simulated measurement points were used, respectively, with corresponding errors of 0.08, 0.38, and 0.60 metres, respectively.

The change in mode shape curvature, damage index, and change in uniform flexibility curvature parameters are shown in Figs. 5.6(b), (d) and (e), respectively; these three methods produced identical results. The predicted locations of the damage were 2.68, 2.98 and 2.98 metres when 79, 15, and 7 FE simulated measurement points were used, respectively. The errors were therefore 0.08, 0.38, and 0.38 metres, respectively. The predicted locations of damage corresponded exactly to the location of measurement points nearest to the damage (2.98 meters from support) when 7 and 15 measurement points were used.

It is evident that the accuracy of the predicted damage location improved as the number of measurement points increased for all five VBDD methods; also, the change in mode shape method performed better than the other methods when a small number of measurement points were used. In addition, the upward peaks of all the curves became sharper (i.e., the clarity of the peak improved) as the number of measurement points increased.

The correlations between predicted and actual damage locations for all 40 longitudinally varying damage cases, as calculated using the change in flexibility and

change in mode shape methods, are plotted in Fig. 5.7. For reference, the gridlines in these plots indicate the locations of measurement points. Data points marked by open circles indicate that parameter distribution peaks were identified at these locations, but they were not very well-defined and peaks of comparable magnitude also existed elsewhere. For example, for the damage case shown in Fig. 5.8 (located 0.52 m from the support), the change in flexibility along the girder had two peaks with identical magnitude regardless of the number of measurement points. On the other hand, a sharper upward peak on the left is more likely to indicate the true damage location when two upward peaks of comparable magnitudes exist, suggesting that some of the ambiguity can be overcome by invoking experience and judgement.

Figs. 5.7(a) and 5.7(d), corresponding to 79 measurement points, show that very well-defined mode shapes allowed damage to be located with great accuracy using either method.

As the number of measurement points decreased, the accuracy in detecting the location of damage also decreased. As long as damage was not located within the "near-support" regions (shown shaded on the graphs), the maximum error observed using the change in flexibility method with 15 measurement points (Fig. 5.7(b)) was 0.45 m, or 60% of the distance between measurement points. When seven measurement points were used (Fig. 5.7(c)), the maximum error was 0.74 m, or 50% of the distance between measurement points. The change in mode shape method produced maximum errors of 0.22 m and 0.37 m, respectively (Figs. 5.7(e) and (f)).

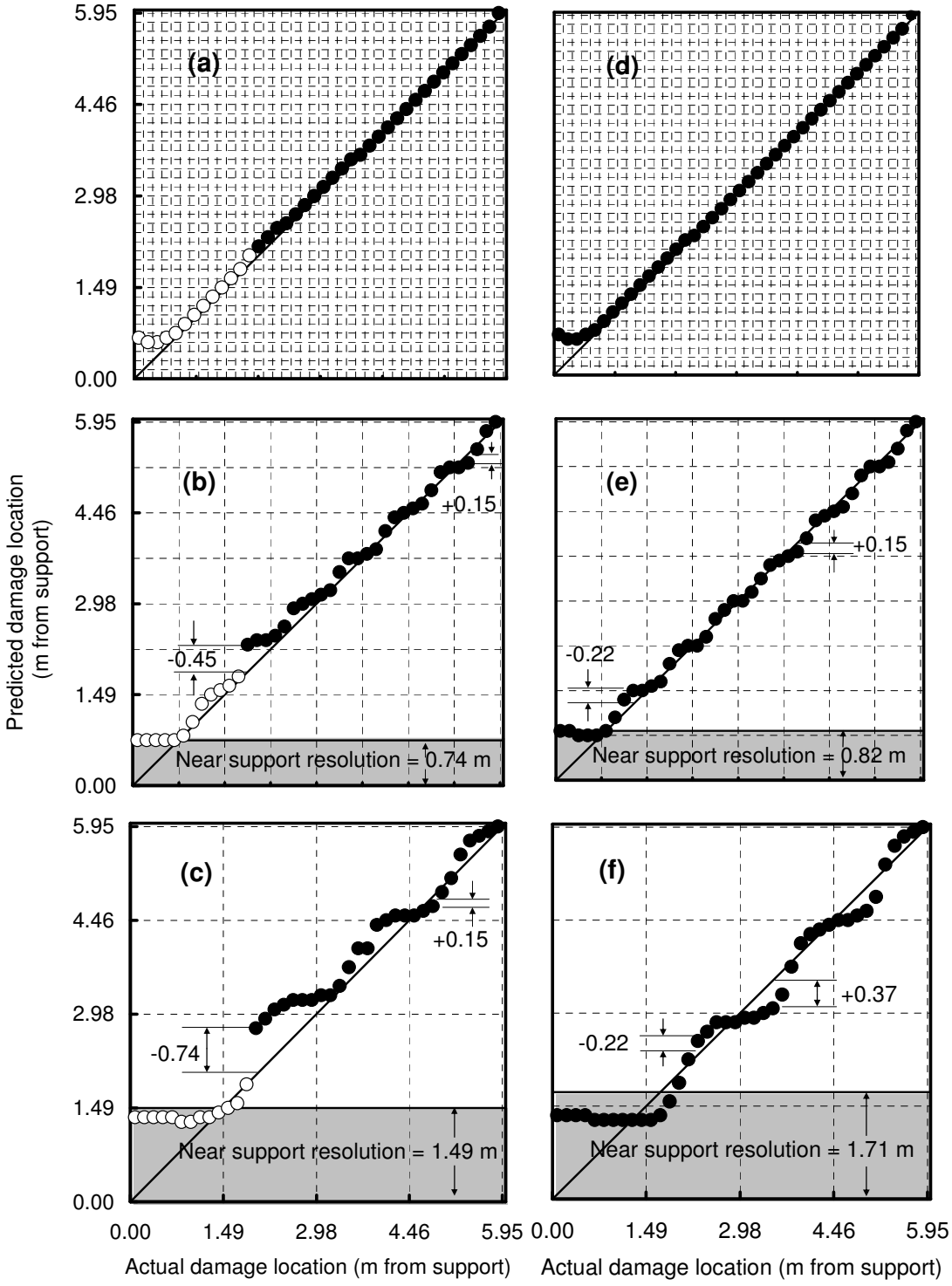

Figure 5.7. Correlation between predicted and actual longitudinal location of damage calculated by the change in flexibility method using a) 79, b) 15, and c) 7 FE simulated measurement points; and by the change in mode shape method using d) 79, e) 15, and f) 7 FE simulated measurement points using only the fundamental mode.

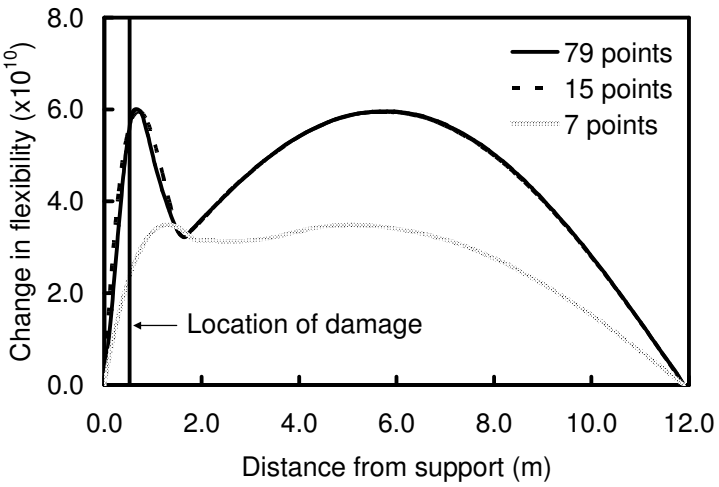

Figure 5.8. Variation of change in flexibility along girder for damage located 0.52 m from support, calculated using 7, 15, and 79 FE simulated measurement points using only the fundamental mode shape.

The correlation between predicted versus actual location of damage using mode shape curvature and change in uniform flexibility methods are plotted in Figs. 5.9(a), (b), and (c), corresponding to the use of 79, 15, and 7 measurement points, respectively. The results obtained from these two methods were plotted on the same figures since both methods produced identical results for all the 40 longitudinally varying damage cases. Figs. 5.9 (d), (e), and (f) provide similar results based on the damage index method when 79, 15 and 7 measurement points were used, respectively.

Figs. 5.9 (a) and (d) represent the damage detection results using 79 simulated measurement points; similar to Fig. 5.7 (a) and (d), excellent results were observed for all damage detection methods investigated, indicating that any of the techniques are capable of detecting and locating small-scale damage with a high degree of precision if

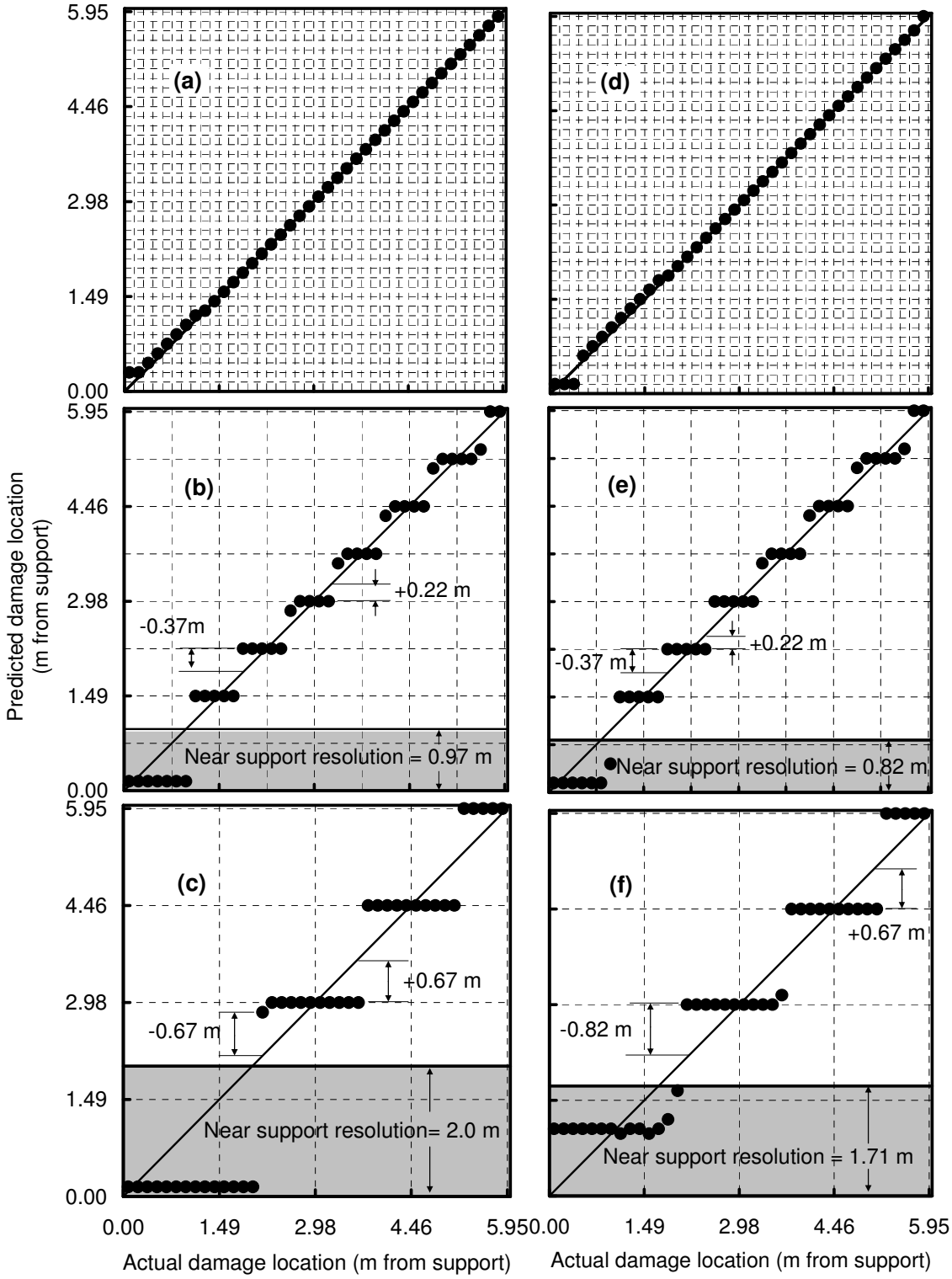

Figure 5.9. Correlation between predicted and actual longitudinal location of damage calculated using the fundamental mode only by the mode shape curvature and change in uniform flexibility curvature methods using a) 79, b) 15, and c) 7 FE simulated measurement points; and by the damage index method using d) 79, e) 15, and f) 7 FE simulated measurement points.

fundamental mode shapes can be defined very precisely. This conclusion is the same as that from the steel-free bridge deck study reported in Chapter 4.

As shown in Figs. 5.9 (b) and (e), when 15 measurement points were used, the mode shape curvature, change in uniform flexibility, and damage index methods located the damage with a maximum error of 0.37 m, or 50% of the distance between measurement points, for the damage cases not located with the "near support" regions. When 7 measurement points were used, as shown in Fig. 5.9(c), the mode shape curvature and change in uniform flexibility methods produced a maximum error of 0.67 m, or 45% of the distance between measurement points, while in Fig. 5.9(f), the damage index method produced maximum error of 0.82 m, or 55% of the distance between measurement points. It is obvious that as the number of measurement points decreased, the accuracy in detecting the location of damage also decreased for these three methods.

As suggested in Figs. 5.9(b), (c), (e), and (f), the mode shape curvature, change in uniform flexibility curvature, and damage index methods showed a pronounced tendency to predict damage to be located exactly at the nearest measurement point. Given this tendency, the best that can be expected from these methods is a maximum error of not less than half the spacing between measurement points. In addition, the maximum error typically occurs when damage is located farthest from measurement points (i.e. one-half the distance between measurement points). Conversely, when damage was located near a measurement point, the accuracy in locating it was very high, regardless of the number of measurement points. This observation is the same as that obtained from the steel-free bride deck in Figs. 4.9 (b), (c), (e), and (f). The reason for this tendency has been explained in Section 4.3.2.2.

5.2.2.3 Influence of proximity of damage to a support

It is seen in Figs. 5.7 and 5.9 that the accuracy with which damage could be located by the VBDD techniques investigated declined when damage was located near the support.

This phenomenon can be demonstrated using the example in Fig. 5.8, which shows a plot of the change in flexibility parameter when damage was located 0.52 metres from the support calculated using 79, 15 and 7 measurement points. In this case, the clarity of the peaks was diminished as compared to damage cases located farther from the support; curves for damage in this region typically indicated that damage was present and that it was likely located near the support, but its location could not be determined with certainty due to the indistinct nature of the peaks and the presence of large values elsewhere. This was true even when mode shapes were precisely defined at 79 points, although in this case the identified peaks were somewhat more distinct than those when fewer points were used; also, these peaks were present close to the actual damage location, as reflected in Fig. 5.7(a). When 15 measurement points were used (Fig. 5.7(b)), an identifiable peak was located near the actual damage location only when damage was located near the first measurement point (at 0.74 m).

5.2.2.4 Influence of numbers of modes considered

All of the above investigations of the VBDD methods are based on the sole use of the fundamental mode shape. Damage detection using the first three flexural modes is investigated next.

Fig. 5.10 shows a plot of the change in flexibility method calculated using the first three flexural modes when damage was located 0.52 metres from the support and 79, 15,

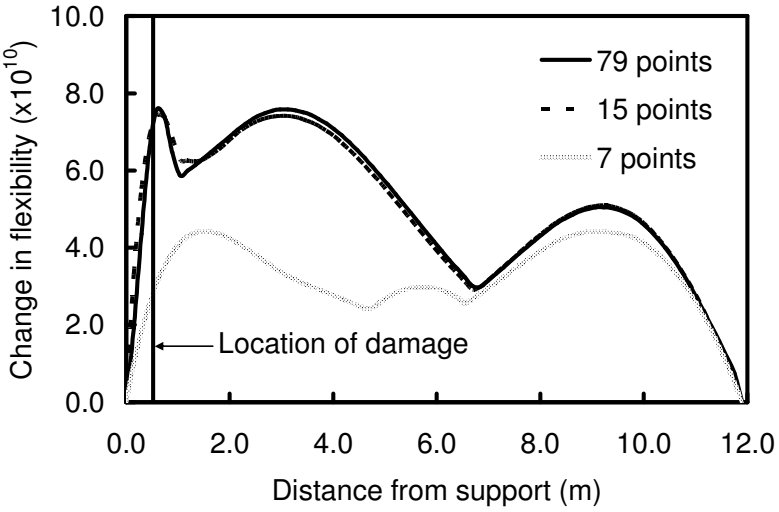

Figure 5.10. Variation of change in flexibility along girder for damage located 0.52 m from support, calculated using 7, 15, and 79 FE simulated measurement points using the first three flexural modes.

and 7 measurement points were used to define mode shapes. Comparing Fig. 5.10 with Fig. 5.8, it is seen that the use of two additional flexural modes did not improve the accuracy for this case.

The correlation between predicted and actual damage locations for all 40 longitudinally varying damage cases, as calculated by the change in uniform flexibility curvature method using 79, 15 and 7 measurement points is plotted in Figs. 5.11 (a), (b), and (c), respectively. Comparing Figs. 5.11(a), (b), and (c) with Figs. 5.9 (a), (b), and (c), it was found that use of the first three flexural modes produced identical results with those obtained using the fundamental mode only regardless of the number of measurement points. Same conclusion was reached for the steel-free bridge deck in Section 4.3.2.4.

For the change in flexibility method, Figs. 5.11(d), (e) and (f) illustrate that the use of two additional flexural modes produced more distinct peaks near the support.

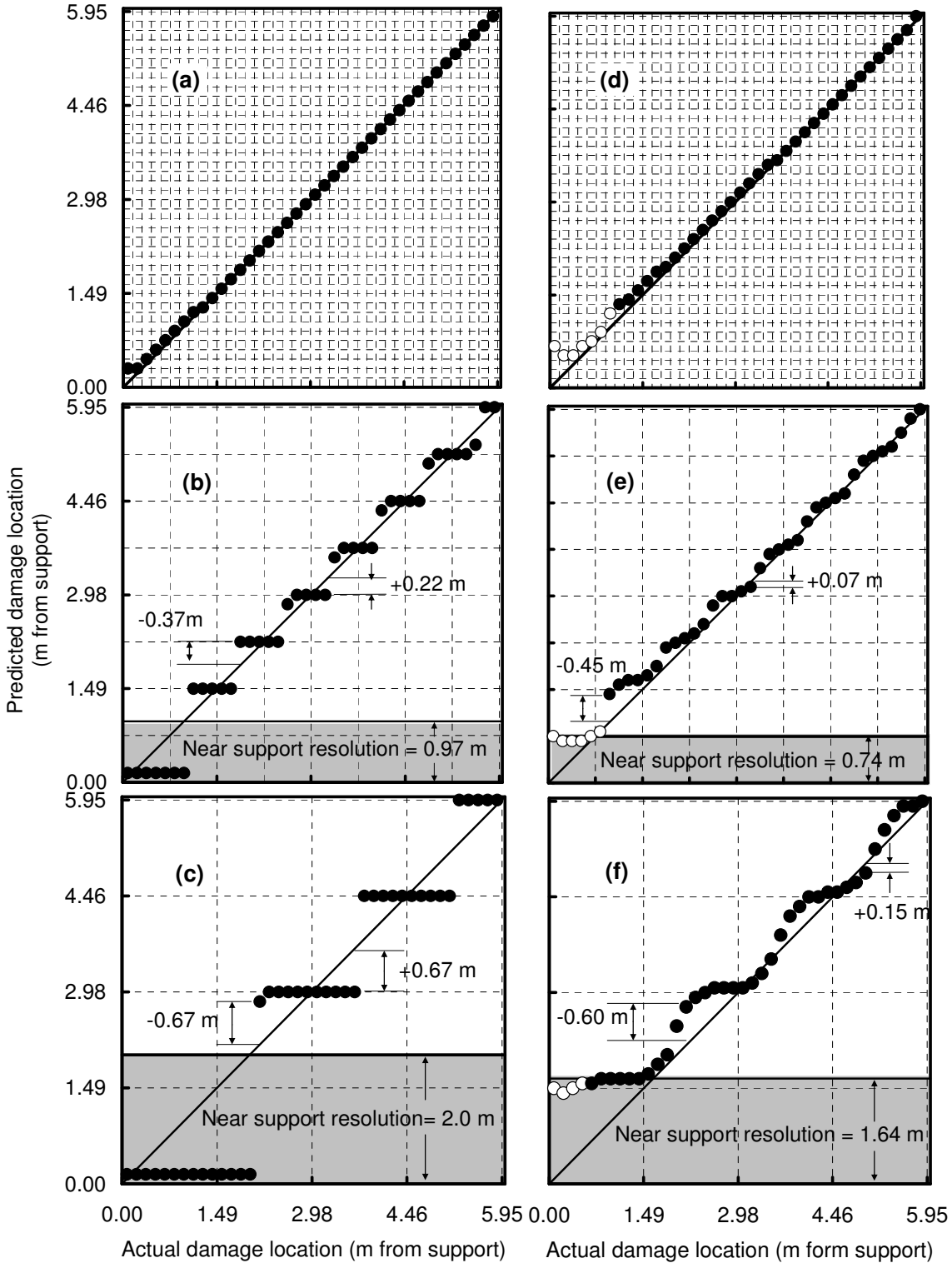

Figure 5.11. Correlation between predicted and actual longitudinal location of damage calculated using first three modes by the change in uniform flexibility curvature methods using a) 79, b) 15, and c) 7 FE simulated measurement points; and by the change in flexibility method using d) 79, e) 15, and f) 7 FE simulated measurement points.

Comparisons with Figs. 5.7(a), (b) and (c) show that the accuracy improved slightly within non-near-support region when 15 and 7 measurement points were used; however, within the near-support region, the accuracy was unchanged when 15 measurement points were used, and even decreased when 7 measurement points were used.

For the mode shape curvature method, comparison of Figs. 5.12 (a), (b), and (c) with Figs. 5.9 (a), (b), and (c) shows that using the first three flexural modes actually decreased the accuracy of predicted damage location slightly within the near-support region when7 measurement points were used. Outside of the support region, the accuracy slightly increased when 7 measurement points were used and slightly decreased when 15 measurement points were used.

A comparison of Figs. 5.12 (d), (e), and (f) with Figs. 5.9 (d), (e), and (f) shows that the accuracy of the damage location predicted by the damage index method using the first three flexural modes decreased significantly when 7 measurement points were used and decreased slightly when 79 and 15 measurement points were used relative to results using the fundamental mode only. This was attributed that the instability of the index when reference modal strain energy is close to zero in a given region; i.e., the nodal points where the value of mode shape curvature is near zero (Kim and Stubbs 2003).

In general, for the VBDD methods investigated, the use of three modes did not improve the accuracy of damage localization over the use of only one mode. In fact, for the damage index method, the accuracy significantly decreased when damage was not located within a near-support region and a small number of measurement points were used.

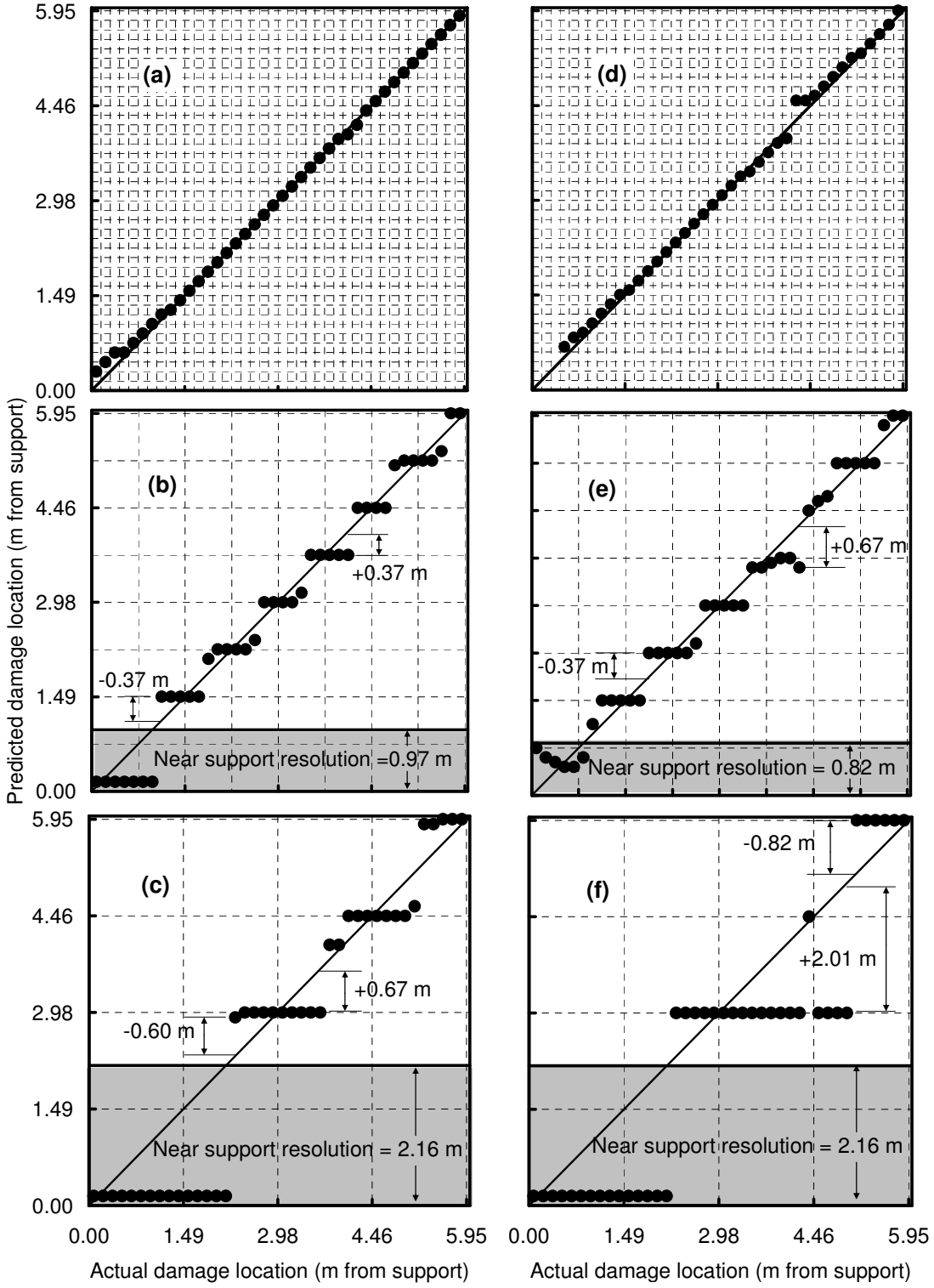

Figure 5.12. Correlation between predicted and actual longitudinal location of damage calculated using first three modes by the mode shape curvature method using a) 79, b) 15, and c) 7 FE simulated measurement points; and by the damage index method using d) 79, e) 15, and f) 7 FE simulated measurement points.

5.2.2.5 Comparison of VBDD techniques in terms of accuracy of damage localization

As defined previously in Section 4.3.2.5, the resolution of a damage localization procedure may be defined as the length of the window within which damage actually lies given that the procedure predicts it to be located at a particular point. In attempting to define the resolution for different techniques, the two observations made in the context of the bridge deck were also found to apply here. First, when damage was predicted to be located within a certain characteristic distance from a support, it could actually be located anywhere within this near-support region. This characteristic distance corresponds to the near-support resolution as indicated in Figs. 5.7, 5.9, 5.11 and 5.12 by the shaded regions. For example, for the change in flexibility method using seven measurement points (Fig. 5.7(c)), the near-support resolution was found to be 1.49 m, since any time the predicted location of damage lay within 1.49 m of the support, the actual damage location could have been located anywhere within this region. For the change in mode shape method using seven measurement points, inspection of Fig. 5.7(f) reveals a near-support resolution of 1.71 m.

A second observation is that when damage was located outside the near-support region, individual techniques tended to produce consistently larger errors on either one side or the other of the actual damage location. This is illustrated in Fig. 5.7 by identifying the maximum errors when the actual damage locations are closer to supports (shown as negative errors) and farther from supports (shown as positive errors) than predicted locations. For example, Figs. 5.7(a) through 5.7(c) show that the change in flexibility method tended to produce larger errors when the actual location lay closer to the support than the predicted location. For the case of seven measurement points, when

the actual location was closer to the support than the predicted location, the maximum error was 0.74 m; when the actual location was farther from the support, the maximum error was only 0.15 m. Therefore, when damage was predicted to be located at a certain point, the actual location was known to lie within a region that was 0.74 m closer to the support or 0.15 m farther from the support; the damage location resolution was 0.89 m, or 60% of the spacing between measurement points, with the resolution window skewed 83-17 toward the support. For the change in mode shape method, the resolution was 0.59 m, skewed 63-37 away from the support.

By inspecting Figs. 5.7, 5.9, 5.11 and 5.12, and employing the definition discussed above, Fig. 5.13 was generated showing the damage locating resolutions achieved using all the VBDD techniques investigated, normalized by the spacing between measurement points, h. The focus of the discussion is on the performance using only the fundamental mode (indicated by solid bars); shaded bars correspond to the use of three flexural modes. Figs. 5.13(a) and 5.13(b) show that the performance of most techniques was comparable, achieving resolutions ranging between 0.8h and 0.9h. As was the case for the bridge deck, the change in mode shape method performed better than this, achieving resolutions of 0.5h and 0.4h for 15 and 7 measurement points, respectively. The change in flexibility method also performed very well, achieving a resolution of 0.6h when 7 points were used. In most cases, an increase in the number of measurement points led to a proportional improvement in resolution (in absolute terms). In other words, resolution was a direct function of measurement point spacing, h.

The use of three modes resulted in only slight improvements at best. The poor performance of the damage index method is attributed to the instability of the index as explained in Section 5.2.2.4.

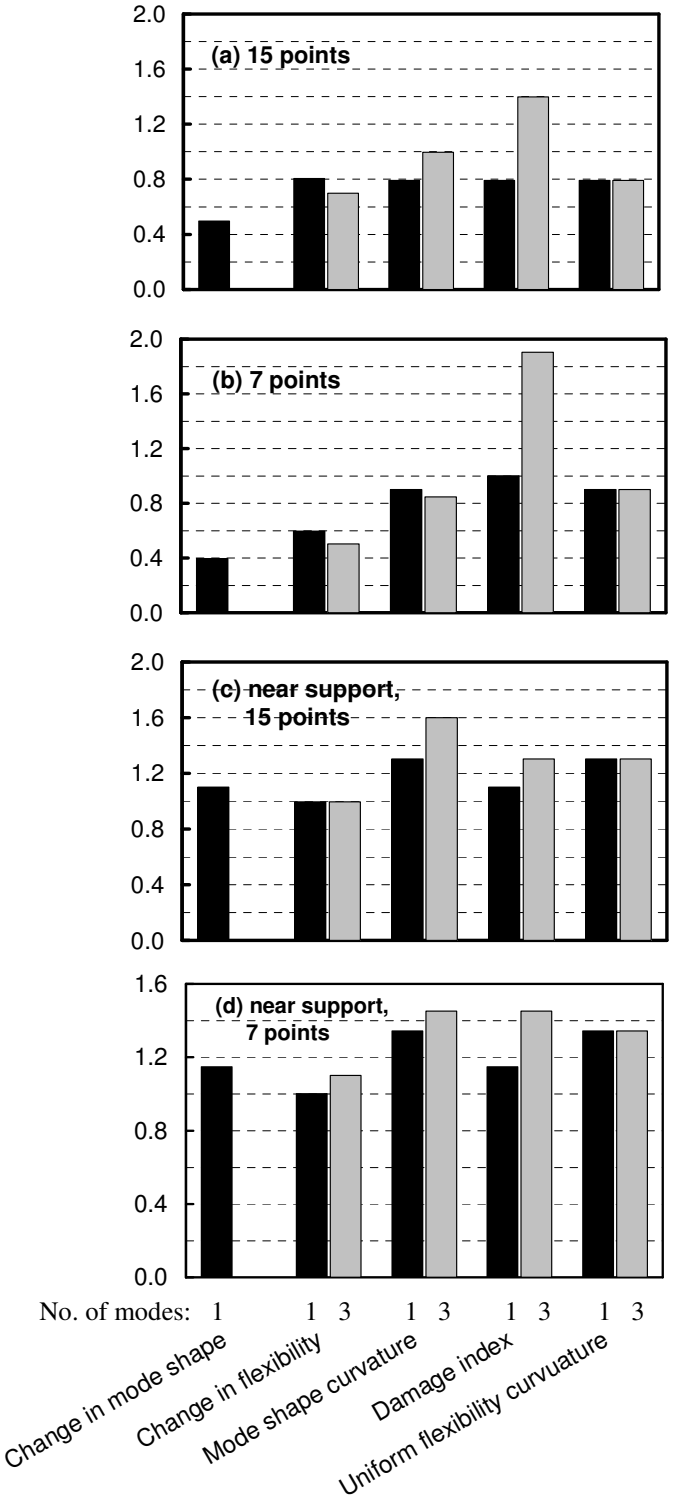

Figure 5.13. FE derived damage localization resolutions, normalized by the spacing between measurement points, using a) 15 and b) seven measurement points; and near-support resolutions for c) 15 and d) seven measurement points.

The near-support resolutions of most methods were also comparable, achieving values between 1.0*h* and 1.6*h* (Figs. 5.13(c) and (d)). The use of additional modes did not improve this performance at all.

An improved damage localization resolution may sometimes be achieved by considering the intersection of overlapping resolution windows produced by different methods. For example, since the window of the change in flexibility method is skewed toward the support relative to the predicted location and the window of the change in mode shape method is skewed away from the support, if both techniques predict damage to be located at the same point, the intersection of the two windows is smaller than either of the individual windows. When seven measurement points were used, the intersection between the windows was 0.37 m or 0.25*h*. This combined resolution could not be quantified precisely for all methods because the different techniques typically predicted different damage locations and the relationship between these locations was not constant.

5.2.2.6 Comparison of the application of VBDD techniques on the deck and the girder

As demonstrated previously, the use of the first three flexural modes did not improve the accuracy of the damage localization significantly for either the bridge deck or the girder. Therefore, the following comparison of the application of VBDD techniques on the deck and the girder will focus on the damage localization using only the fundamental mode.

The resolution of damage localization on the bridge deck and the girder are compared in Fig. 5.14. The solid bars correspond to the resolutions achieved on the prestressed concrete girder, while the shaded bars correspond to the resolutions achieved

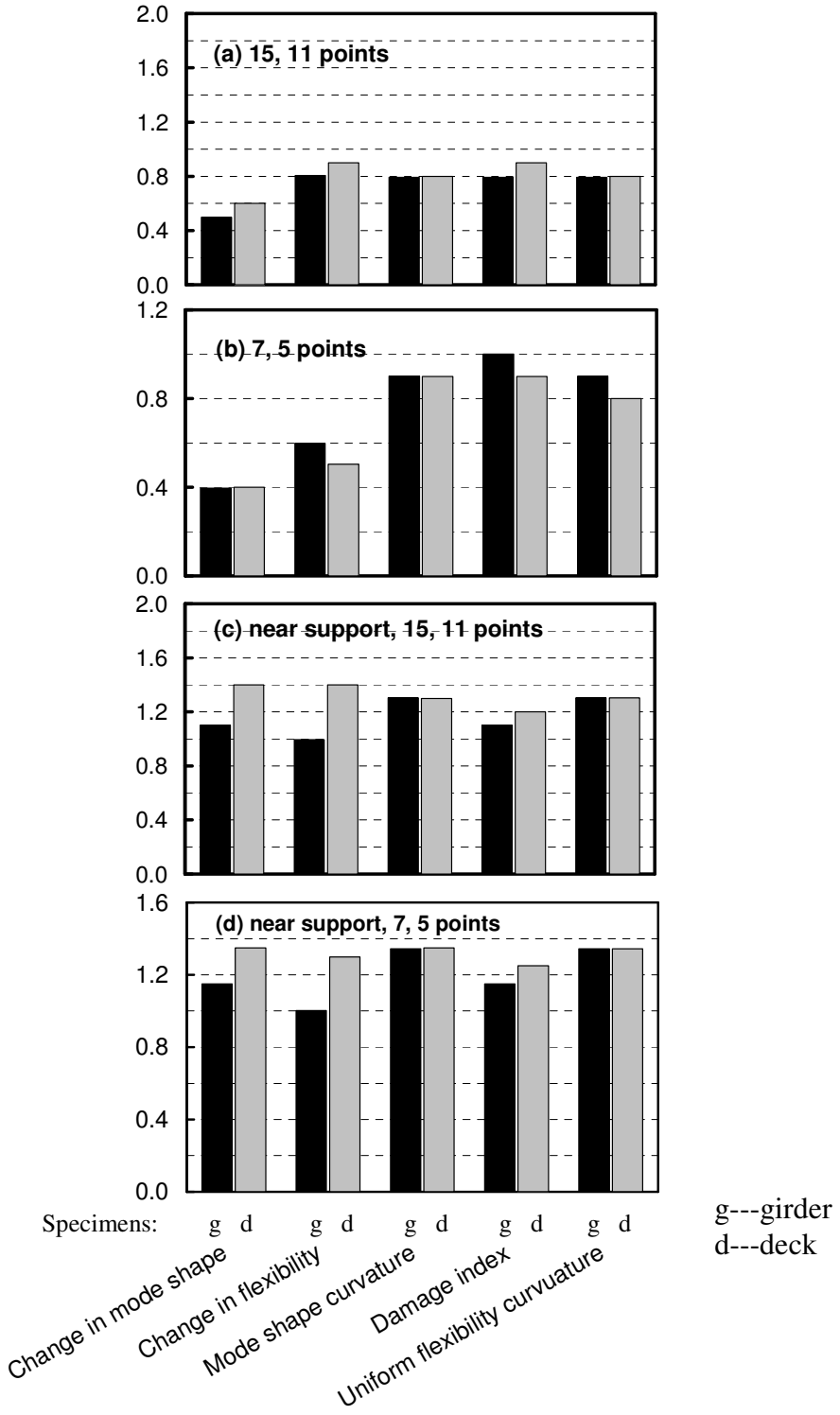

Figure 5.14. Comparison of damage localization resolutions of the girder and the deck, normalized by the spacing between measurement points using a) 15 or 11 and b) 7 or 5 measurement points; and near-support resolutions for c) 15 or 11 and d) 7 or 5 measurement points.

on the bridge deck. In Figs. 5.14 (a) and (c), "15, 11 points" indicates that 15 measurement points were used for the girder, and 11 points were used for the bridge deck. Similarly, "7, 5 points" indicates that 7 and 5 measurement points were used for the girder and the bridge deck, respectively.

Fig. 5.14 shows that the five methods produced comparable results for the two structures. Except when seven or five points were used in the non-near-support region, the change in mode shape method, the change in flexibility method, and the damage index method tended to work slightly better for the girder. Differences may be attributed to the fact that the girder was a uniform cross section beam, while the cross sections of both ends of the bridge deck were different from those at mid-span of the deck. In addition, the studs connecting the concrete slab and steel girder were distributed at a spacing 750 mm so that the connection between the concrete slab and the steel girder was not continuous.

In general, numerical investigation results are highly consistent between the bridge deck and the girder.

5.2.2.7 Transverse damage localization

Finally, the determination of the transverse location of damage is discussed in this section. In this study, an original procedure was developed to estimate the transverse damage location on a prestressed concrete girder using measured mode shapes along each edge, before and after damage had taken place. In this method, Δ_s is defined as the difference between the damaged and undamaged unit-norm-normalized mode shapes at the point of maximum change in mode shape (calculated by Eq. 2.11) for the edge with the smaller difference, and Δ_l is defined as that difference for the edge with the larger

difference. Then, the transverse distance z_d from the edge with the larger difference to the location of damage may be estimated by

$$z_d = 1.134 \cdot S \cdot \sqrt{\frac{\Delta_s}{\Delta_l}} - 0.807, \qquad [5.1]$$

where S is the girder width.

Eq. 5.1 is based on a similar principle to that underlying Eq. 4.1, which was used to determine the transverse location of damage on a steel-free bridge deck. Eq. 5.1 was derived from the finite element simulation results for the 11 transverse damage cases described in Section 5.2.1. The derivation procedure consisted of plotting z_d versus $S \cdot \sqrt{\frac{\Delta_s}{\Delta_l}}$ for the 11 transverse damage cases. The distribution approximated a straight line, and a linear regression equation was fitted to the data using Excel software (see Appendix D).

Figs. 5.15(a), (b), and (c) show results of the transverse localization procedure when 79, 15 and 7 measurement points were used, respectively. Excellent correlation is seen between predicted and actual damage locations, with a maximum error 0.025 m, 0.052 m, and 0.053 m for 79, 15, and 7 measurement points, respectively, corresponding to 2%, 4% and 4% of the girder width, respectively. However, the accuracy was thought to be very sensitive to measurement uncertainties because the difference between the changes of mode shapes along both edges of the girder were very small due to the large torsional stiffness of the girder; this supposition was confirmed by the experimental results presented in Section 5.3.

In summary, in the absence of experimental uncertainty, small-scale damage may be detected and located on the simply supported prestressed concrete girder with a

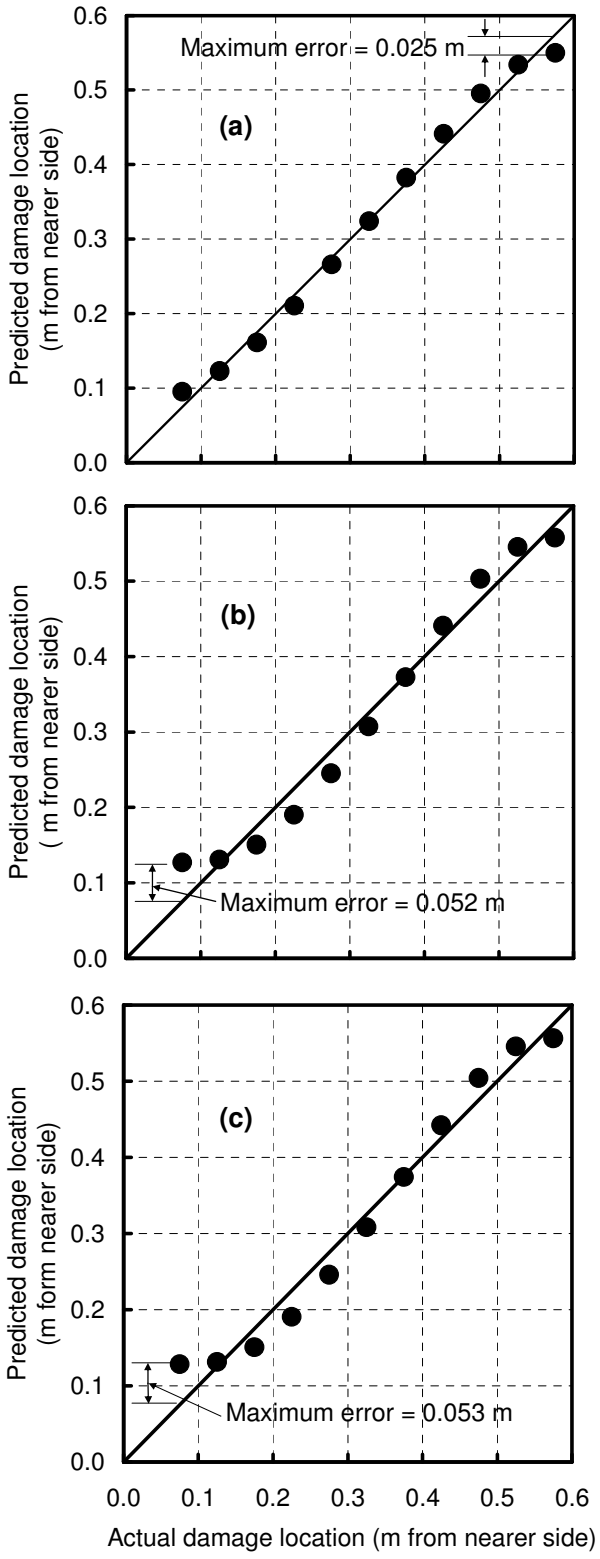

Figure 5.15. Correlation between predicted and actual transverse location of damage, calculated using a) 79, b) 15, and c) 7 FE simulated measurement points.

longitudinal resolution of approximately 40% of the spacing between seven evenly spaced measurement points, and transversely with a resolution of 4% of the girder width, provided the damage does not occur too near a support. When damage was located near the support, the resolution and level of certainty was diminished; however, the presence and approximate location of damage could still be determined.

5.3 EXPERIMENTAL STUDY

5.3.1. Description of experimental study

The experimental setup for the prestressed concrete girder is shown in Fig. 5.16. The hydraulic shaker was mounted on the centre of the girder, while both the accelerometers and strain gauges sets were positioned at six evenly spaced locations along each side of the girder.

The girder was simply supported at both ends. One end was supported on a steel angle as shown in Fig. 5.17(a), allowing freedom of rotation for the girder but not translation. The other end was supported using a roller, allowing the girder freedom of both rotation and longitudinal movement, as shown in Fig. 5.17(b).

The configuration of damage induced into the physical system was similar to that modelled numerically: small square blocks of concrete, 150 x 150 mm in plan and 30 mm deep, were physically removed from the top surface of the deck, as shown in Fig. 5.18. It should be noted that this was a very low level of damage for the bridge girder, corresponding to a local reduction in flexural rigidity of approximately 2.49 %. Damage was induced incrementally at twelve different locations, as shown in Fig. 5.19, in which damage states are numbered according to the sequence in which they were introduced. The twelve cases represented a wide variation in longitudinal and transverse location to

(a)

(b)

Figure 5.16. Photographs of the experimental setup of the girder: (a) a view of the entire girder, and (b) installation of the accelerometer and strain gauges on the girder.

(a)

(b)

Figure 5.17. Photographs of the supports of the girder: (a) steel angle support at one end of the girder, and (b) roller support at the other end.

test the damage locating capability of the VBDD techniques over a wide range of possible damage locations. The experimental procedure consisted of measuring the initial (undamaged) dynamic properties of the system, and then incrementally inducing a new state of damage and measuring the properties associated with each damage state. The "undamaged" dynamic signature for a particular damage state was taken to be that measured for the previous state of damage.

The dynamic excitation and measurement procedures were described in Chapter 3. The locations of accelerometers and strain gauges are shown in Fig. 5.19.

The five VBDD techniques were applied experimentally for localizing the damage longitudinally using both accelerometer and strain gauge data. The method proposed in Section 5.2.2.7 for determining the transverse location of damage on a girder was applied experimentally using only the accelerometer data.

Figure 5.18. Experimental damage induced on the surface of the girder.

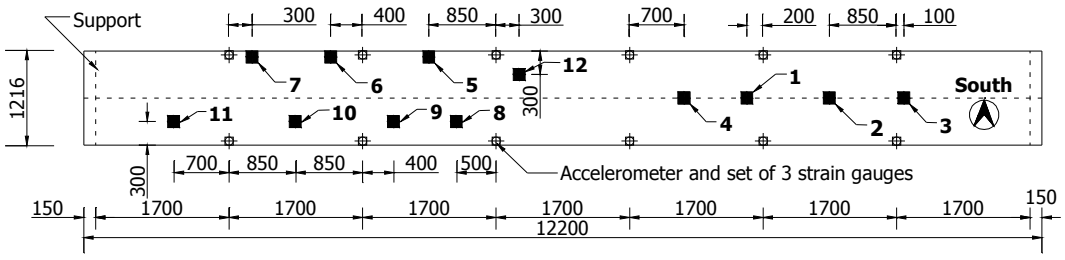

Figure 5.19. Schematic plan of girder showing locations of damage and sensors (dimensions in mm).

5.3.2 Results and discussion

5.3.2.1 Strain gauge data

Fig. 5.20 shows representative plots of change in mode shape curvature, $\Delta\phi''_1$, calculated using flexural curvatures associated with the fundamental mode shape derived from strains measured on a vertical surface along one side of the girder. The plots of change in mode shape curvature for remaining nine damage cases are shown in Appendix E. Other methods were not applied using the strain gauge data. It should be recalled that the baseline ("undamaged") curvature for each successive state of damage was that associated with the previous state of damage. The highest positive peaks in these plots indicate the predicted longitudinal location of damage.

It can be seen that no ambiguity is apparent with respect to identifying the highest positive peaks, which were observed to occur near the actual location of damage for the cases shown. As was the case for the bridge deck study, these plots also show significant negative peaks, which correspond to reductions in mode shape curvature associated with the introduction of damage, and do not indicate a damage location.

Correlations between predicted and actual damage locations for all damage states are shown in Fig. 5.21, with data points labelled according to the damage cases of Fig. 5.19. The gridlines correspond to the locations of measurement points along the girder. Good agreement was observed for nine of the twelve damage cases. Not including damage cases 3, 7, and 11, the maximum absolute error was 0.85 m, attained for damage cases 2, 5 and 10, which corresponds to a relative error of 50% of the spacing between measurement points.

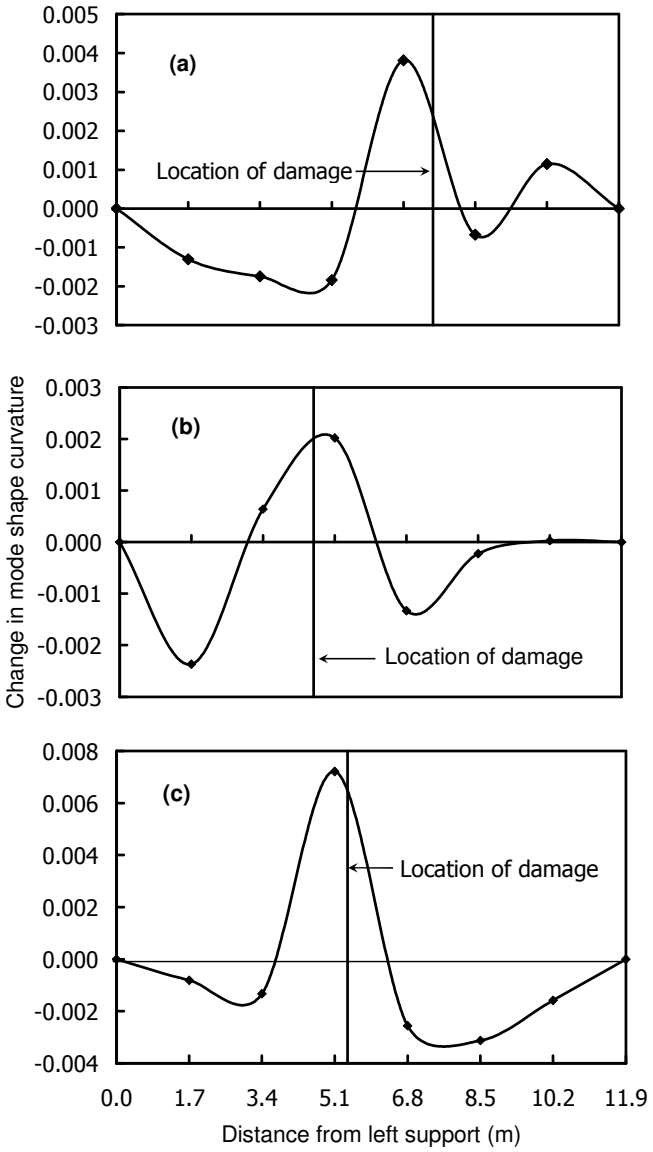

Figure 5.20. Change in mode shape curvature along one side of the girder, calculated using strain gauge derived measured curvature for a) damage case 4, b) damage case 8, and c) damage case 12.

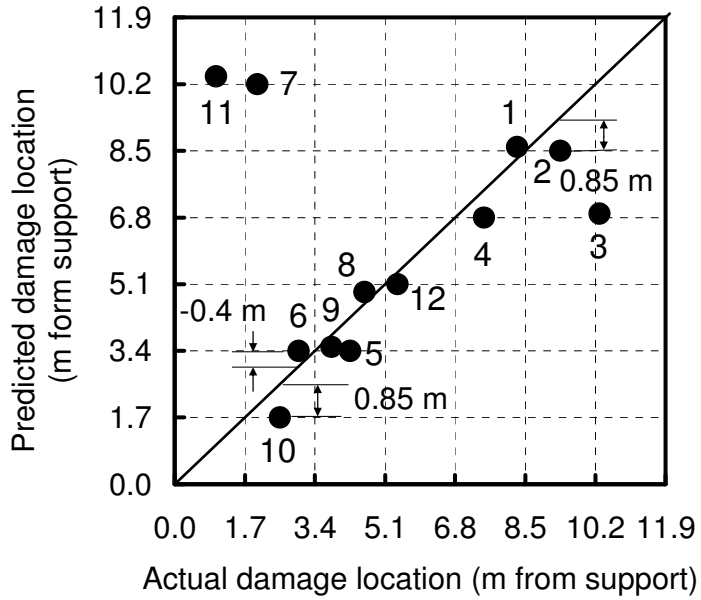

Figure 5.21. Correlation between predicted and actual longitudinal locations of damage, as calculated by the mode shape curvature method using strain gauge derived measured curvature (data labels refer to damage cases as defined in Fig. 5.19).

The detection technique failed to successfully locate damage cases 3, 7 and 11, all of which were located relatively close to supports. In fact, the results for these three cases—particularly case 7—were misleading in that the predicted location, denoted by a clear peak, was nowhere near the actual location. The fact that these damage states were very near the support is believed to have contributed to this failure. The absolute curvatures, and therefore strain measurements near supports, were small. This led to smaller signal-to-noise ratios and smaller changes in curvature in these regions. In addition, it was suspected that one of the four supports was not in intimate contact with the girder, preventing successful detection of the damage near support. This suggests that it is necessary to place an accelerometer on the girder at a support location to identify the vibration of the girder at the support. As was mentioned in Chapter 4, it is

reasonable to assume that regions near mode shape inflection points for indeterminate structures may also require special attention when this type of VBDD technique is used.

The proximity of damage to a measurement point was found to significantly influence the accuracy with which damage could be located. In Fig. 5.22, a plot of absolute localization error versus the longitudinal distance to the nearest gauge shows a high correlation (R = 0.95) between these two variables, when cases 3, 7 and 11 (near support cases) were excluded.

The resolution of damage localization, defined as the length of the window within which damage actually lies when the procedure predicts it to be located at a particular point, was found to be 1.7 m (or approximately h, where h is the spacing between measurement points) when damage was not located between a support and the nearest measurement point and damage case 7 was excluded. Unlike the numerical results, the resolution window derived from experimental results was not skewed.

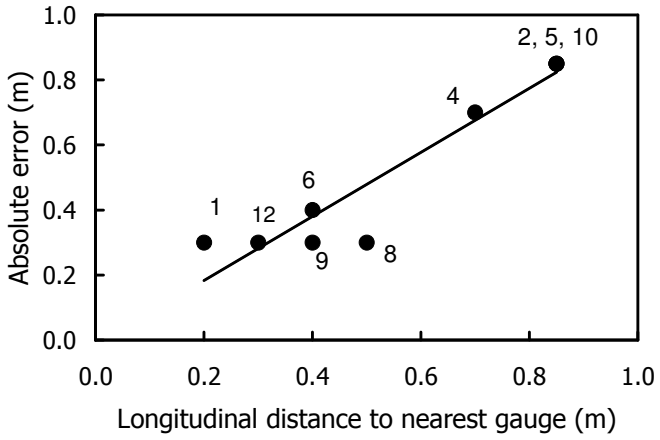

Figure 5.22. Absolute error in locating damage, as a function of longitudinal distance to nearest strain gauge group, calculated by the mode shape curvature method using strain gauge derived measured curvature.

The level of resolution was similar to that achieved numerically in the absence of experimental uncertainty using the mode shape curvature method, as described in Section 5.2.2.2. (see also Fig. 5.13) The inability of the method to locate damage cases 3, 7 and 11 precluded the formation of a near-support damage localization resolution for this method.

5.3.2.2 Accelerometer data

Fig. 5.23 shows the distributions of all five damage detection parameters, as calculated using accelerometer data, corresponding to the first damage case, for which damage was located 8.3 m from the support. The highest positive peak in each plot indicates the predicted longitudinal location of damage. In these plots, parameters are normalized relative to their maximum values as they were in the previous chapter. Similar plots for all damage cases are included in Appendix F.

The same observations made in Section 4.4.2.2 with respect to the steel-free bridge deck were also found to apply here. First, the highest peak occurred at or close to the same location (8.5 m from the support in this case) for each method. Second, the predicted location coincided with the location of an accelerometer (see Fig. 5.19). Third, the mode shape curvature and change in uniform flexibility curvature methods produced virtually identical distributions, in which the parameters varied linearly between measurement points, a feature that results from the use of cubic polynomials to interpolate mode shape displacements between measurement points. The damage index method, which also makes use of mode shape curvatures (though not as linear functions), produced distributions which were similar to those of the two methods just mentioned, but which differred from them by taking on smaller values near the supports.

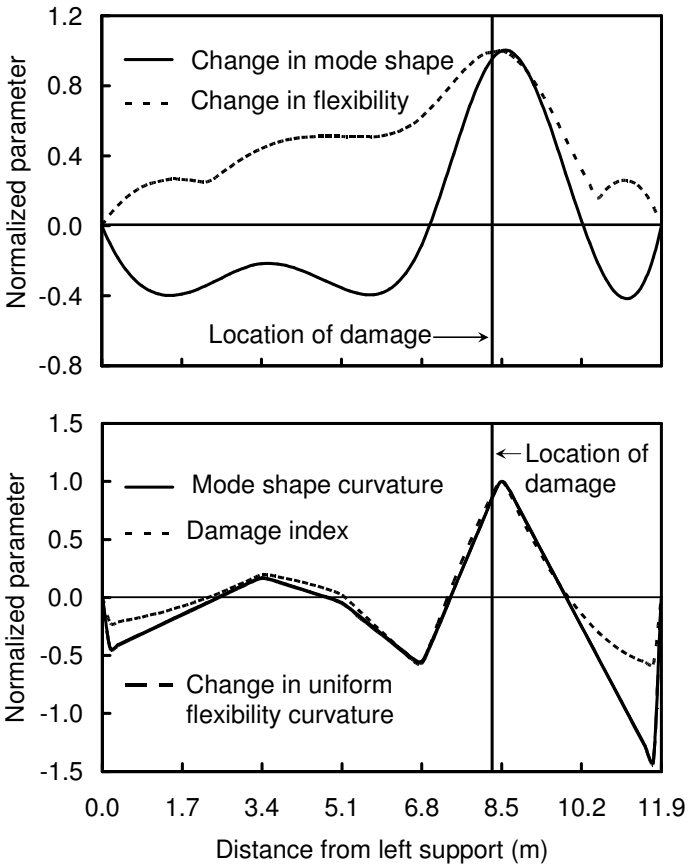

Figure 5.23. Distribution of normalized damage detection parameters, calculated along north side of the girder for damage case 1 by all methods.

The correlations between predicted and actual damage locations for all damage cases are shown in Fig. 5.24, in which gridlines correspond to accelerometers locations, filled circle symbols indicate the location of unambiguous peaks in the damage detection parameters, and open circle symbols indicate ambiguous cases when two positive peaks with similar magnitudes were observed. All techniques are seen to have performed relatively well. Not including the near-support damage cases (3, 7, and 11) and damage case 10, which must be treated separately, and ignoring for the moment the fact that some results were ambiguous, the maximum observed error was 0.85 m (0.5*h*) for all

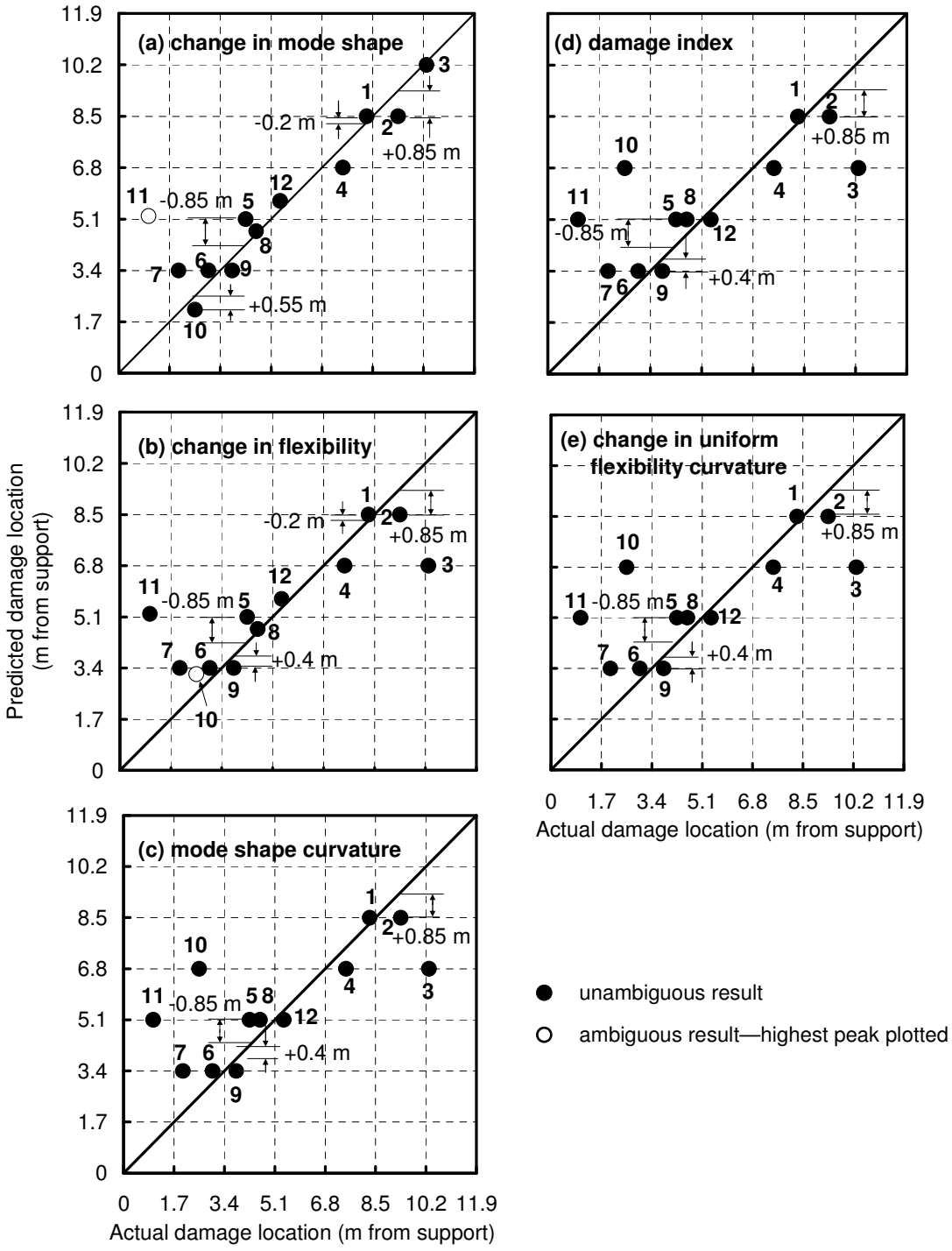

Figure 5.24. Correlation between predicted and actual longitudinal locations of damage calculated by a) change in mode shape, b) change in flexibility, c) mode shape curvature, d) damage index, and e) change in uniform flexibility curvature methods.

methods. It should be noted that the change in mode shape method successfully located damage cases 3 and 10, whereas the other methods failed.

As already alluded to, the mode shape curvature, change in uniform flexibility curvature and damage index methods produced identical results. All three of these methods predicted damage to be located exactly at measurement points, as evidenced by the position of data points along horizontal gridlines. This phenomenon has been explained in Sections 4.3.2.2 and 4.4.2.2.

It was not possible to quantify the resolution of the damage locating procedures with the same level of confidence as was done using numerical results in Section 5.2.2.5, since a relatively small number of cases were examined experimentally. Nonetheless, it should be observed that when damage was not located too near a support, with only three exceptions for each VBDD technique (two exceptions for the change in flexibility method), the actual damage was located closer to the nearest support than the predicted location (i.e. farther from mid-span than the predicted location). It was also true for the deck, suggesting that it may be more generally true for simply supported systems. If considered, however, the resolution window was 1.25 to 1.40 m for all methods, skewed 60% to 70% toward the nearest support.

Comparison of Fig. 5.24 with Figs. 5.7 and 5.9 shows that the experimental results were in general agreement with those of the numerical study. The experimental resolution for damage location prediction (0.74h to 0.82h) was within the range found numerically (0.4h to 0.9h), though it was not as good as the best resolution achieved numerically (0.4h). Thus, the presence of experimental uncertainty does not appear to have had a significant effect on the performance of the VBDD techniques, provided the mode shapes were measured reliably and the damage was not too near a simple support.

The direct use of curvature obtained using strain gauge measurements achieved a maximum error (0.85 m) that was similar to that achieved by the methods that used accelerometer measurements (0.85 m). However, the resolution of the former method (1.0 *h*) was different from that of the latter, owing to the fact that the resolution window for the acceleration derived techniques was skewed toward supports, while the strain gauge derived window was not skewed. It should also be noted that higher amplitude vibrations were required to obtain strain signals with sufficiently high signal-to-noise ratios to achieve the observed level of resolution using strain gauge measurements. This may prove not to be feasible in field applications.

When damage was located between a support and the first measurement point (cases 3 and 11) or near the first measurement point (case 7), Fig. 5.24 indicates that the predicted damage location was subject to greater error. The experimental results were much worse than the numerically observed near-support resolution of approximately 1.2*h* due to the measurement uncertainties. A comparison of Fig. 5.24 and Fig. 4.23 shows that the performance of the VBDD methods for damage cases within the near support region on the girder was much worse than that on the bridge deck. This was attributed to the fact that the torsional stiffness of the girder is much larger than that of the bridge deck, making it very difficult to ensure that each of the four supports was in contact with the girder at all times; even a small variation in the support condition could affect the measurement accuracy of the mode shape in the near-support region. If an accelerometer was mounted on the girder above each support, it would have provided information about the support condition and may have improved near support prediction.

5.3.2.3. Transverse damage localization

Fig. 5.25 shows the correlation between predicted and actual transverse locations of damage when experimental acceleration data were used. Comparison with Fig. 5.15(c) shows that the experimental accuracy was significantly worse than that achieved numerically, with the location of damage successfully determined to lie within the bounds of the girder surface in only eight of twelve cases. For these eight cases, a maximum error of 0.51 m was observed, or 42% of girder width. Damage case 4 was located outside of the girder, with a error of 0.72 m, or 60% of the girder width.

The poor performance is thought to be due to uncertainty in mode shape measurement, particularly along the side farther from the damage location, for which changes in mode shape would have been smaller. It appears, then, that greater measurement accuracy is required to determine the transverse location using the proposed method. The success of the technique numerically suggests that its performance is limited by the level of measurement uncertainty.

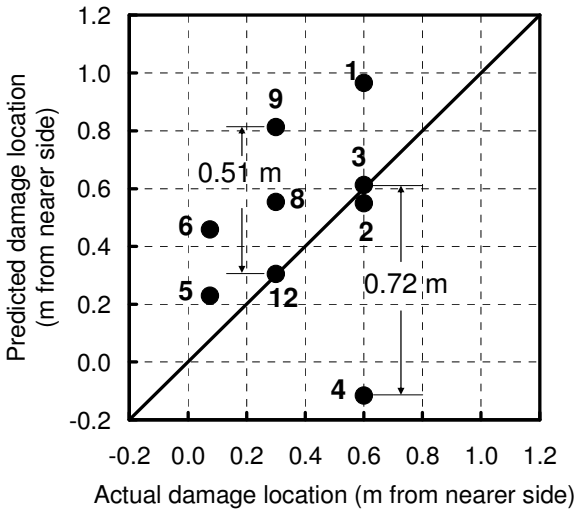

Figure 5.25. Correlation between predicted and actual transverse locations of damage, calculated using experimentally measured accelerations at six locations along each side of the girder.

5.4 CONCLUSIONS

5.4.1 Conclusions from the Numerical Study

Using an FE analysis, this study has shown that the presence of small-scale damage on a prestressed concrete girder can be detected and located with reasonable accuracy using vibration-based damage detection (VBDD) techniques which use measurements of only the fundamental mode shape before and after damage. When damage was detected, the extent of the region within which it could be confidently predicted to lie—i.e. the resolution of damage localiztion—depended upon how accurately the mode shapes could be defined.

When mode shapes were well-defined with a large number of measurement points, the damage localization could be pinpointed with great accuracy using any of the five VBDD techniques investigated. In practice, though, only a relatively small number of measurement points are feasible, and damage localization resolution in this case was found to depend upon the number and spacing between measurement points. In the absence of experimental uncertainty, and provided the damage was not located too near a support, the resolution of damage localization was found to be 40 to 90% of the spacing between measurement points when seven evenly spaced points were used along each side. The best results were achieved by the change in mode shape and change in flexibility methods. In some cases, particularly when these two techniques predicted the same damage location, their simultaneous use could improve the resolution to approximately 25% of measurement point spacing by accounting for characteristic skews in the resolution windows. The use of additional modes, however, did not improve the performance of the techniques. On the other hand, an increase in the

number of measurement points from 7 to 15 improved their performance, since the localization resolution remained between 50 and 80% of measurement point spacing, while the spacing was cut in half.

When damage was located near a support, the resolution of damage location was found to be approximately 15% greater than the distance from the support to the first measurement point. In addition, the proposed transverse damage localization procedure allowed damage to be located within 5% of girder width transversely.

Comparison of the performance of the five VBDD methods investigated on the steel-free bridge deck with that on the prestressed concrete girder in Fig. 5.13 shows that the damage detection resolutions were consistent for both systems when the damage was not located near a support. For the change in mode shape and change in flexibility methods, however, the damage detection resolution on the girder was slightly better than that on the deck when the damage was located near a support; this was thought to be due to the fact that the cross section of concrete slab of the bridge deck dramatically changed near a support, leading to variation in the stiffness of the deck in that region. Similarities in the performance of the VBDD methods applied to the girder and the deck show that the results from a scale model also apply to full-scale components.

5.4.2 Conclusions from the Experimental Study

Using experiments conducted on a full-scale laboratory model, this study has shown that the presence of small-scale damage on a prestressed concrete girder can be reliably detected and located using vibration-based damage detection (VBDD) techniques that employ measurements of only the fundamental mode shape before and after damage. The location of damage was determined with a resolution of approximately 82 to 100%

of measurement point spacing when six measurement points were distributed along each side of the girder, unless the damage was located too near the support.

When vertical acceleration measurements were used to determine mode shapes, the reported level of resolution accounted for the fact that the resolution windows were skewed toward supports—i.e. the actual location of damage was typically located closer to the supports than the predicted location. This observation is consistent with experimental results on the steel-free bridge deck. The simultaneous application of several VBDD techniques was required to remove ambiguities that any one technique might produce and to narrow the resolution window when the predicted location was near mid-span. Due to the relative small number of damage cases considered in the experimental study, however, the skewed nature of the observed resolution windows may, in part, be a reflection of the damage locations relative to the sensors.

The use of strain gauges bonded to the vertical surface of the girder to measure mode shape curvatures was found to result in similar errors in the predicted damage locations, but had a larger damage localization resolution since the resolution window was not skewed. Comparison of these results with those of the companion numerical study demonstrated that the presence of experimental uncertainty resulted in only a slight decline in damage localization resolution, unless the damage was located too near a support.

Although only a small number of near-support damage cases were studied, the resolution of damage localization near supports was found to be worse than that achieved in the numerical study. Near-support damage detection and localization appears to present significant challenges. Although not investigated thoroughly, closer spacing of measurement points near supports appears to be an important factor

influencing the accuracy and reliability of locating damage in this region. Additional work is required to confirm this and to improve the performance of VBDD techniques near supports.

Of the five VBDD techniques investigated, the change in mode shape method, which simply uses the difference between damaged and undamaged unit-norm normalized fundamental mode shapes, appeared to perform the best. It produced the smallest errors in predicted locations, including near supports. It was also able to locate one damage case when all other methods failed. While the simultaneous use of several techniques is recommended, the change in mode shape method should be among the methods used.

It was found that the levels of damage localization resolution and the characteristic skews of the resolution windows observed in the prestressed concrete girder study were consistent with those observed for the steel-free bridge deck. This is very helpful information for damage detection. However, eventual field application of these techniques will likely require calibration studies to determine appropriate levels of resolution and skew for particular types of structures. This is likely to require the use of numerical models that incorporate reasonable levels of measurement uncertainty.

The proposed transverse damage localization procedure did not perform well experimentally, being able to determine the location of damage in only eight of twelve cases, and then with an accuracy of approximately 42% of girder width. Given that the procedure was able to achieve an accuracy of 4% of girder width using numerically generated data, the proposed procedure appears to be very sensitive to measurement uncertainty. Determining the transverse location of damage for both the deck and the girder was found to be very challenging, and additional work is required in this area.

Results of this study demonstrate that existing VBDD algorithms are adequate for detecting and locating low levels of damage on a bridge girder, at least for a prestressed concrete girder and simple support conditions. However, as was noted in Chapter 4, in order to take advantage of the potential of the algorithms, mode shapes must be known with a high level of accuracy since changes to mode shapes caused by low levels of damage are very small. Measurement methods that demonstrate a very high level of repeatability are required. In addition, it is believed that when a small number of measurement points are used, the accuracy of mode shape estimation—and therefore the performance of the VBDD algorithms—may be improved to a certain extent by refining the methods used for data manipulation prior to applying the VBDD algorithms, with particular attention paid to the interpolation methods used.

In summary, the resolution of damage localization on the full-scale prestressed concrete box girder was slightly poorer than that for the half-scale steel-free bridge deck since the size and the type of structure are different. In general, both the numerical and experimental studies on the full-scale prestressed concrete girder confirmed the reliability of the results and conclusions obtained from the study on the half-scale steel-free bridge deck. It is believed that the size and type of structure will not affect the performance of the five VBDD methods investigated significantly; therefore, the size and type of structure should not be a major obstacle for the application of these VBDD methods to real structures.

CHAPTER 6. DETECTION OF MULTIPLE DAMAGE STATES ON A PRESTRESSED CONCRETE GIRDER

6.1 INTRODUCTION

In Chapter 5, it was demonstrated that a single, small scale damage state on a full-scale prestressed concrete box girder could be reliably detected and located longitudinally by certain VBDD techniques using as few as six measurement points equally spaced along each side of the girder, provided the damage was not located too near a simple support. In practice, however, damage is unlikely to occur at single isolated locations. Rather, damage may develop at several locations simultaneously. In an attempt to determine whether the VBDD techniques work well when multiple new damage states appear simultaneously, experimental and numerical studies were undertaken using a full-scale prestressed concrete box girder similar to that described in the previous chapter.

Since the best method for single damage detection was not necessarily found to be the best method for multiple damage detection, all five VBDD techniques described in Chapter 2 were investigated as part of this study. For example, as is shown later in this chapter, some methods failed in distinguishing two closely spaced damage states, while other methods succeeded in distinguishing them. Specifically, the following issues were investigated: (1) the influence of the spacing between measurement points on the minimum distance between two separate damage states that could be distinguished; (2)

determination of the minimum distance between two separate damage states for different methods when a large number of measurement points were used; (3) the influence of the distance between two damage states on the resolution of the predicted damage location; and (4) the role of higher modes in distinguishing two closely spaced damage states.

To facilitate the experimental design for the multiple damage state investigation, a different prestressed was used for this phase of the study, having the same dimensions of that described in Section 5.2.1. The girder was 12.2 metres long, featured a simple span of 11.9 metres, and had a 1216 x 508 mm cross section as shown in Fig. 5.1. In addition, the girder was simply supported at four corners.

6.2 NUMERICAL STUDY

6.2.1 Description of numerical study

The primary purpose of the numerical study was to evaluate the capabilities of the damage detection methods in the absence of excitation and measurement uncertainties.

The commercial finite element (FE) analysis package ANSYS (2003) was used to perform an eigenvalue analysis to generate the natural frequencies and mode shapes of the system. The finite element model was the same as that used in single damage detection described in Section 5.2.1, except that it was recalibrated to match the slightly different dynamic properties of the new girder. The mode shapes of the first four modes generated by the FE model were shown in Fig. 5.3.

The model was calibrated to the first four natural frequencies and mode shapes of the undamaged physical system. Table 6.1 shows that good agreement between predicted

Table 6.1. Comparison of FE and experimental natural frequencies and mode shapes for the undamaged system.

Parameter	1st Mode	2nd Mode	3rd Mode	4th Mode
Natural Frequencies(Hz)				
Experimental model	7.50	26.3	31.1	58.2
Finite element model	7.48	26.85	35.75	58.03
Relative error	0 %	2.1 %	15.0 %	-0.3%
Modal Assurance Criteria:	0.9999	0.9963	0.9874	0.9861

and measured natural frequencies was achieved and that the modal assurance criterion (MAC) values for the first four mode shapes were excellent. Comparing Table 6.1 with Table 5.2, it was found that the measured natural frequencies of the first four modes of the girder used for multiple damage detection were very close for those of the girder used to single damage detection.

Once the model had been calibrated, pairs of simultaneously applied damage states on the girder were simulated by eliminating two spatially separated groups of elements, each group comprising three transversely adjacent elements (each element being 149 mm long, 50 mm wide and 35 mm thick), from the top surface of the girder. A total of 41 pairs of damage cases were simulated, with each pair representing different damage locations. These 41 cases were sub-divided into two investigations; the first considered multiple damage states spaced at a uniform distance apart, while the second considered varying distances between damage states.

Investigation A*: *Constant distance between damage states

Initially, 19 pairs of damage states were investigated for which the longitudinal spacing between the states was kept constant at 1.488 m, as shown in Fig. 6.1(a). For these damage pairs, the transverse location of damage was set at 0.225 metres from the

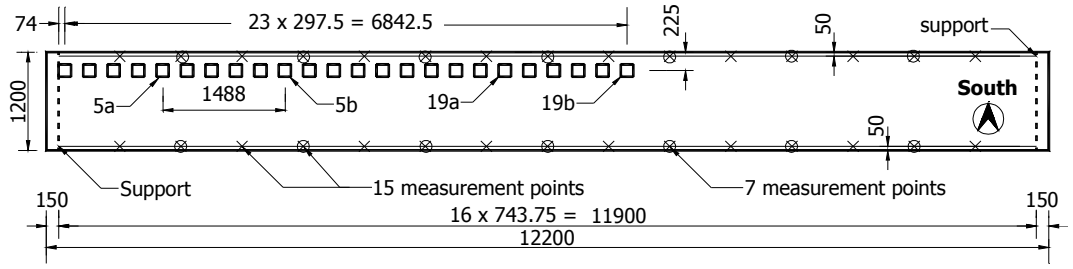

(a) Locations of damage used for the Investigation A

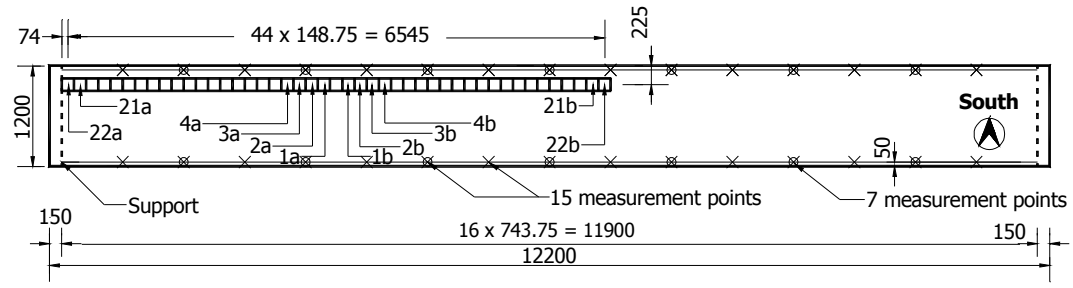

(b) Locations of damage used for the Investigation B

Figure 6.1. Schematic plan of girder showing locations of damage used for (a) the investigation A, and (b) the investigation B numerical study. (dimensions in mm)

centre of the damage to one edge of the girder, while the longitudinal location of the centre of the removed elements for the most easterly of the pair of damage states varied between 0.074 and 6.917 m from the support, increasing in increments of 0.298 m. For example, the fifth pair of damage states (denoted in Fig. 6.1a as 5a and 5b) were located 1.264 m and 2.752 m from the east support.

Investigation B*: *Varying distance between the two damage states

For the remaining 22 pairs of damage, the transverse location of damage was set at 0.225 metres from the centre of damage to one edge of the girder, while the longitudinal location of the centre of the removed elements varied between 0.074 and 6.619 m from

the support, increasing in 0.298 m intervals, as shown in Fig. 6.1(b). Unlike Investigation A, though, the longitudinal distance between pairs of damage states varied; for the first pair of damage states (1a and 1b), the separation distance was 0.298 metres, the longitudinal distance between the second pair of damage states (2a and 2b) was 0.596 metres, and so on, with the separation distance increasing by 0.298 m for each subsequent pair of damage states.

The FE analysis was intended to simulate the acquisition of measured data from sensors attached to a physical system at a small number of locations. Therefore, displacement data were extracted from the FE-generated mode shapes of the system at a small number of uniformly spaced "measurement" points along each side of the girder. Three cases were investigated: one in which seven measurement points were used, one in which fifteen measurement points were used, and a well-defined reference case in which 79 measurement points were used. In addition to these measurement points, mode shape deflections at supports were assumed to be zero.

Of primary interest was the performance of the damage detection techniques when only the fundamental mode shape was used, since accurate measurement of higher mode shapes is more difficult in practice. However, the use of the first three flexural mode shapes was also investigated to determine whether significant improvements could be realized. As described above, mode shapes were defined by "measurements" at seven, fifteen, or 79 points, in addition to zero displacements at supports. However, in order to obtain a better estimate of mode shapes when seven or fifteen measurement points were used, intermediate displacements between measurement locations were generated using a cubic spline interpolation technique described in Chapter 4, by which cubic polynomials were used to define the mode shapes between data points. In this way,

displacements at a total of 81 points were used to define the flexural mode shapes along girders, regardless of the number of measurement points. These mode shape vectors were unit-norm normalized prior to applying the damage detection techniques.

6.2.2. Results and discussion

This section presents the distribution of the damage indices for each of the five VBDD methods when they are applied selected cases of multiple damage detection. The results of "Investigation A" were then used to investigate the influence of the location of damage and the number of measurement points on the ability of the VBDD techniques to locate two simultaneously occurring damage states. Next, the results of "Investigation B" were used to investigate the influence of the distance between two damage states on the accuracy of the predicted damage locations. In addition, this section compares the detection capabilities for single and multiple damage states on the prestressed concrete girder.

6.2.2.1. Performance of the VBDD methods using well defined mode shapes

Fig. 6.2 shows the distributions of the five VBDD parameters when a pair of damage states were located 2.75 m and 4.24 m from the support, using only the fundamental mode shape and 79 measurement points. The distributions for this damage case are typical and representative of all damage cases, except those damage cases near a support that will be described separately later.

The change in mode shape method results are shown in Fig. 6.2(a). Two upward peaks were produced, each one clearly and accurately indicating the location of one of the two separated damage states. The amplitudes of the two peaks are 0.000074 and 0.000076, respectively, larger than the peak amplitude of 0.000056 caused by a single damage state of the same size, as shown in Fig. 5.5(a).

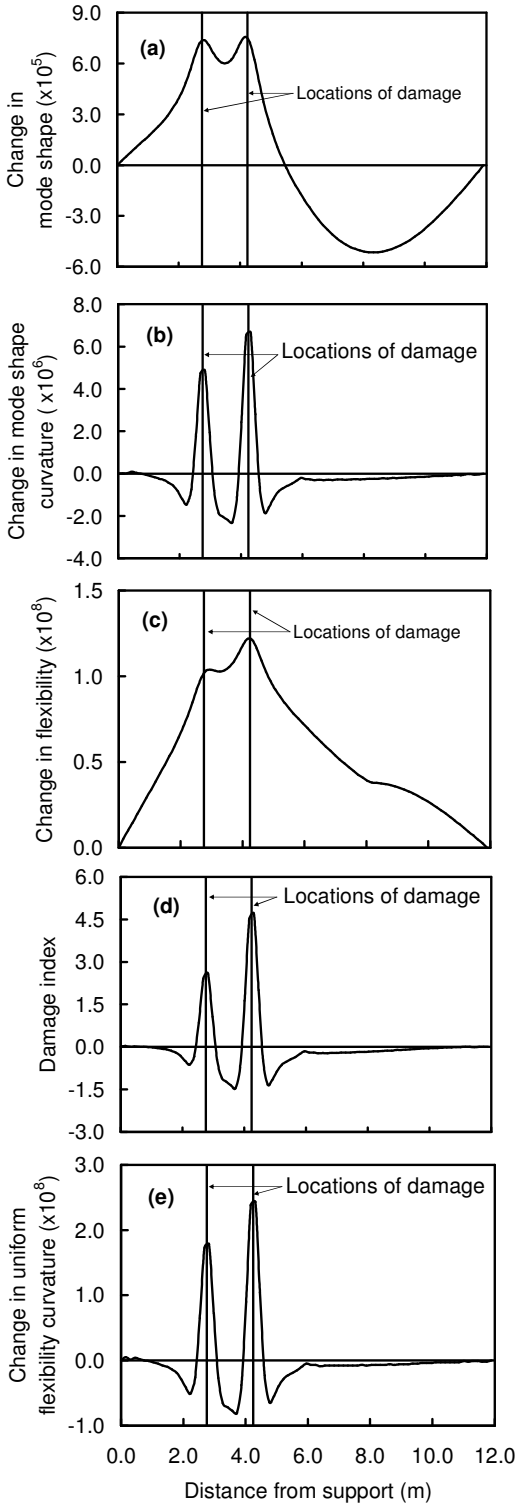

Figure 6.2. Distribution of the index of damage of the five VBDD methods for locating simultaneous damage states located 2.75 m and 4.24 m from support, respectively, when 79 measurement points were used.

A plot of the change in mode shape curvature is shown in Fig. 6.2(b). Again, two upward peaks appear in the figure, each one clearly and accurately indicating the location of one of the two damage states. In contrast to the change in mode shape, the two peaks in the change in mode shape curvature are much sharper, which makes distinguishing the two separated damage states easier and clearer.

The change in flexibility data are shown in Fig. 6.2(c). In this case, two upward peaks occur in the figure; however, the second highest peak is less distinct, which may suggest that the change in flexibility method is not as efficient for distinguishing two damage states separated by the distance considered here.

The damage index results are shown in Fig. 6.2(d). The shape of this distribution is similar to that of the change in mode shape curvature in Fig. 6.2(b); however, the ratio of the amplitude of the highest peak to that of the second peak is larger for the damage index method. The amplitudes of the highest and second highest peaks are 4.7 and 2.6, respectively, supporting Stubbs et al.'s finding (1995) that the value of a damage index greater than 2.0 is deemed to be indicative of a possible damage location. The damage index method is the only one of the five VBDD methods to give a threshold value to indicate the presence of damage.

The change in uniform flexibility curvature plot is shown in Fig. 6.2(e). The two sharp upward peaks clearly and accurately indicate the locations of damage. Comparing Figs. 6.2(e) and 6.2(b), it is evident that the shapes of these two graphs are almost identical.

6.2.2.2. Influence of a small number of measurement points

Fig. 6.2 indicates that all five VBDD methods can accurately predict the longitudinal locations of two damage states on the prestressed concrete girder when 79 measurement

points were used. However, a small number of measurement points is more practical for the application of VBDD methods; therefore, the influence of the number of measurement points on the accuracy of the predicted longitudinal location of damage by these five VBDD methods is discussed next.

Fig. 6.3 shows the distributions of the five VBDD parameters calculated using the fundamental mode shapes defined by 7, 15, and 79 FE simulated measurement points when the pair of damage states were located 2.75 m and 4.24 m from the support.

The change in mode shape results are shown in Fig. 6.3a. Two upward peaks appear when 15 and 79 measurement points were used, but only one is apparent when 7 measurement points were used; therefore, the two damage states could not be distinguished in latter case. The predicted locations of the damage states and associated errors are listed in Table 6.2. It was observed that the maximum error in the predicted location of the multiple damage states in this case was 0.90 m when seven measurement points were used, which is much larger than the 0.23 m error associated with the predicted location of single damage state in Fig. 5.6(a).

The change in flexibility plots are shown in Fig. 6.3(c). Once again, there were two upward peaks when 15 and 79 measurement points were used, but only one upward peak occurred when 7 measurement points were used; therefore, the two damage states could not be distinguished in that case. As shown in Table 6.2, the accuracy of the predicted location for multiple damage states by the change in flexibility method was worse than that achieved by the change in mode shape method for this particular damage state, no matter how many measurement points were used. Here and in subsequent discussion, the accuracy of the predicted location of multiple damage states is defined by the largest error for the two damage sites.

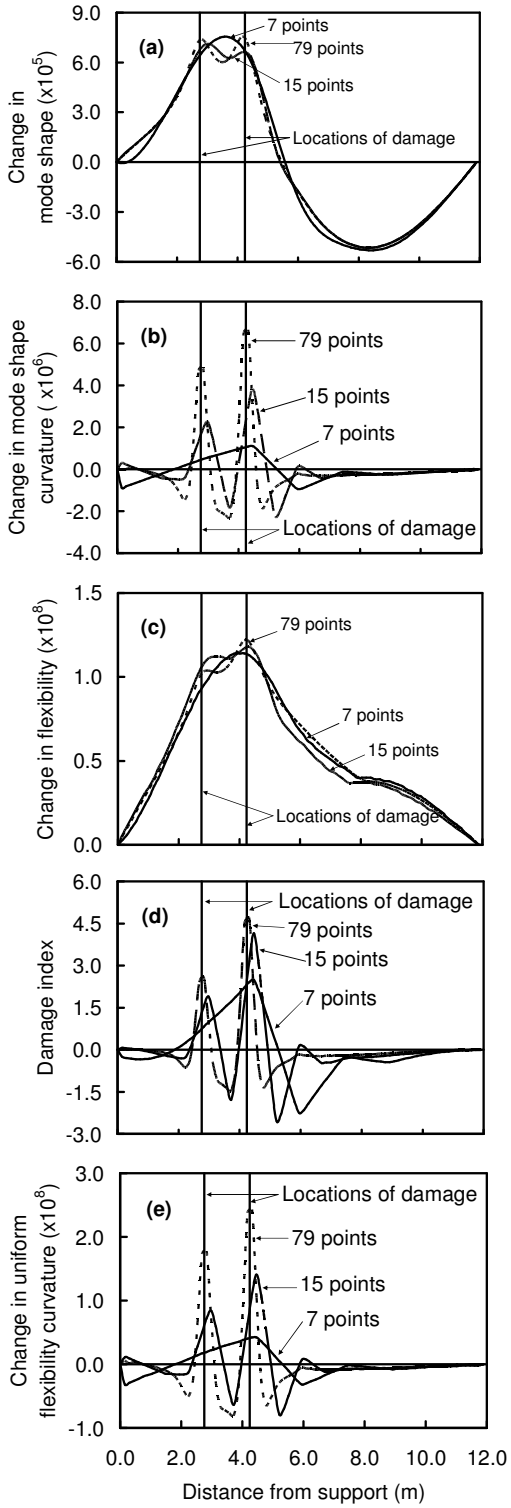

Figure 6.3. The influence of the number of measurement points on the accuracy of the predicted longitudinal location of damage states located 2.75 m and 4.24 m from the support by five VBDD methods.

Table 6.2. Predicted damage locations and errors (m) using five VBDD methods for the pair of damage states located 2.75 m (A) and 4.24 m (B) from the support.

Damage states		*Fig.6.3(a)*		*Fig.6.3(b),(d),(e)*		*Fig.6.3(c)*	
		A	B	A	B	A	B
79 points	Location	2.83	4.16	2.83	4.32	2.98	4.24
	Error	0.08	-0.08	0.08	0.08	0.23	0.00
15 points	Location	2.98	4.16	2.98	4.46	3.27	4.31
	Error	0.23	-0.08	0.23	0.22	0.52	0.07
7 points	Location	3.65	3.65	4.46	4.46	4.02	4.02
	Error	0.90	-0.59	1.71	0.22	1.27	-0.29

The distributions of the change in mode shape curvature, damage index, and change in uniform flexibility curvature are shown in Figs. 6.3(b), (d) and (e), respectively. In each of these three figures, there were two upward peaks when 15 and 79 measurement points were used, but only one upward peak when 7 measurement points were used. These methods all obtained identical results in terms of accuracy of localizataion, as shown in Table 6.2.

It is evident that multiple damage detection is similar to single damage detection in that the accuracy of the predicted damage location improved as the number of measurement points increased for all five VBDD methods. Also, the change in mode shape method performed better than other methods when a small number of measurement points were used. In addition, the upward peaks of the curves produced by both the change in mode shape and change in flexibility methods become sharper (i.e., the clarity of the peak improved) as the number of measurement points increased. However, the accuracy of the predicted location of multiple damage states was much worse than that of single damage detection when a small number of measurement points were used. In other words, multiple damage detection requires a larger number of

measurement points than single damage detection in order to predict the damage location with a reasonable level of accuracy.

Figs. 6.2 and 6.3 present the results for only one pair of damage states. However, investigation of a larger number of damage pairs with different locations and with different spacings between two damage states is required in order to better understand the performance of the VBDD methods for multiple damage detection.

6.2.2.3. Investigation A---Influence of damage location

"Investigation A" was undertaken to investigate the influence of the location of damage relative to the support, the number of measurement points (or the spacing between measurement points), and the use of higher modes on the accuracy of predicted damage location by each of the five VBDD methods.

The correlations between predicted and actual damage locations for all 19 pairs of longitudinally varying damage cases considered in Investigation A (see Fig. 6.1a), as calculated using the change in mode shape method, are plotted in Fig. 6.4. The solid squares indicate damage-a and the open circles indicate damage-b, where damage-a and damage-b represent a pair of damage states. It should be recalled that the spacing between damage states was held constant at 1.488 metres in this phase of the investigation. For reference, the gridlines in Figs. 6.4(b) and (c) indicate the locations of measurement points. Only the first mode was investigated here because the change of mode shape method is the only method out of the five investigated that cannot simultaneously use several modes to locate damage, as was explained in Section 4.3.2.4.

In Fig. 6.4a, corresponding to 79 measurement points, all points fall on the diagonal line, except for those points near the support, showing that very well-defined mode shapes allowed damage to be located with great accuracy using this method provided the

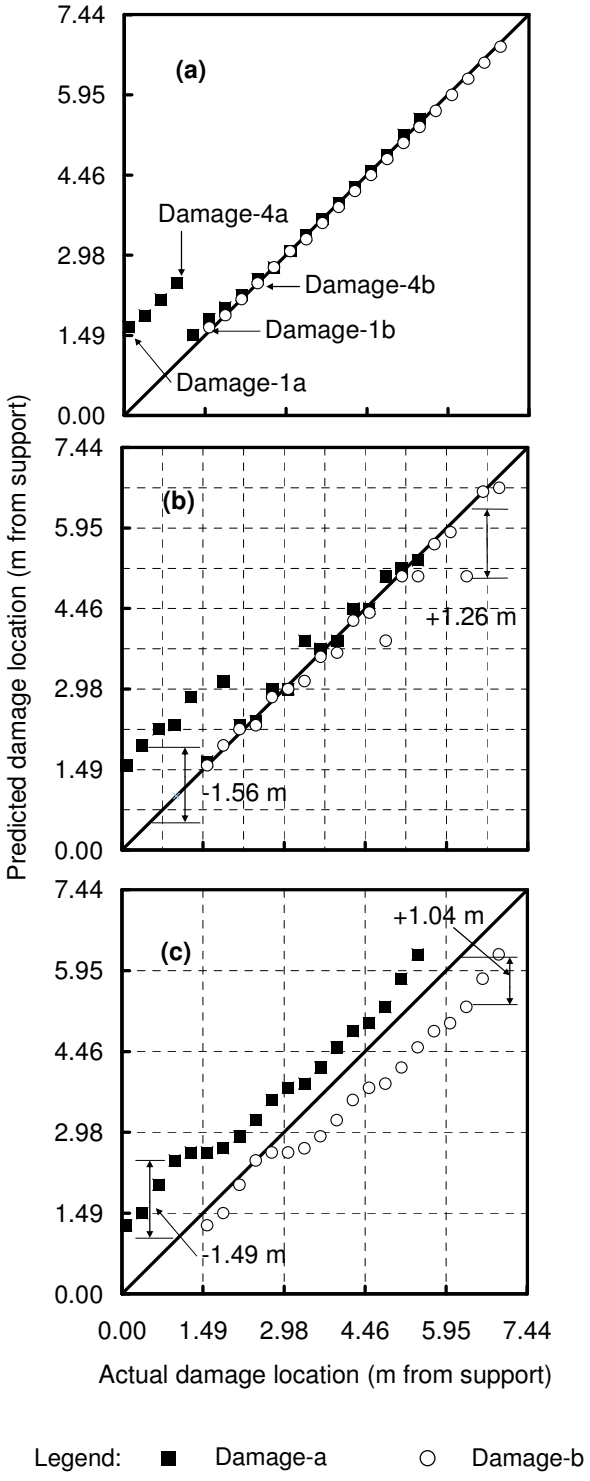

Figure 6.4. Correlation between predicted and actual longitudinal location of the damage cases in Investigation-A by the change in mode shape method using a) 79, b) 15, and c) 7 FE simulated measurement points.

damage was not located too near a support. It indicates that this technique is capable of detecting and locating small-scale damage with a high degree of precision if fundamental mode shapes can be defined very accurately. In the near support region, Damage-1a through Damage-4a have same predicted locations as Damage-1b through Damage-4b, respectively; therefore, the accuracy of the predicted location of Damage-1a through Damage-4a was very low.

As an example of near-support damage, Fig. 6.5 shows that the distribution of the change in mode shape for the damage-3a and damage-3b that were located 0.82 m and 2.31 m from a support, respectively. The two damage states could not be distinguished since only one peak occurred near the location of damage-3b regardless of the number of the measurement points, and the predicted location of damage-3a has a larger error. Comparing Fig. 6.4(a) with Fig. 5.6(d), it is evident that the resolution of multiple

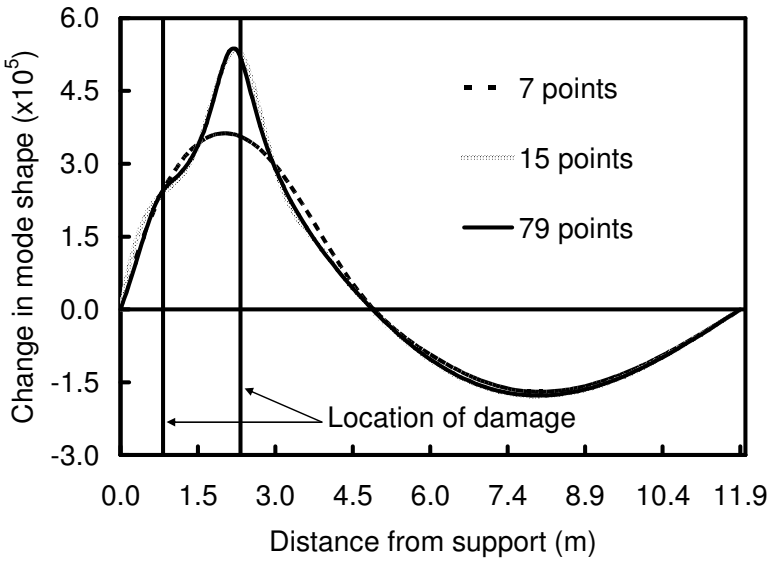

Figure 6.5. Distribution of the change in mode shape for locating simultaneous damage states located 0.82 m and 2.31 m from support, respectively, when 79, 15, and 7 measurement points were used.

damage detection was much lower than that of single damage detection when damage is located near a support, even if a large number of measurement points was used.

Fig. 6.4b and Fig. 6.4c correspond to correlations between actual and predicted damage locations for 15 and 7 measurement points, respectively. Comparing Fig. 6.4b with Fig. 6.4a, it is observed that as the number of measurement points decreased, the accuracy in detecting the location of damage also decreased when damage was not located near the support.

However, comparing Fig. 6.4b with Fig. 6.4c, it is found that increasing the number of measurement points does not necessarily increase the accuracy of the predicted location of damage for every individual multiple damage case if the accuracy is defined as the worst of the two in a given damage pair. The maximum error observed using the change in mode shape method with 15 measurement points (Fig. 6.4b) was 1.56 m, which was larger than 1.49 m, the maximum error when seven measurement points were used (Fig. 6.4c).

Comparing Fig. 6.4b with Fig. 5.7e, and Fig. 6.4c with Fig.5.7f, it is found that the accuracy of the predicted location of multiple damage states is much worse than that of single damage detection in non-near support regions when a small number of measurement points were used. It is also observed that for single damage state detection, the errors of predicted damage locations within the near-support region (shaded area) were much larger than those of non-near support region. For multiple damage detection, however, the change in mode shape method produced similar errors no matter the damage was located, whether near support or not, when a small number of measurement points were used. In addition, for single damage detection (Fig. 5.7(e) and 5.7(f)), all the damage states located within the near-support region had almost same predicted

location. For multiple damage detection, however, the predicted damage locations were proportional to the actual damage locations even if the damage was located near the support. Therefore, the definition of the near-support resolution used for single damage detection was found not to be suitable for multiple damage detection. Instead, for multiple damage detection, a common resolution could be defined for both near-support and other regions for the change in mode shape method.

The correlations between predicted and actual damage locations for all 19 pairs of longitudinally varying damage cases in Investigation-A, as calculated using the change in flexibility method with the first mode and the first three modes, are plotted in Fig. 6.6.

As seen in Fig. 6.6, when 15 measurement points were used, the maximum errors were 1.86 m using only the first mode and 1.71 m using the first three modes, respectively. When 7 measurement points were used, the maximum errors were 2.01 m and 1.71 m, respectively. Therefore, using higher modes appears to improve the accuracy of the predicted damage location slightly. Similar to the change in mode shape method, no near-support resolution could be defined clearly for the change in flexibility method. Also, the accuracy of the predicted damage location was not improved when the number of measurement points was increased from 7 to 15. Again, it was found from the comparison between Fig. 6.6 and Fig. 5.7 that the accuracy of multiple damage state detection was much worse than that of single damage state detection when 7 and 15 measurement points were used.

The correlations between predicted and actual damage locations calculated using the change in mode shape curvature method, with the first mode and the first three modes, are plotted in Fig. 6.7. Fig. 6.7(a), which corresponds to 79 measurement points, shows that very well-defined mode shapes allowed damage to be located with great accuracy

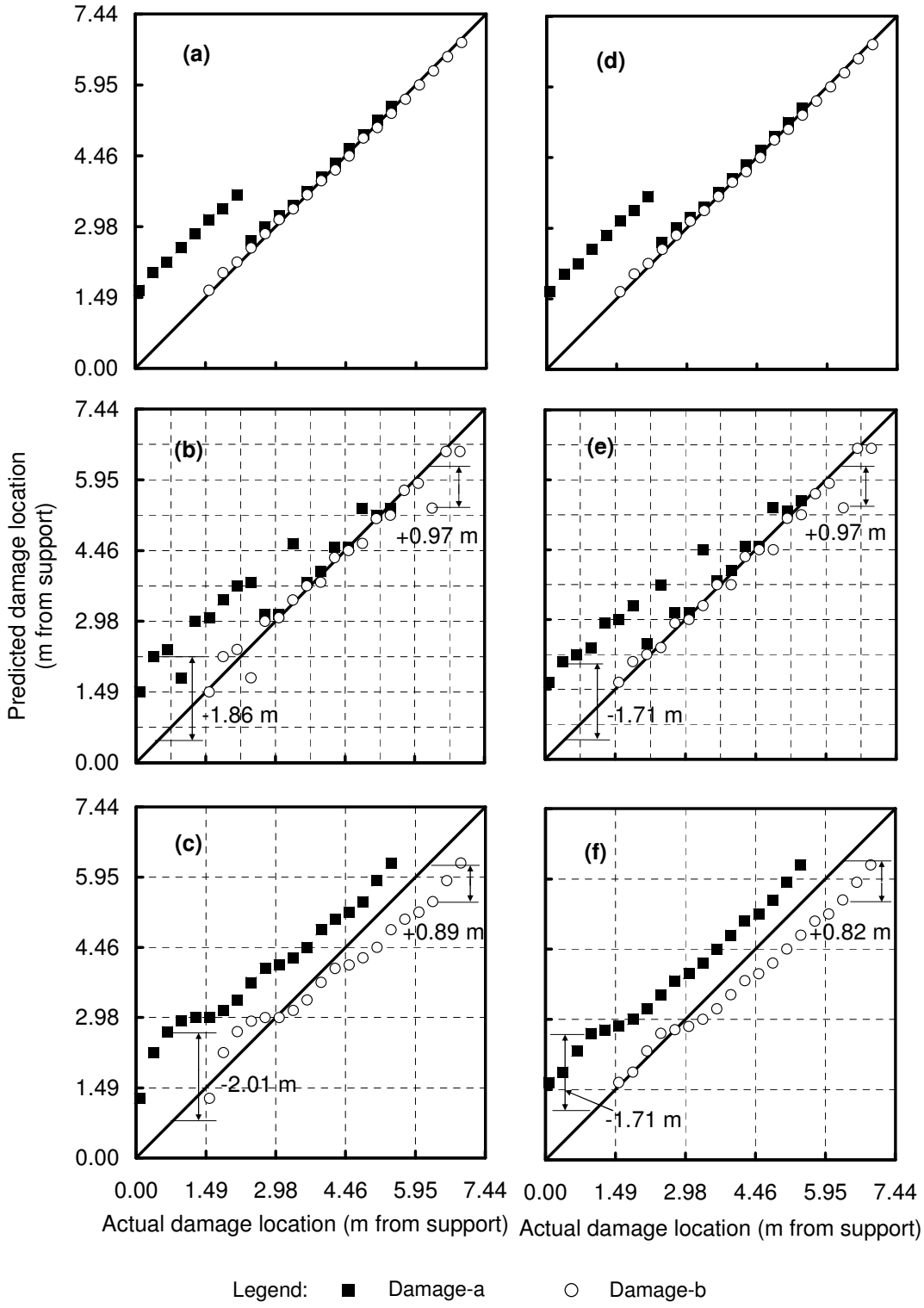

Figure 6.6. Correlation between predicted and actual longitudinal location of damage calculated by the change in flexibility method and the first mode using a) 79, b) 15, and c) 7 FE simulated measurement points; and by the first three modes using d) 79, e) 15, and f) 7 FE simulated measurement points.

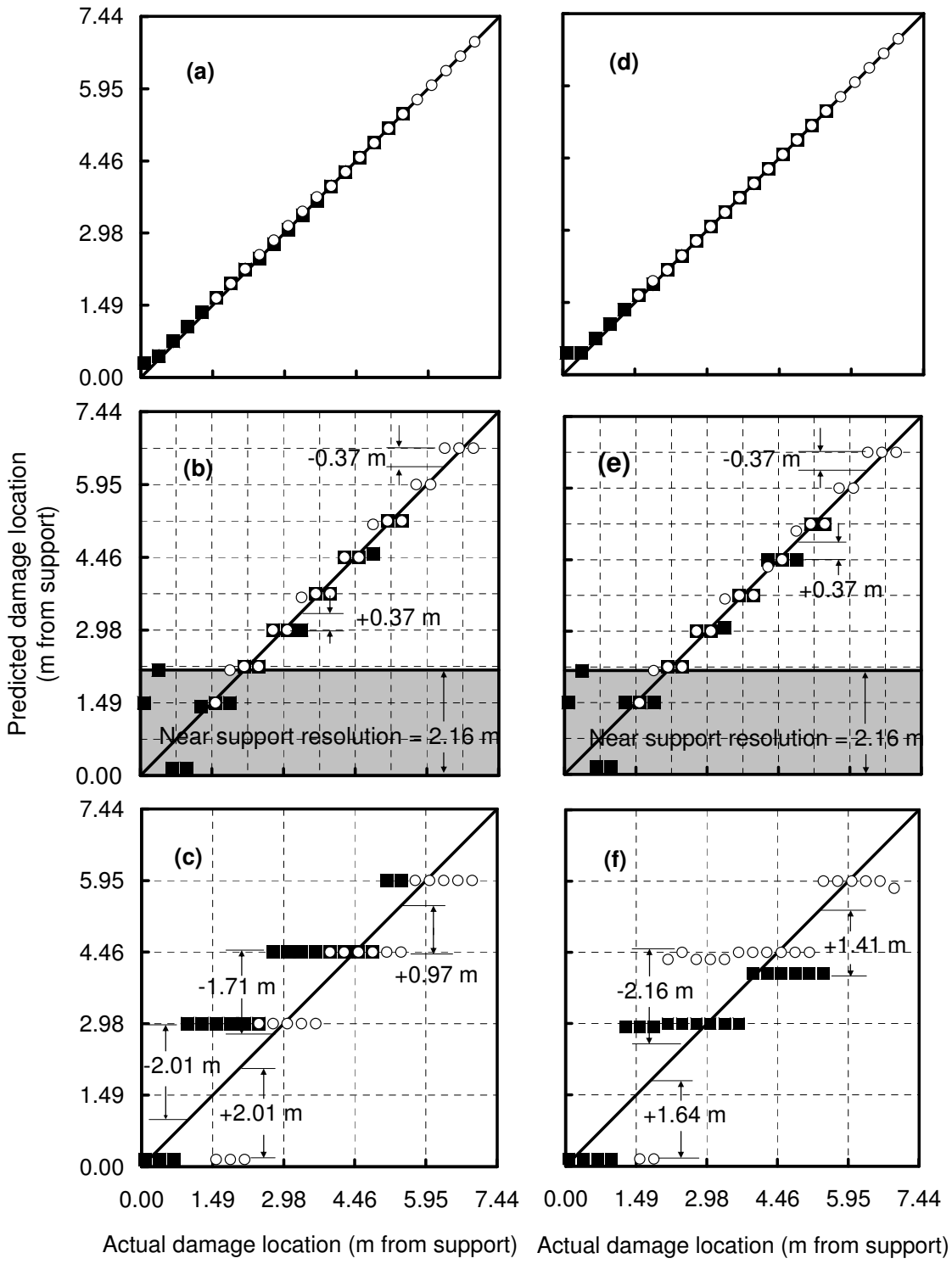

Figure 6.7. Correlation between predicted and actual longitudinal location of damage calculated by the change in mode shape curvature method and the first mode using a) 79, b) 15, and c) 7 FE simulated measurement points; and by the first three modes using d) 79, e) 15, and f) 7 FE simulated measurement points.

using this method, even when the damage was located near a support. This result indicates that the change in mode shape curvature technique is capable of detecting and locating small-scale damage with a high degree of precision if fundamental mode shapes can be defined very accurately.

As demonstrated in Fig. 6.7(b), when 15 measurement points were used, near support resolutions were 2.16 m using either the first mode by itself, or using the first three modes, while the maximum errors were 0.37 m in either case outside of the near support regions. Therefore, the accuracy was much better than that for the change in mode shape method or the change in flexibility method.

When 7 measurement points were used, it became very difficult to identify the near support region; in addition, the maximum errors were 2.01 m using the first mode and 2.16 m using the first three modes. Therefore, using higher modes actually decreased the accuracy in the predicted damage location. For the change in mode shape curvature method, using 15 measurement points produced much better results than using 7 measurement points when the damage was not located near the support. In this case, the spacing between adjacent measurement points was 0.744 m when using 15 measurement points, equivalent to exactly half of 1.488 m, the distance between the two damage states.

Fig. 6.8 compares the distributions of change in mode shape curvature when one and three modes were used. The distributions in Figs. 6.8(a), (b), (d), and (e) are shown for the case when two damage states were located 4.24 m and 5.73 m from support. Figs. 6.8(a) and (d) show results when 79 measurement points were used. In Fig. 6.8(a), using the first mode only, the two damage locations were clearly predicted. In Fig. 6.8(d), on the other hand, use of the first three modes is seen to produce three upward peaks which

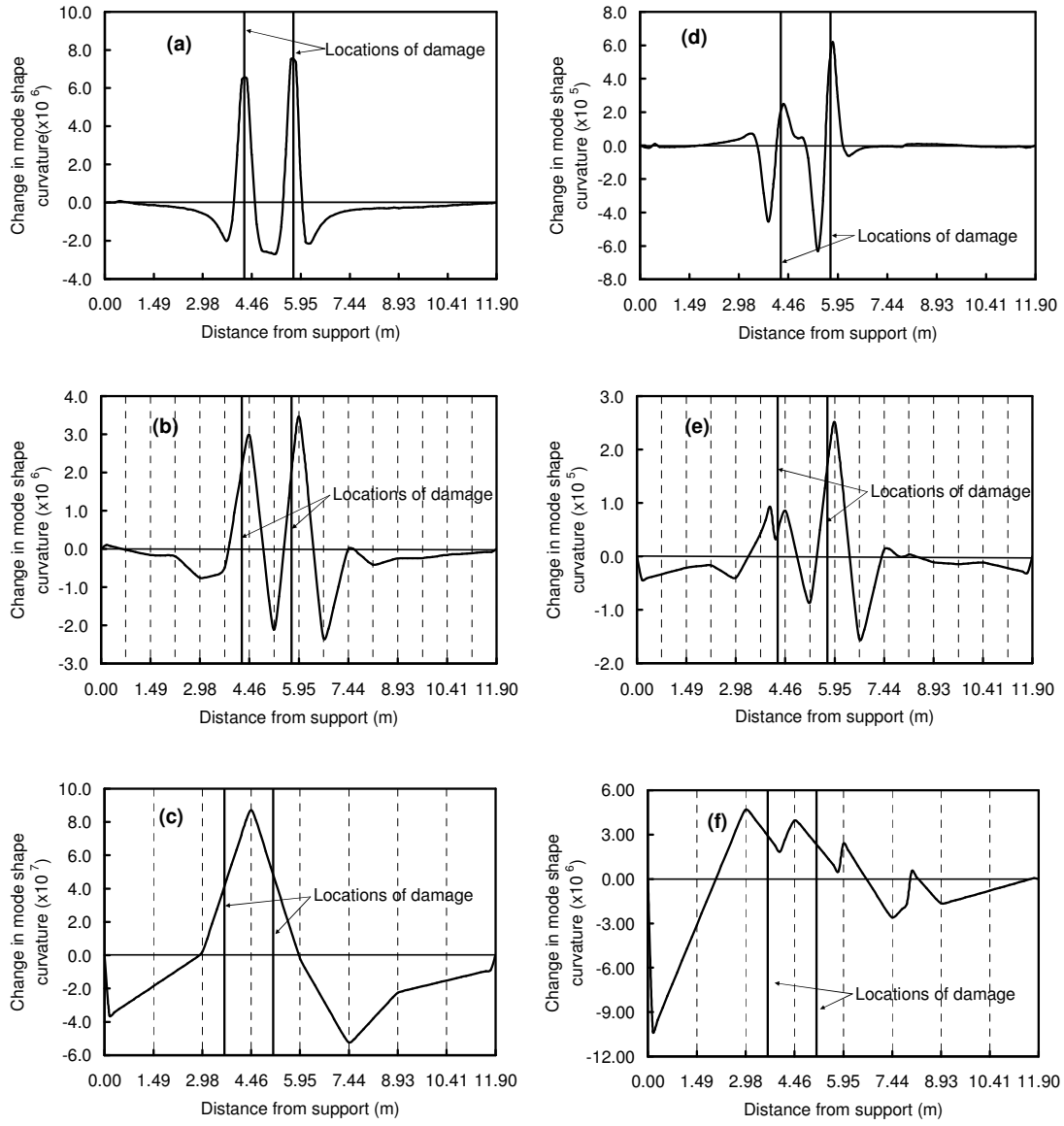

Figure 6.8. Variation of change in mode shape curvature along girder for different damage states by first mode using a) 79, b) 15, and c) 7 FE simulated measurement points; and by the first three modes using d) 79, e) 15, and f) 7 FE simulated measurement points.

reduced the clarity of the predicted damage locations. As shown in Figs. 6.8(b) and 6.8(e), corresponding to the use of 15 measurement points, two upward peaks were produced using the first mode only, while three upward peaks resulted when three

modes were used, making it difficult to determine whether three or two damage states occurred.

In Figs. 6.8(c) and 6.8(f), the results using only 7 measurement points are plotted. The vertical grid lines indicate the locations of measurement points. It should be noted that, in order to show the worst case of damage detection when three modes and 7 measurement points were used, the two damage states in the pair were located 3.64 m and 5.13 m from support, making them different from the damage cases in Figs. 6.8(a), (b), (d) and (f). As seen in Fig. 6.8(c), when only the first mode was used, only one upward peak occurred since the distance between the two damage states was very small relative to the spacing between measurement points. By contrast, Fig. 6.8(f) shows that the use of the first three modes resulted in four upward peaks, although only two damage states actually existed. Therefore, using higher modes to detect damage did not necessarily improve the ability of the change in mode shape curvature method to locate multiple damage states as compared to using only the fundamental mode, regardless of how many measurement points were used.

The correlations between predicted and actual damage locations calculated by the damage index method using the first mode and the first three modes are plotted in Fig. 6.9. Fig. 6.9(a), corresponding to 79 measurement points, shows that very well-defined mode shapes allowed damage to be located with great accuracy using this method, even when the damage was located relatively close to a support. This result indicates that the damage index method is capable of detecting and locating multiple instances of small-scale damage with a high degree of precision if the fundamental mode shape is accurately defined.

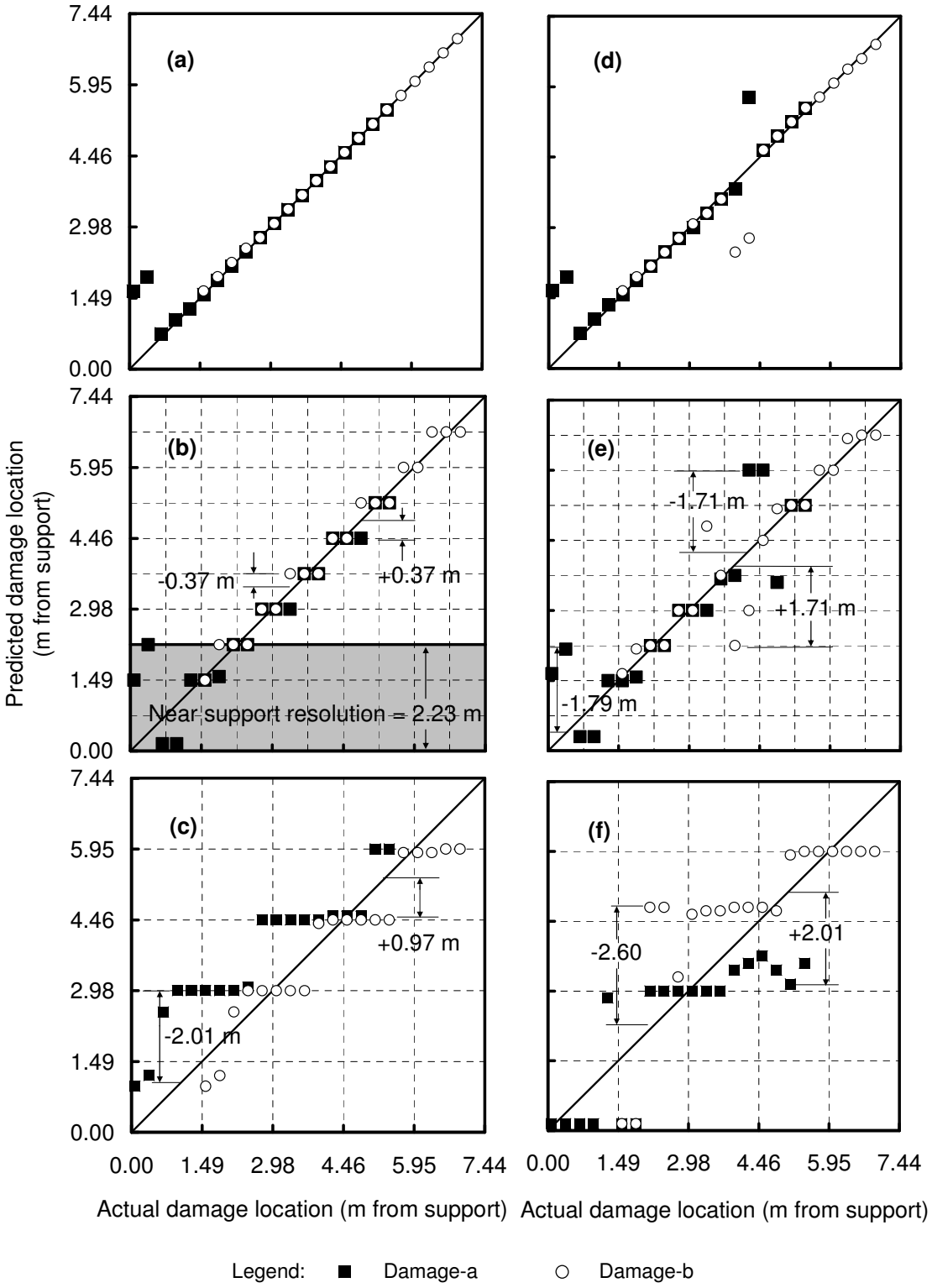

Figure 6.9. Correlation between predicted and actual longitudinal location of damage calculated by the damage index method and the first mode using a) 79, b) 15, and c) 7 FE simulated measurement points; and by the first three modes using d) 79, e) 15, and f) 7 FE simulated measurement points.

As seen in Figs. 6.9(d) and 6.9(e), when the first three modes were used, the predicted damage location featured large errors when the damage was located about 4 metres from the support, even when a large number of measurement points were used. An examination of Fig. 6.10(a) and Fig. 6.10(b) can be used to explain this phenomenon.

Fig. 6.10(a) and Fig. 6.10(b) show distributions of the damage index calculated using 79 and 15 measurement points, respectively, when damage states were located 2.75 m and 4.24 m from the support. When only the fundamental mode shape was used, two upward peaks occurred in each figure. When the first three modes were used, however, only one upward peak occurred in each figure, regardless of the number of measurement points. Because the nodal point of the third mode was located 4 metres from the support, the change of mode shape curvature of the third mode therefore was almost zero at this location, meaning that no upward peak occurred at that location. It reflected the instability of the index when the reference modal strain energy is close to zero in a given region (Kim and Stubbs 2003). It has to be noted that the weight of a higher mode is much larger than that of a lower mode for the damage index method, since higher modes have higher overall strain energy levels (see Eq. 2.16), which means that the third mode played the key role in the damage index method in this case.

In Fig. 6.10(c), seven measurement points were used to detect two damage states which were located 0.67 m and 2.16 m from support, respectively. When the first three modes were used, the two upward peaks appeared at 0.15 m and 4.8 m from the support, respectively. Compared to use of the first mode only, therefore, using higher modes to detect damage did not improve the accuracy of damage detection when a small number of measurement points were used because higher mode shapes could not be well defined by a small number of measurement points.

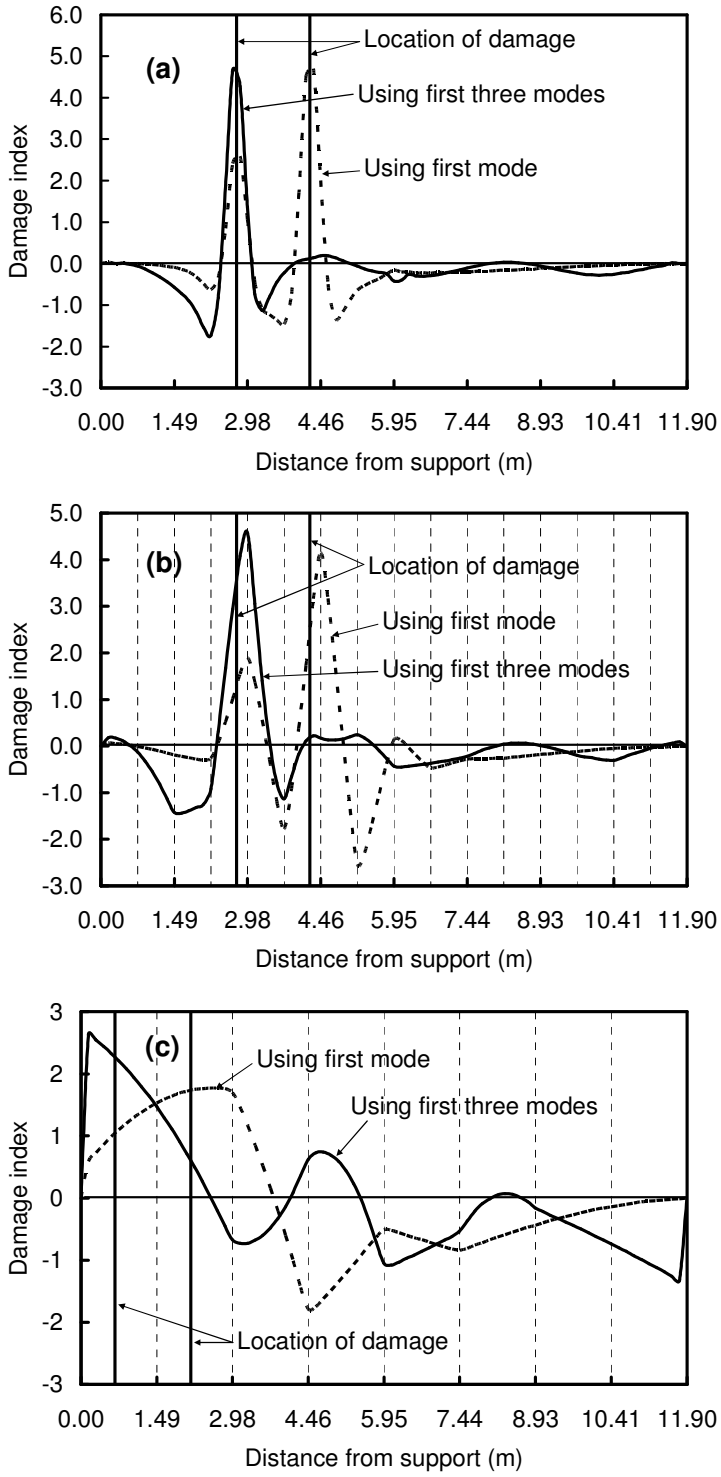

Figure 6.10. Variation of damage index along girder for different damage states using a) 79, b) 15, and c) 7 FE simulated measurement points.

The correlations between predicted and actual damage locations calculated using the change in uniform flexibility curvature method with only the first mode and the first three modes are plotted in Fig. 6.11. For this method, it was found that using only the first mode and using the first three modes produced identical results no matter how many measurement points were used. This result may be attributed to the fact that the relative weight of higher modes is much smaller than that of lower modes because the flexibility of each mode is divided by the square of its natural frequency to calculate the uniform flexibility curvature. It is also evident in comparing Figs. 6.7(a), (b), and (c) with Figs. 6.11(a), (b), and (c) that the change in mode shape curvature method and the change in uniform flexibility curvature method generated identical results when only the first mode was used to detect damage.

In addition, the change in mode shape curvature, damage index and change in uniform flexibility curvature methods showed a pronounced tendency to predict damage to be located exactly at a measurement point as shown in Fig. 6.7, Fig. 6.9 and Fig. 6.11. The reason for this tendency when the mode shape curvature method was used was discussed earlier; it is related to the use of cubic polynomials to interpolate mode shapes between measurement points, which leads to piecewise linear distributions of curvature. The reliance of the damage index and change in uniform flexibility curvature methods on different forms of mode shape curvature must be responsible for a similar tendency with these two methods. Given this tendency, the best that can be expected from these methods is a maximum error of not less than half the spacing between measurement points. In addition, the maximum error typically occurs when damage is located furthest from measurement points. Conversely, when damage is located near a measurement point, the accuracy is very high, regardless of the number of measurement points.

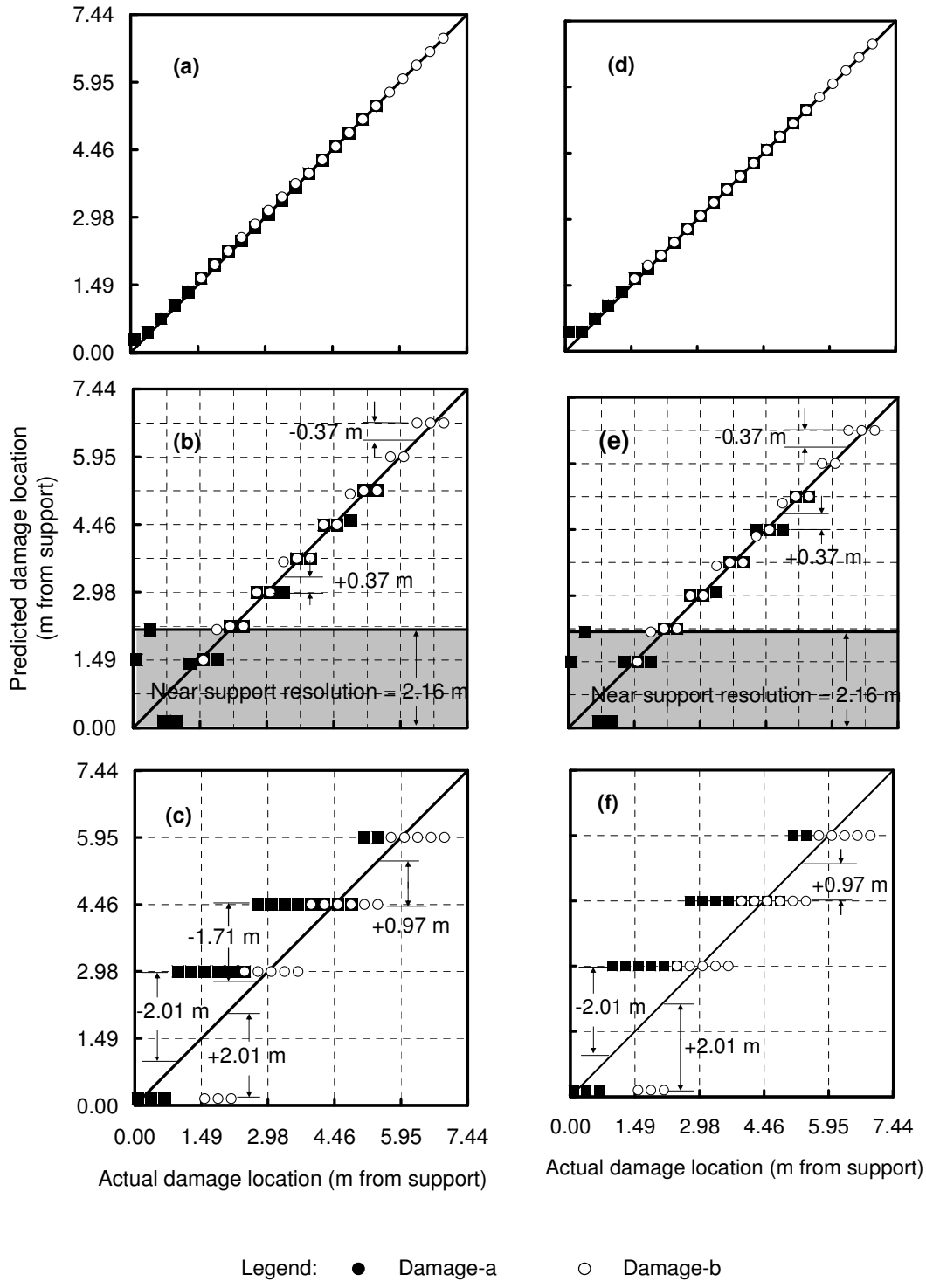

Figure 6.11. Correlation between predicted and actual longitudinal location of damage calculated by the change in uniform flexibility curvature method and the first mode using a) 79, b) 15, and c) 7 FE simulated measurement points; and by the first three modes using d) 79, e) 15, and f) 7 FE simulated measurement points.

The resolution of a damage locating procedure was defined in Section 4.3.2. It should be noted, however, that for multiple damage detection, the resolution is defined as the worst of the two in the damage pairs.

Employing this definition, Fig. 6.12 shows the damage locating resolutions achieved using all the VBDD techniques investigated, normalized by the spacing between measurement points, h. The focus of the discussion is on the performance using only the fundamental mode (indicated by solid bars); shaded bars correspond to the use of three flexural modes. It is observed that the performance of these five techniques was significantly different, with resolutions varying between 1.0h and 3.8h when 15 measurement points and only the fundamental mode were used. The mode shape curvature, damage index, and change in uniform flexibility curvature methods performed the best using 15 measurement points, achieving resolutions of 1.0h. The change in mode shape method, on the other hand, performed the best using 7 measurement points, achieving a resolution of 1.7h. For the mode shape curvature, change in uniform flexibility curvature and damage index methods, when only the first mode was used, an increase in the number of measurement points led to a more than proportional improvement in resolution (in absolute terms). An improvement in relative resolution was also achieved with an increase in the number of measurement points. However, for the change in mode shape method and the change in flexibility method, the resolution in relative terms was much better when 7 measurement points were used. In absolute terms, a decline in resolution of only 0.07 m was observed when the number of measurement points decreased from 15 to 7 for the change in flexibility method, while for the change in mode shape method, surprisingly, an improvement in resolution of 0.29 m was achieved when the number of measurement points was decreased.

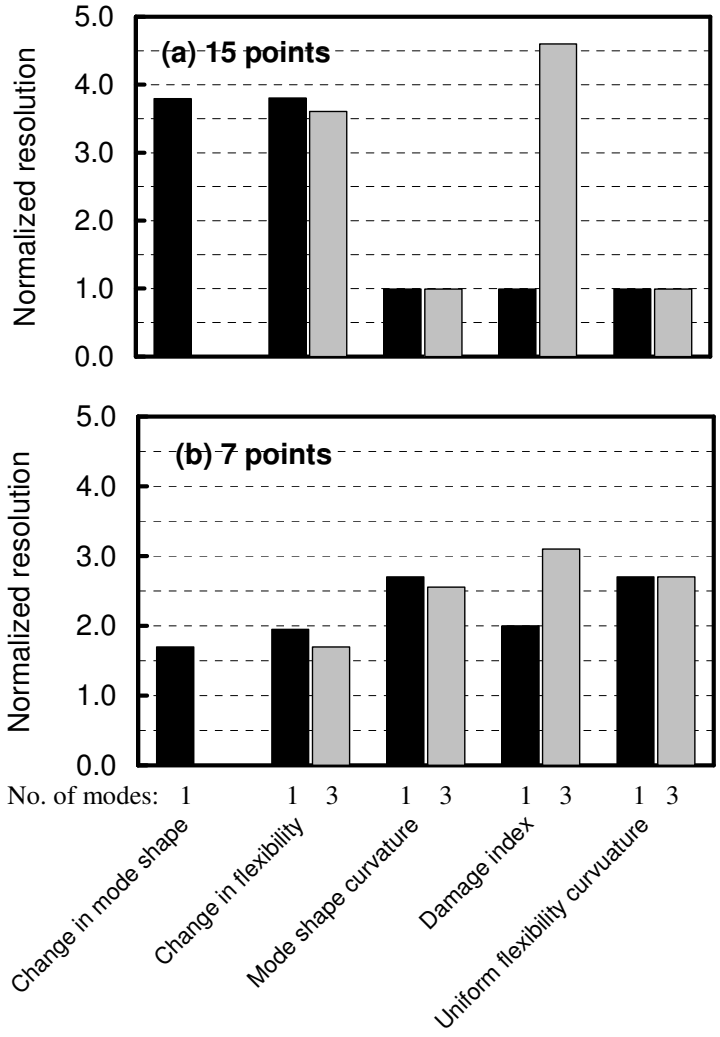

Figure 6.12. FE derived damage localization resolutions, normalized by the spacing between measurement points, using a) 15 and b) seven measurement points.

In general, the use of three modes did not improve the performance of these techniques significantly. The poor performance of the damage index method when three modes were used is a reflection of the instability of the index when the reference modal strain energy is close to zero in a given region (Kim and Stubbs 2003).

Comparing Figs. 6.12(a) and (b) with Figs. 5.13(a) and (b), it was found for the change in mode shape and change in flexibility methods that the accuracy of multiple

damage detection was much worse than that of single damage detection, regardless of the number of measurement points or the number of modes used. For the change in mode shape curvature, damage index and change in uniform flexibility curvature methods, the accuracy of multiple damage detection was also much worse than that of single damage detection when 7 measurement points were used, and slightly worse than that of single damage detection when 15 measurement points were used.

The near-support resolutions were only calculated for the change in mode shape curvature method (Figs. 6.7(b) and 6.7(e)), the damage index method (Fig. 6.9(b)), and the change in uniform flexibility curvature method (Figs. 6.11(b) and 6.11(e)) when 15 measurement points were used. The near support resolutions for the mode shape curvature and change in uniform flexibility methods were 2.16 m (2.9h relative resolution) when 15 measurement points were used. The near support resolution for the damage index method was 2.23 m (3.0h relative resolution) when 15 measurement points and the first mode were used. These near-support resolutions were therefore much worse than those for corresponding single damage detection (1.1h to 1.3h in Fig. 5.13(c)).

No near-support resolution was calculated for the mode shape curvature method (Figs. 6.7(c) and 6.7(f)), the damage index method (Figs. 6.9(c) and 6.9(f)), and the change in uniform flexibility curvature method (Figs. 6.11(c) and 6.11(f)) when 7 measurement points were used based on one or three modes, and the damage index method (Fig. 6.9(e)) when 15 measurement points and the first three modes were used. For these cases, the maximum errors of predicted locations of the damage states located near the support were not significantly larger (even smaller in Figs. 6.7(f) and 6.9(f)) than those of damage states located far away from the support. It was therefore difficult

to determine the dividing line between near-support region and non-near support region. As a result, one common resolution was calculated for all the regions of the girder.

In general, the accuracy of multiple damage detection was much worse than that of single damage detection, regardless of whether the damage was located near the support or not. However, a damage localization resolution of one to two times measurement points spacing may still prove useful in many cases.

6.2.2.4 Investigation B---influence of the spacing two damage states

As described previously, Investigation B was undertaken to investigate the influence of the distance between two separated damage states on the accuracy of the predicted damage locations.

The distributions of each of the five VBDD parameters calculated using the fundamental mode shapes defined by 7, 15 and 79 measurement points were previously shown in Fig. 6.3. In that case, the two damage states were located close to each other. In contrast, Fig. 6.13 shows representative distributions when two damage states were located relatively far away from each other. In this case, the damage states were located 1.12 m and 5.58 m from the support, respectively. In other words, one damage state was located near the support, while another was near mid-span.

In Fig. 6.13(a), the two predicted locations of damage are clearly indicated by two distinct peaks by the change in mode shape method, no matter how many measurement points were used. As seen, both the clarity of peaks and the accuracy of the predicted damage locations improved as the number of measurement points increased.

However, only one upward peak appears in Fig. 6.13(c), such that the presence of one of the damage states could not be determined by the change in flexibility method, even when 79 measurement points were used. This result suggests that the change in

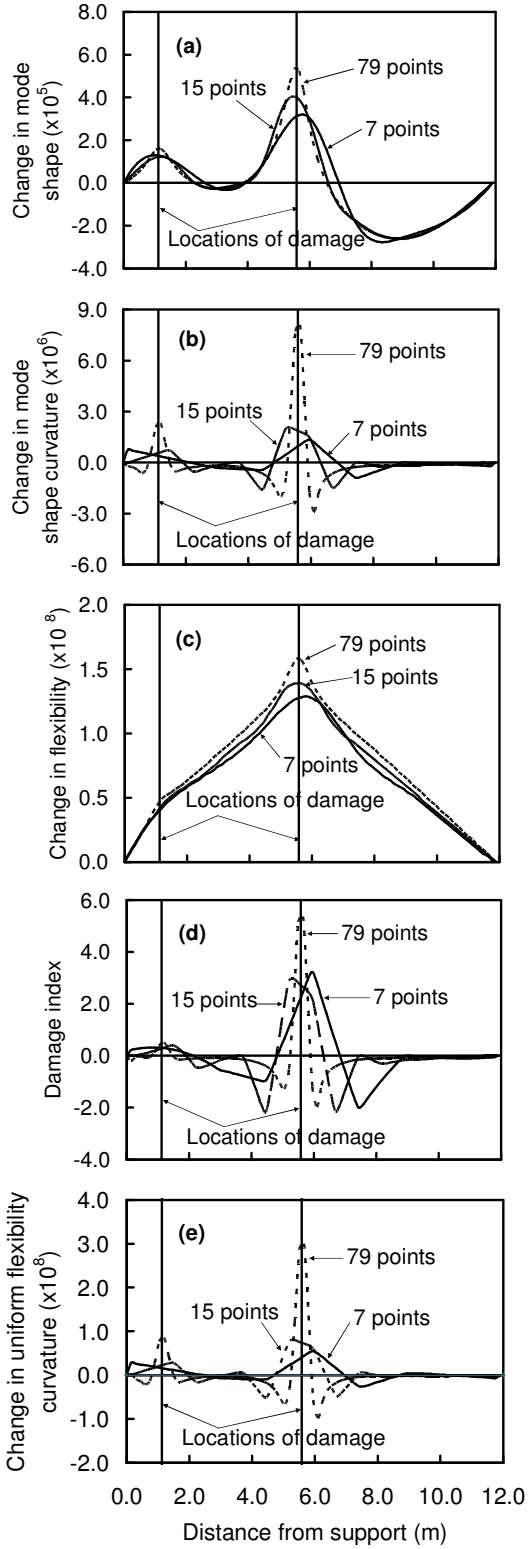

Figure 6.13. The influence of the number of measurement points on the accuracy of predicted longitudinal location of two damage states located 1.12 m and 5.58 m from the support by five VBDD methods.

flexibility method may not be suitable for multiple damage detection, especially when one damage state is close to a support, and another damage state is closer to mid-span.

The change in mode shape curvature method (Fig. 6.13(b)) and the change in uniform flexibility curvature method (Fig. 6.13(e)) produced identical results. When 79 measurement points were used, the locations of both damage states were predicted clearly and accurately. When 15 measurement points were used, the two damage states were identified 1.49 m and 5.21 m from the support, respectively, at the location of measurement points nearest to the two damage states. When 7 measurement points were used, the two damage states were predicted to lie 0.149 m and 5.95 m from the support, respectively, the second location corresponding to the measurement point nearest to the actual damage state. As seen in the figures, the clarity of the peak near the support decreased when the number of measurement points decreased.

The damage index method (Fig. 6.13(d)) produced results similar to the last two mentioned, but the clarity of the small upward peak near the support was diminished compared to those in Fig. 6.13(b) and Fig. 6.13(e). When only 7 measurement points were used, only one upward peak was produced near mid-span, and the damage state near the support could not be identified.

It is clear from Fig. 6.13 that when one of a pair of damage states was located near the support and another was located near mid-span, the former was much more difficult than the latter to be identified because the value of the upward peak near the support was much smaller than that of the upward peak near mid-span. The change in flexibility method exhibited the worst performance among all of the five VBDD methods investigated in this case.

The correlations between predicted and actual damage locations for all 22 pairs of longitudinally varying damage cases, as calculated using the change in mode shape method, are plotted in Fig. 6.14. The horizontal axis indicates the actual location of damage, while the vertical axis indicates the predicted location in these plots. For reference, the gridlines in Fig. 6.14(b) and (c) indicate the locations of measurement points. The solid and open circles indicate damage-a and damage-b, respectively, corresponding to the locations shown in Fig. 6.1(b).

When 79 measurement points were used (Fig. 6.14(a)), damage-1a, damage-1b, damage-2a, and damage-2b all had the same predicted locations. Therefore, damage-1a could not be distinguished from damage-1b, and damage-2a could not be distinguished from damage-2a since the damage states in each pair were located very close to each other. Damage-3a and damage-3b had different predicted locations; they were distinguished successfully using 79 measurement points. Thus, the minimum spacing between damage states that could be distinguished was 0.89 metres in these trials.

In addition, when damage was located very close to a support (damage-21a and damage-22a), there was only one peak near the second damage state (damage-21b and damage-22b, respectively). On the other hand, damage-20a, located 0.37 m from the support, could be distinguished from damage-20b. This suggests that very well-defined mode shapes allowed damage to be located with great accuracy using this method, provided the damage was located more than 0.37 metres from the support and the distance between the two separated damage states was not less than 0.89 metres.

Figs. 6.14(b) and 6.14(c) represent results when 15 and 7 measurement points were used to detect damage, respectively.

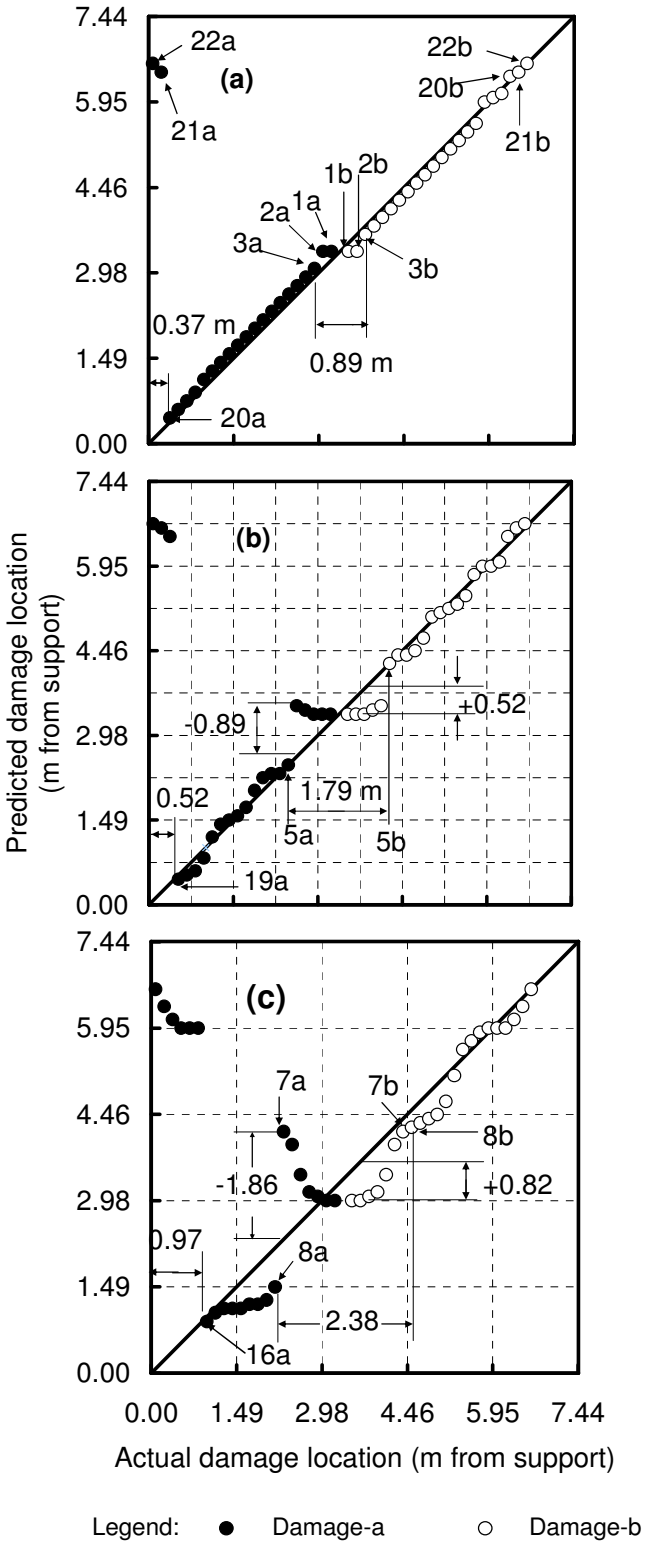

Figure 6.14. Correlation between predicted and actual longitudinal location of damage calculated by the change in mode shape method using a) 79, b) 15, and c) 7 FE simulated measurement points.

Similar results for the change in flexibility, the change in mode shape curvature, the damage index, and the change in uniform flexibility curvature methods are presented in Figs. 6.15, 6.16, 6.18, and 6.20, respectively. Tables 6.3, 6.4, and 6.5 show the resolutions of predicted damage location, the minimum distance between two damage states that could be clearly distinguished, and the minimum distance between damage and the support that the damage could be located accurately using the five VBDD methods when 15 and 7 measurement points were used, respectively.

For the change in mode shape method, as the number of measurement points decreased, the accuracy in the worst predicted location of the two damage states also decreased. Specifically, the resolution of predicted damage location was approximately proportional with the sensor spacing, while the resolution expressed relative to the sensor spacing remained approximately constant. Also, as the number of measurement points decreased, the minimum distance between two damage states that could be clearly distinguished, and the minimum distance between damage and the support that the damage could be located accurately increased.

Table 6.3. The resolution of the predicted longitudinal damage location using five VBDD methods in Figs.6.14, 6.15, 6.16, 6.18, and 6.20.

		Fig.6.14		*Fig.6.15*		*Fig.6.16*		*Fig.6.18*		*Fig.6.20*	
		A*	R**	*A*	*R*	*A*	*R*	*A*	*R*	*A*	*R*
15 points	1st mode	1.41	1.9	1.79	2.41	1.34	1.80	1.34	1.80	1.34	1.80
	3 modes	N/A	N/A	1.71	2.30	1.34	1.80	3.57	2.70	1.34	1.80
7 points	1st mode	2.68	1.8	2.76	1.86	2.98	2.00	3.57	2.40	2.98	2.00
	3 modes	N/A	N/A	3.05	2.05	2.88	1.94	3.05	2.05	2.98	2.00

Note: * "A" indicates absolute resolution (m)
** "R" indicates resolution normalized to sensor spacing *h*

Table 6.4. The minimum distance between two damage states that could be distinguished using five VBDD methods in Figs.6.14, 6.15, 6.16, 6.18, and 6.20.

		Fig.6.14		*Fig.6.15*		*Fig.6.16*		*Fig.6.18*		*Fig.6.20*	
		A*	R**	*A*	*R*	*A*	*R*	*A*	*R*	*A*	*R*
15 points	1st mode	1.49	2.00	1.79	2.41	1.49	2.00	1.19	1.60	1.49	2.00
	3 modes	N/A	N/A	1.79	2.41	1.49	2.00	2.68	2.70	1.49	2.00
7 points	1st mode	2.38	1.60	2.98	2.00	2.08	1.40	2.68	1.80	2.08	1.40
	3 modes	N/A	N/A	2.98	2.00	2.38	1.60	0.30	0.20	2.08	1.40

Note: * "A" indicates absolute minimum distance (m)
** "R" indicates minimum distance normalized to sensor spacing *h*

Table 6.5. The minimum distance between damage and the support that the damage could be located accurately using five VBDD methods in Figs.6.14, 6.15, 6.16, 6.18, and 6.20.

		Fig.6.14		*Fig.6.15*		*Fig.6.16*		*Fig.6.18*		*Fig.6.20*	
		A*	R**	*A*	*R*	*A*	*R*	*A*	*R*	*A*	*R*
15 points	1st mode	0.52	0.70	1.26	1.69	0.37	0.50	1.12	1.51	0.37	0.50
	3 modes	N/A	N/A	1.26	1.69	0.37	0.50	0.52	0.70	0.37	0.50
7 points	1st mode	0.97	0.65	1.26	0.85	0.97	0.65	1.26	0.85	0.97	0.65
	3 modes	N/A	N/A	1.26	0.85	0.52	0.35	0.52	0.35	0.97	0.65

Note: * "A" indicates absolute minimum distance (m)
** "R" indicates minimum distance normalized to sensor spacing *h*

The correlations between predicted and actual damage locations for all 22 pairs of longitudinally varying damage cases, as calculated using the change in flexibility method and when only the first mode and the first three modes were used, are plotted in Fig. 6.15. The solid and open circles indicate damage-a and damage-b, respectively. The grey circles also indicate damage-a, but identify cases for which the detection

results were ambiguous. Fig. 6.13c shows an example of an ambiguous result, since the upward peak is not obvious for the damage state nearest the support.

In Fig. 6.15, the resolutions of predicted damage location were improved as the number of measurement points increased when the damage was not located near the support. However, using higher modes did not necessarily improve the accuracy of the predicted damage location. In addition, Figs. 6.15(a) and (b) indicate that even when mode shapes were well-defined, the change in flexibility method did not clearly indicate the second damage state.

The correlations between predicted and actual damage locations calculated using the change in mode shape curvature method using only the first mode and also the first three modes, are plotted in Fig. 6.16. Fig. 6.1(a), corresponding to 79 measurement points using only the fundamental mode, shows that very well-defined mode shapes allowed damage to be located with great accuracy using this method, even when the damage was located near the support. The minimum distance between two separated damage states that could be distinguished was found to be 0.60 m. These results indicate that this technique is capable of detecting and locating small-scale damage with a high degree of precision if fundamental mode shapes can be defined accurately.

The resolutions of predicted damage localization when 15 and 7 measurement points (Figs. 6.16(b), (c), (e), and (f)) were used were listed in Table 6.3. It was observed that using higher modes improved the accuracy in the predicted damage location only slightly. In contrast, using a larger number of measurement points consistently improved the accuracy significantly.

In Fig. 6.17, results using the first and the first three modes to detect damage by the change in mode shape curvature method using 7 measurement points are compared. The

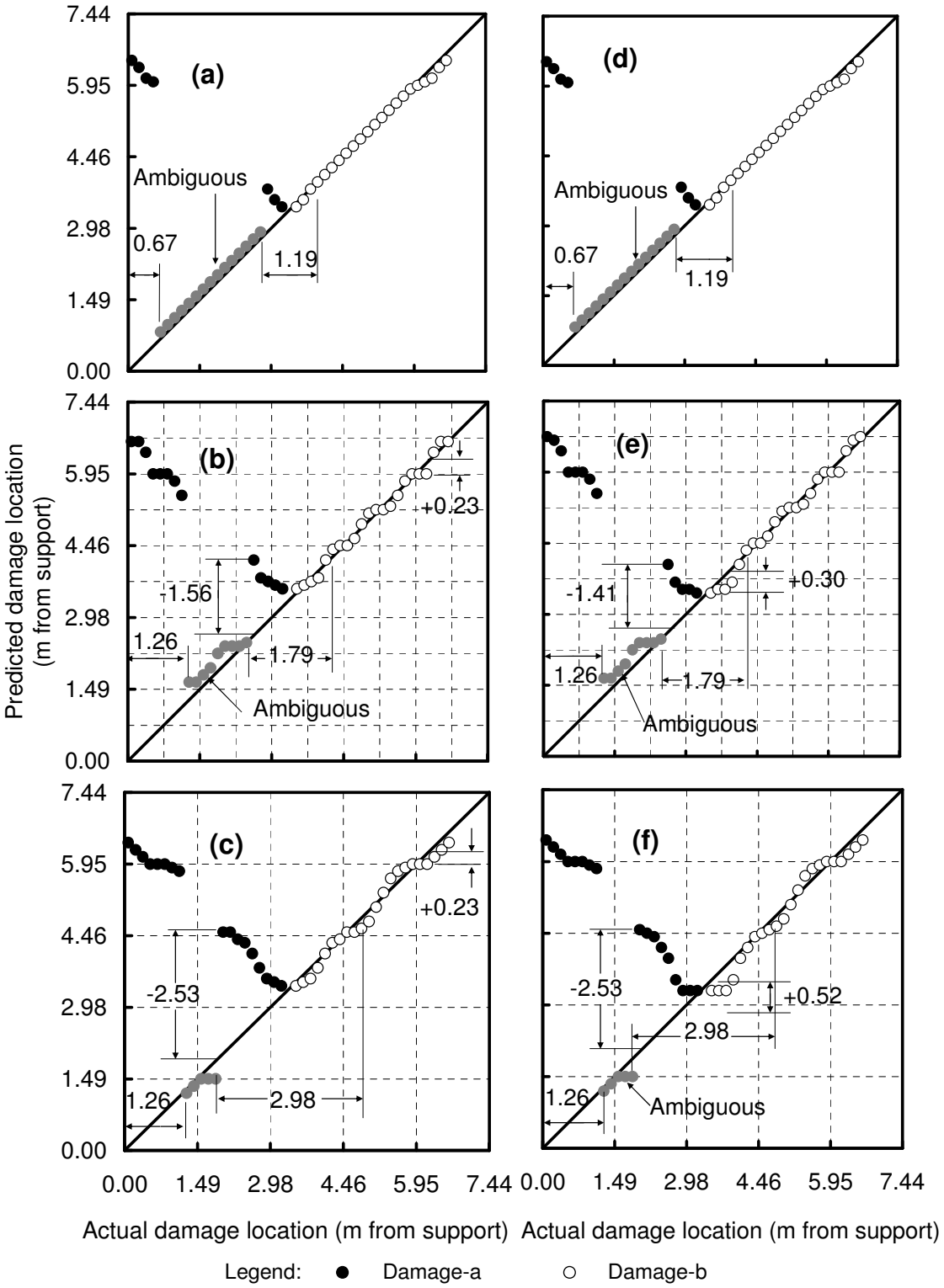

Figure 6.15. Correlation between predicted and actual longitudinal location of damage calculated by the change in flexibility method and the first mode using a) 79, b) 15, and c) 7 FE simulated measurement points; and by the first three modes using d) 79, e) 15, and f) 7 FE simulated measurement points.

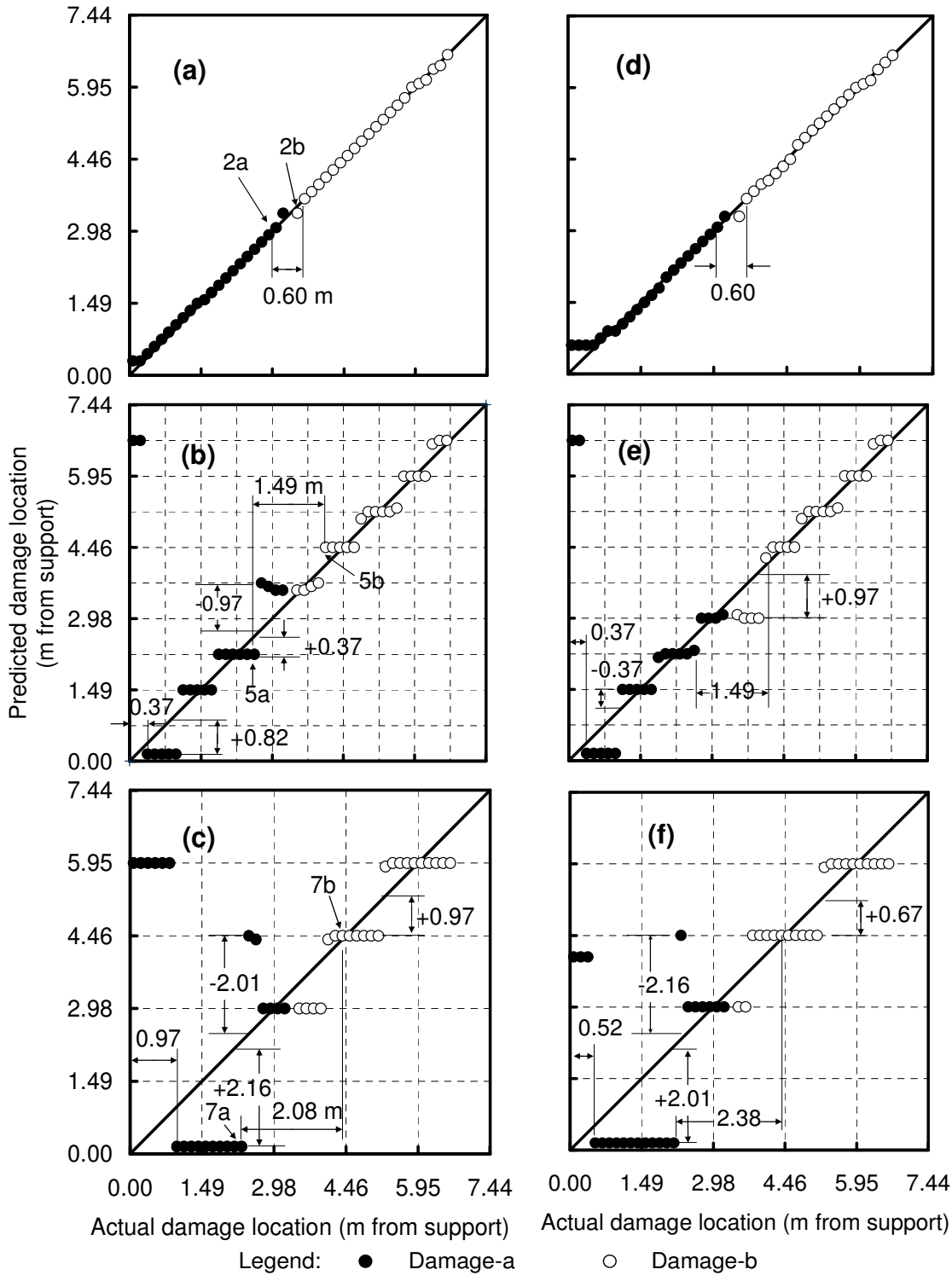

Figure 6.16. Correlation between predicted and actual longitudinal location of damage calculated by the change in mode shape curvature method and the first mode using a) 79, b) 15, and c) 7 FE simulated measurement points; and by the first three modes using d) 79, e) 15, and f) 7 FE simulated measurement points.

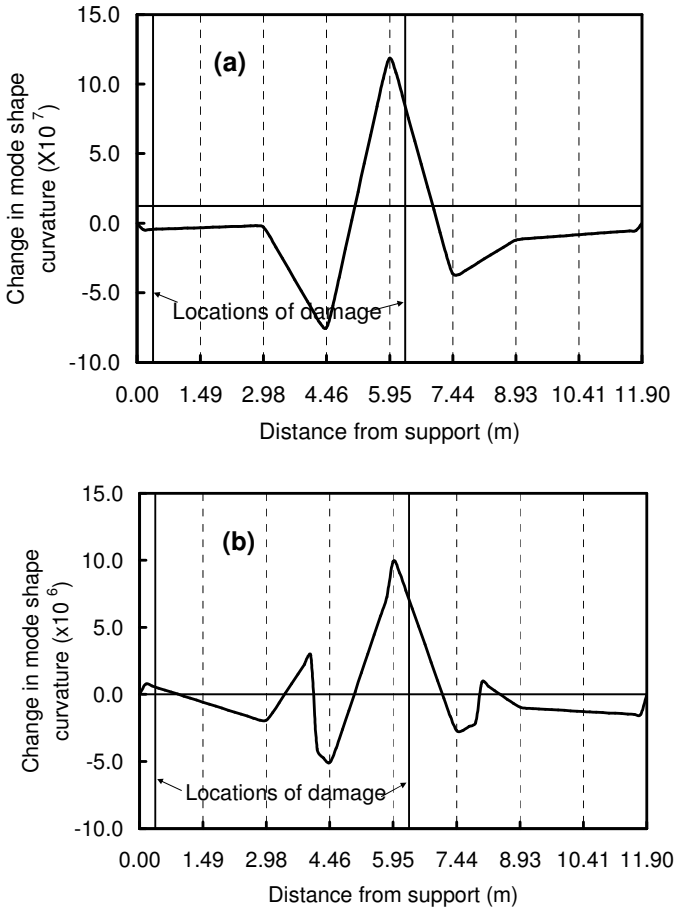

Figure 6.17. Variation of change in mode shape curvature along girder for damage states located 0.37 m and 6.32 m from the support by a) the first mode and b) the first three modes using seven FE simulated measurement points.

two damage states were located 0.37 m and 6.32 m from support, respectively. When only the first mode was used (Fig. 6.17(a)), only one damage location was predicted near mid span; the other damage state near the support was not identified. The plot in Fig. 6.17(b), produced using the first three modes, had four upward peaks, making it impossible to determine the true number and locations of damage states. Therefore, using higher modes to detect damage was not necessary better than using only the fundamental mode for the change in mode shape curvature method.

Correlations between predicted and actual damage locations calculated by the damage index method, using only the first mode and the first three modes, are plotted in Fig. 5.18. Fig.5.18a, corresponding to 79 measurement points, shows that very well-defined fundamental mode shapes allowed damage to be located with great accuracy using this method, except when the damage was located very near a support. It indicates that this technique is capable of detecting and locating small-scale damage with a high degree of precision if fundamental mode shapes can be defined accurately.

As seen in Figs. 6.18(d) and 6.18(e), when the first three modes were used, the predicted damage location had large errors when the damage was located about 4 metres from the support even when a large number (79) of measurement points were used. An examination of Fig. 6.19 can be used to explain this phenomenon. In Fig. 6.19, 15 measurement points were used to detect the two damage states located 2.60 m and 4.09 m from a support, respectively; however, it is evident that only one upward peak occurred near these locations when the first three modes were used. This may be attributed to the fact that a nodal point of the third mode was located 4 metres from the support; the change of mode shape curvature of the third mode was therefore almost zero around its nodal point, so that no upward peak could occur.

Correlations between the predicted and actual damage locations, calculated using the change in uniform flexibility curvature method, and using only the first mode and the first three modes, are plotted in Fig. 6.20. It was found that using only the first mode and using the first three modes produced identical results no matter how many measurement points were used. This result is attributed to the fact that the weights of higher modes are much smaller than those of lower modes because the flexibility of each mode is divided by the square of its angular natural frequency in this method (see

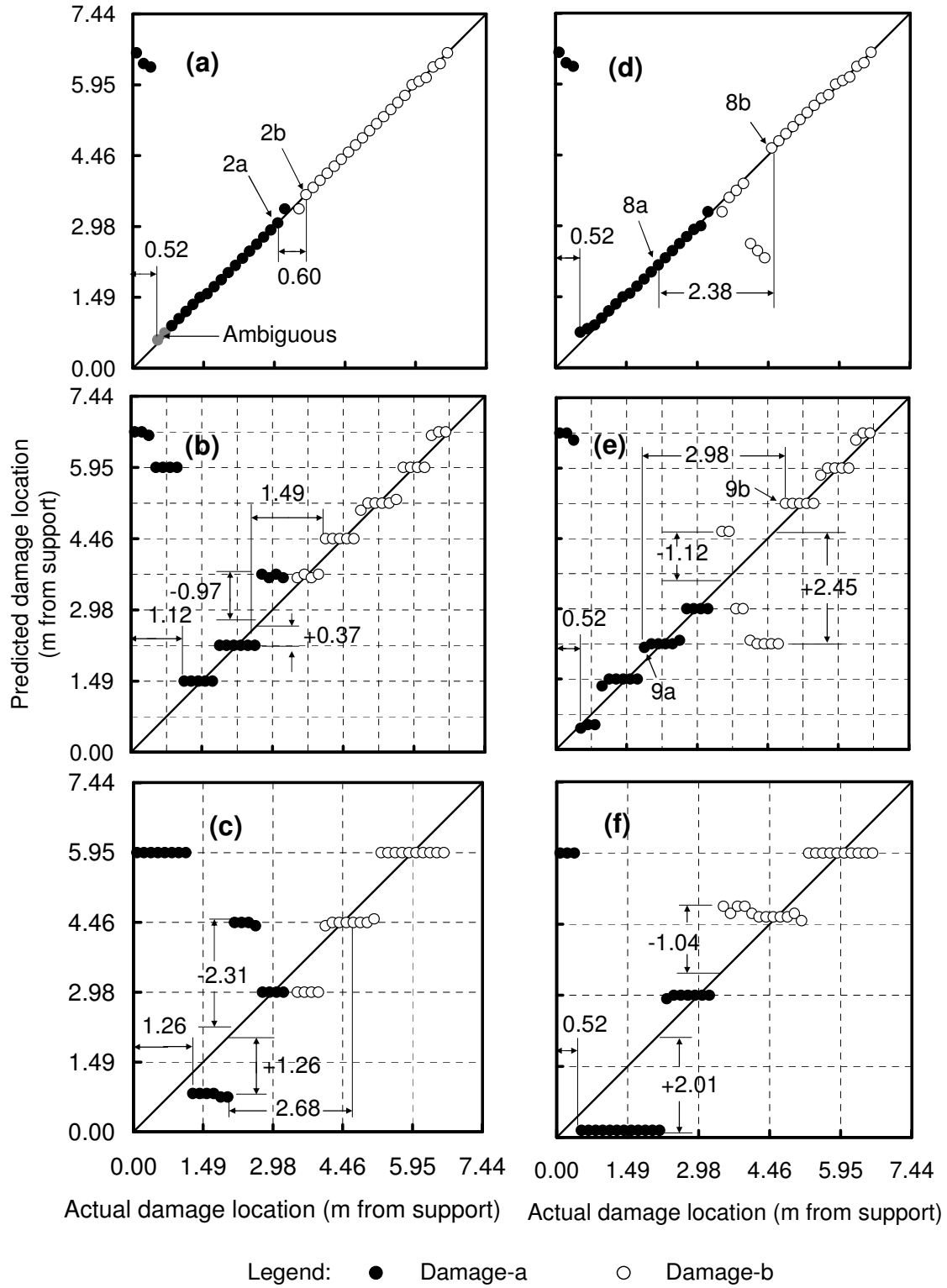

Figure 6.18. Correlation between predicted and actual longitudinal location of damage calculated by the damage index method and the first mode using a) 79, b) 15, and c) 7 FE simulated measurement points; and by the first three modes using d) 79, e) 15, and f) 7 FE simulated measurement points.

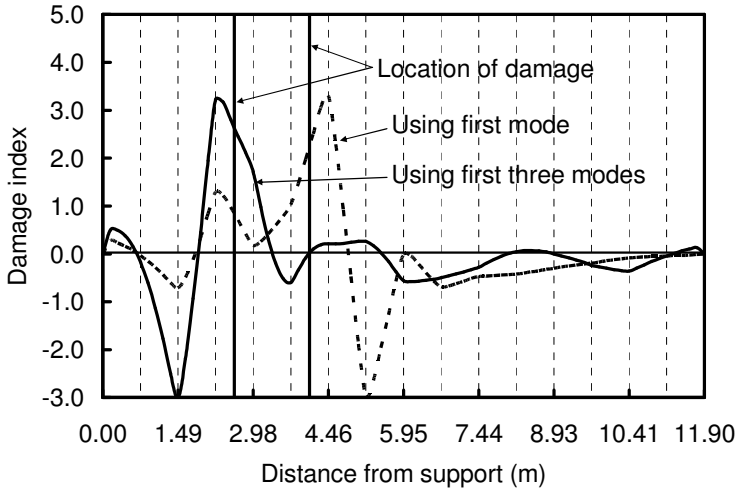

Figure 6.19. Variation of damage index along girder for damage states located 2.60 m and 4.09 m from the support using 15 FE simulated measurement points.

Section 2.2.4). It was also found by comparing Figs. 6.16(a), (b), and (c) with Figs. 6.20(a), (b), and (c) that the change in mode shape curvature method and the change in uniform flexibility curvature method produced identical results when only the first mode was used to detect damage.

As noted previously in the context of single damage detection in Chapter 5 and multiple damage detection using Investigation A, the change in mode shape curvature, damage index and change in uniform flexibility curvature methods all showed a pronounced tendency to predict damage locations at measurement points, as shown in Figs. 6.16, 6.18 and 6.20. Given this tendency, the best that can be expected from these methods is a maximum error of not less than half the spacing between measurement points provided two damage states were not located too close to each other.

Fig. 6.21 shows the damage locating resolutions achieved using all the VBDD techniques investigated, normalized by the spacing between measurement points, h. The

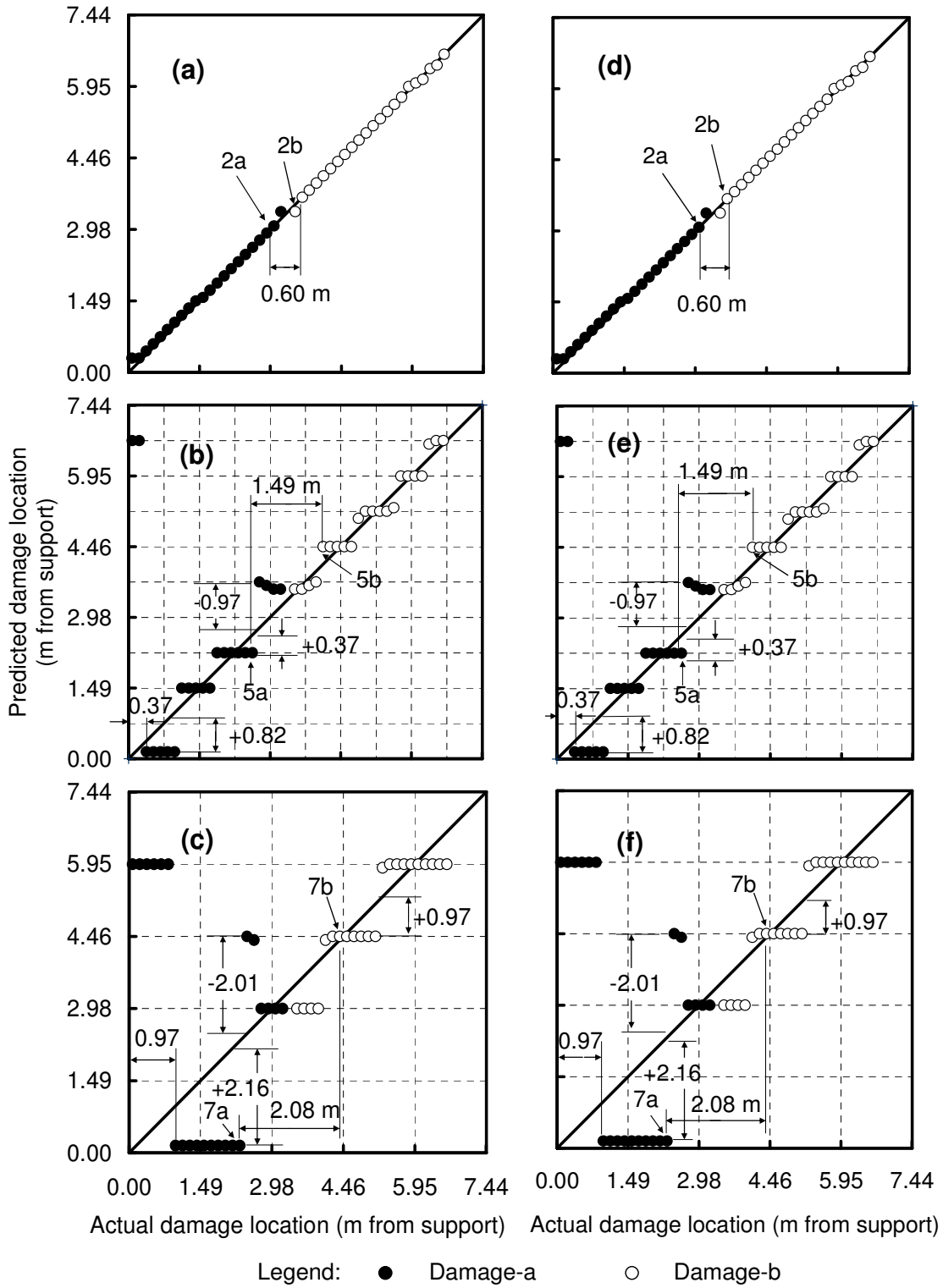

Figure 6.20. Correlation between predicted and actual longitudinal location of damage calculated by the change in uniform flexibility curvature method and the first mode using a) 79, b) 15, and c) 7 FE simulated measurement points; and by the first three modes using d) 79, e) 15, and f) 7 FE simulated measurement points.

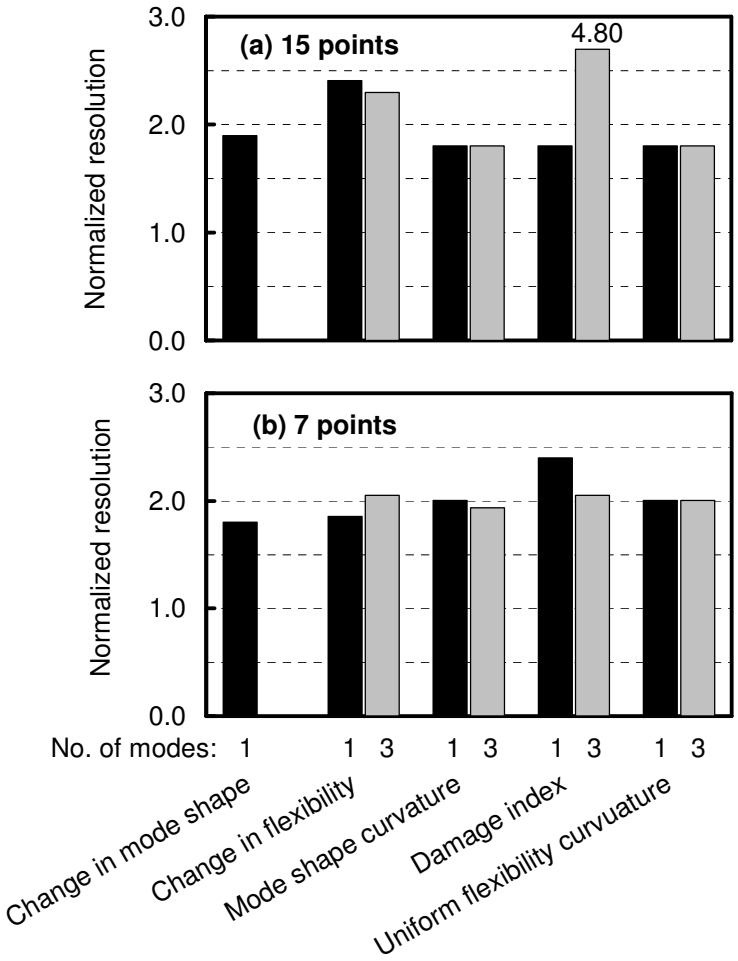

Figure 6.21. FE derived damage localization resolutions, normalized by the spacing between measurement points, using a) 15 and b) seven measurement points.

performance using only the fundamental mode is indicated by solid bars, while shaded bars correspond to the use of three flexural modes. Fig. 6.21 shows that the performance of these five techniques was comparable, achieving resolutions between 1.8*h* and 2.4*h*, the only exception being for the damage index method using the first three modes, for which a resolution of 4.8*h* was observed. In most cases, an increase in the number of measurement points led to a proportional improvement of the resolution. In other words, resolution was approximately a direct function of measurement point spacing, *h*.

The use of three modes did not really improve the performance of these techniques. The poor performance of the damage index method when three modes were used is a reflection of the instability of the index when the reference modal strain energy is close to zero in a given region (Kim and Stubbs 2003).

Thus, in the absence of experimental uncertainty, pairs of small-scale damage states could be detected and located on the simply supported prestressed concrete girder with a longitudinal resolution of approximately double the spacing between seven evenly spaced measurement points, provided it did not occur too near a support. This level of accuracy was much worse than that of single damage detection, for which a resolution of 40% of the spacing between measurement points was achieved. This is because the two separated damage states affected the predicted location of each other when they were located close to each other. Therefore, the detection of multiple damage states is more challenging than single damage state detection.

For the purposes of this discussion, the minimum distinguishable distance is defined as the distance between two damage states such that the two damage states could be distinguished; for separations that are less than this distance, the two damage states could not be distinguished as separate occurrences.

Employing this definition, Fig. 6.22 shows the minimum distinguishable distance achieved using all the VBDD techniques investigated, normalized by the spacing between measurement points, h. The performance of these five techniques was comparable, achieving minimum distinguishable distance between $1.4h$ and $2.4h$ except when the damage index method was employed using the first three modes, for which a value of $3.6h$ and $0.2h$ was achieved when 15 and 7 measurement points were used, respectively. In most cases, an increase in the number of measurement points led to a

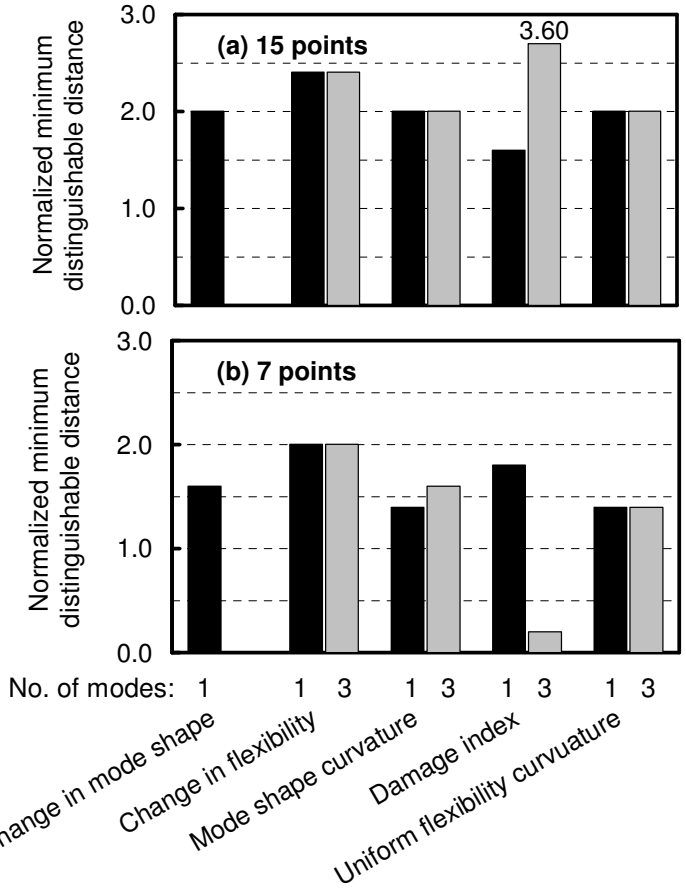

Figure 6.22. FE derived minimum distinguishable distance, normalized by the spacing between measurement points, using a) 15 and b) seven measurement points.

proportional decrease in minimum distinguishable distance. In other words, the minimum distinguishable distance was a direct function of measurement point spacing, *h*. The use of three modes did not really improve the performance of these techniques.

In Figs. 6.14, 6.16, 6.18, and 6.20, when one of a pair of damage states was located near the support and another was located near mid-span, the two damage states could not be distinguished when 15 and 7 measurement points were used. These figures also indicate the minimum distance between a damage state located near a support and that support for which this damage could be located accurately when 15 and 7 measurement points were used. The results of minimum distance of damage from the support for the

five VBDD methods were summarized in Fig. 6.23. The change in flexibility method performed the worst, with minimum detection distances of 1.69*h* and 0.85*h* when 15 and 7 measurement points were used, respectively. The mode shape curvature and change in uniform flexibility curvature methods exhibited the best performance for this case when only the first mode was used, for which a value of 0.5*h* and 0.65*h* was achieved when 15 and 7 measurement points were used, respectively. The mode shape curvature and damage index methods performed best when the first three modes and 7 measurement points were used, for which a value 0.35*h* was achieved. It appears that the use of higher

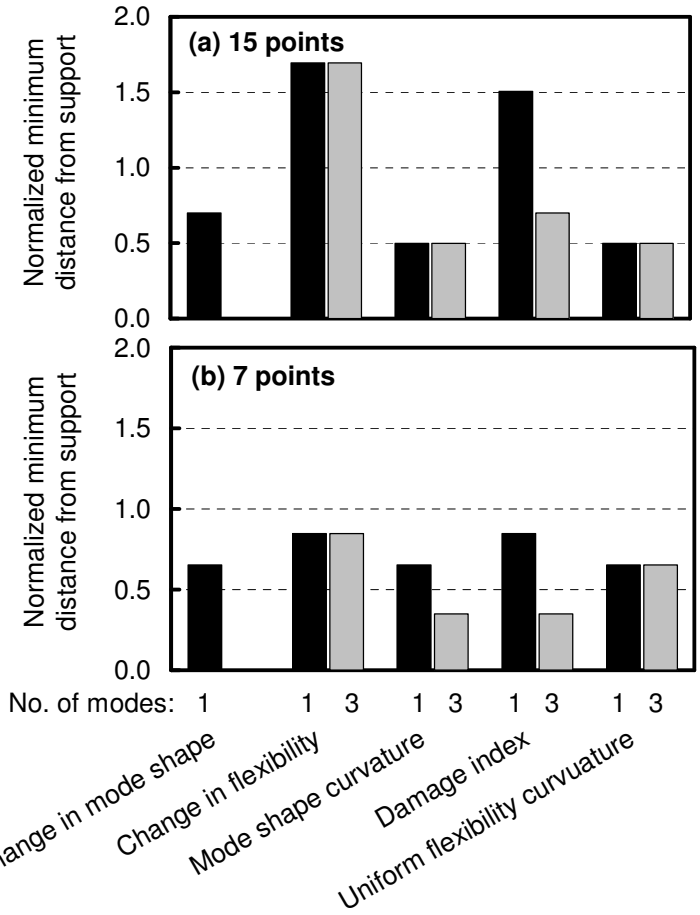

Figure 6.23. FE derived minimum distance of damage from support, normalized by the spacing between measurement points, using a) 15 and b) seven measurement points.

modes improved the performance of the damage index method, and improved the performance of the mode shape curvature method when 7 measurement points were used.

6.3 EXPERIMENTAL STUDY

6.3.1 Description of experimental study

The experimental procedure was described in Chapter 3. For this investigation, damage was induced by removing two separate small square blocks of concrete simultaneously, each 150 x 150 mm in plan and 35 mm deep, from the top surface of the girder, as shown in Fig. 6.24. This was done at sixteen damage locations, indicated in Fig. 6.25, in eight pairs as shown by the labels in the figure (e.g. 1a and 1b, etc.).

The first pair of damage states (1a and 1b) was the easiest to detect because both damage states were located near mid span, and very close to the nearest sensors; in addition, the distance between the pair was about double the spacing between sensors, conforming to the results of the numerical study which indicated that the minimum distinguishable distance between two damage states was about 1.5h when seven evenly spaced sensors were used (Fig. 6.22).

The second pair of damage states (2a and 2b) were designed for the case for which one damage state was located near mid span and another located farther from mid span but not very close to the support.

The third pair of damage states (3a and 3b) was similar to the second pair except with regards to their transverse locations: damage-3a was located on the central line of the girder whereas damage-3b was located at north edge of the girder.

Figure 6.24. Photograph of the damage induced on the surface of the laboratory model.

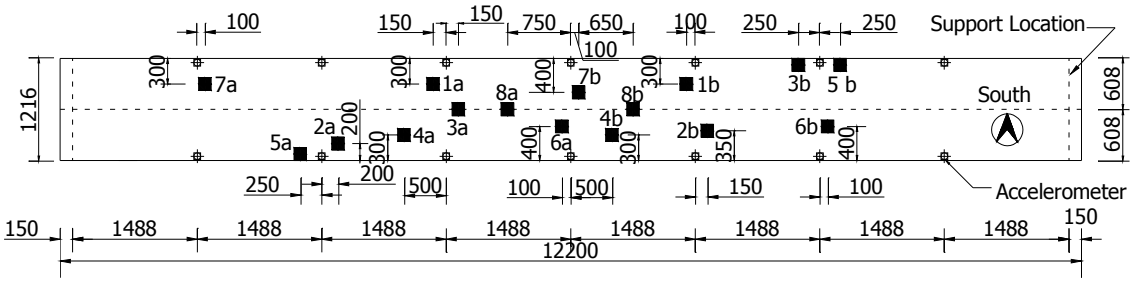

Figure 6.25. Schematic plan of the girder showing locations of damage and sensors (dimensions in mm)

The fourth pair of damage states (4a and 4b) were located farther from the nearest sensors than the first three pairs. This pair was therefore intended to evaluate the influence of the location of damage relative to sensors on the level of difficulty of damage detection and the accuracy of predicted damage location. In addition, the distance between these two damage states was only approximate 1.5*h*, less than those of the first three pairs of damage states, and close to the minimum distinguishable distance between two damage states found in the numerical study.

The fifth pair of damage states was designed to evaluate the capabilities of the five VBDD methods when one damage states was located at north edge of the girder, while the other was located at south edge of the girder.

The sixth pair of damage states differed from the second pair of damage states in that damage 6a was located very close to mid span. As a result, the difference in magnitudes of the change of mode shape (or mode shape curvature) between damage 6a and 6b should have been much larger than that of the second pair of damage states, a fact that would increase the difficulty in identifying both damage states.

The seventh pair of damage states was used to evaluate the minimum distance of damage from the support for which the near support damage could be identified. It was expected that the minimum distance should be much larger than that of numerical study (Fig. 6.23) due to the effect of the measurement uncertainties in the experiment; this result has been demonstrated for single damage detection in Chapter 5.

The eighth and last pair of damage states were located longitudinally farthest from the nearest sensors and closest to each other of all these damage cases.

The set up of the experiment was slightly different from that for the single damage detection study described in Section 5.3.1. In this case, seven measurement points were used along each edge of the girder, as shown in Fig. 6.25, instead of the six measurement points used in single damage detection. It should be noted that the finite element model of the prestressed concrete girder was built after the experiment of single damage detection and before the experiment of multiple damage detection. The use of 80 longitudinal elements between supports in FE model was selected to make the length of each element (148.75 mm) very close the size of damage (150 x 150 mm) in the experiment. Since the numerical study used 79, 15 and 7 measurement points, it was

decided that 7 measurement points should also be used in the experiment of multiple damage detection in order to make the results more comparable with the numerical studies.

Electric foil strain gauges were also used to measure the vibration response of the girder, but failed to detect the damage because of the poor condition of the vertical surface upon which the gauges were mounted, as shown in Fig. 6.26. Therefore, only results using accelerometer data are presented here.

6.3.2 Results and discussion

Fig. 6.27 shows the distributions of all five damage detection parameters, as calculated using accelerometer data, corresponding to the first pair of damage states, located 4.31 m and 7.34 m from the support, respectively. The two highest positive peaks in each plot indicate the predicted longitudinal locations for the two damage states. In these plots, parameters are normalized relative to their maximum values. The damage index parameter would not ordinarily be normalized, since its magnitude is of significance (a threshold value of two is used to indicate damage); however, normalization for this purpose permits the plotting of all parameters on a common scale.

The plots illustrate three features observed more generally when the entire set of results is examined. First, the highest peak and second highest peak occurred at or close to the same locations (7.5 m and 4.5 m from the support, respectively, in this case) for each method. Second, the predicted locations coincided with the locations of accelerometers (indicated by vertical gridlines and defined in Fig. 6.25). Third, the mode shape curvature and change in uniform flexibility curvature methods produced virtually identical distributions in which the parameters varied linearly between measurement points, a feature that resulted from the use of cubic polynomials to

Figure 6.26. The deteriorated vertical surface of the girder near a stain gauge installation.

interpolate mode shape displacements between measurement points. The damage index method, which also makes use of mode shape curvatures (though not as linear functions), produced distributions which were similar to those of the two methods just mentioned, but differed from them by taking on smaller values near the supports.

The correlations between predicted and actual damage locations for all damage cases are shown in Fig. 6.28, in which gridlines correspond to the locations of accelerometers. All techniques are seen to have performed relatively well. The maximum absolute error in the predicted locations found using the mode shape curvature and damage index methods was 0.99 m for damage state 4b, approximately 66% of sensor spacing, if damage state 7a is omitted (for reasons explained below). For the change in mode shape method, the maximum absolute error in predicted damage location was 1.85 m for damage states 4b. For the change in flexibility method, the maximum absolute error was 2.08 m for damage states 3a and 3b.

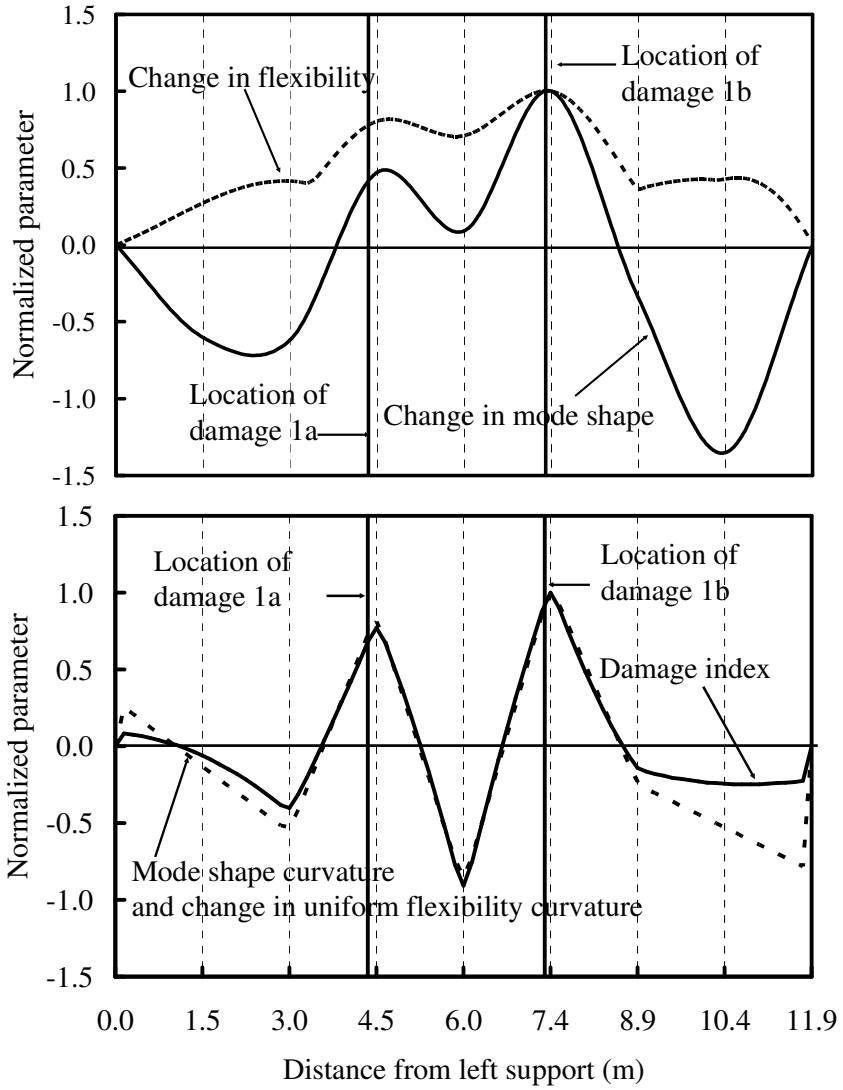

Figure 6.27. Distributions of normalized damage detection parameters, calculated along the south side of the girder for damage case 1a and 1b by five VBDD methods.

The mode shape curvature, change in uniform flexibility curvature and damage index methods produced identical results. These three methods successfully distinguished damage states 4a and 4b (i.e. two distinct peaks occurred), whereas the change in flexibility and change in mode shape methods failed to do so (only a single peak appeared). As a result, for multiple damage state detection, both the mode shape curvature and damage index methods appear to be more robust methods, with the change

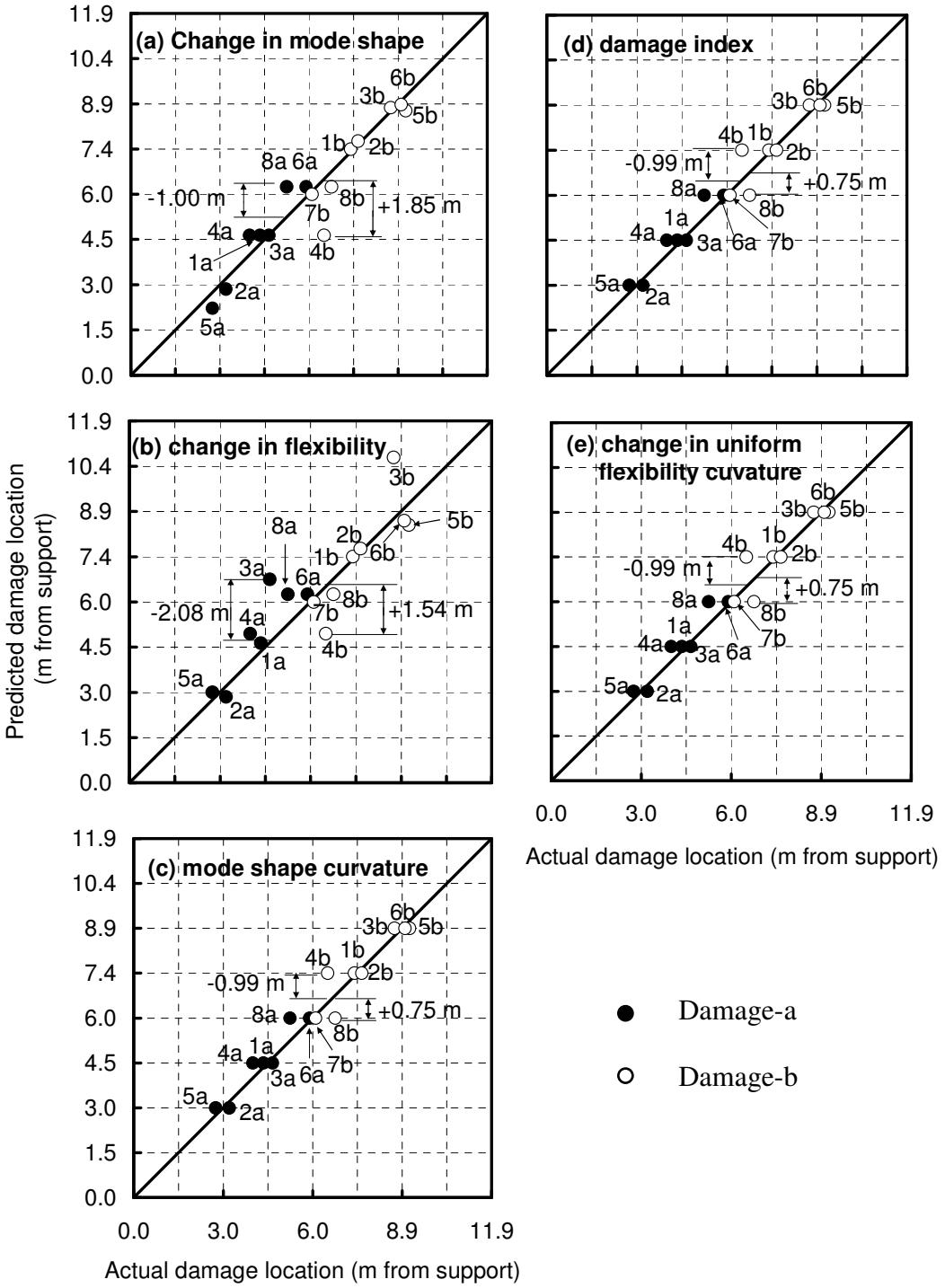

Figure 6.28. Correlation between predicted and actual damage locations of damage calculated by five VBDD methods.

in mode shape method next in terms of reliability, and the change in flexibility method performing the worst. This conclusion is different from that for detecting and locating single damage states on a prestressed concrete girder in Section 5.3.2, where the change in mode shape method performed the best, while the performance of the remaining methods was comparable to each other.

For any of these methods, damage states 8a and 8b could not be distinguished because they were located too close (1.50 m) to each other. Failure of all of the methods to locate damage state 7a is believed to be due to its proximity to a simple support, which was found to introduce difficulties even for single state damage detection.

6.3.3 Comparison between numerical and experimental studies

6.3.3.1 Comparison between numerical Investigation A and experimental study

The numerical study of Investigation A (Fig. 6.12) shows that the accuracies of predicted damage locations by the mode shape curvature, the damage index, and the change in uniform flexibility curvature methods were much better than those of the change in mode shape and the change in flexibility methods when 15 measurement points and only the first mode were used, while the accuracies of predicted damage locations of the former three methods were slightly worse than those of the latter two methods when 7 measurement points were used. It should be noted that the spacing between the two damage states in each pair of the Investigation A was 1.49 m, double the spacing between measurement points when 15 measurement points, or equal to the spacing between measurement points when 7 measurement points were used.

In experimental study, as shown in Fig. 6.25, the distance between the two damage states of each pair were close to or larger than double the spacing between sensors, except in the case of the eighth pair of damage states. Therefore, the experimental results

(Fig. 6.28) verified the conclusions of numerical study (Fig. 6.12(a)) when 15 measurement points were used, instead of the conclusion of numerical study (Fig. 6.12(b)) when 7 measurement points were used, although 7 measurement points were used in the experiment. In other words, both experimental and numerical studies show that the accuracies of predicted damage locations by the mode shape curvature, the damage index, and the change in uniform flexibility methods were better than those of the change in mode shape and the change in flexibility methods when the spacing between the two damage states was double the spacing between sensors. In addition, the resolution of the predicted damage localization by the former three methods in the experiment was 1.17*h* (1.74 m), a value close to the resolution in the numerical study of 1.0*h* (Fig. 12(a)) for non-near support regions, while the change in mode shape method and the change in flexibility method using experimental results (Fig. 6.28(a) and (b)) achieved resolutions of 1.91h and 2.43h, much smaller than those of numerical study, for which resolutions of 3.79h and 3.81h (Fig. 12(a)), respectively, were found. This finding may be attributed to the fact that the number of damage cases was relatively small in the experimental study, and damage was not located very near the support.

6.3.3.2 Comparison between numerical Investigation B and experimental study

The numerical study in Investigation B demonstrated that the minimum distinguishable distance between two separate damage states for damage detection purposes varied from 1.4*h* to 2.0*h* when 7 measurement points were used (Fig. 6.22(b)). Experimental results verified that two damage states could be successfully distinguished by all five VBDD methods if the distance between the damage was larger than 2.0*h*, while the two damage states could not be distinguished by any methods when the distance between them was less than 1.4*h* (the eighth damage case). In addition, it was

found that the two damage states could be distinguished by some of these methods if the distance between them was between 1.4*h* and 2.0*h* (the fourth damage cases, the distance is 1.67*h*).

The resolution of the predicted damage localization by the five VBDD methods in the numerical study of Investigation B was comparable, being about 2.0*h* regardless the number of measurement points. Resolutions found in the experimental study, on the other hand, were 1.17*h* for the mode shape curvature, the damage index, and the change in uniform flexibility curvature methods. This difference may be attributed to the small number of damage cases considered in the experiment. The resolutions of the experimental results were 1.91h and 2.43h for the change in mode shape method and the change in flexibility method, values that were fairly close to the numerical results (Fig. 6.22(b)).

The minimum distance from the support that one of a pair of damage states could be successfully detected in the numerical study was about 0.5*h*, while the experimental results showed that damage could not be detected even when it was located 1.0*h* from the support (damage 7a), This finding demonstrated that damage located near the support is very hard to detect in practice due to the very small magnitude of the vibration response in this region and the correspondingly more significant measurement uncertainties.

6.4 SUMMARY AND CONCLUSIONS

Using FE analysis, it has been shown that the presence of multiple small-scale damage states on a simply-supported full-scale prestressed concrete girder can be

detected and located with reasonable accuracy using vibration-based damage detection (VBDD) techniques which use measurements of only the fundamental mode shape before and after damage. When damage is detected, the size of the region within which it can be confidently predicted to lie—i.e. the resolution of damage localization—depends upon how accurately the mode shapes can be defined. When mode shapes are well-defined with a large number of measurement points, the damage location can be pinpointed with great accuracy using any of the three curvature-based VBDD techniques investigated.

In practice, only a relatively small number of measurement points are feasible, and damage localization resolution in this case was found to depend upon the number and spacing between measurement points. In the absence of experimental uncertainty, and provided the damage was not located too near a support, the resolution of damage location was found to be double the spacing between measurement points when seven evenly spaced points were used along each side of the girder. This accuracy was much worse than that of the detection of a single damage state for which the resolution was 40% of the spacing between measurement points; the presence of two separated damage states appeared to affect the prediction of each other when they were located close to each other. The change in flexibility method was found to be unsuitable for multiple damage detection, as it often gave ambiguous results. The use of additional modes did not improve the performance of the techniques; however, an increase in the number of measurement points from 7 to 15 improved their performance considerably.

When one damage state was located near a support, and another damage state was located close to mid span, only one state could be identified, resulting in larger errors with respect to the predicted damage location. If a small number of measurement points

were used, two separated damage states could be distinguished if the distance between them was greater than 150~200% of the spacing between adjacent measurement points.

Using experiments conducted on a full-scale laboratory model, it was shown that the presence of multiple small-scale damage states on a simply-supported prestressed concrete girder could be reliably detected and located using VBDD techniques that employed measurements of only the fundamental mode shape before and after damage. At best, the location of damage could be determined with a resolution of approximately 117% of measurement point spacing when as few as seven measurement points were distributed along each edge of the girder, unless the damage was located too near the support. These results appear to be superior to those of the numerical study in Investigation B; however, the number of damage cases investigated experimentally was very limited, and may not have included the worst situation.

The use of strain gauges bonded to vertical side surfaces of the girder failed to provide useful information for detecting damage, a fact that was attributed to the poor condition of the vertical side surfaces of the girder used in this portion of the study.

Of the five VBDD techniques investigated, the change in flexibility method appeared to be the least reliable. The three curvature-based VBDD techniques (the mode shape curvature method, the damage index method, and the change in uniform flexibility curvature method) performed better than the change in mode shape and the change in flexibility methods, a conclusion that is consistent with results of the numerical study. However, this conclusion is contrary with the conclusion reached for single damage state detection. Therefore, the simultaneous use of several techniques is recommended for the practical case where there is an unknown number of damage states.

The results of this study demonstrate that existing VBDD algorithms are adequate for detecting and locating low levels of multiple damage states on a bridge girder, at least for simple support conditions. However, in order to take advantage of the potential of the algorithms, mode shapes must be known with a high level of accuracy since changes to mode shapes caused by low levels of damage are very small. Measurement methods that demonstrate a very high level of repeatability are required.

The studies described in this chapter, as well as those in Chapters 4 and 5, were limited to harmonic excitation for the experimental studies and eigenvalue analyses for the numerical study. The following chapter considers the use of transient dynamic analysis to investigate the application of random vibrations to detect damage.

CHAPTER 7. DAMAGE DETECTION ON A STEEL-FREE BRIDGE DECK USING RANDOM VIBRATION

7.1 INTRODUCTION

Vibration-based damage detection (VBDD) methods utilize measured changes in the dynamic characteristics of structural systems (natural frequencies, mode shapes, and damping characteristics) to indicate the presence and location of damage. The results presented in previous chapters have demonstrated that small-scale damage can be reliably located in simple bridge systems when resonant harmonic loading is used as the excitation source for the VBDD measurements. In full-scale bridge applications, however, random loading due to traffic or wind is often more readily achievable. A numerical study was therefore undertaken to investigate the use of random loading for damage detection in the simple-span, slab-on-girder bridge deck described in Chapter 4.

Transient dynamic analyses of a finite element model of the bridge deck subjected to randomly varying loading were performed for nine different simulated small-scale damage states. To reduce the inherent uncertainty arising from the random loading, averaged results from a large number of repeated random trials were used. Several factors that may influence the probability of successfully locating the damage were investigated, including the number of repeated random trials used, the distance from the damage to the nearest sensor, the proximity of the damage to simple supports, the severity of the damage and the presence of random measurement error. The ratio of the

standard deviation over the mean value of the modal assurance criteria (MAC's) of the change in mode shape, a new indicator for damage detection, was introduced to successfully predict the presence of damage, as well as the probability and resolution of damage localization.

7.2 DESCRIPTION OF TRANSIENT DYNAMIC ANALYSIS

The system used as the basis for the numerical study in this chapter was the same steel-free bridge deck used in the harmonic vibration study described in Chapter 4.

The commercial finite element (FE) analysis package ANSYS (Version 7.1, 2003) was used to perform a transient dynamic analysis of the system in response to simulated random excitation. The finite element model was also same as that used for the harmonic vibration study described in Chapter 4. Linearly elastic material properties were used. Proportional (Rayleigh) structural damping of approximately 1.5% of critical was used; more specifically, the modal damping ratios were set at 1.5% for both the first mode (7.36 Hz) and the second mode (18.8 Hz). In this formulation, the Rayleigh damping matrix $[C]$could then be expressed by following equation:

$$[C] = 0.9969[M] + 1.825 \times 10^{-4}[K] \qquad [7.1]$$

where $[M]$and $[K]$ are the mass matrix and stiffness matrix of the bridge deck, respectively.

The model was calibrated to match the first three measured natural frequencies and mode shapes of the undamaged physical system, as described in Chapter 4. Once the FE model had been calibrated, simulated damage was induced into the deck slab by eliminating elements from the top surface of the slab, each of which measured 100 x

100 mm in plan by 25 mm thick. A total of 9 damage cases were simulated, each of which consisted of four contiguous elements being deleted at the locations shown in Fig. 7.1. To investigate the influence of the extent of damage, damage state 1 was repeated with three additional damage configurations: damage state 1b with three contiguous deleted elements, damage state 1c with two deleted elements, and damage state 1d with a single deleted element.

The FE analysis was intended to simulate the acquisition of measured data from sensors attached to the physical system at a limited number of locations. Therefore, displacement data were extracted from the FE-generated response of the system at a small number of uniformly spaced "measurement points" aligned along the girders. In this study, just five uniformly spaced "measurement points" along the north girder were utilized. In addition to the calculated response at these simulated measurement points, deflections at the supports were assumed to be zero when subsequently using the "measured" data to define the required mode shapes.

Dynamic excitation used for the FE model replicated the effects of a single

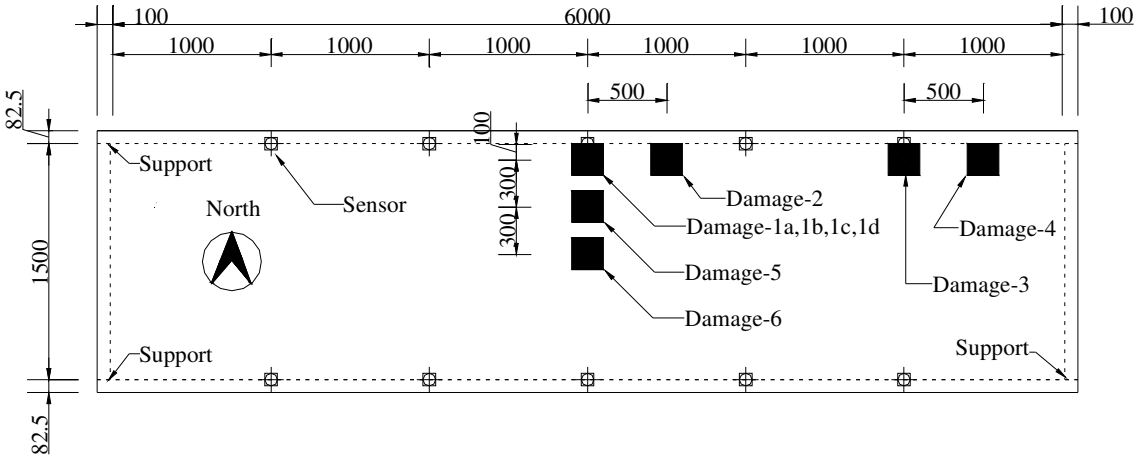

Figure 7.1. Schematic plan of deck showing locations of damage and sensors used for the random excitation numerical study (dimensions in mm).

hydraulic "shaker" applying a random vertical force to the slab. The load was applied on the top surface of the deck above the north girder and positioned 2.0 m from the west support in order to be effective in exciting at least the first three modes. A unique simulated random load time history, characterized by an approximately uniform (white noise) spectrum and a root-mean-square magnitude of 100 N, was generated automatically for every FE analysis by the FE analysis package ANSYS (Version 7.1, 2003). Each random load history was generated at uniform time increments of 0.00333 s over a simulated period of 21 s.

Transient dynamic analyses were performed using Newmark's β method as the time marching scheme, assuming constant-average acceleration (Bathe and Wilson 1976). Displacement time histories at each measurement point were extracted from the analysis output and passed through a Fast Fourier Transform (FFT) to generate the corresponding displacement response spectra; in order to reduce leakage effects in the response spectra, displacement time histories were modified by a Parzen window function (Ramirez 1985) prior to application of the FFT. Natural frequencies and mode shape amplitude values were extracted from the displacement spectra using a peak-picking method. The assembled mode shapes were then unit-norm normalized equivalent, in effect, to unit-mass normalized (assuming a uniform distribution of mass along the span of the girder).

7.3 DAMAGE DETECTION METHOD

The change in mode shape method (see Section 2.2.3), as the most straightforward of the vibration-based damage detection schemes, was selected for this study to facilitate

the large number of required analyses. The experimental and numerical investigations in Chapter 4 demonstrated the ability of this method to detect small-scale damage reliably in the bridge deck when harmonic loading was used to excite the system at its lowest natural frequency.

For the random vibration study, only the fundamental mode shape was considered. As well, the mode shapes were defined at the five measurement points only, in addition to the support locations; therefore, the baseline and damaged mode shape vectors, $\boldsymbol{\phi}$ and $\boldsymbol{\phi}^*$, each had a dimension of seven.

To reduce the uncertainty arising from random excitation, dynamic analyses for each damage state, including the undamaged condition, were repeated a specified number of times. By averaging mode shapes from the repeated trials, mean values for the mode shape coordinates ϕ_j and ϕ_j^* were obtained, denoted here as $\overline{\phi}_j$ and $\overline{\phi}_j^*$, respectively. The corresponding standard error values, $\overline{S}_j$ and $\overline{S}_j^*$, associated with the sample means $\overline{\phi}_j$ and $\overline{\phi}_j^*$ could then be determined using the expressions

$$\overline{S}_j = \frac{S_j}{\sqrt{N}}, \text{ and } \overline{S}_j^* = \frac{S_j^*}{\sqrt{N}} \qquad [7.2]$$

where S_j and S_j^* are the computed standard deviations of the mode shape coordinates ϕ_j and ϕ_j^*, and N is the sample population (i.e. the number of repeated trials).

Based on the averaged results, an improved damage indicator $\Delta\overline{\phi}_j$ was defined as

$$\Delta\overline{\phi}_j = \overline{\phi}_j^* - \overline{\phi}_j \qquad [7.3]$$

the standard deviation of which could be calculated using the equation

$$S_{\Delta j} = \sqrt{\bar{S}_j^2 + \bar{S}_j^{*2}} = \sqrt{\frac{S_j^2 + S_j^{*2}}{N}} \qquad [7.4]$$

If the damage occured near the i^{th} measurement point, it was expected that the highest peak in the mode shape change curve ($\boldsymbol{\Delta\bar{\phi}}$) would be found in the vicinity of the i^{th} measurement point. As a result, a necessary condition for successfully detecting the damage and locating it at the nearest measurement point may be expressed as

$$D_{ij} \geq 0 \;;\; \text{where} \quad D_{ij} = \Delta\bar{\phi}_i - \Delta\bar{\phi}_j \;\text{ and }\; i \neq j \qquad [7.5]$$

In other words, the change in the averaged mode shape should be larger at the i^{th} measurement point than at any other point if the i^{th} point is closer to the damage. Although necessary, the condition expressed in Eq. 7.5 is not a sufficient condition to locate the damage reliably, as it is possible to have multiple, simultaneous peaks of similar magnitudes in $\boldsymbol{\Delta\bar{\phi}}$. The standard deviation of D_{ij} can be calculated as follows:

$$S_{dij} = \sqrt{S_{\Delta i}^2 + S_{\Delta j}^2} = \sqrt{\left(S_i^2 + S_i^{*2} + S_j^2 + S_j^{*2}\right)/N} \qquad [7.6]$$

Finally, the probability of successfully locating damage near the i^{th} measurement point is given by the series

$$f_{\text{detect}} = \prod_{j=1,\, j\neq i}^{n} P(D_{ij} \geq 0) \qquad [7.7]$$

where $P(D_{ij} \geq 0)$ denotes the probability that $D_{ij} \geq 0$, and n is the total number of measurement points. In effect, Eq. 7.7 expresses the joint probability that the average change in mode shape at the i^{th} measurement point is greater than that at any other measurement point.

In this study, the probability $P(D_{ij} \geq 0)$ was calculated on the basis of m_{ij} and S_{dij}, the mean and the sample standard deviation of D_{ij} for all trials, assuming that D_{ij} was normally distributed. As an alternative approach, m_{ij} for a large number of trials may be determined from the difference between the damaged and undamaged mode shapes determined directly from eigenvalue analyses of the respective finite element models since the average of an infinite number of mode shapes derived on the basis of random vibration will tend to converge to the theoretical values from the eigenvalue analysis.

To prove that random variations in the mode shape at different locations were statistically independently so that D_{ij} was, in fact, normally distributed, the normalized covariance C_{ij} between the change in mode shape at any two points was calculated by following equation:

$$C_{ij} = \frac{\sum_{n=1}^{N} (\Delta\phi_i^{(n)} - \Delta\bar{\phi}_i)(\Delta\phi_j^{(n)} - \Delta\bar{\phi}_j)}{\frac{N}{S_i^2}} \qquad [7.8]$$

where n is the trial number. The covariance between $\Delta\phi$ at different measurement points is shown in Fig. 7.2. It may be observed that C_{12}, C_{13}, C_{14}, and C_{15} were nearly zero and much smaller than C_{11}; similarly, $C_{31,} C_{32}, C_{34}$, and C_{35} were nearly zero and much smaller than C_{33}. Therefore, it was concluded that $\Delta\phi_i$ and $\Delta\phi_j$ were independent of each other, and that D_{ij} was normally distributed.

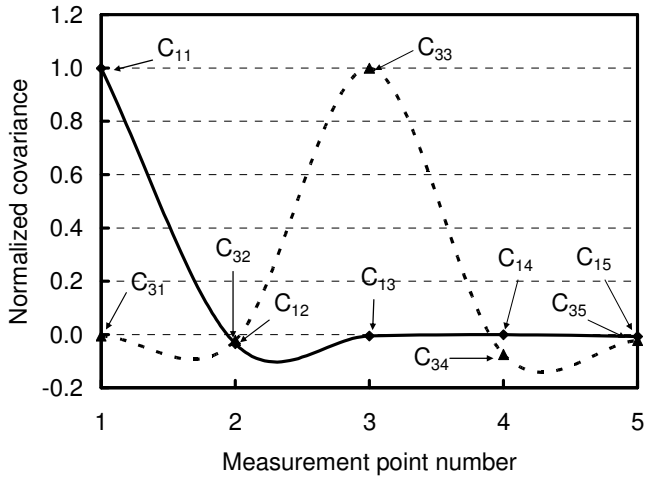

Figure 7.2. Covariance between the change in mode shape at different measurement points.

7.4 RESULTS AND DISCUSSION

7.4.1 Damage detection without measurement errors

As a first step, damage detection was investigated using random vibrations without including the effects of random measurement errors. For a physical system, this would imply that sensors used to measure dynamic displacements could do so exactly and that there were no extraneous sources of ambient interference acting on the structure or data acquisition system. Based on this assumption, the probabilities of successfully locating damage were calculated for the various damage states described previously; in addition, for each damage state, the analyses were carried out for different numbers of repeated trials to evaluate the influence of the number of trials on the accuracy of damage detection results.

To illustrate the damage detection procedure, averaged results from 100 repeated trials were used in an attempt to detect damage state 1c, which was aligned

longitudinally with the 3rd measurement point (see Fig. 7.1). The corresponding theoretical change in mode shape derived from eigenvalue analyses of the damaged and undamaged finite element models is shown in Fig. 7.3; m_{ij} values, the expected mean value of D_{ij} calculated on the basis of the eigenvalue results, are also indicated on Fig. 7.3. Statistical results from the 100 random loading trials are listed in Table 7.1 for each measurement point, along with their corresponding detection probabilities $P(D_{ij} \geq 0)$.

As an example, S_{d13} was calculated using the data in Table 7.1 in the following manner:

$$S_{d13} = \sqrt{\left(0.00314^2 + 0.00275^2 + 0.00283^2 + 0.00288^2\right)/100} = 0.000581 \qquad [7.9]$$

For this case, then, the probability of successfully locating damage state 1c using the average of 100 tests was

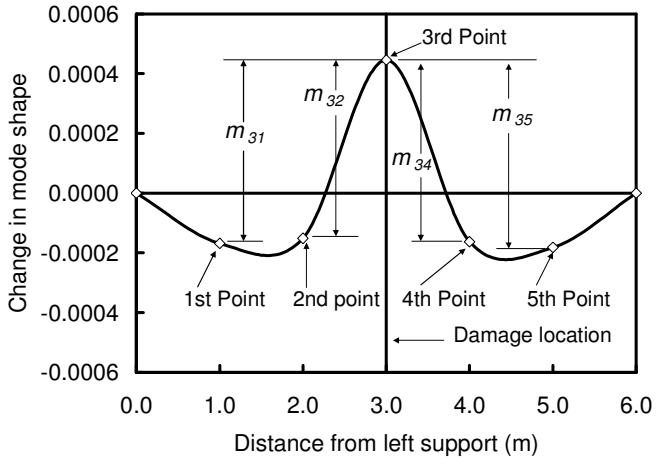

Figure 7.3. The change in mode shape caused by damage state 1c, as derived from eigenvalue analyses.

Table 7.1. Statistical results of 100 repeated trials for detecting damage state 1c.

Measurement point	*1st*	*2nd*	*3rd*	*4th*	*5th*
S_j	0.00314	0.00271	0.00283	0.00283	0.00351
S_j^*	0.00275	0.00308	0.00288	0.00277	0.00303
S_{dij}	0.000581	0.000576	N/A	0.00566	0.00615
m_{ij}	0.000614	0.000597	N/A	0.000609	0.000627
m_{ij} / S_{dij}	1.06	1.04	N/A	1.08	1.02
$P(D_{ij} \geq 0)$	0.855	0.851	N/A	0.860	0.846

$$f_{\text{detect}} = 0.855 * 0.851 * 0.860 * 0.846 = 52.9\% \qquad [7.10]$$

Due to the random nature of the loading, however, the detection probability presented above is not unique, but will vary for every set of 100 trials attempted. To demonstrate this fact, three additional sets of 100 trials were run for damage state 1c. The average change in mode shape at each measurement point is plotted for the four sets of 100 trials in Fig. 7.4. Based on a visual inspection of these curves, only the second and third sets of 100 trials located the damage successfully, as indicated by the dominant positive peak in the change in mode shape plots at the location of the induced damage. This illustrates that the use of 100 random trials to estimate mode shapes results in a probability of successfully locating damage of roughly 50%, which is close to the expected 52.9%.

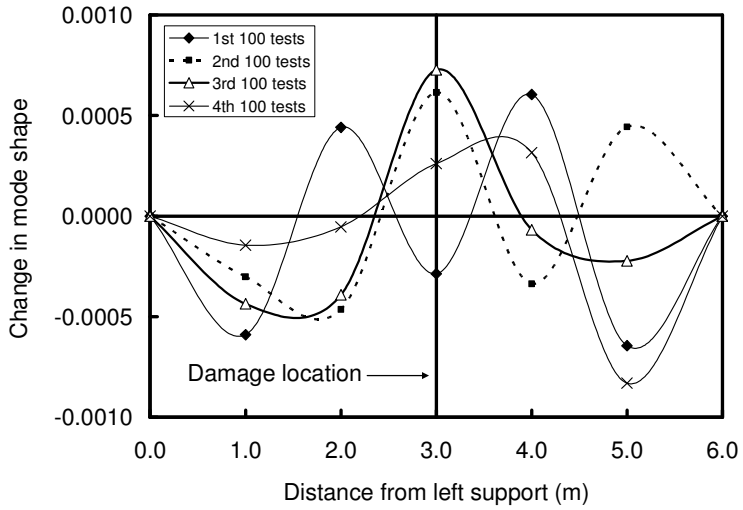

Figure 7.4. Detection of damage state 1c using the average of 100 repeated trials.

When detection of the same damage state was attempted using sets of 25 trials, the probability of successfully locating the damage dropped significantly as compared to attempts using sets of 100 trials. For example, the probability of successfully locating damage state 1c was found to be only 21.8% using the first set of 25 trials. Fig.7.5 shows plots of average change in mode shape at the five measurement points for sixteen different sets of 25 trials each. It can be seen that only the 5^{th} and 12^{th} sets of 25 trials successfully detected the damage at the correct location, while the 14^{th} set of 25 tests exhibits two large peaks of similar size, making it difficult to uniquely locate the damage. It is therefore obvious that there is a low probability of success for locating the damage using the average of any set of 25 trials.

Conversely, when sets of 400 trials were used for damage detection, the probability of success increased dramatically as compared to similar efforts using sets of 100 trials. Using the first set of 400 trials, for example, the probability of success was found to be

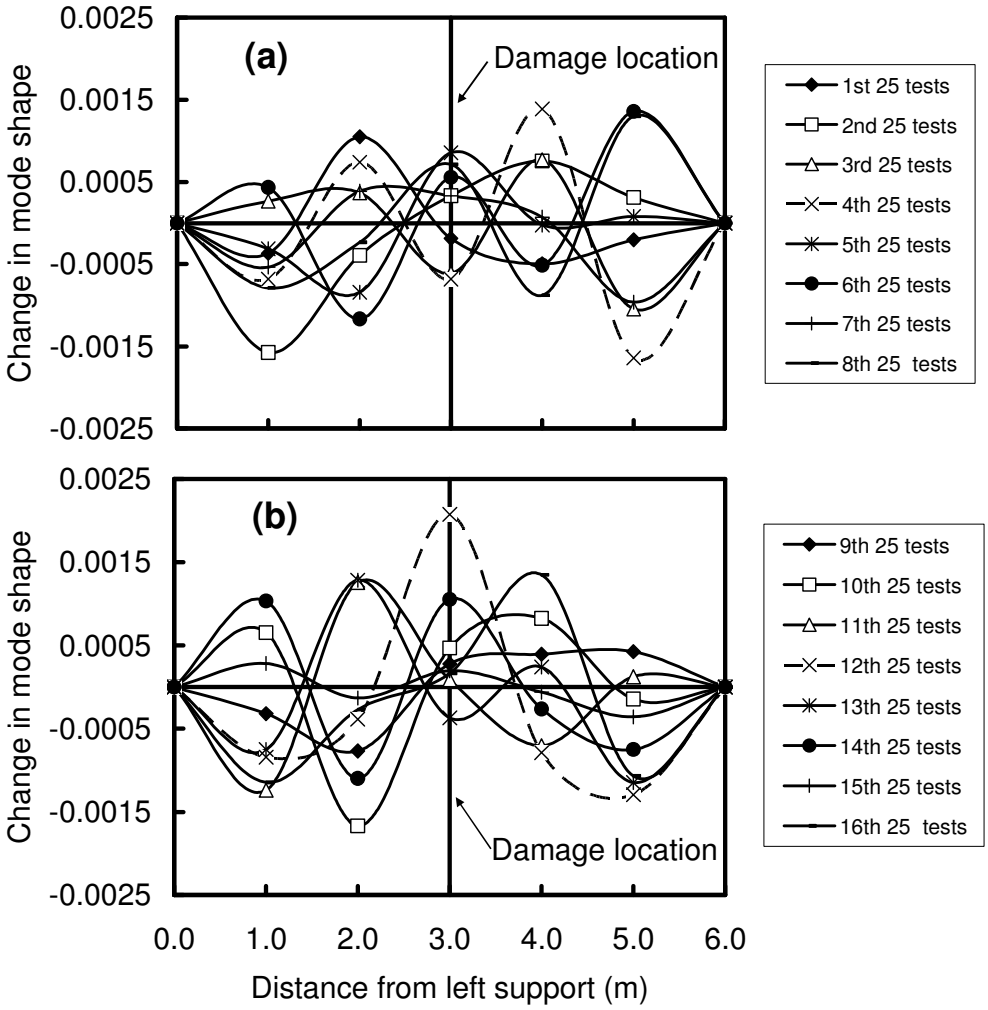

Figure 7.5. Detection of damage state 1c using the average of 25 repeated trials.

91.1%. For this set of 400 trials, the average change in mode shape at the measurement points due to damage state 1c is shown in Fig. 7.6. The "true" change in mode shape derived from eigenvalue analyses of the damaged and undamaged finite element models is also plotted for comparison. It is evident that there is considerable similarity between the average results from the set of 400 random trials and the numerically exact behaviour.

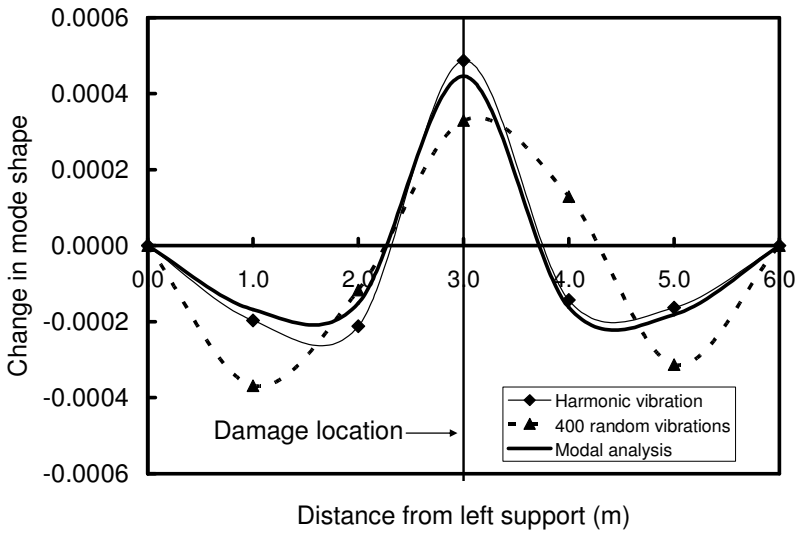

Figure 7.6. Detection of damage state 1c using harmonic vibration and the average of 400 repeated random trials.

However, the change in mode shape found experimentally using averaged data from ten repeated trials using excitation that varied harmonically with time at the fundamental natural frequency of the system, rather than randomly, is seen in Fig. 7.6 to produce results that were more accurate than the numerical random excitation trials, even when the results from a set of 400 random trials were averaged. This finding provides strong evidence that harmonic excitation is significantly more reliable, and efficient, for detecting damage than random excitation.

Fig. 7.7 shows the probabilities of successfully locating damage for the nine different damage states considered in this study, with the results of each shown using sets of 25, 100 and 400 repeated random trials; a detailed listing of this data is provided in Appendix H. Measurement error was not considered in any of these analyses. It was found that sets with a larger number of repeated trials had a higher probability of successful damage localization for all damage states.

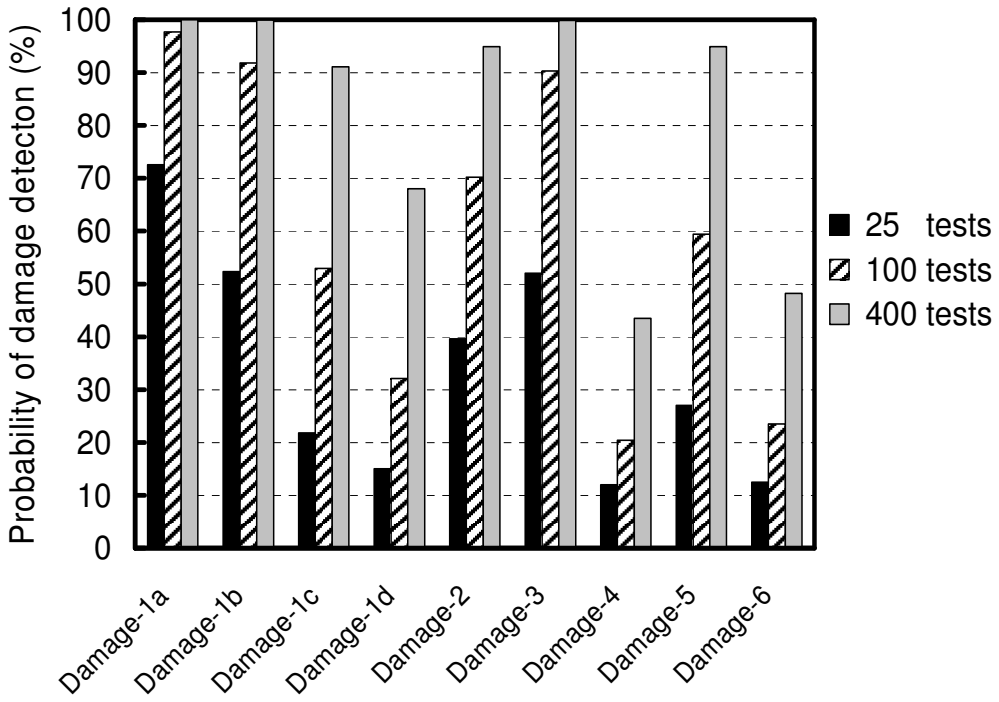

Figure 7.7. Probabilities of successfully locating damage for different damage states without measurement errors.

In Fig. 7.7, a comparison of the results from damage states 1a, 1b, 1c and 1d, which were located at the same position but featured different scales of damage (four, three, two and one contiguous damaged elements, respectively), shows that, as expected, smaller scale damage was less likely to be successfully located using same number of repeated tests. This trend held true, regardless of the number of trials used in averaging the data.

An examination of Fig. 7.7 also demonstrates that the location of damage relative to the nearest sensor influenced the probability of success. For example, damage state 2 had a much lower probability of being successfully located than damage state 1a, regardless of the number of trials used, since it was located farther away longitudinally from the nearest sensor. Similarly, damage state 5 and damage state 6 had much lower

probabilities of detection than damage state 1a, since both were located farther away from the nearest sensor in the transverse direction.

Finally, proximity to a simple support is seen to hinder the probability of successful detection. Damage state 4, which was located 500 mm from the east support, was found to have a much lower probability of being successfully located than damage states 1a, 2 or 3. On the other hand, damage state 3, which was located 1.0 m from the east support but coincided with a measurement point, exhibited detection probabilities that were comparable to damage states 1a and 2, which were located closer to midspan. It appears, therefore, that accurately locating damage is particularly difficult in the region between the last measurement point and a simple support, a finding that agrees with the VBDD studies using harmonic excitation in Chapter 4.

7.4.2 Damage detection with random measurement errors

In physical systems, random errors due to measurement inaccuracies and ambient interference add to the uncertainty in the measured mode shapes. To investigate this effect, the damage detection studies described in the previous section were repeated with numerically simulated random errors introduced into the dynamic response of the slab. After the displacement time histories at the measurement points had been extracted from the transient dynamic FE analysis results, a unique random signal was superimposed on each time history before mode shapes were calculated. The uncertainty associated with the random measurement errors was therefore embedded in the "measured" mode shapes.

The intensity of the simulated random measurement noise was selected such that the resulting reliability of the numerically generated mode shapes was comparable to

those derived experimentally from random excitation tests of the physical model of the slab in question. The average modal assurance criteria (MAC) between fundamental mode shapes (10 trials) derived from experimental data was found to be 0.9995, while the average MAC value calculated from the transient dynamic FE analysis (1200 trials) without measurement noise was 0.9999. The corresponding standard deviations in the unit-norm normalized modal amplitudes were calculated to be 0.0062 for the experimental results compared to 0.0036 for the numerical results. To produce levels of uncertainty in the numerical results comparable to those found in the experimental data, therefore, a white noise random signal was added to the displacement time history obtained from the numerical analysis; based on the results a calibration exercise, the random signal for each displacement record was scaled to have a root-mean-square (rms) value equal to 35% of that of the original displacement record. The procedure used for the calibration exercise is described in Appendix I.

Fig. 7.8 summarizes the results, showing the probabilities of successfully locating damage in the presence of random measurement errors for the nine damage states considered in this study, for details, see Appendix J. Comparing Fig. 7.8 with Fig. 7.7, it is evident that that the presence of measurement errors lowered the probabilities of success by as much as 30-40%, with the extent of the reduction depending on the damage state, regardless of the number of trials used in the averaging process. Aside from the lower probabilities, though, Fig. 7.8 suggests conclusions similar to those from Fig. 7.7 regarding the influence of the number of trials, the severity of damage, and the location of damage relative to the nearest sensor.

Results from this numerical investigation are consistent with those from the experimental study of the same bridge deck system, as described in Chapter 4. In that

experimental study, VBDD techniques were unable to successfully locate the damage using averaged results from 10 random vibration trials. Since the damage induced in the physical model (a saw-cut section of the slab 100 mm x 100 mm in plan, by 25 mm deep) was similar in size and location to damage state 1d from the present study, Fig. 7.8 suggests that even if 100 repeated random vibrations trials had been carried out, rather than 10, the probability of successfully locating the damage would still have been just 16%. When harmonic loading was applied at the fundamental natural frequency of the physical system, on the other hand, the damage was reliably located using the average of 10 trials. Again, this demonstrates that harmonic loading is a more efficient and reliable form of excitation than random loading for use with VBDD methods.

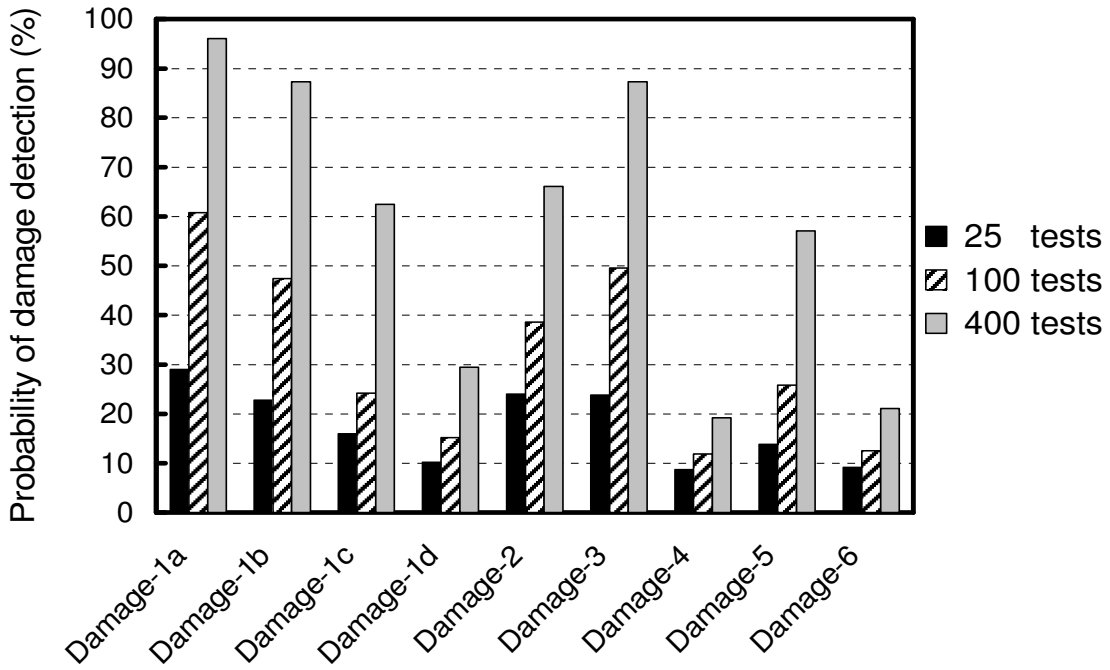

Figure 7.8. Probabilities of successfully locating damage for different damage states with measurement errors.

7.4.3 Assessing levels of confidence in damage localization

In the foregoing discussion, the VBDD approach was used to identify the most likely location of a small-scale damage state that was known to exist, taking into account the presence of uncertainty in the measured mode shapes. In practice, however, the first and perhaps most significant task is to establish the actual existence of damage (i.e. Level I damage detection) using uncertain measurements. Given the fact that loading and measurement induced uncertainties generate spurious indications of change in the dynamic response characteristics, differentiating real damage from random noise presents a major challenge.

To provide a quantitative indicator as to the probable existence of damage, the modal assurance criterion (MAC) was adapted to compare changes in mode shapes, rather than the mode shapes themselves. Assume, for example, that two independent sets of trials were undertaken to measure a particular mode shape of a bridge deck in condition-1 of structural health, resulting in two estimates of the mode shape vectors of condition-1, $\bar{\phi}_k$ and $\bar{\phi}_l$ (the mean value of the mode shapes of each set). Then another two independent sets of trials were undertaken to measure the mode shape of the deck in condition-2 of structural health, again resulting in two different estimates of the mode shape vectors of condition-2, $\bar{\phi}_m^*$ and $\bar{\phi}_n^*$, both of which contain experimental uncertainty. A "change in mode shape assurance criteria" Δ_{MAC} can then be defined as

$$\Delta_{MAC} = \frac{\left[\sum_{j=1}^{p}\left\{\left[\left(\bar{\boldsymbol{\phi}}_m^*\right)_j - \left(\bar{\boldsymbol{\phi}}_k\right)_j\right]\left[\left(\bar{\boldsymbol{\phi}}_n^*\right)_j - \left(\bar{\boldsymbol{\phi}}_l\right)_j\right]\right\}\right]^2}{\left[\sum_{j=1}^{p}\left[\left(\bar{\boldsymbol{\phi}}_m^*\right)_j - \left(\bar{\boldsymbol{\phi}}_k\right)_j\right]^2\right]\left[\sum_{j=1}^{n}\left[\left(\bar{\boldsymbol{\phi}}_n^*\right)_j - \left(\bar{\boldsymbol{\phi}}_l\right)_j\right]^2\right]} \qquad [7.11]$$

where p is the number of elements in the mode shape vectors. If damage actually occurred during the period between the assessment of condition-1 and condition-2, so that the mode shapes of condition-2, $\overline{\phi}_m^*$ and $\overline{\phi}_n^*$, were truly different from those of condition-1, $\overline{\phi}_k$ and $\overline{\phi}_l$, and there was no experimental uncertainty, so that $\overline{\phi}_m^*$ would be identical to $\overline{\phi}_n^*$, and $\overline{\phi}_k$ would be identical to $\overline{\phi}_l$, the expected value of Δ_{MAC} would be unity. If, on the other hand, all of the differences in mode shape measurements could be attributed to random noise, the expected value of Δ_{MAC} would approach zero. Finally, if damage actually existed but the measured mode shapes $\overline{\phi}_m^*$, $\overline{\phi}_n^*$, $\overline{\phi}_k$ and $\overline{\phi}_l$ contained random errors, Δ_{MAC} would fall somewhere between unity and zero, depending on the relative magnitudes of the damaged induced mode shape changes and the measurement noise.

Instead of two sets of measurements in condition-1 and condition-2, if a large number of independent sets of trials were carried out to measure the mode shape $\overline{\phi}$ in condition-1, and the mode shape $\overline{\phi}^*$ in condition-2, the Δ_{MAC} value calculated from any pair of sets would represent a random sample from an approximately normally distributed population. The probability distribution of possible Δ_{MAC} values could then be characterized by a standard deviation, $\tilde{\Delta}_{MAC}$ and a mean value $\overline{\Delta}_{MAC}$. The ratio of these two statistical parameters

$$\beta_{MAC} = \frac{\tilde{\Delta}_{MAC}}{\overline{\Delta}_{MAC}} \qquad [7.12]$$

would be expected to vary from a value close to zero in the case of a damage state that produces significant changes in the mode shape relative to the measurement uncertainty, to a value close to unity for the case when either the damage induced changes in the mode shape are small or the uncertainty is large. The parameter β_{MAC} therefore provides an indication of the level of confidence that damage can be successfully detected (and located) from a given set of measured mode shapes.

For all possible combinations of the four change in mode shape plots shown in Fig. 7.4 (each representing the average of 100 trials for damage state 1c), for example, the values of $\tilde{\Delta}_{MAC}$ and $\overline{\Delta}_{MAC}$ were calculated to be 0.249 and 0.289, respectively, producing a ratio of $\beta_{MAC} = 0.864$. For this case, the probability of successfully locating the damage was 52.9%. Similarly, the sixteen change in mode shape plots shown in Fig. 7.5 (each representing the average of 25 trials for damage state 1c), produced $\tilde{\Delta}_{MAC}$, $\overline{\Delta}_{MAC}$ and β_{MAC} values of 0.259, 0.265 and 0.980, respectively. The higher level of uncertainty in this case, caused by averaging only 25 instead of 100 random trials, is seen to produce a higher β_{MAC} value, as well as a lower probability of successful damage location (21.8%). This example illustrates that a smaller β_{MAC} value corresponds to a higher probability of successfully locating damage.

The results considering all nine damage cases using 25, 100 and 400 tests are plotted in Fig. 7.9, and the corresponding data are listed in Appendix K. For this investigation, 48 sets of 25 tests in both undamaged and damaged conditions for each damage case were considered, resulting in 48 x 48=2304 change of mode shape vectors; 12 sets of 100 tests in both undamaged and damaged conditions were considered,

resulting in 12 x 12 =144 change of mode shape vectors; and only 3 sets of 400 tests in undamaged and damaged conditions were considered, resulting in 3 x 3 = 9 change of mode shape vectors. This produced 2304x(2304-1)/2=2,653,056, 144x(144-1)/2=10,296 and 9x8/2=36 corresponding $\tilde{\Delta}_{MAC}$ and $\overline{\Delta}_{MAC}$ values for 25, 100 and 400 tests, respectively. The open circle symbols in Fig. 7.9 signify cases in which no damage occurred.

The uncertainties associated with mode shape definition introduce the possibility of detecting damage where none actually exists (i.e., a "false positive" result). Since, in that case, there would be no physical changes in the system, the expected value of the differences $m_{ij} \approx 0$ between all points i and j within any set of measurement trials. It would therefore be equally likely that the observed mode shape changes at any point be larger or smaller than those at any other point; in other words, $P(D_{ij} \geq 0) = 50\%$ for all i and j. Using Eq. 7.7, the probability of detecting nonexistent damage at any measurement point on the system in question would then be f_{detect} = 50% x 50% x 50% x 50% = 6.25%.

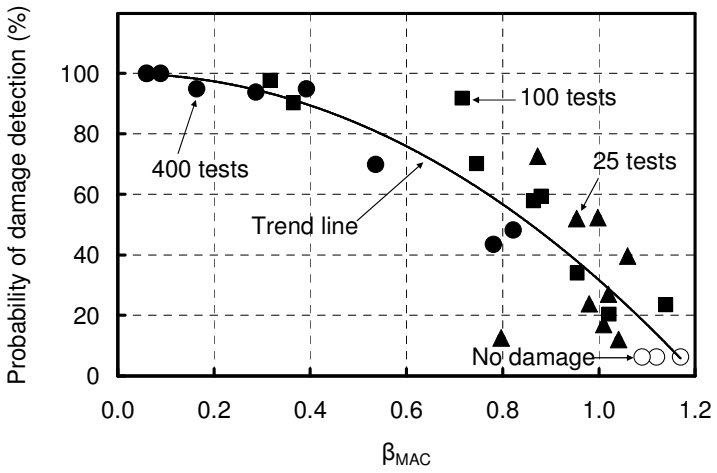

Figure 7.9. Relationship between the probability of damage detection and β_{MAC}.

It was found that smaller β_{MAC} values corresponded to higher probabilities of successfully locating damage, and that the damage could be detected with more than 90% probability if β_{MAC} was less than 0.3. It should be noted that this method does not depend on the use of a finite element model, but can be used just as readily to determine the presence and the location of damage from field measurements, since β_{MAC} could also be calculated from measured mode shapes.

The relationship between the probability of successful damage detection and β_{MAC} using 400 tests is plotted in Fig. 7.10, illustrating the influence of damage size and location on these two variables. Fig. 7.10a indicates that β_{MAC} increased and the probability of damage detection decreased when the damage size became smaller. Figure 7.10b indicates that β_{MAC} increased and the probability of damage detection decreased when the damage was located longitudinally farther from the nearest sensor or closer to a support. Finally, Fig. 7.10c indicates that β_{MAC} increased and the probability of damage detection decreased when the damage was located transversely farther away from the nearest sensor.

It was found that when no damage existed, β_{MAC} was greater than 1.0. Also, the damage could be detected and located with 90% probability if β_{MAC} was smaller than 0.3. However, further studies are required to determine whether these findings are specific to the structure considered or can be applied more generally.

7.4.4 Accuracy of predicted longitudinal location of damage

The probability of damage detection using random vibration was presented in previous sections; this section focuses on the resolution of predicted longitudinal

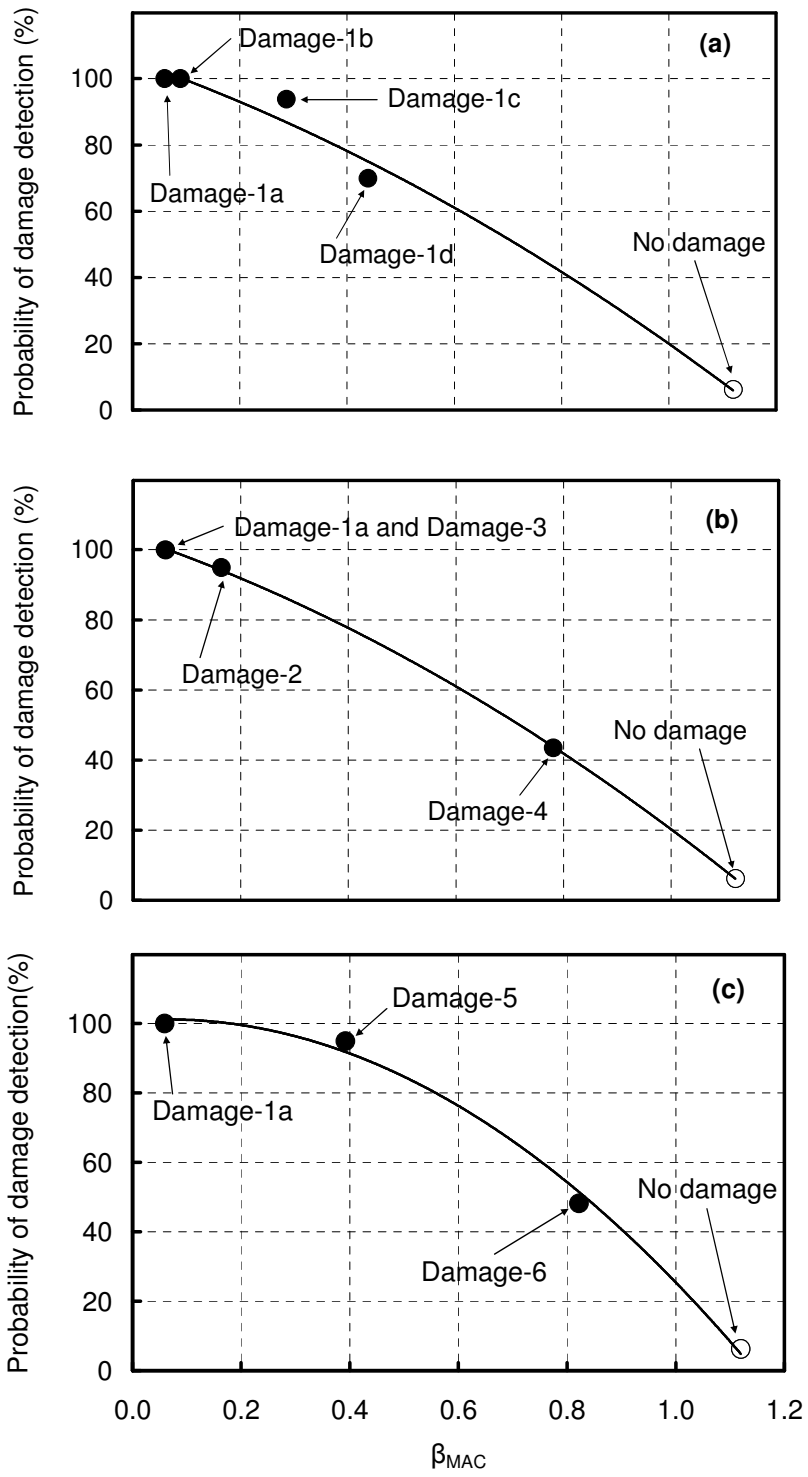

Figure 7.10. Relationship between the probability of damage detection and β_{MAC} using 400 tests, showing the influence of (a) change of damage size, (b) change of longitudinal location, and (c) change of transverse location.

location of damage when a random excitation source is used. A cubic spline function was used to interpolate between the five measurement points, producing displacement values at 61 points along the fit curve that were extracted and used to define the mode shapes between the supports. Different combinations of nine sets of 400 trials and 144 sets of 100 trials were investigated. The mean mode shape from each set of trials was used as input for the change in mode shape method to predict the damage location; the standard deviation and the mean of the predicted damage location were then calculated.

Fig. 7.11 shows the standard deviation of the predicted damage location for the nine different damage states considered in this study, with the results of each shown using sets of 100 and 400 repeated random trials. It was found that sets with a larger number of repeated trials had a smaller standard deviation for the predicted damage location for all damage states. Measurement error was not considered in any of these analyses because measurement error made the probability of detection of small scale damage very low and β_{MAC} very large, leading to scattered investigation results, which was not conducive for identifying patterns.

A comparison of the results from damage states 1a, 1b, 1c and 1d, which were located at the same position but featured different scales of damage (four, three, two and one damaged contiguous elements, respectively), shows that, as expected, smaller scale damage exhibited a larger standard deviation in the predicted damage location using the same number of repeated tests. This trend held true, regardless of the number of trials used in averaging the data.

An examination of Fig. 7.11 also demonstrates that the location of damage relative to the nearest sensor also influenced the standard deviation of the predicted damage

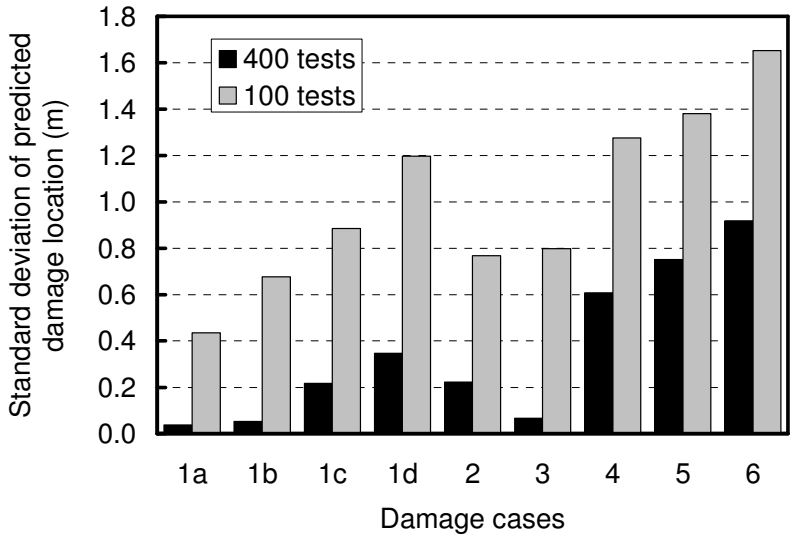

Figure 7.11. Standard deviation of predicted damage locations using random vibration.

location. For example, damage state 2 had a much larger standard deviation in the predicted damage location than damage state 1a, regardless of the number of trials used, since it was located farther away longitudinally from the nearest sensor. Similarly, damage state 5 and damage state 6 had much larger standard deviations in predicted damage location than damage state 1a, since both were located farther away from the nearest sensor in the transverse direction.

Finally, proximity to a simple support is seen to decrease the accuracy of damage locating. Damage state 4, which was located 500 mm from the east support, was found to have a much larger standard deviation in the predicted damage location than damage states 1a, 2 or 3. Similarly, damage state 3, which was located 1.0 m from the east support but coincided with a measurement point, had a larger standard deviation in the predicted damage location than damage state 1a, which was located closer to midspan. It appears, therefore, that accurately locating damage is particularly difficult in the region

between the last measurement point and a simple support, a finding that agrees with previous VBDD studies using harmonic excitation described in Chapter 4.

Fig. 7.12 shows the correlation between the standard deviation of the predicted damage location and the calculated value of β_{MAC}. It was found that the standard deviation of predicted damage location was approximately proportional to β_{MAC}.

Fig. 7.13 shows the difference between the mean of the predicted damage location and the actual damage location. It was found that smaller scale damage had larger errors in the predicted damage locations using same number of repeated tests. Damage located closer to the support or farther away from the nearest sensor also had larger errors in the predicted damage locations. These findings agree with the previous VBDD studies using harmonic excitation in Chapter 4.

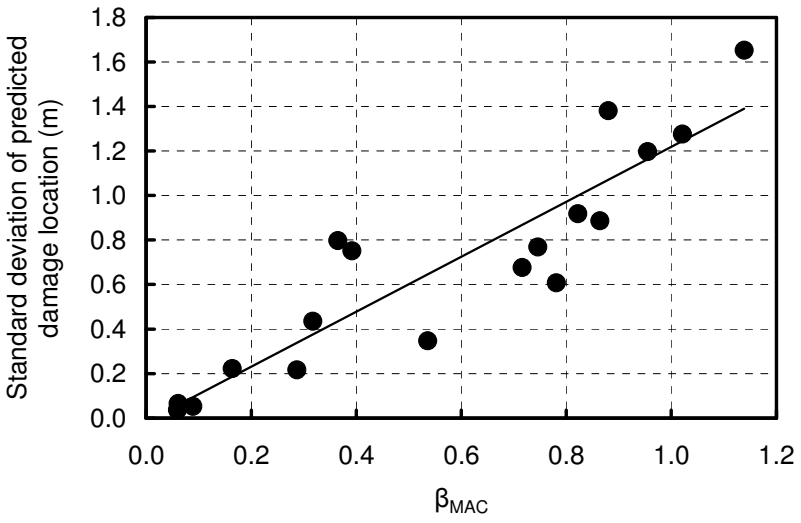

Figure 7.12. Correlation between standard deviation of predicted damage location and β_{MAC}.

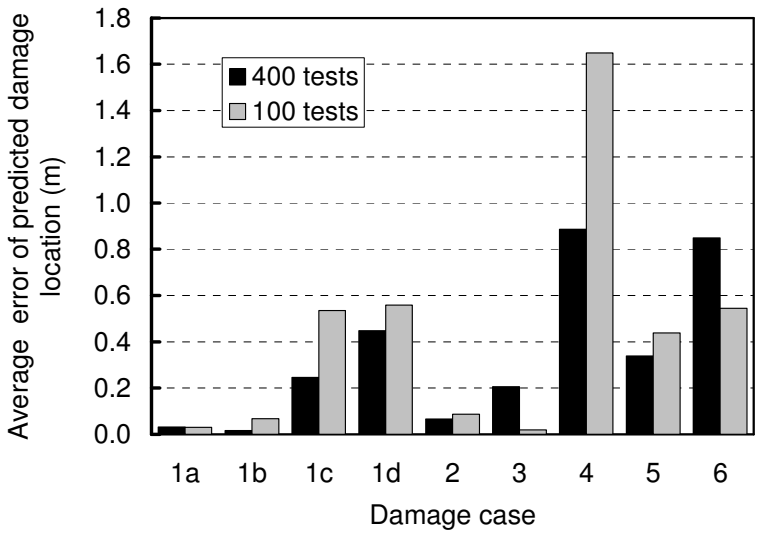

Figure 7.13. The difference between the mean value of the predicted damage location and actual damage location using random excitation.

7.5 SUMMARY AND CONCLUSIONS

A numerical study was undertaken to evaluate the use of a randomly varying point load as an excitation source for vibration-based damage detection (VBDD) in a two-girder, simple-span, slab-on-girder bridge deck. The same bridge deck system was also studied, both experimentally and numerically, under harmonic loading conditions, the results for which were presented in Chapter 4. In the random excitation investigation, the change in mode shape method was adopted as the sole VBDD scheme.

Statistical uncertainty introduced by the random loading was found to be detrimental to the successful application of VBDD methods. In order to locate small scale damage in the deck with a reasonable probability of success, averaged results from a large number of repeated random trials (more than 400 in some cases) were required to reduce the effects of variability to acceptable levels. Even then, successful location of

the damage was not assured. In contrast, resonant harmonic loading was used to locate small-scale damage on the same bridge deck system with a high degree of precision using measurements from the average of 10 trials as described in Chapter 4. This suggests that random loading is not a reliable excitation source for VBDD, at least for the structural system and type of damage considered in this study.

The probability and resolution of successfully locating the damage were seen to be influenced by a number of factors:

- an increase in the severity (size) of the damage enhanced the success rate and improved the resolution of localization (i.e. potential error in the predicted location);
- an increase in the number of repeated random trials used to generate averaged results for use in VBDD techniques was beneficial;
- an increase in the distance, either longitudinally or laterally, between the damage and the nearest sensor location reduced the probability of successfully locating the damage and caused the resolution to deteriorate;
- damage detection was least successful for damage located between a simple support and the nearest sensor location; and
- random measurement errors further reduced the probability of successfully locating the damage and decreased the accuracy.

Furthermore, a new parameter was introduced to quantify the reliability of a given damage location estimate, to investigate the existence of damage in the presence of uncertainty, and to provide an indication of likely resolution level. This parameter, designated β_{MAC}, was simply the ratio of the standard deviation to the mean of MACs of the change of mode shape. It was found to be a good indicator to predict the presence of

damage, as well as the probability and resolution of successful damage localization. Lower β_{MAC} ratios corresponded to a higher probability of successful damage localization, as well as better resolutions of damage localization. This ratio provides VBDD methods with a quantifiable index of reliability and accuracy when random excitation sources are used, making the method more practical for field trials, and also eliminating the need for FE validation of results.

CHAPTER 8. CONCLUSIONS AND FUTURE RESEARCH

8.1 SUMMARY

This thesis addresses the experimental and numerical study of vibration-based damage detection (VBDD) techniques for use in structural health monitoring (SHM) of bridge superstructures. The primary objective was to investigate the capability of VBDD techniques to detect and locate small scale damage in bridge superstructures using a relatively small number of sensors.

Five VBDD techniques were investigated, including the change in mode shape, the change in flexibility, the mode shape curvature, the damage index, and the change in uniform flexibility curvature methods. All of these are non-model based VBDD methods; they only rely on the measured mode shapes and natural frequencies.

The experimental studies were undertaken on a half-scale simply-supported steel-free bridge deck and two full-scale simply-supported prestressed concrete girders removed from an abandoned bridge. The laboratory setting permitted an investigation of the feasibility of VBDD techniques under a well-controlled laboratory environment. Detection of single damage state was investigated on the steel-free bridge deck, as well as one of the girders, while the simultaneous detection of multiple damage states was investigated on the second girder.

Finite element models of the bridge deck and girders were generated for the numerical portion of the study. Eigenvalue analyses of the FE model were used to

evaluate the capabilities of the damage detection methods in the absence of experimental uncertainties. In addition, transient dynamic analyses were used to investigate the use of random loading for damage detection.

8.2 CONCLUSIONS

8.2.1 Single damage detection on the bridge deck and the girder

Results of this study demonstrate that the five non-model based VBDD algorithms investigated are adequate for detecting and locating low levels of damage on a simply supported bridge deck or bridge girder. However, in order to take advantage of the potential of the algorithms, mode shapes must be known with a high level of accuracy since changes to mode shapes caused by low levels of damage are very small.

The type of dynamic excitation source used significantly affected the accuracy and repeatability of measured mode shapes; only harmonic vibration generated by a hydraulic shaker was found to successfully localize the small scale damage. White noise random vibration, ambient vibration, use of an impact hammer, and the dropping a sand bag achieved much lower accuracy of measured mode shapes, resulting in a failure to successfully detect small scale damage.

Electrical resistance strain gauges, configured to measure bending curvature, could be used to detect small scale damage, provided that harmonic vibration with large amplitudes was used. Accelerometers, on the other hand, were seen to be much less sensitive to noise due to their built-in amplifier, meaning that a large amplitude of vibration was not required to detect small scale damage.

In general, the use of higher modes in the experimental phase of the study did not result in successful damage detection because of the relatively larger measurement errors. Even in the absence of measurement uncertainties, the use of higher modes did not improve the performance of the techniques. In other words, higher modes do not necessarily improve, and may actually hinder successfully damage localization as compared to exclusive use of the fundamental mode.

In the numerical study, the resolution of damage localization was found to be 40% to 100% of the spacing between measurement points when a small number of measurement points were used, provided the damage was not located too near a support. Of the five VBDD techniques considered, the change in mode shape method performed the best, while the change in flexibility method was next best. When damage was located near a support, the resolution of damage localization was found to be approximately 0~30% greater than the distance from the support to the first measurement point.

In the experimental study, the resolution of damage localization was found to be 65% to 100% of the spacing between measurement points when a small number of measurement points were used, provided the damage was not located too near a support. This was slightly worse than that of the numerical study.

Both the numerical and experimental studies demonstrated that better accuracy for the damage localization was achieved when damage was located longitudinally closer to the nearest measurement point.

The five VBDD techniques investigated performed consistently on both the steel-free bridge deck and the prestressed concrete girder. This finding indicated these techniques could be used reliably on different types of structures.

The proposed transverse damage localization procedure worked very well in the absence of measurement uncertainties, but did not perform well experimentally due to inherent sensitivities to measurement uncertainties.

8.2.2 Multiple damage detection on the prestressed concrete girder

Both the numerical and experimental studies demonstrated the presence of multiple small-scale damage states inflicted simultaneously on a simply-supported prestressed concrete girder could reliably detected and located using the five VBDD techniques that employed measurements of only the fundamental mode shape before and after damage, provided that the damage was not located too near a simple support. When two separated damage states were located too close to each other, a single predicted location was generally observed.

The numerical study demonstrated that the resolution of damage detection was about double the spacing between measurement points, much worse than that found for detection of isolated damage states. In order to achieve the same level of resolution, a much larger number of measurement points were required for multiple damage detection than for single damage detection. Two separate damage states could not be distinguished if the distance between them was less than 180% of the spacing between measurement points; otherwise, a single predicted location resulted.

The mode shape curvature method, change in uniform flexibility curvature method and damage index method produced much better results for the multiple damage state tests than the change in mode shape method and the change in flexibility methods when a large number of measurement points were used. Higher modes did not improve the resolution of damage detection, and sometimes made the result worse, particularly when the damage index method was used and one of the damage states was located near a

nodal point of the higher mode. The change in flexibility method performed the worst in this phase, no matter how many measurement points were used, largely because damage states closer to the support were often not clearly identifiable.

The experimental study also demonstrated that the mode shape curvature method, change in uniform flexibility curvature method and damage index method achieved much better results for multiple damage states than either the change in mode shape method or the change in flexibility method, a conclusion that was consistent with results from the numerical study.

8.2.3 Random vibration on the steel-free bridge deck

The main conclusions of the transient dynamic analysis on a steel-free bridge deck are the following.

The probability of successfully locating the damage, and the resolution of the localization, were influenced by a number of factors: (1) an increase in the severity (size) of the damage enhanced the success rate and improved the resolution; (2) an increase in the number of repeated random trials used to generate averaged results for use in VBDD techniques was beneficial; (3) an increase in the distance, either longitudinally or laterally, between the damage and the nearest sensor location reduced the probability of successfully locating the damage and produced a decline in the resolution; (4) damage detection was least successful and had a poor resolution for damage located between a simple support and the nearest sensor location; and (5) random measurement errors further reduced the probability of successfully locating the damage and caused the resolution to decline.

A new index, β_{MAC}, defined as the ratio of the standard deviation to the mean of Modal Assurance Criteria (MACs) calculated based on the change of mode shape was a good indicator for predicting the presence of damage and indicating probability and likely resolution of successful damage localization. A lower ratio implied a higher probability of success and better resolution. This ratio enables a quantitative evaluation of VBDD results using random vibration independent from the need for a finite element model. If the findings of this study prove to be representative in general, this ratio would help make VBDD methods more practical for field tests.

8.3 RECOMMENDATIONS FOR FUTURE RESEARCH

It is suggested that the following areas of VBDD techniques be further investigated.

The study in this thesis focused on a simply supported deck and girders. More complex indeterminate structures, such as multiple span continuous beams, multiple-girder bridge decks should be investigated. The study in this thesis only investigated saw-cut forms of damage to the concrete deck surface. Other damage types, such as cracks or corrosion of the tendons in a prestressed concrete girder, or corrosion of rebar in reinforced concrete should be investigated. The effect of temperature on the dynamic characteristics of determinate and indeterminate structures should also be investigated. This could involve the use of numerical models to ascertain the principles underlying these effects, as well as experimental studies to find the patterns of mode shape associated with temperature effects. Transient dynamic analyses could be used to simulate the excitation of a bridge caused by traffic and wind. This could be used to

determine how the weight and speed of traffic affects dynamic test results. At the same time, through field testing, traffic and wind excitation could be compared to determine which one produces better repeatability of dynamic parameters.

A combination of the use of wavelet packets and neural networks may prove to be a powerful tool for damage detection, especially for traffic-like impulse excitation; these techniques should be investigated. Level-3 damage detection---determining the severity, degree, or extent of the damage--- should be investigated more systematically using VBDD techniques.

Finally, enhancements to data processing procedures may well improve VBDD results. For example, a cubic spline function was used in this study to interpolate the values of mode shapes between measurement points. However, the use of other interpolation methods may improve the resolution of damage localization of VBDD methods. Therefore, more work is suggested in this area.

REFERENCES

Adams, R.D., Walton, D., Flitcroft, J.E. and Short, D. 1975. Vibration testing as a non-destructive test tool for composite materials. Composite Reliability, ASTM STP 580, pp.159-175 (American Society For Testing and Materials).

Aktan, A.E., Lee, K.L., Chuntavan, C., and Aksel, T. 1994. Modal testing for structural identification and condition assessment of constructed facilities. Proceedings of the 12th International Modal Analysis Conference, Honolulu, H.I., pp. 462-468.

Allemang, R.J. 2002. The modal assurance criterion (MAC): twenty years of use and abuse. Proceedings of the 20th International Modal Analysis Conference, Los Angeles, Calif., pp. 397-405.

Amin Abdel Zeher, M.S. 2002. An integrated vibration-based structural health monitoring system. Ph.D. thesis, Dept. of Civil and Environmental Engineering, Carleton University, Ottawa, Canada.

ANSYS user's manual—version 7.1. 2003. ANSYS, Inc., Canonsburg, PA.

Bakht, B. and Csagoly, P.F. 1980. Diagnostic testing of a bridge. Journal of Structure Division, ASCE, **106**(7): 1515-1529.

Bakht, B. and Mufti, A.A. 1998. Five steel-free deck slabs in Canada. Structural Engineering International, **8**(3): 196-200.

Bathe, K.J., and Wilson, E.L. 1976. Numerical Methods in Finite Element Analysis. Prentice-Hall, Inc., Englewood Cliffs, N.J.

Beck, J.L. and Katafygiotis, L.S. 1992a. Probabilistic system identification and health monitoring of structures. Proceedings of the 10th World Conference on Earthquake Engineering, International Association for Earthquake Engineering, Tokyo, Japan, pp. 3721-3726.

Beck, J.L. and Katafygiotis. L.S. 1992b. Updating dynamic models and their associated uncertainties for structural systems. Proceedings of the 9th Conference on Engineering Mechanics, ASCE, New York, pp. 681-684.

Brincker, R., Zhang, L., and Anderson, P. 2000. Modal identification from ambient response using frequency domain decomposition. Proceedings of the 18th International Modal Analysis Conference, San Antonio, Texas, pp. 625-630.

Cartz, L. 1995. Non-destructive testing. ASM International, Materials Park, OH.

Casas, J.R. and Aparicio, A.C. 1994. Structural damage identification from dynamic-test data. Journal of Structural Engineering, ASCE, **120**(8): 2437-2450.

Catbas, F.N. and Aktan, A.E. 2002. Condition and damage assessment: issues and some promising indices. Journal of Structural Engineering, ASCE, **128**(8): 1026-1036.

Cawley, P. and Adams, R.D. 1979. The location of defects in structures from measurements of natural frequencies. Journal of Strain Analysis, **14**(2): 49-57.

Chance, J., Tomlinson, G.R. and Worden, K. 1994. A simplified approach to the numerical and experimental modeling of the dynamics of a cracked beam. Proceedings of the 12th International Modal Analysis Conference, pp. 778-785.

Chang, F.K., ed. 1997. Structural Health Monitoring: Current Status and Perspectives. Proceedings of the 1st International Workshop on Structural Health Monitoring, Stanford, CA, Technomic Publishing Co., Lancaster, PA.

Chang, F.K., ed. 1999. Structural Health Monitoring 2000. Proceedings of the 2nd International Workshop on Structural Health Monitoring, Stanford, CA, Technomic Publishing Co., Lancaster, PA.

Chase, S.B. and Washer G. 1997. Non-destructive evaluation for bridge management in the next century. Public Road, 61 (1), Available from http://www.tfhrc.gov/pubrds/july97/ndejuly.htm

Chen, S.E., Venkatappa, S., Petro, S. and GangaRao, H. 1999. Damage detection using 2-D strain energy distribution and scanning laser. Proceedings of the 17th International Modal Analysis Conference, pp. 869-875.

Chong, K.P., Carino, N.J., and Washer, G. 2001. Health monitoring of civil infrastructures. Health Monitoring and Management of Civil Infrastructure Systems, Proceedings of SPIE's International Symposium on NDE and Health Monitoring Diagnostics, Vol. 4337, S.B. Chase and A.E. Aktan, eds., SPIE, Bellingham, WA, pp. 1-16.

Clough, R.W. and Penzien, J. 1975. Dynamics of Structures. 2nd Edition, McGraw-Hill.

Doebling, S.W., Farrar, C.R., and Prime, M.B. 1998. A summary review of vibration-based damage identification methods. Shock Vibration Digest, **30**(2): 91-105.

Doebling, S.W., Farrar, C.R., Prime, M.B., and Shevitz, D.W. 1996. Damage identification and health monitoring of structural and mechanical systems from changes in their vibration characteristics: a literature review. Reprot No. LA 13070-MS, Los Alamos National Laboratory, Los Alamos, NM.

Ewins, D.J. 2000. Model Testing: Theory, Practice and Applications. 2nd Edition, Research Studies Press Ltd., Hertfordshire, England.

Fares, N. and Maloof, R. 1997. A probabilistic framework for detecting and identifying anomalies. Probability Engineering Mechcanics, **12**(2):63-73.

Farrar, C.R, Baker, W.E., Bell, T.M., Cone, K.M., Darling, T.W., Duffey, T.A., Eklund, A., and Migliori, A. 1994. Dynamic Characterization and Damage Detection in the I-40 Bridge Over the Rio Grande. Report No. LA 12767-MS, Los Alamos National Laboratory, Los Alamos, NM.

Farrar, C.R. and Jauregui, D.A. 1998a. Comparative study of damage identification algorithms applied to a bridge: I. Experiment. Smart Materials and Structures, **7:** 704-719.

Farrar, C.R. and Jauregui, D.A. 1998b. Comparative study of damage identification algorithms applied to a bridge: II. Numerical study. Smart Materials and Structures, **7:** 720-731.

Farrar, C.R. and Duffey, T.A. 1999. Vibration-based damage detection in rotating machinery. Key Engineering Materials, **167-168:** 224-235.

Federal Highway Administration (FHWA). 2001. Reliability of visual inspection. Report Nos. FHWA-RD-01-020 and FHWA-RD-01-021, Washington, DC.

Fox, C.H.J. 1992. The location of defects in structures: a comparison of the use of natural frequency and mode shape data. Proceedings of the10th International Modal Analysis Conference, San Diego, California, pp. 522-528.

Fujino, Y. and Abe, M. 2001. Structural Health Monitoring in Civil Infrastructures and R&D of SHM of Bridges at the University of Tokyo. Proceedings of the 3rd International Workshop on Structural Health Monitoring: The Demands and Challenges, Stanford, CA, USA, pp. 61-79.

Hajela, P. and Soeiro, F.J. 1990. Recent developments in damage detection based on system identification methods. Structural Optimization, **2**(1): 1-10.

Hou, Z., Noori, M., and St.Amand, R. 2000. Wavelet-based approach for structural damage detection. Journal of Engineering Mechanics Division, ASCE, **126**(7): pp. 667-683.

Hu, N., Wang, X., Fukunaga, H., Yao, Z.H., Zhang, H.X., and Wu, Z.S. 2001. Damage assessment of structures using modal test data. International Journal of Solid Structure, **38**(18): 3111-3126.

Hunt, D.L., Weiss, S.P., West, W.M., Dunlap, T.A., and Freemeyer, S.R. 1990. Development and implementation of a shuttle modal inspection system. Sound and Vibration, **24**(8): 34-42.

Jauregui, D.V. and Farrar, C.R. 1996. Comparison of damage identification algorithms on experimental modal data from a bridge. Proceedings of the 14th International Modal Analysis Conference, Dearborn, MI, pp. 1423-1429.

Jenkins, C.H., Kjerengtroen, L., and Oestensen, H. 1997. Sensitivity of parameter changes in structural damage detection. Shock and Vibration, **4**(1): 27-37.

Kim, J.T. and Stubbs, N. 1995. Model uncertainty impact and damage-detection accuracy in plate girder. Journal of Structural Engineering, ASCE, **121**(10): 1409-1417.

Kim, J.T. and Stubbs, N. 2003. Non-destructive crack detection algorithm for full-scale bridges. Journal of Structural Engineering, ASCE, **129**(10): 1358-1366.

Kitada, Y. 1998. Identification of nonlinear structural dynamic systems using wavelets. Journal of Engineering Mechanics Division, ASCE, **124**: 1059-1066.

LabView™—version 6i. 2000. National Instruments Corporation, Austin, Texas.

Loland, O. and Dodds, J.C. 1976. Experience in developing and operating integrity monitoring system in North Sea. Proceedings of the 8th Annual Offshore Technology Conference, pp. 313-319.

Masri, S.F., Chassiakos, A.G., and Caughey, T.K., 1993. Identification of nonlinear dynamic system using neural networks, Journal of Applied Mechanics, **60**: 123-133.

Masri, S.F., Nakamura, M., Chassiakos, A.G., and Caughey, T.K. 1996. Neural network approach to detection of changes in structural parameters. Journal of Engineering Mechanics, ASCE, **122**(4): 350-360.

Masri, S.F., Smyth, A.W., Chassiakos, A.G., Caughey, T.K., and Hunter, N.F. 2000. Application of neural networks for detection of changes in nonlinear systems. Journal of Engineering Mechanics, ASCE, **126**(7): 666-676.

MathCAD 2000 Professional user's Manual. Mathsoft, Inc. Cambridge, MA.

Mayes, R.L. 1995. An experimental algorithm for detecting damage applied to I-40 bridge over Rio Grande. Proceedings of the 13th International Modal Analysis Conference, Nashville, TN, pp. 219-225.

Microsoft Office Excel 2003 user's Manual, 2003. Microsoft Corporation, Seattle, WA.

Mufti, A.A. 2001. Guidelines for Structural Health Monitoring. ISIS Canada (The Canadian Network of Centres on Intelligent Sensing for Innovative Structures), Design Manual No.2, Sept. 2001.

Mufti, A.A., Jaeger, L.G., Bakht, B., and Wegner, L.D. 1993. Experimental investigation of FRC deck slabs without internal steel reinforcement. Canadian Journal of Civil Engineering, **20**(3): 398-406.

Nasser, H., Mevel, L. and Chapelle, D. 2005. Damage detection under environmental perturbation. Proceedings of the 23rd International Modal Analysis Conference, Orlando, Florida, Paper No. 114, (CD-ROM).

Newhook, J.P. and Mufti, A.A. 1996. A reinforcing steel-free concrete deck slab for the Salmon River Bridge. Concrete International, **18**(6): 30-34.

Pai, P.F. and Young, L.G. 2001. Damage detection of beams using operational deflection shapes. International Journal of Solids and Structures, **38**(8): 3161-3192.

Pandey, A.K. and Biswas, M. 1994. Damage detection in structures using changes in flexibility. Journal of Sound Vibration, **169**(1): 3-17.

Pandey, A.K., Biswas, M., and Samman, M.M. 1991. Damage detection from changes in curvature mode shapes. Journal of Sound Vibration, **145**(2): 321-332.

Peeters, B. 2000. System identification and damage detection in civil engineering. Ph.D. thesis, Dept. of Civ. Engrg., Katholieke Universiteit Leuven, Belgium.

Proakis, J.G. and Manolakis, D.G. 1992. Digital signal processing-Principles, algorithms, and applications. Macmillan Publishing Company, New York.

Raj, B., Jayakumar, T., and Thavasimuthu, M. 2002. Practical non-destructive testing. 2nd ed., Narosa Publishing House, New Delhi, India.

Ramirez, R.W. 1985. The FFT: Fundamentals and Concepts. Prentice-Hall, Englewood Cliffs, New Jersey, USA.

Roth, J.T. and Pandit, S.M. 1999. Condition monitoring and failure prediction for various rotating equipment components. Proceedings of the 17th International Modal Analysis Conference, Kissimee, Florida, pp. 1674-1680.

Rytter, A. 1993. Vibration-based inspection of civil engineering structures. Doctoral Dissertation, Department of Building Technology and Structural Engineering, University of Aalborg, Aalborg, Denmark.

Salawu, O.S. 1997. Detection of structural damage through changes in frequency: a review. Engineering Structures, **19**(9): 718-723.

Salawu, O.S. and Williams, C. 1995. Bridge assessment using forced-vibration testing. Journal of structural engineering, **121**(2): 161-173.

Salawu, O.S. and Williams, C. 1994. Damage location using vibration mode shapes. Proceedings of the 12th International Modal Analysis Conference, Honolulu, HI, pp. 933-939.

Schulz, J.L., Command, B., Goble, G.G. and Frangopol, D.M. 1995. Efficient field testing and load rating of short- and medium-span bridges. Structural Engineering Review, **7**(3): 181-194.

Shih, C.Y., Tsuei, Y.G., Allemang, R.J., and Brown, D.L. 1998. Complex mode indication function and its application to spatial domain parameter estimation. Mechanical System and Signal Processing, **2**(4): 367-377.

Shives, T.R. and Mertaugh, L.J. eds. 1986. Detection, diagnosis and prognosis of rotating machinery to improve reliability, maintainability, and readiness through the application of new and innovative techniques. Cambridge University Press, Cambridge, UK.

Srinivasan, M.G. and Kot, C.A. 1992. Effects of damage on the modal parameters of a cylindrical shell. Proceedings of the 10th International Modal Analysis Conference, San Diego, Calif., pp. 529-535.

Steenackers, G. and Guillaume, P. 2005. Structural health monitoring of the Z-24 Bridge in presence of environmental changes using modal analysis. Proceedings of the 23rd International Modal Analysis Conference, Orlando, Florida, Paper No. 297, (CD-ROM)

Stubbs, N., Kim, J.T., and Topple, K. 1992. An effect and robust algorithm for damage localization I offshore platforms. Proceedings of ASCE 10th Structural Congress, San Antonio, Texas, pp. 543-546.

Stubbs, N. and Kim, Y.I. 1995. Field verification of a non-destructive damage localization and severity estimation algorithm. Proceedings of the 13th International Modal Analysis Conference, Nashville, TN, pp. 210-218.

Toksoy, T. and Aktan, A.E. 1994. Bridge-condition assessment by modal flexibility. Experimental Mechanics, **34**(3): 271-278.

Uomoto, T., ed. 2000. Non-destructive testing in civil engineering 2000. Elsevier Science Ltd., Amsterdam.

Ventura, C.E., Brincker, R., Andersen, P., and Cantieni, R. 2002. Identification and damage detection studies of the Z24 highway bridge in Switzerland. Proceedings of the 6th International Conference on Short and Medium-span Bridges, Vancouver, Canada, pp. 851-858.

Wang, Q., and Deng, X. 1999. Damage detection with spatial wavelets. International Journal of Solids Structures, **36**(23): 3443-3468.

West, W.M. Jr. 1982. Single point random model test technology application to failure detection. Shock and Vibration Bulletin, May, pp. 25-31.

West, W.M., 1984. Illustration of the use of Model Assurance Criterion to detect structural changes in an orbit test specimen. Proceedings of Air Force Conference on Aircraft Structural Integrity, pp. 1-6.

Wu, X., Ghaboussi, J. and Garrett, J.H. Jr. 1992. Use of neural networks in detection of structural damage. Computation Structure, **42**(4): 649-659.

Younger, M.S. 1979. Handbook for Linear Regression. Duxbury Press, North Scituate, Massachusetts, pp. 28-37.

Zhang, Z. and Aktan, A.E. 1995. The damage indices for constructed facilities. Proceedings of the 13th International Modal Analysis Conference, Nashville, TN, pp. 1520-1529.

Zhang, Z. and Aktan, A.E. 1998. Application of modal flexibility and its derivatives in structural identification. Research of Non-destructive Evaluation, **10**(1): 43-61.

Zimmerman, D.C. and Kaouk, M. 1994. Structural damage detection using a minimum rank update theory. Journal of Vibration and Acoustics, ASME, **116**(2): 222-231.

Zimmerman, D.C. and Kaouk, M. 1992. Structural damage detection using a subspace rotation algorithm. Proceedings of the AIAA/ASME/ASCE/AHS/ASC, 33rd structures structural dynamics and materials conference, Dallas, Texas, pp. 2341-2350.

Zimmerman, D.C. and Smith, S.W. 1992. Model refinement and damage location for intelligent structures. Intelligent structural systems. H.S. Tzou and G.L. Anderson, eds., Boston: Kluwer Academic Publishers. pp. 403-452.

Appendix A. The procedure of the deflection deriving from acceleration

The procedure of the deflection deriving from acceleration is shown in Fig. A1.

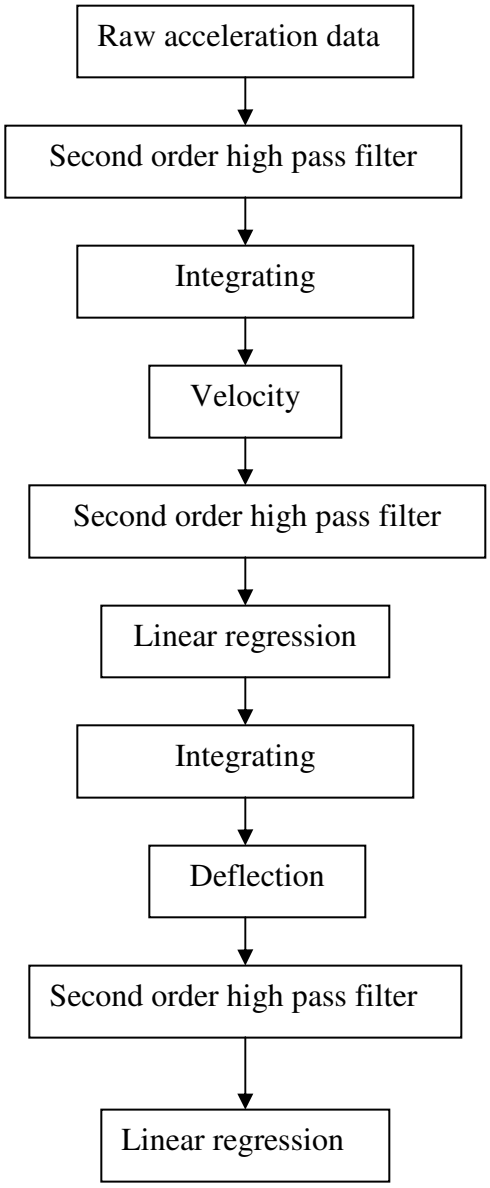

Figure A.1 The framework of deriving deflection from acceleration

Each step is described as follows.

Step 1. Using a second order high pass filter to remove the drift of the raw acceleration data (Proakis 1992).

$$A_i^* = (1+\alpha)A_{i-1}^* - \alpha A_{i-2}^* + (1+\alpha)\frac{A_i - 2A_{i-1} + A_{i-2}}{2} \qquad [A.1]$$

where A_i, A_{i-1}, and A_{i-2} are the raw acceleration data before filtering. A_i^*, A_{i-1}^*, and A_{i-2}^* are filtered acceleration, i is the number of the acceleration sequence, α is the coefficient of filter, its value is between 0 and 1.0.

Step 2. Integrating acceleration A_i^* to obtain the velocity V_i

$$V_i = V_{i-1} + \frac{\Delta t}{2}(A_i^* + A_{i-1}^*) \qquad [A.2]$$

where Δt is the interval of the sampling of acceleration.

Step 3. Using a second order high pass filter to remove the drift of the velocity V_i

$$V_i^* = (1+\alpha)V_{i-1}^* - \alpha V_{i-2}^* + (1+\alpha)\frac{V_i - 2V_{i-1} + V_{i-2}}{2} \qquad [A.3]$$

Where V_i^*, V_{i-1}^*, and V_{i-2}^* are filtered velocities.

Step 4. Using a linear regression to remove the linear trend of the velocity sequence (Younger 1979).

$$V_i^{**} = V_i^* - (\gamma i + \frac{\sum_{i=1}^{N} V_i^* - \gamma \sum_{i=1}^{N} i}{N}), \text{ and } \quad \gamma = \frac{N\sum_{i=1}^{N} iV_i^* - \sum_{i}^{N} i \sum_{i=1}^{N} V_i^*}{N\sum_{i=1}^{N} i^2 - \left(\sum_{i=1}^{N} i\right)^2} \qquad [A.4]$$

Where ***N*** is the total number of the velocity sequence.

Step 5. Integrating velocity V_i^{**} to obtain the deflection D_i

$$D_i = D_{i-1} + \frac{\Delta t}{2}(V_i^{**} + V_{i-1}^{**}) \qquad [A.5]$$

Step 6. Using a second order high pass filter to remove the drift of the deflection D_i

$$D_i^* = (1+\alpha)D_{i-1}^* - \alpha D_{i-2}^* + (1+\alpha)\frac{D_i - 2D_{i-1} + D_{i-2}}{2} \qquad [A.6]$$

Where D_i^*, D_{i-1}^*, and D_{i-2}^* are filtered deflection.

Step 7. Using a linear regression to remove the linear trend of the velocity sequence.

$$D_i^{**} = D_i^* - (\gamma i + \frac{\sum_{i=1}^{N} D_i^* - \gamma \sum_{i=1}^{N} i}{N}), \text{ and } \quad \gamma = \frac{N\sum_{i=1}^{N} iD_i^* - \sum_{i}^{N} i \sum_{i=1}^{N} D_i^*}{N\sum_{i=1}^{N} i^2 - \left(\sum_{i=1}^{N} i\right)^2} \qquad [A.7]$$

D_i^{**} is the deflection of the beam in vibration, can be used to obtain deflection mode shapes by applying Parzen window and FFT.

Appendix B. Implementation of five VBDD methods on MathCAD

Introduction: This is an example of multiple damage detection of VBDD methods on a prestressed concrete girder. The mode shapes are from the accelerometer data. Only the first mode is used in this example.

Step 1. Input the values of mode shapes at each measurement point before and after damage in matrix form.

The mode shape before damage was induced.

$$Y_{i1} := \begin{pmatrix} 0 \\ 0.198825 \\ 0.358543 \\ 0.461914 \\ 0.498733 \\ 0.458392 \\ 0.350307 \\ 0.192296 \\ 0 \end{pmatrix}$$

The mode shape after damage was induced.

$$Y_{d1} := \begin{pmatrix} 0 \\ 0.198683 \\ 0.358397 \\ 0.462026 \\ 0.498755 \\ 0.458628 \\ 0.350225 \\ 0.191978 \\ 0 \end{pmatrix}$$

Location of measurement points $j := 1, 2 .. 9$ $x_j := (j - 1) \cdot 1.5$

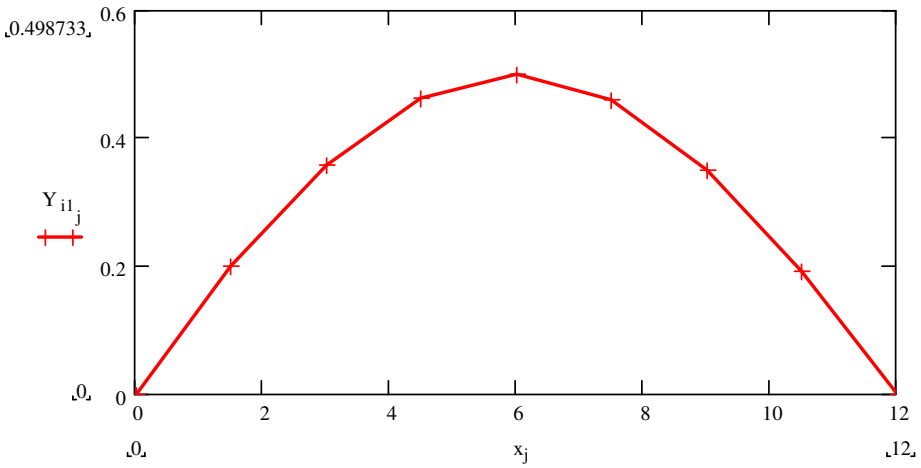

Figure B.1 The mode shape before damage before curve fitting

Step 2. Use conventional cubic spline to fit the mode shapes

The coefficient of cubic spline for the mode shape before damage

$$vs1 := cspline\left(x, Y_{i1}\right)$$

Location of measurement points from west support

Generate the locations of the intermediate points between measurement points

$$xi := \left| \begin{array}{l} \text{for } i \in 1..81 \\ \quad x_i \leftarrow \dfrac{i-1}{10} \cdot 1.5 \\ x \end{array} \right.$$

Get the values of the mode shape before damage of the intermediate points between measurement points

$$Z_{i1} := interp\left(vs1, x, Y_{i1}, xi\right)$$

The mode shape after damage can be curve fitted by same procedure.

Step 3. Normalizing the mode shapes

$$Z_{i1} := \frac{Z_{i1}}{\left[\left(Z_{i1}^{T} \cdot Z_{i1}\right)^{0.5}\right]_1}$$

Convert the vector to scalar

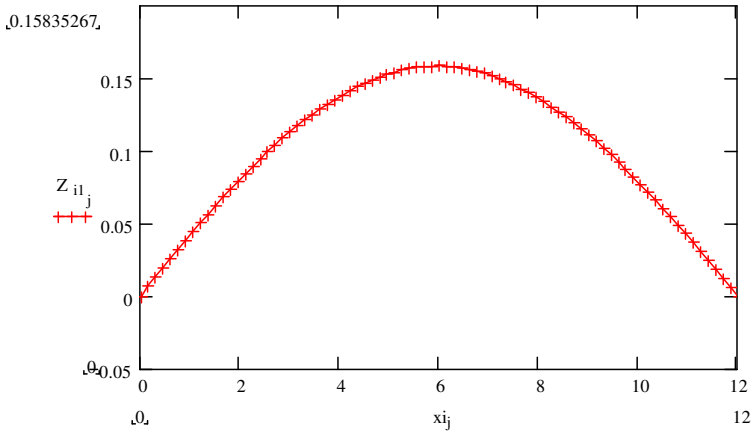

Figure B.2 The unit-mass normalized mode shape before damage by the curve fitting method

Step 4. Applying each method on the unit-mass normalized mode shapes

A. Change in mode shape method

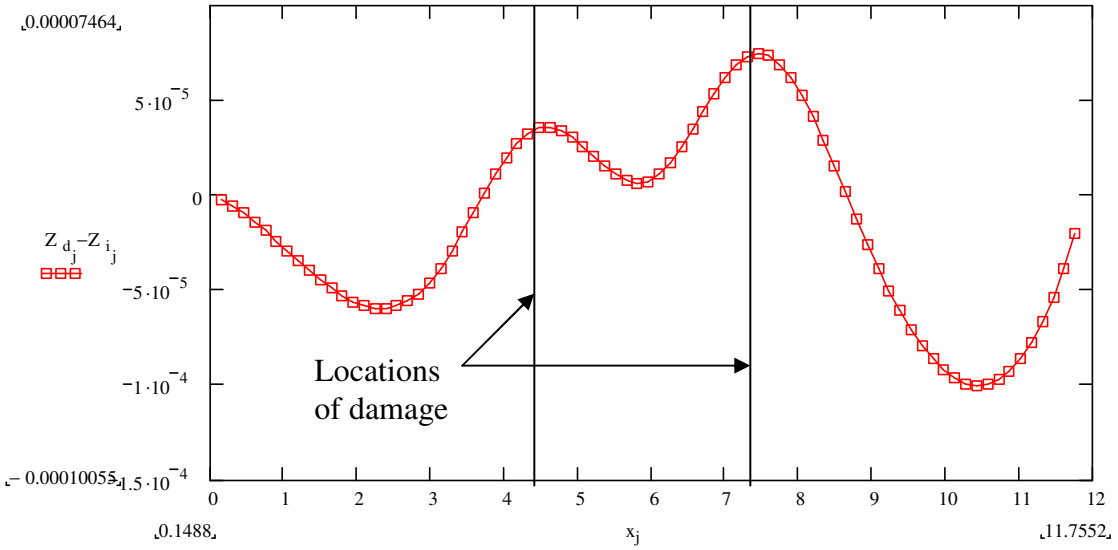

Figure B.3 Change in mode shape method detects the damage

B. Mode shape curvature method

$$v_{i1} := \left| \begin{array}{l} \text{for } j \in 2..80 \\ \quad v_j \leftarrow \left(Z_{i1_{j+1}} + Z_{i1_{j-1}} - 2 \cdot Z_{i1_j}\right) \\ v \end{array} \right.$$

$$v_{d1} := \left| \begin{array}{l} \text{for } j \in 2..80 \\ \quad v_j \leftarrow \left(Z_{d1_{j+1}} + Z_{d1_{j-1}} - 2 \cdot Z_{d1_j}\right) \\ v \end{array} \right.$$

$$v := \overrightarrow{|v_{d1}|} - \overrightarrow{|v_{i1}|}$$

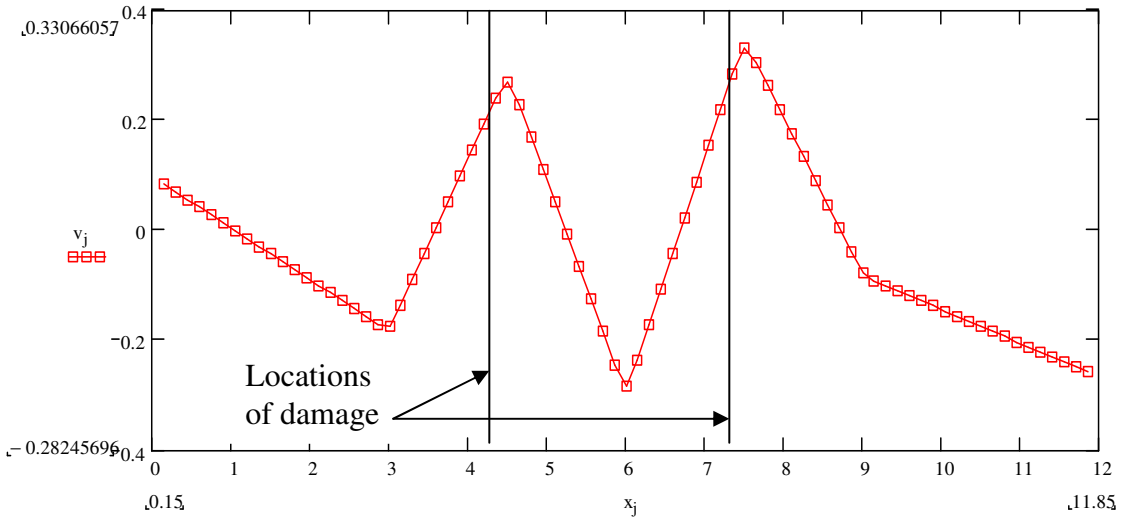

Figure B.4 Mode shape curvature method

C. Damage index method

$$A_{i1} := \left| \begin{array}{l} a \leftarrow 0 \\ \text{for } j \in 2..80 \\ \quad a \leftarrow a + \left(Z_{i_{j+1}} + Z_{i_{j-1}} - 2 \cdot Z_{i_j}\right)^2 \\ a \end{array} \right| \qquad A_{d1} := \left| \begin{array}{l} a \leftarrow 0 \\ \text{for } j \in 2..80 \\ \quad a \leftarrow a + \left(Z_{d_{j+1}} + Z_{d_{j-1}} - 2 \cdot Z_{d_j}\right)^2 \\ a \end{array} \right|$$

$$v_{i1} := \left| \begin{array}{l} \text{for } j \in 2..80 \\ \quad v_j \leftarrow \left(Z_{i_{j+1}} + Z_{i_{j-1}} - 2 \cdot Z_{i_j}\right)^2 \\ v \end{array} \right| \qquad v_{d1} := \left| \begin{array}{l} \text{for } j \in 2..80 \\ \quad v_j \leftarrow \left(Z_{d_{j+1}} + Z_{d_{j-1}} - 2 \cdot Z_{d_j}\right)^2 \\ v \end{array} \right|$$

$$\beta := \left| \begin{array}{l} \text{for } j \in 2..80 \\ \quad b_j \leftarrow \dfrac{\left[\left(v_{d1_j} + A_{d1}\right) \cdot A_{i1}\right]}{\left(v_{i1_j} + A_{i1}\right) \cdot A_{d1}} \\ b \end{array} \right|$$

$$\mu := \left| \begin{array}{l} b \leftarrow 0 \\ \text{for } j \in 2..80 \\ \quad b \leftarrow b + \beta_j \\ c \leftarrow \dfrac{b}{79} \\ c \end{array} \right| \qquad \sigma := \left| \begin{array}{l} b \leftarrow 0 \\ \text{for } j \in 2..80 \\ \quad b \leftarrow b + \left(\beta_j - \mu\right)^2 \\ c \leftarrow \sqrt{\dfrac{b}{78}} \\ c \end{array} \right| \qquad Z := \left| \begin{array}{l} \text{for } j \in 2..80 \\ \quad z_j \leftarrow \dfrac{\left(\beta_j - \mu\right)}{\sigma} \\ z \end{array} \right|$$

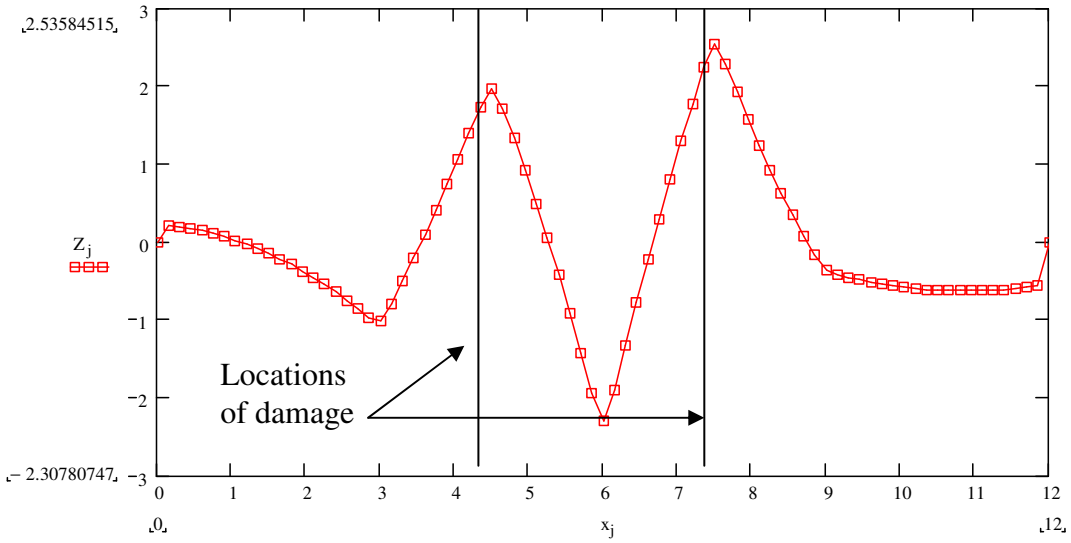

Figure B.5 Damage index method

D. Change in flexibility method

First natural frequency before damage

$$\lambda_{i1} := (7.561342 \cdot \pi)^2$$

First natural frequency after damage

$$\lambda_{d1} := (7.560082 \cdot \pi)^2$$

$$F := \frac{1}{\lambda_{i1}} \cdot Z_i \cdot Z_i^T$$

$$F_d := \frac{1}{\lambda_{d1}} \cdot Z_d \cdot Z_d^T$$

$$\Delta := F - F_d$$

$$\begin{aligned}
&\delta := \left| \begin{array}{l}
\text{for } j \in 1..80 \\
\quad a_1 \leftarrow \max(|\Delta_{1,j}|, |\Delta_{2,j}|, |\Delta_{3,j}|, |\Delta_{4,j}|, |\Delta_{5,j}|, |\Delta_{6,j}|, |\Delta_{7,j}|, |\Delta_{8,j}|, |\Delta_{9,j}|, |\Delta_{10,j}|) \\
\quad a_2 \leftarrow \max(|\Delta_{11,j}|, |\Delta_{12,j}|, |\Delta_{13,j}|, |\Delta_{14,j}|, |\Delta_{15,j}|, |\Delta_{16,j}|, |\Delta_{17,j}|, |\Delta_{18,j}|, |\Delta_{19,j}|, |\Delta_{20,j}|) \\
\quad a_3 \leftarrow \max(|\Delta_{31,j}|, |\Delta_{32,j}|, |\Delta_{33,j}|, |\Delta_{34,j}|, |\Delta_{35,j}|, |\Delta_{36,j}|, |\Delta_{37,j}|, |\Delta_{38,j}|, |\Delta_{39,j}|, |\Delta_{40,j}|) \\
\quad a_4 \leftarrow \max(|\Delta_{41,j}|, |\Delta_{42,j}|, |\Delta_{43,j}|, |\Delta_{44,j}|, |\Delta_{45,j}|, |\Delta_{46,j}|, |\Delta_{47,j}|, |\Delta_{48,j}|, |\Delta_{49,j}|, |\Delta_{50,j}|) \\
\quad a_5 \leftarrow \max(|\Delta_{51,j}|, |\Delta_{52,j}|, |\Delta_{53,j}|, |\Delta_{54,j}|, |\Delta_{55,j}|, |\Delta_{56,j}|, |\Delta_{57,j}|, |\Delta_{58,j}|, |\Delta_{59,j}|, |\Delta_{60,j}|) \\
\quad a_6 \leftarrow \max(|\Delta_{21,j}|, |\Delta_{22,j}|, |\Delta_{23,j}|, |\Delta_{24,j}|, |\Delta_{25,j}|, |\Delta_{26,j}|, |\Delta_{27,j}|, |\Delta_{28,j}|, |\Delta_{29,j}|, |\Delta_{30,j}|) \\
\quad a_7 \leftarrow \max(|\Delta_{61,j}|, |\Delta_{62,j}|, |\Delta_{63,j}|, |\Delta_{64,j}|, |\Delta_{65,j}|, |\Delta_{66,j}|, |\Delta_{67,j}|, |\Delta_{68,j}|, |\Delta_{69,j}|, |\Delta_{70,j}|) \\
\quad a_8 \leftarrow \max(|\Delta_{71,j}|, |\Delta_{72,j}|, |\Delta_{73,j}|, |\Delta_{74,j}|, |\Delta_{75,j}|, |\Delta_{76,j}|, |\Delta_{77,j}|, |\Delta_{78,j}|, |\Delta_{79,j}|, |\Delta_{80,j}|) \\
\quad \delta_j \leftarrow \max(a_1, a_2, a_3, a_4, a_5, a_6, a_7, a_8) \\
\delta
\end{array} \right.
\end{aligned}$$

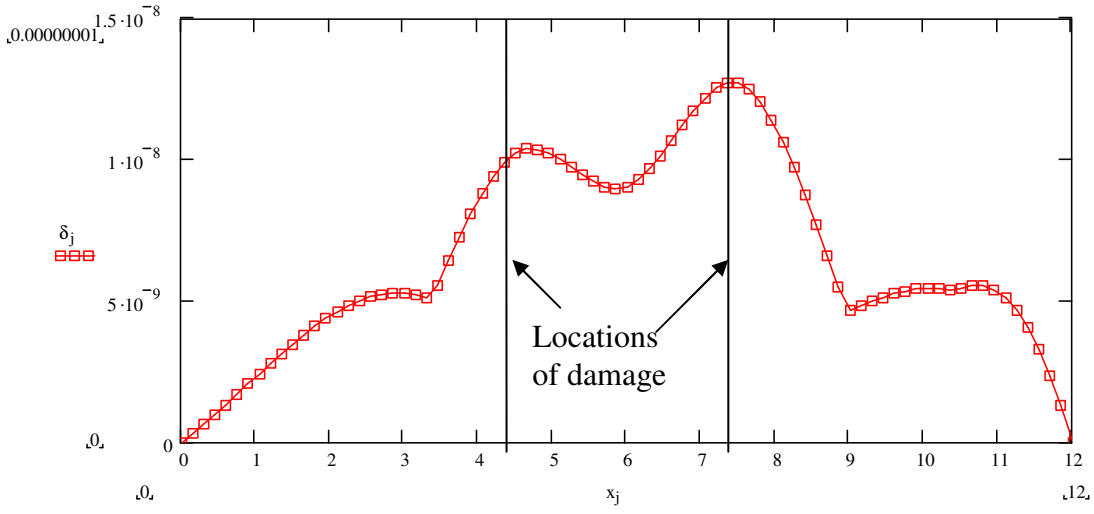

Figure B.6 Change in flexibility method

E. Change in uniform flexibility curvature method

First natural frequency before damage

$\lambda_{i1} := (7.56134 \cdot 2 \cdot \pi)^2$ $\quad K := (\lambda_{i1})^{-1} \cdot Z_i \cdot Z_i^T$

First natural frequency after damage

$\lambda_{d1} := (7.56008 \cdot 2 \cdot \pi)^2$ $\quad K_d := (\lambda_{d1})^{-1} \cdot Z_d \cdot Z_d^T$

$f :=$ for $i \in 1..81$: $f_i \leftarrow 0$; for $j \in 1..81$: $f_i \leftarrow f_i + K_{i,j}$; f

$f_d :=$ for $i \in 1..81$: $f_i \leftarrow 0$; for $j \in 1..81$: $f_i \leftarrow f_i + Kd_{i,j}$; f

$F :=$ for $j \in 2..80$: $F_j \leftarrow (f_{j+1} + f_{j-1} - 2 \cdot f_j)$; F

$F_d :=$ for $j \in 2..80$: $F_{d_j} \leftarrow (f_{d_{j+1}} + f_{d_{j-1}} - 2 \cdot f_{d_j})$; F_d

$\Delta F := F - F_d$

$\Delta :=$ for $j \in 2..80$: $a_j \leftarrow \Delta F_j$; a

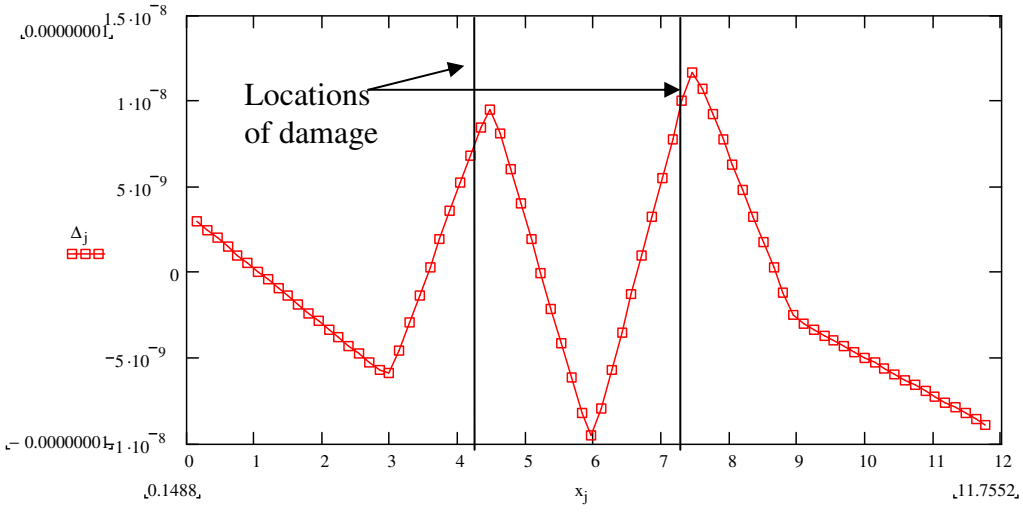

Figure B.7 Change in uniform flexibility curvature method

Appendix C. Damage detection on a bridge deck using strain gauges

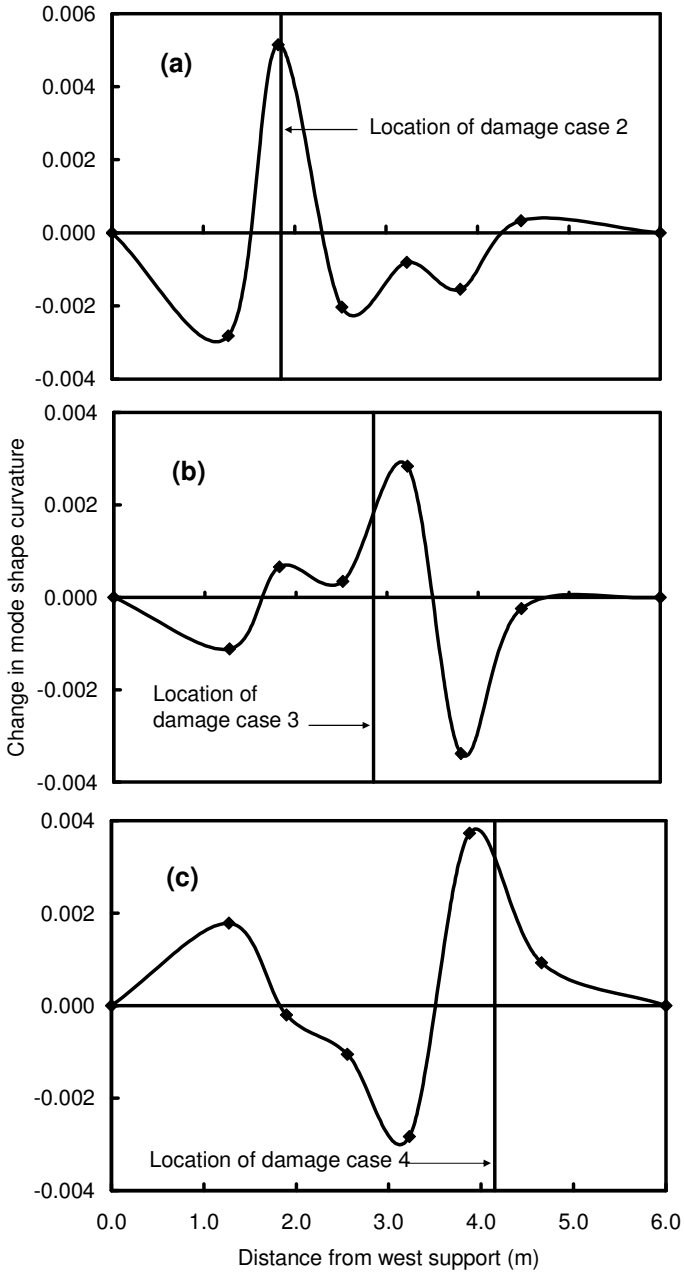

Figure C.1. Change in mode shape curvature along south girder for a) damage case 2, and damage case b), and along north girder for c) damage case 4, calculated using strain gauge measured curvature.

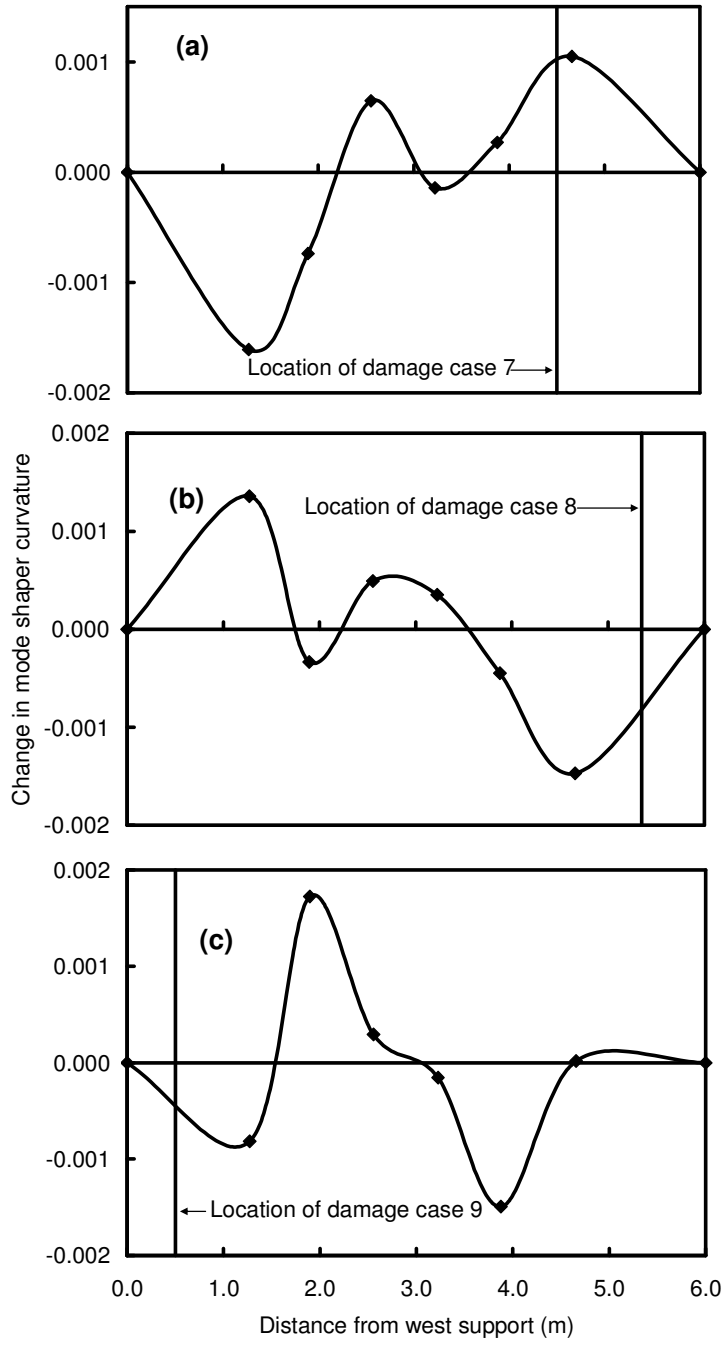

Figure C.2. Change in mode shape curvature along north girder, calculated using strain gauge measured curvature for a) damage case 7, b) damage case 8, and c) damage case 9.

Appendix D. Damage detection on a bridge deck using accelerometers

Five VBDD methods were used to detect damage on the bridge deck in following figures, (a) change in mode shape method, (b) mode shape curvature method, (c) change in flexibility method, (d) damage index method, and (e) change in uniform flexibility curvature method.

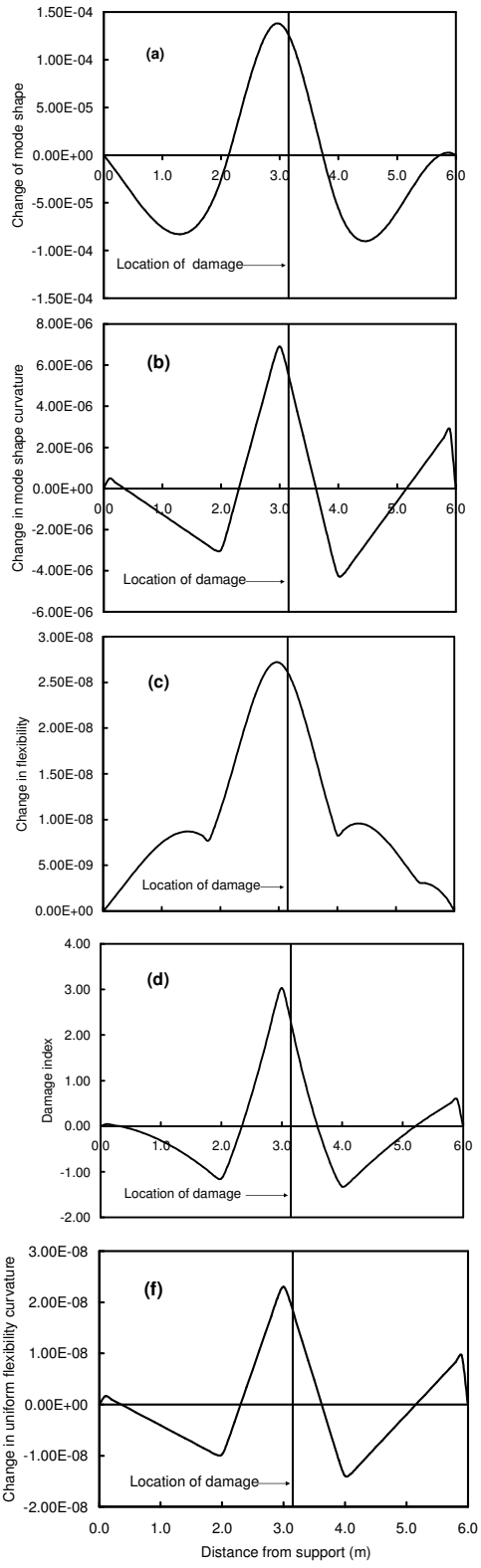

Figure D.1. Localization of damage case 1 of the bridge deck

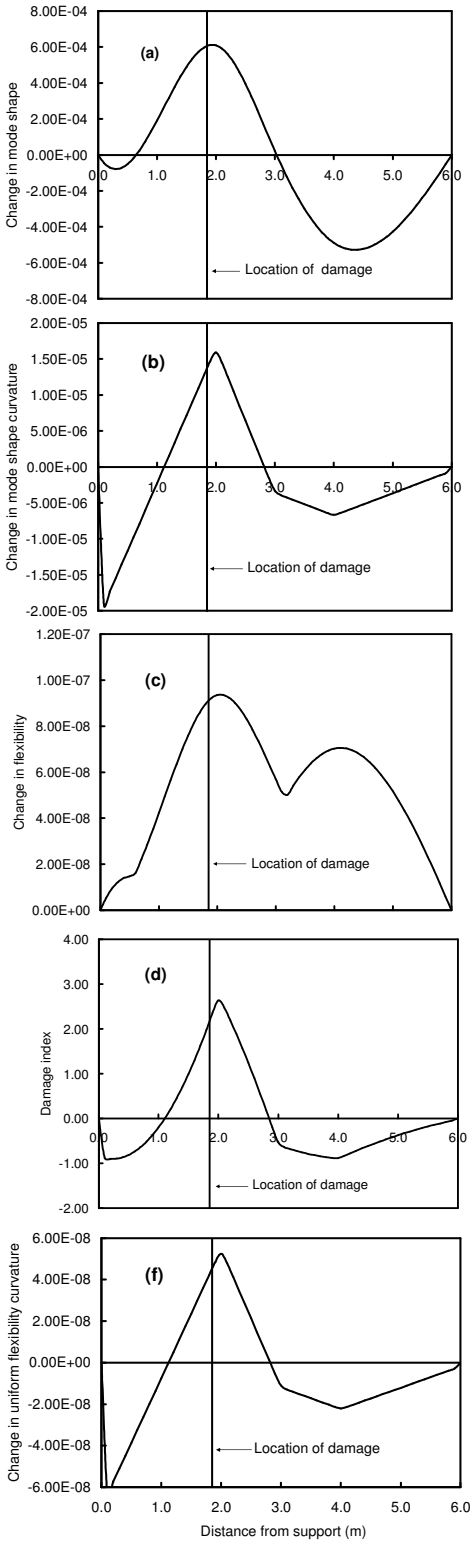

Figure D.2. Localization of damage case 2 of the bridge deck

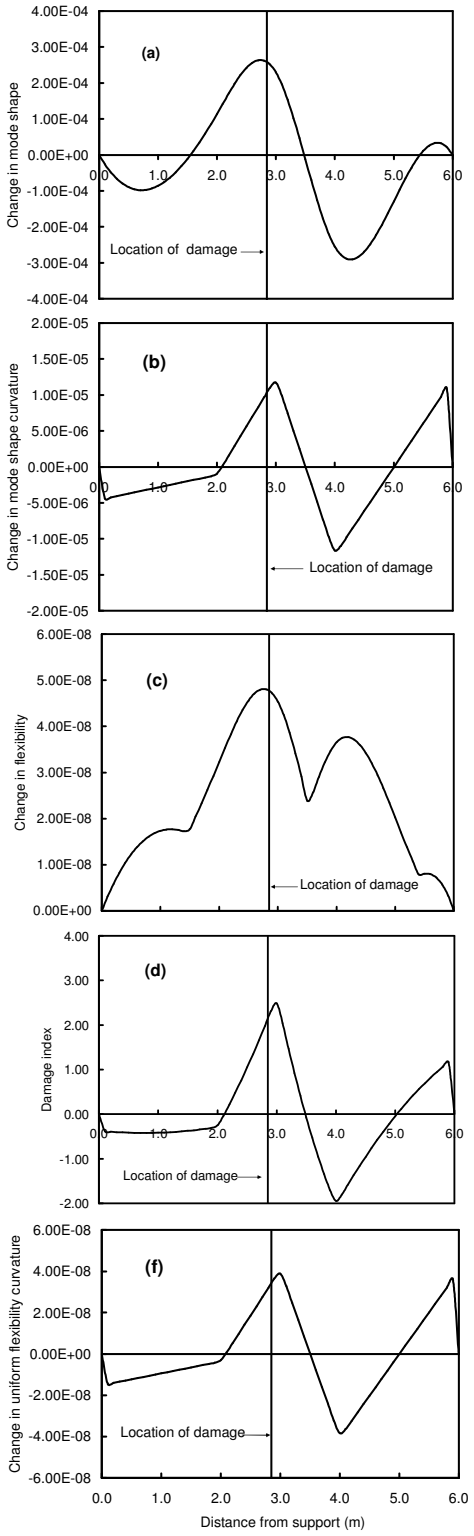

Figure D.3. Localization of damage case 3 of the bridge deck

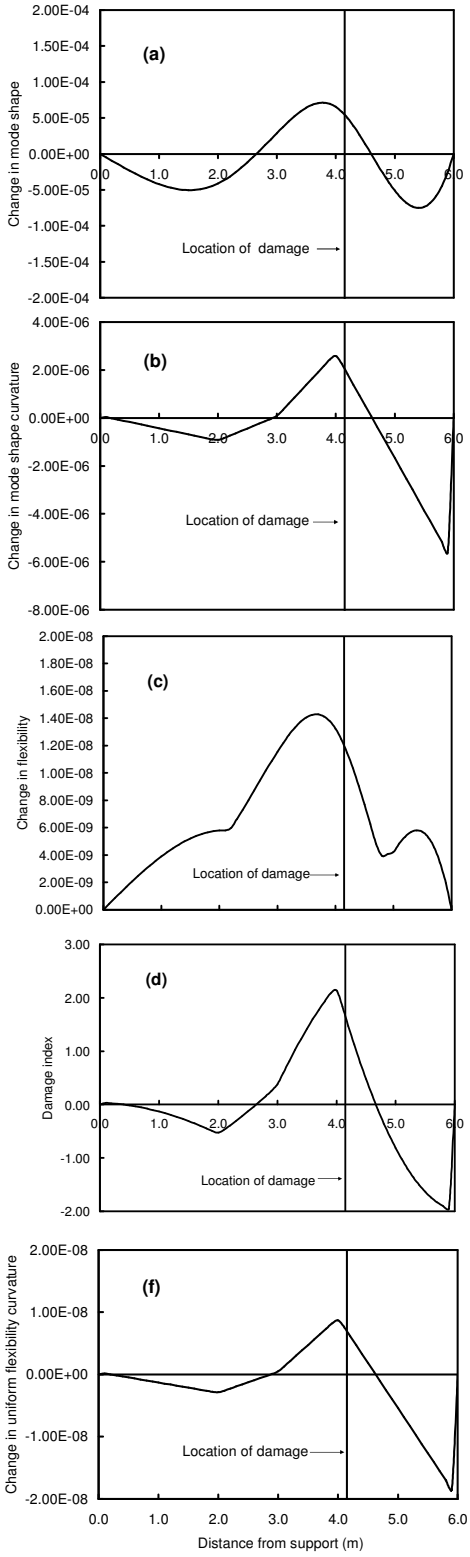

Figure D.4. Localization of damage case 4 of the bridge deck

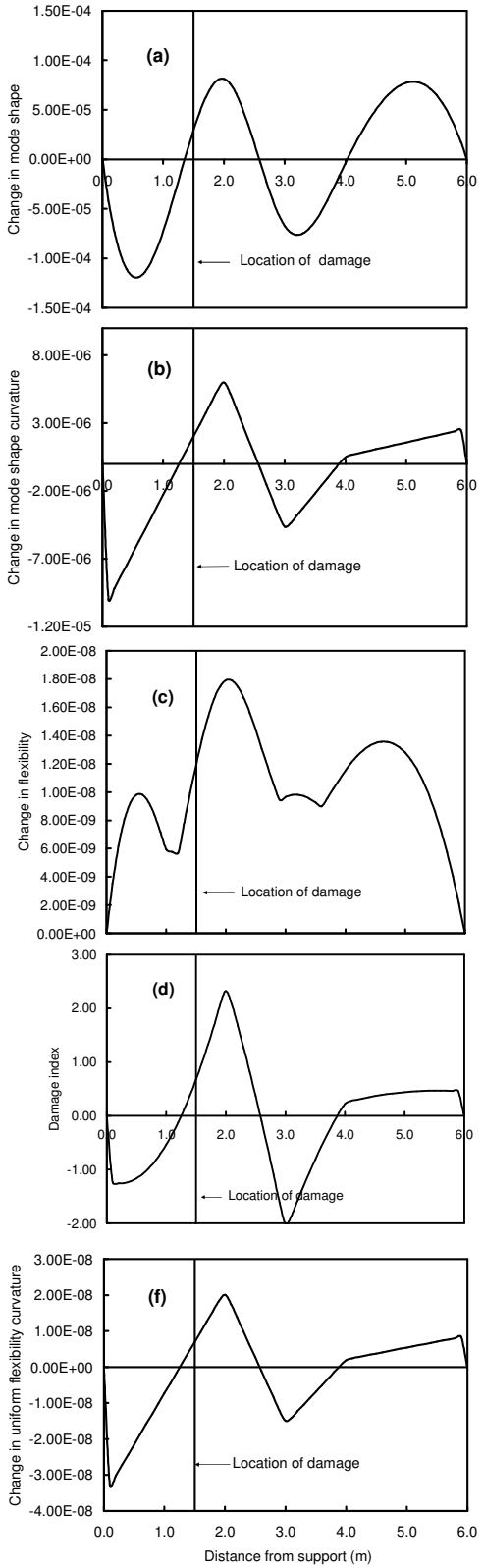

Figure D.5. Localization of damage case 5 of the bridge deck

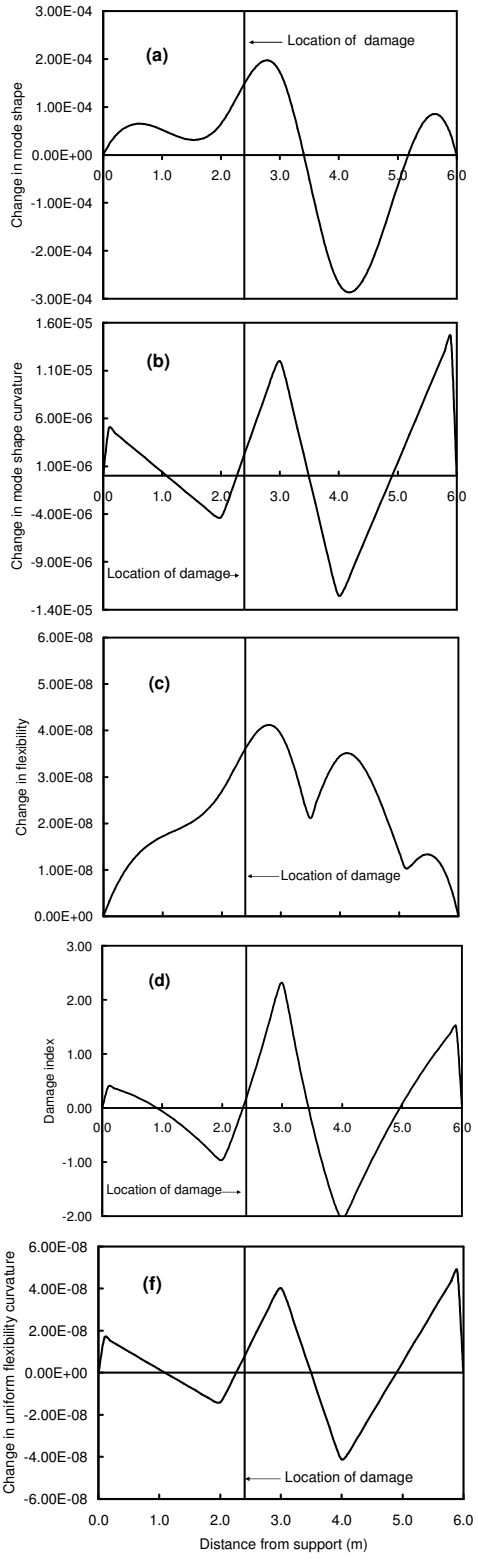

Figure D.6. Localization of damage case 6 of the bridge deck

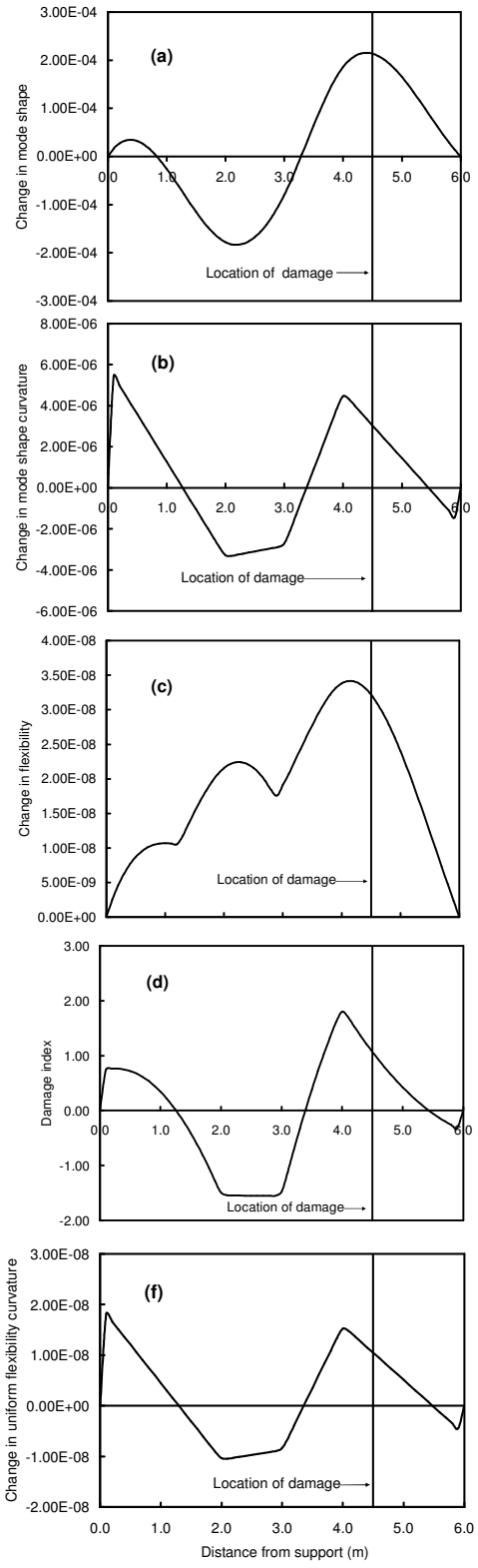

Figure D.7. Localization of damage case 7 of the bridge deck

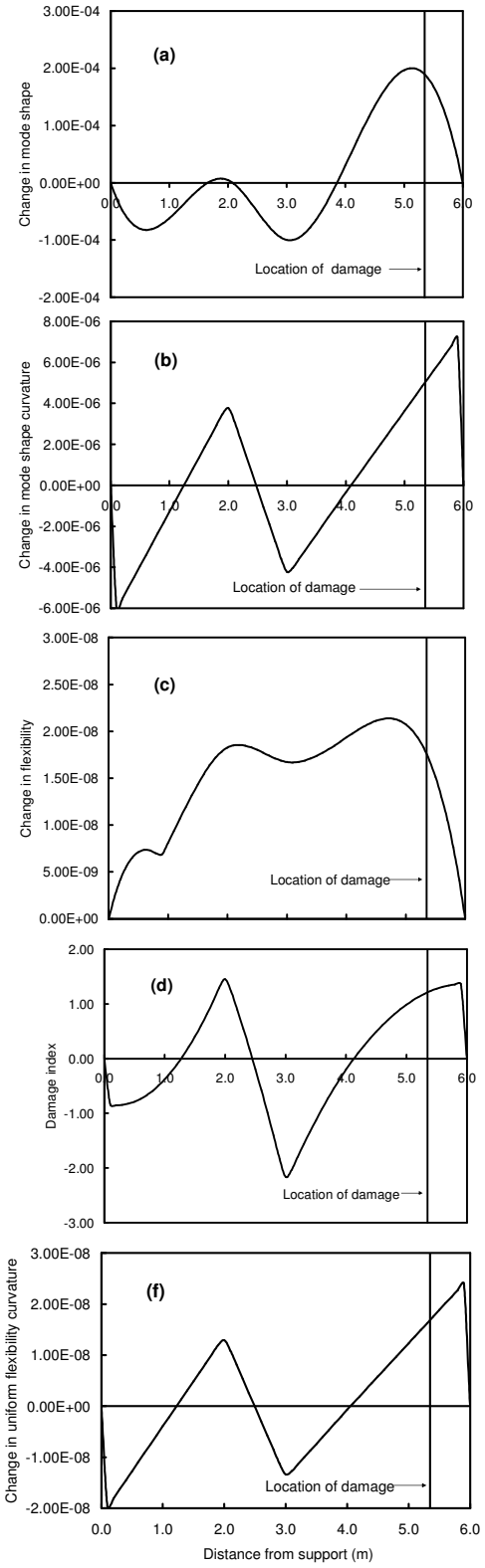

Figure D.8. Localization of damage case 8 of the bridge deck

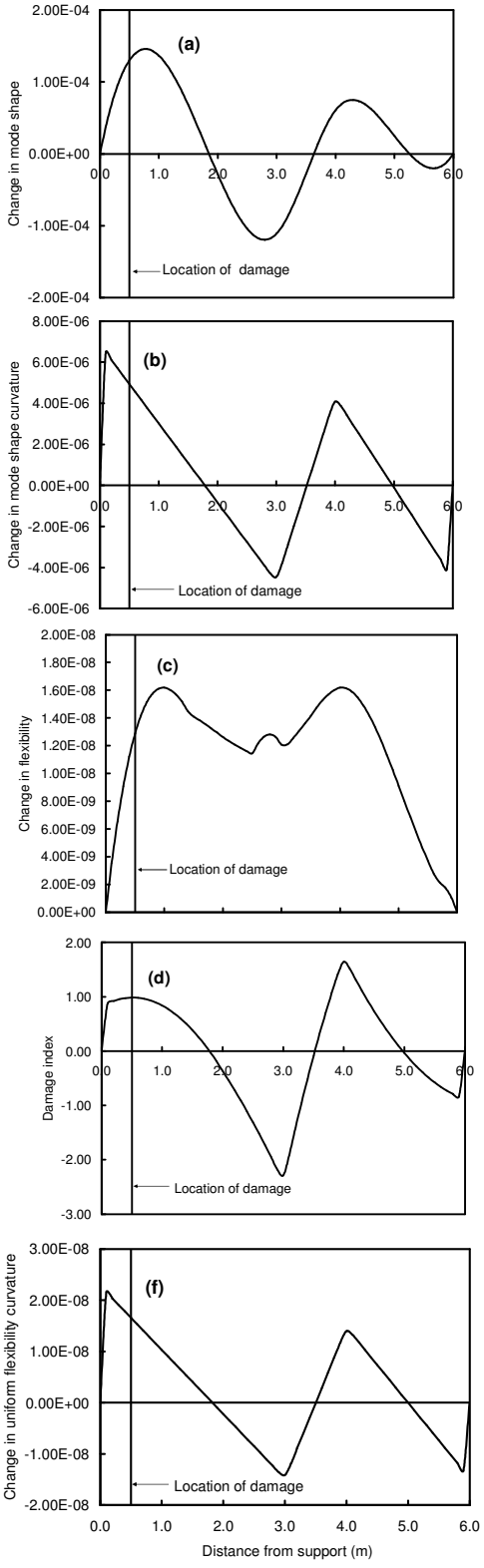

Figure D.9. Localization of damage case 9 of the bridge deck

Appendix E. Single damage detection on a prestressed concrete girder using strain gauges

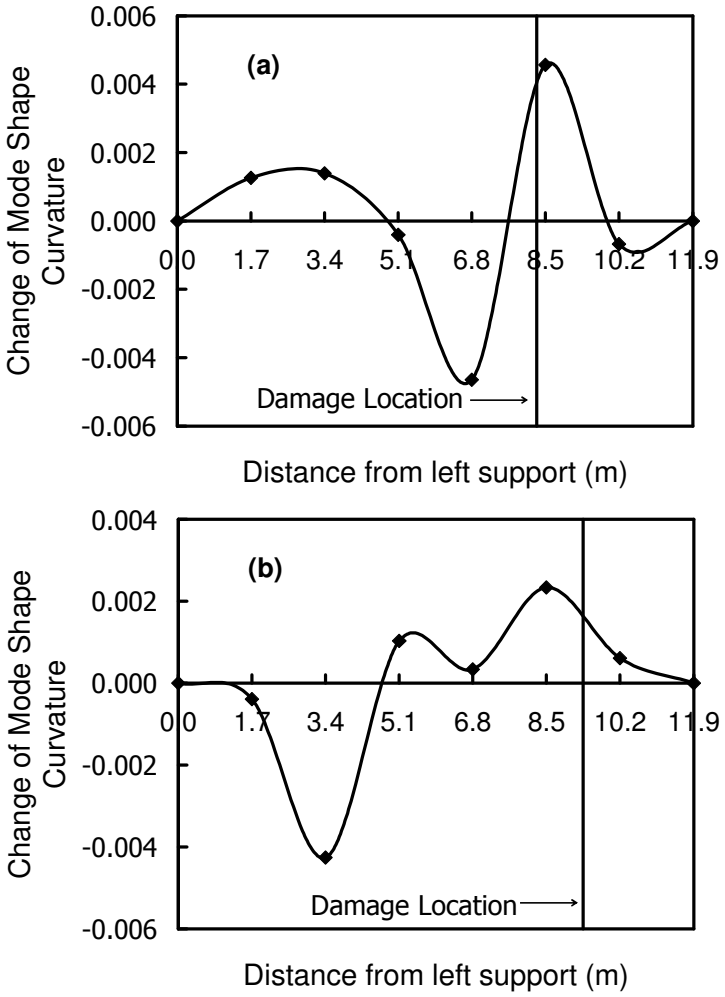

Figure E.1. Change in mode shape curvature along north edge for a) damage case 1, and along south girder for b) damage case 2, calculated using strain gauge measured curvature.

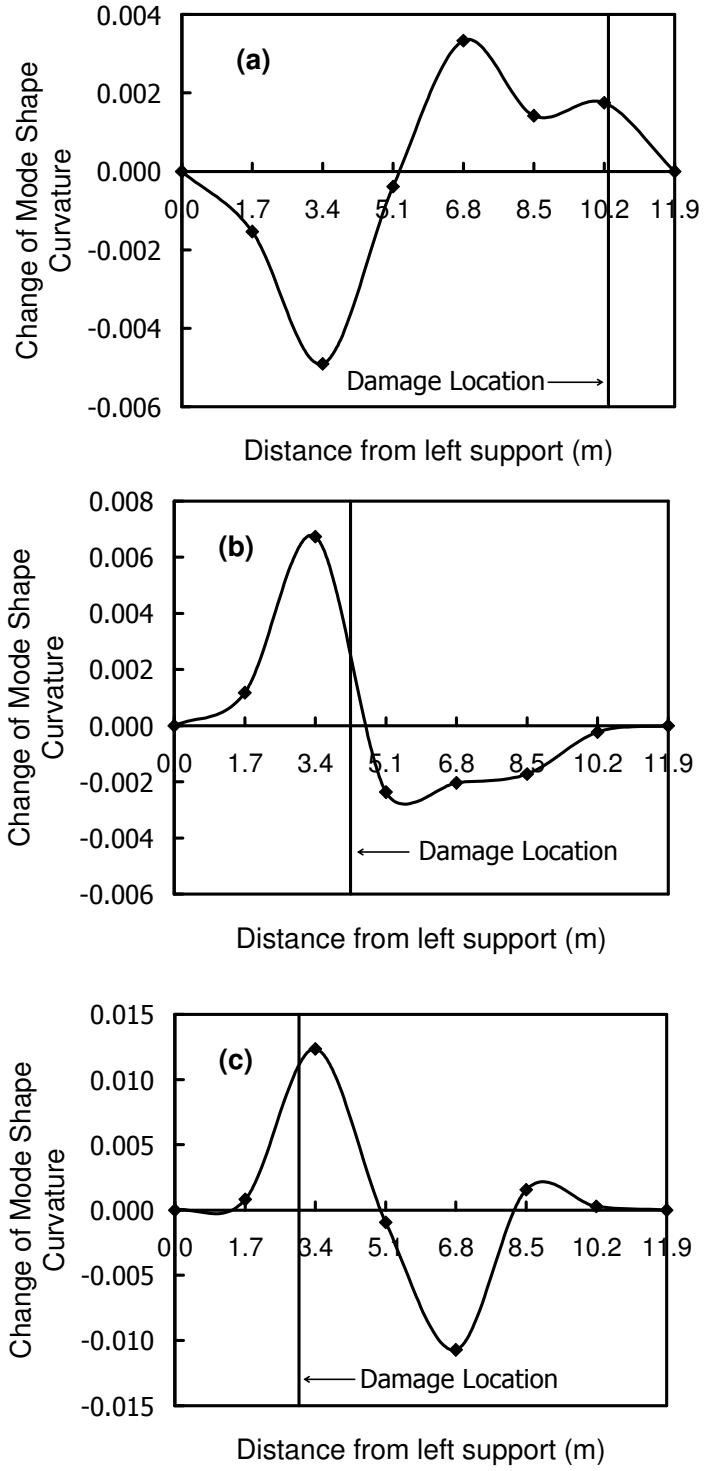

Figure E.2. Change in mode shape curvature along north edge for a) damage case 3, and along south girder for b) damage case 5, and c) damage case 6, calculated using strain gauge measured curvature.

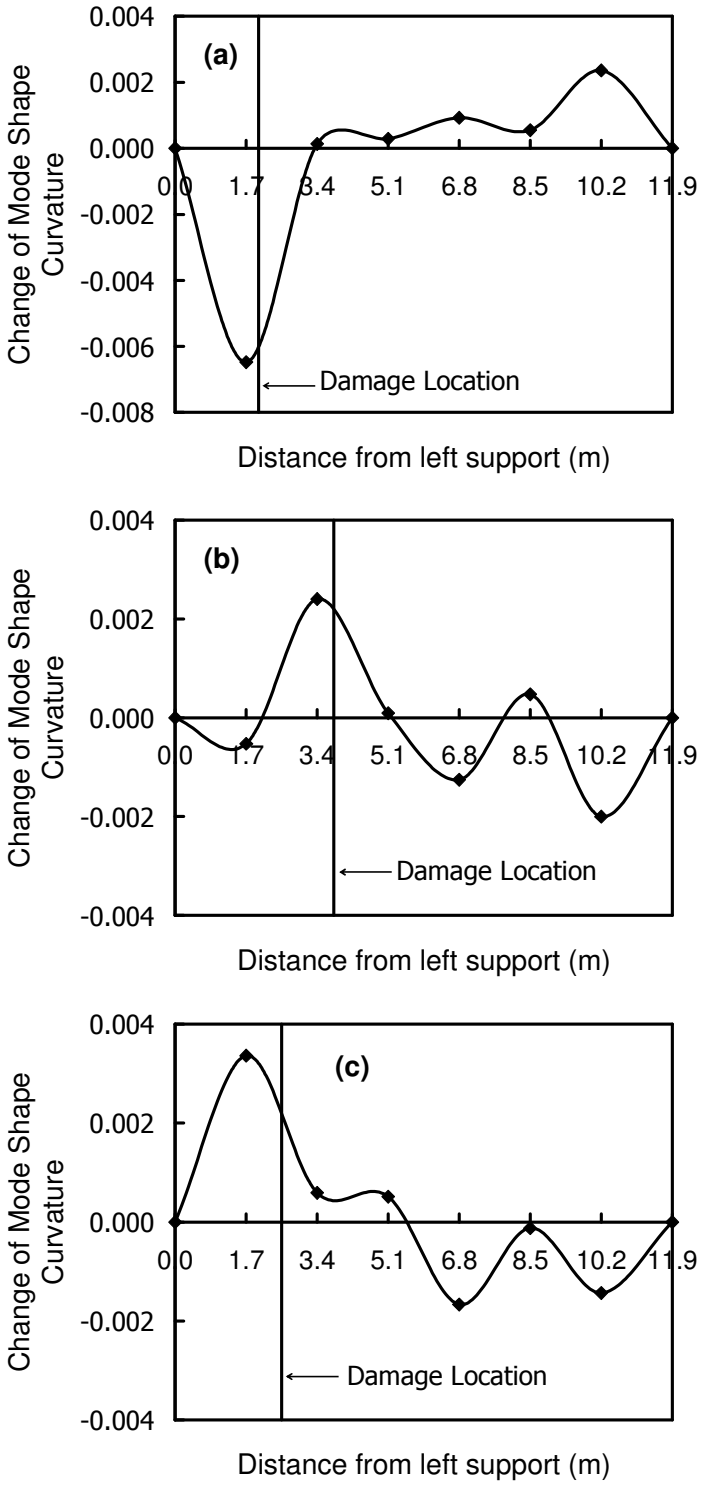

Figure E.3. Change in mode shape curvature along south edge for a) damage case 7, and along north edge for b) damage case 9, c) damage case 10, calculated using strain gauge measured curvature.

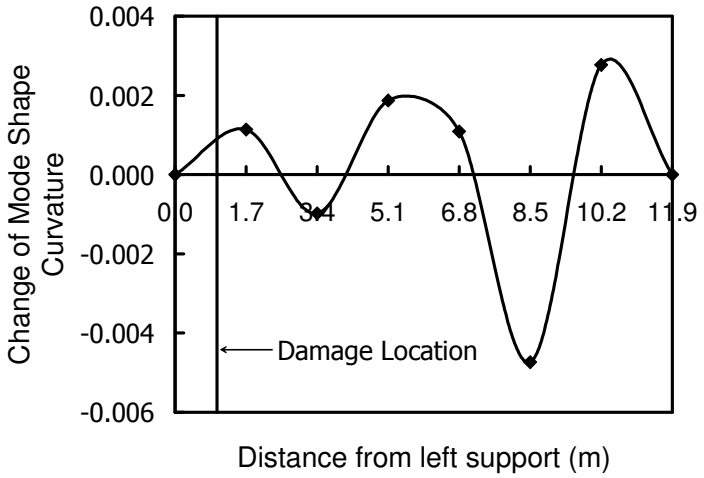

Figure E.4. Change in mode shape curvature along north edge calculated using strain gauge measured curvature for damage case 11.

Appendix F. Damage detection on a bridge girder using accelerometers

Five VBDD methods were used to detect damage on the bridge girder in following figures, (a) change in mode shape method, (b) mode shape curvature method, (c) change in flexibility method, (d) damage index method, and (e) change in uniform flexibility curvature method.

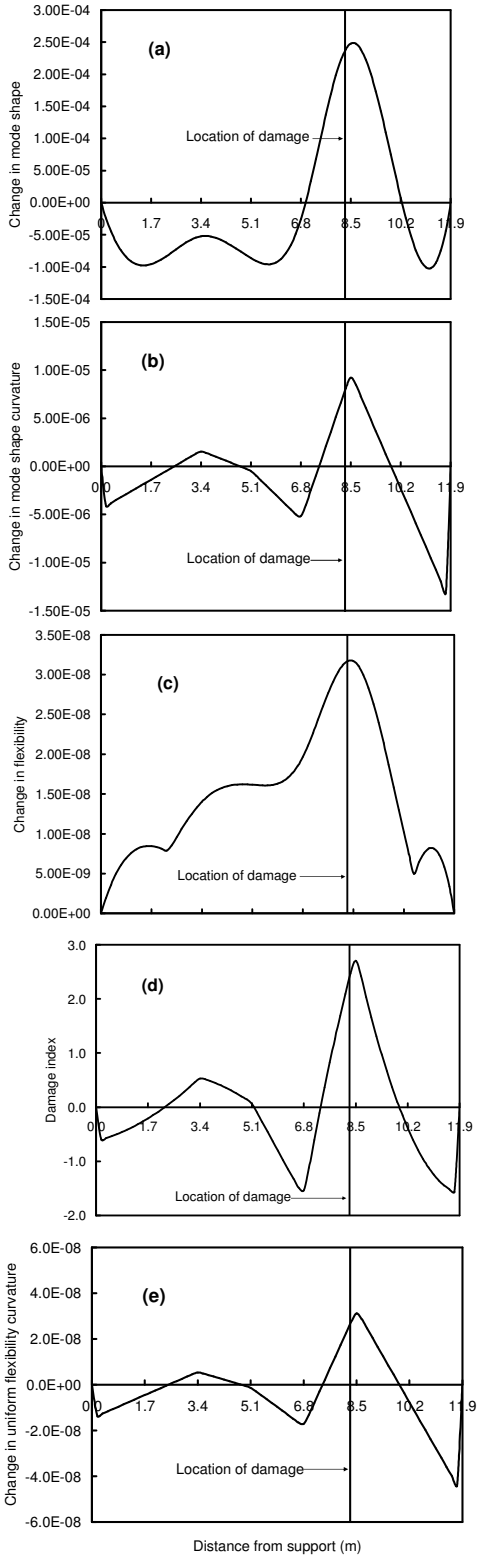

Figure F.1. Localization of damage case 1 on the bridge girder

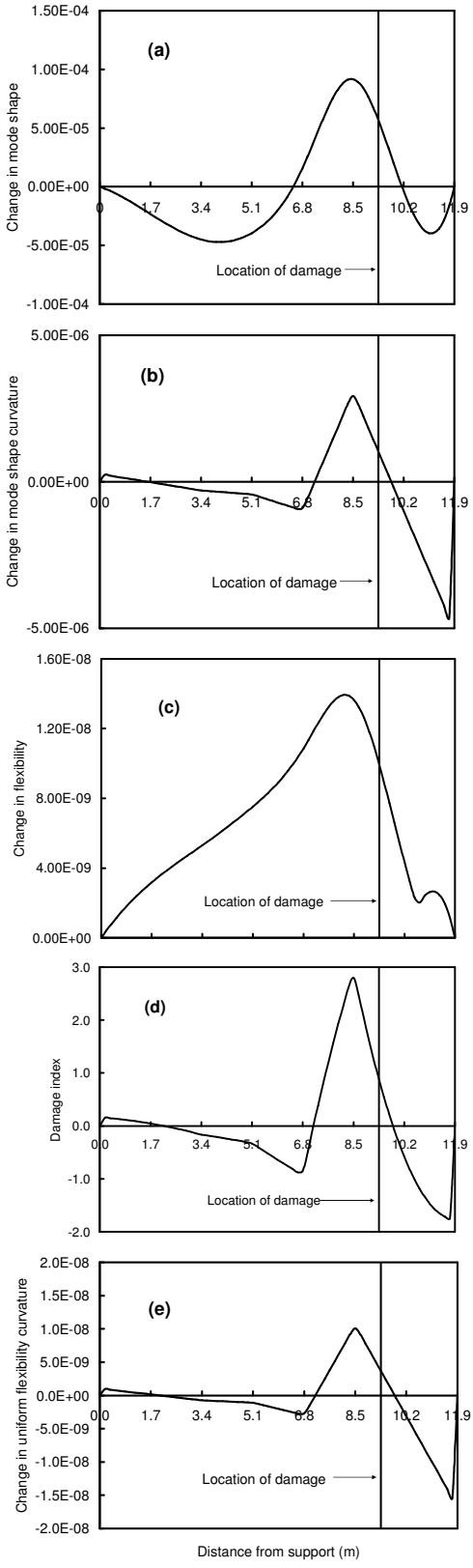

Figure F.2. Localization of damage case 2 on the bridge girder

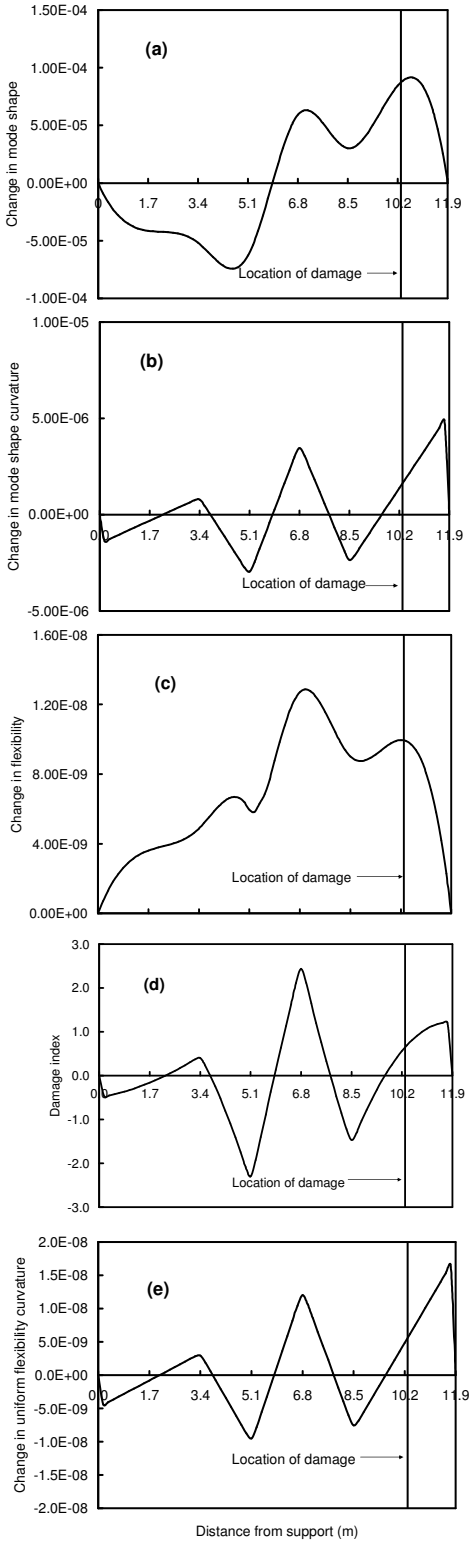

Figure F.3. Localization of damage case 3 on the bridge girder

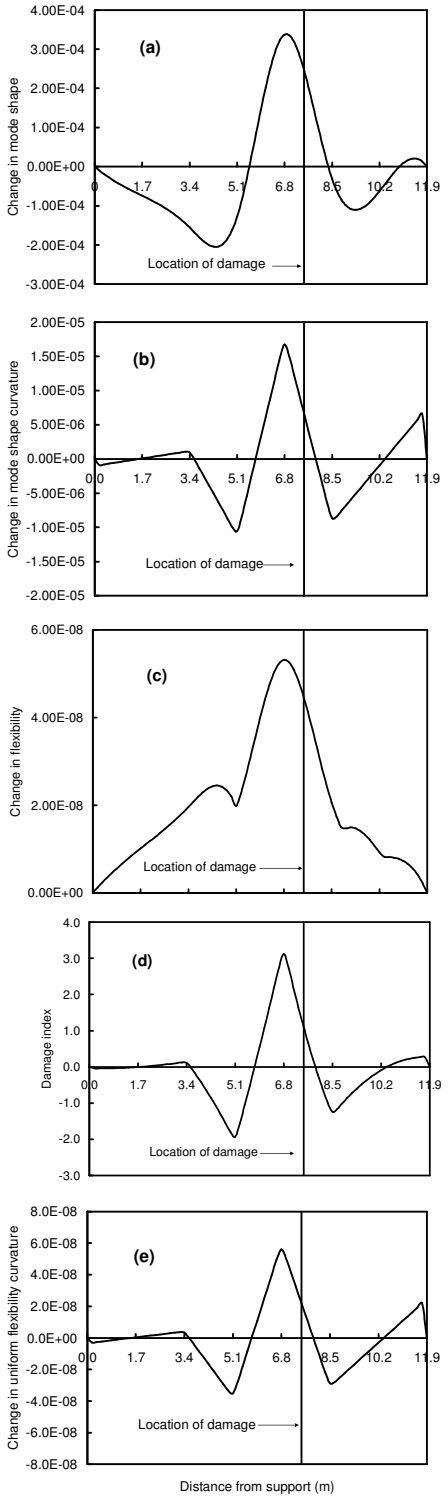

Figure F.4. Localization of damage case 4 on the bridge girder

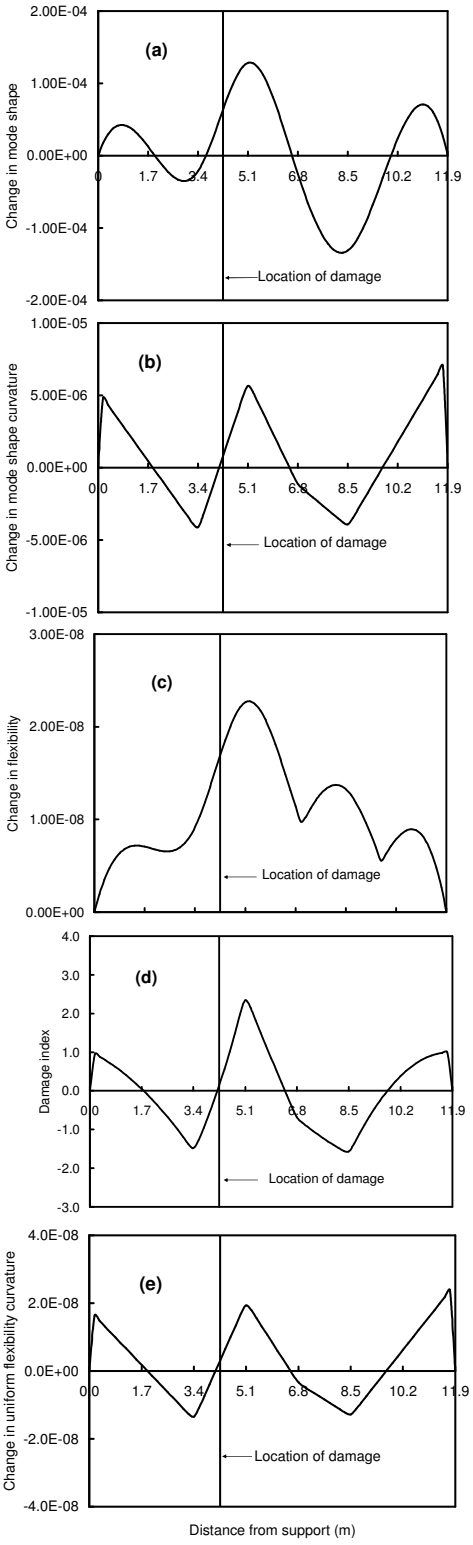

Figure F.5. Localization of damage case 5 on the bridge girder

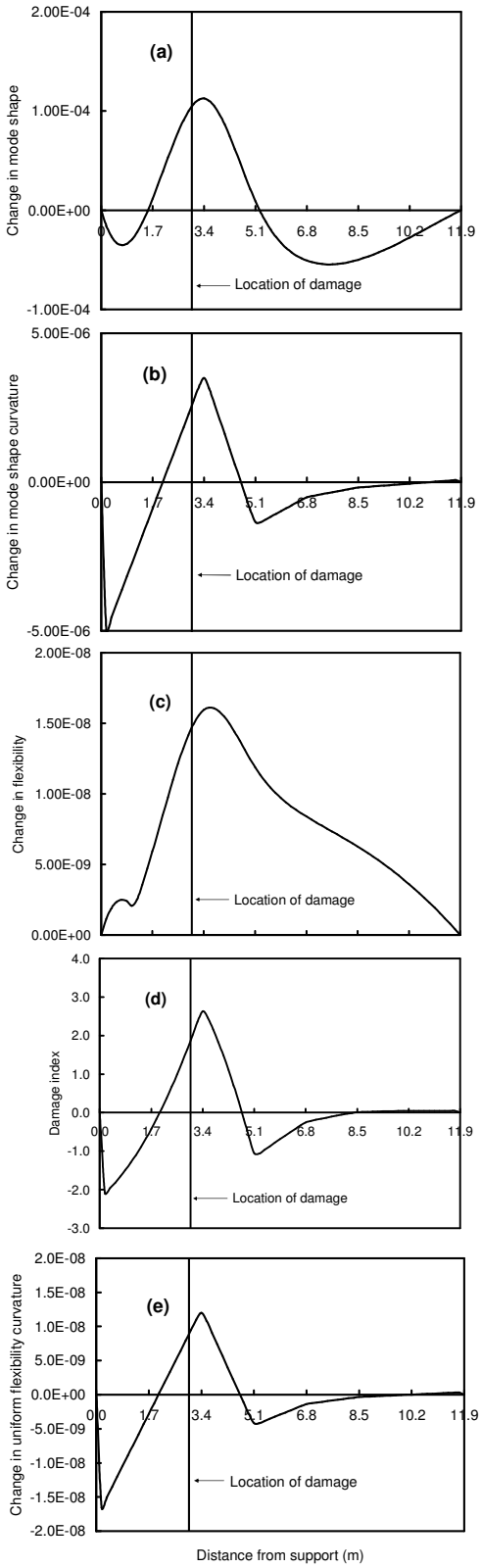

Figure F.6. Localization of damage case 6 on the bridge girder

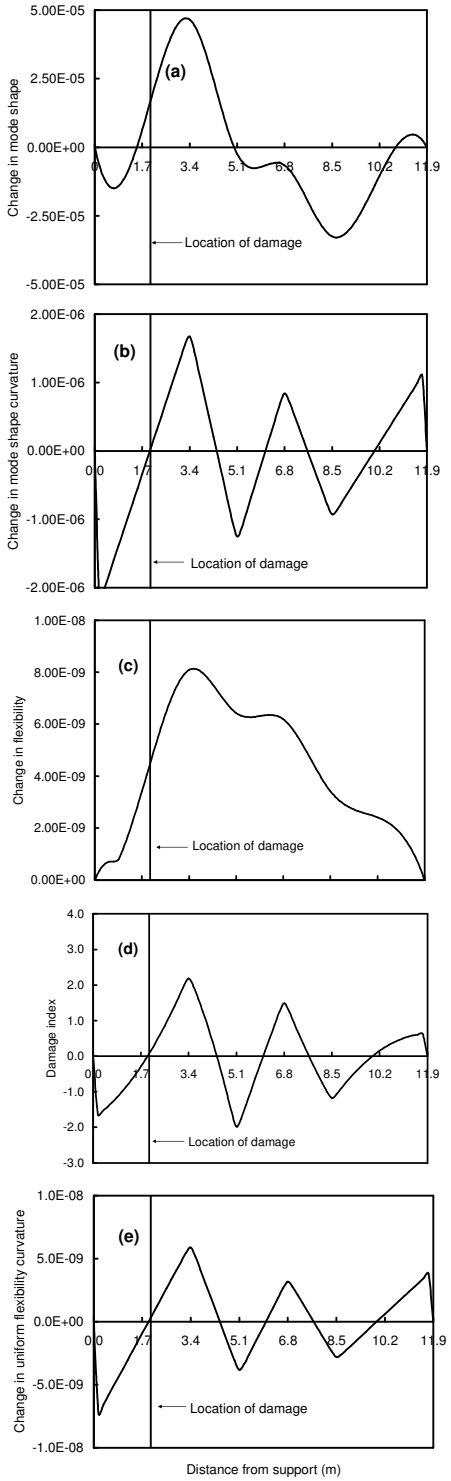

Figure F.7. Localization of damage case 7 on the bridge girder

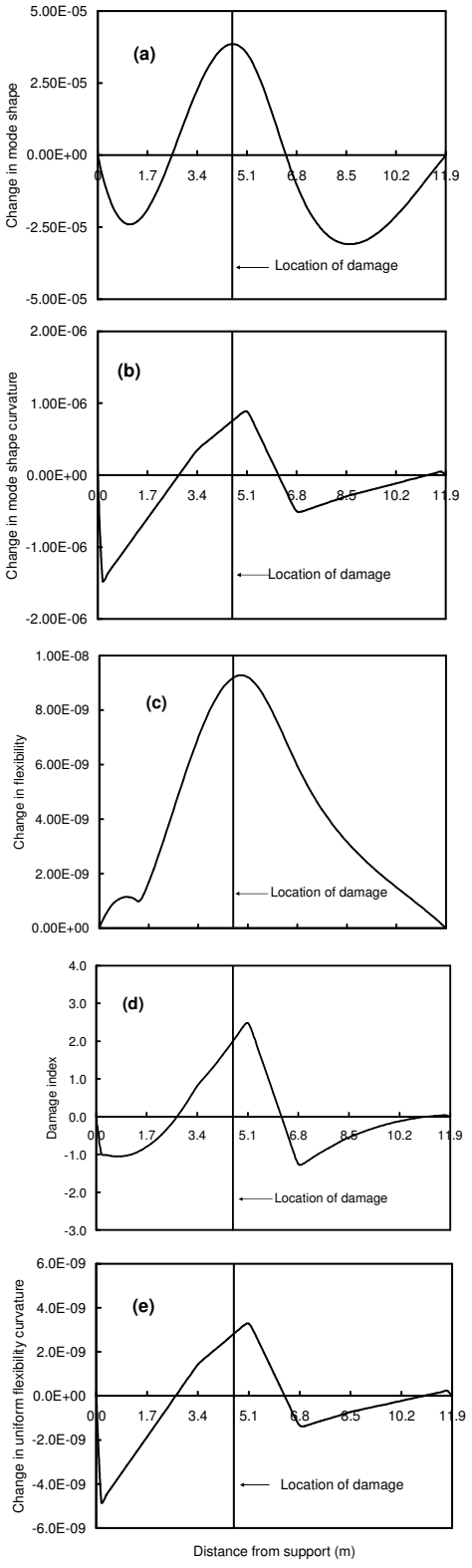

Figure F.8. Localization of damage case 8 on the bridge girder

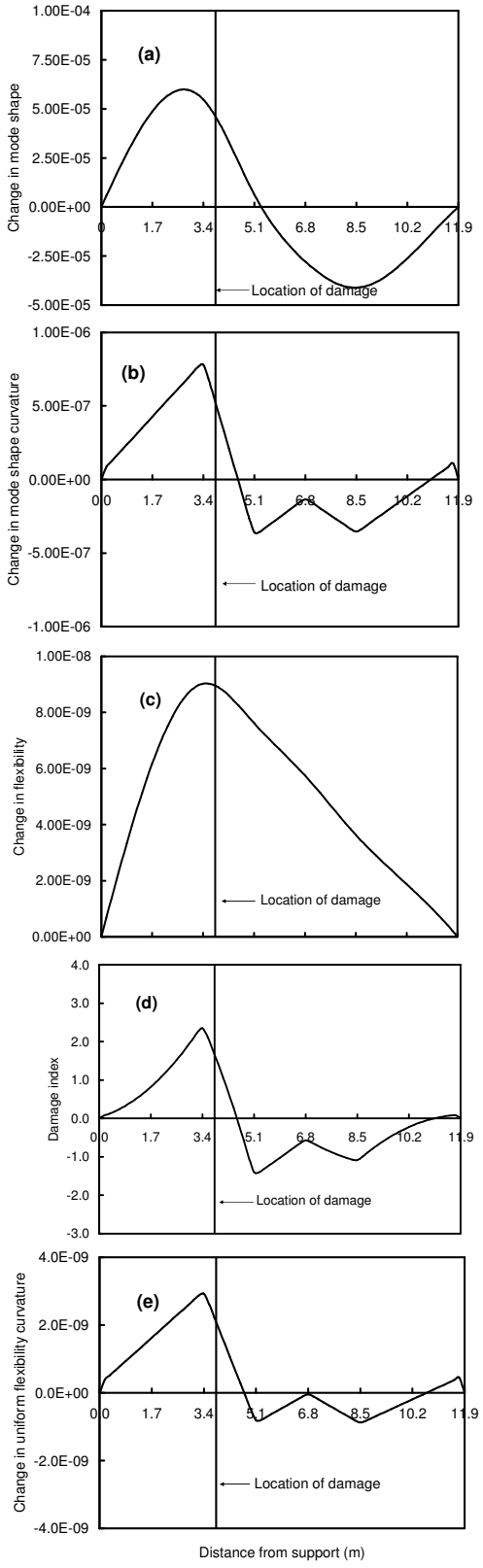

Figure F.9. Localization of damage case 9 on the bridge girder

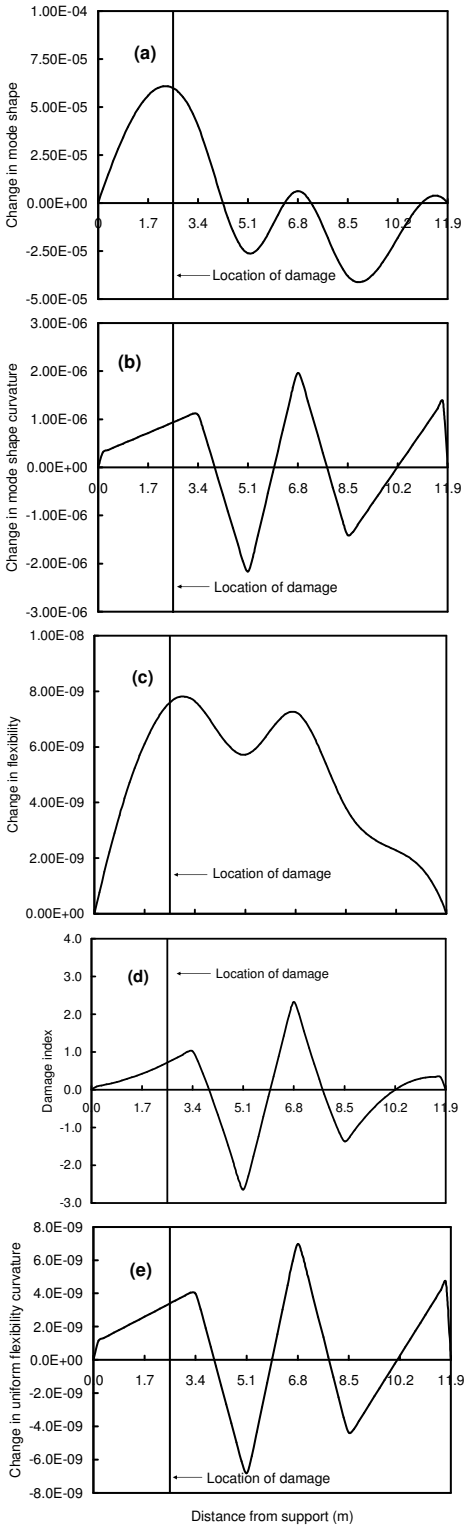

Figure F.10. Localization of damage case 10 on the bridge girder

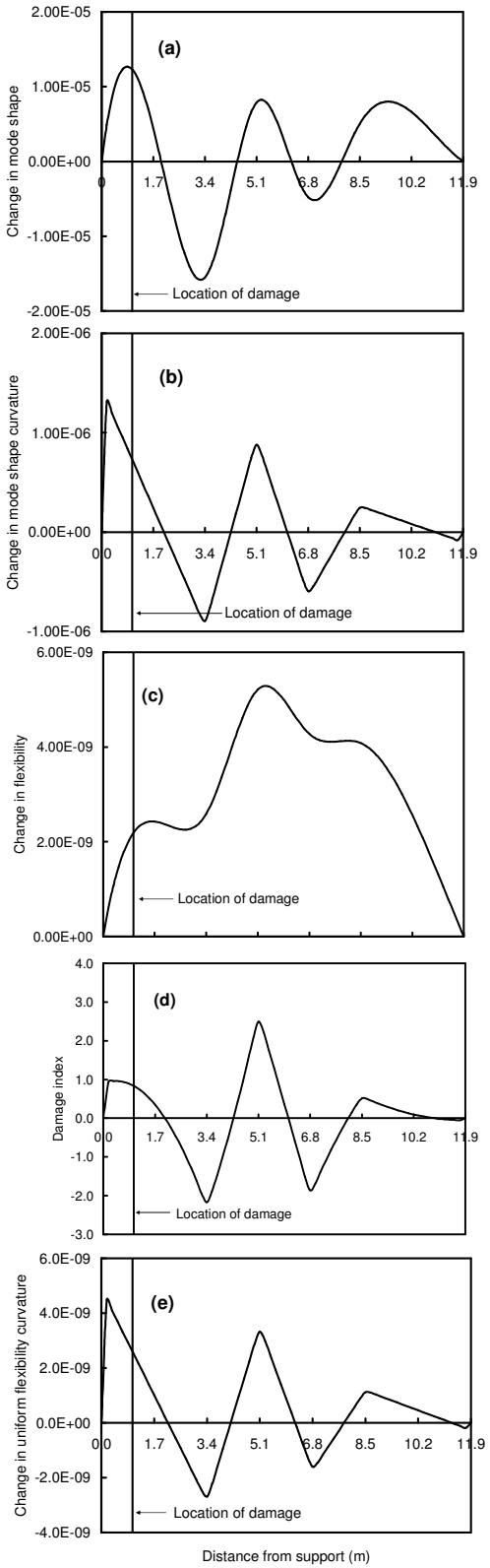

Figure F.11. Localization of damage case 11 on the bridge girder

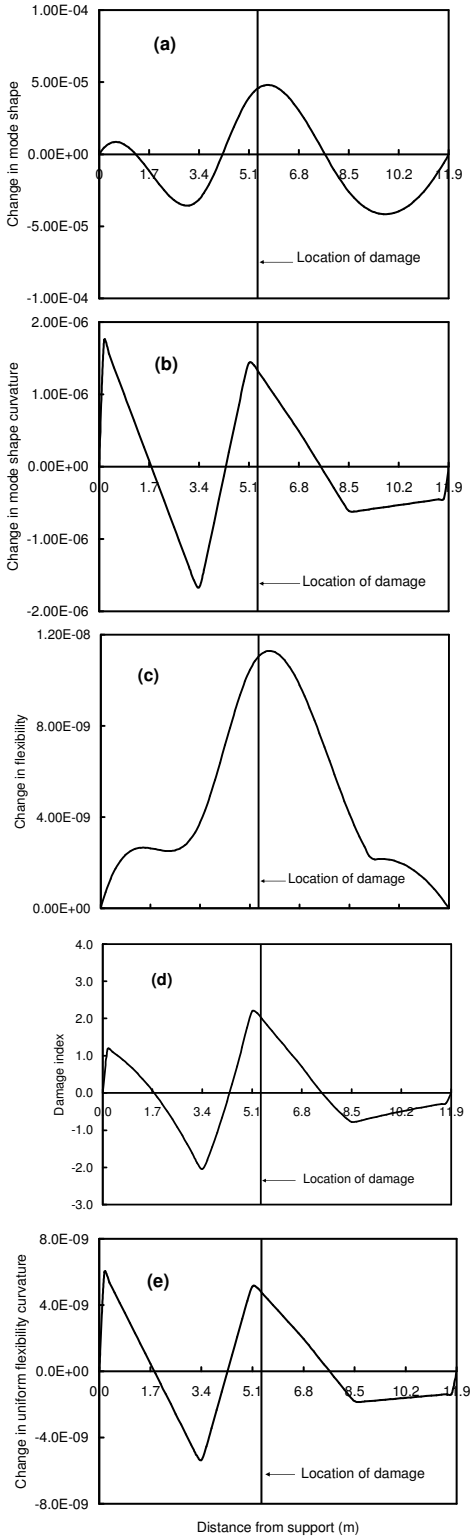

Figure F.12. Localization of damage case 12 on the bridge girder

Appendix G. Multiple damage detection on a bridge girder using accelerometers

Five VBDD methods were used to detect damage on the bridge girder in following figures, (a) change in mode shape method, (b) mode shape curvature method, (c) change in flexibility method, (d) damage index method, and (e) change in uniform flexibility curvature method.

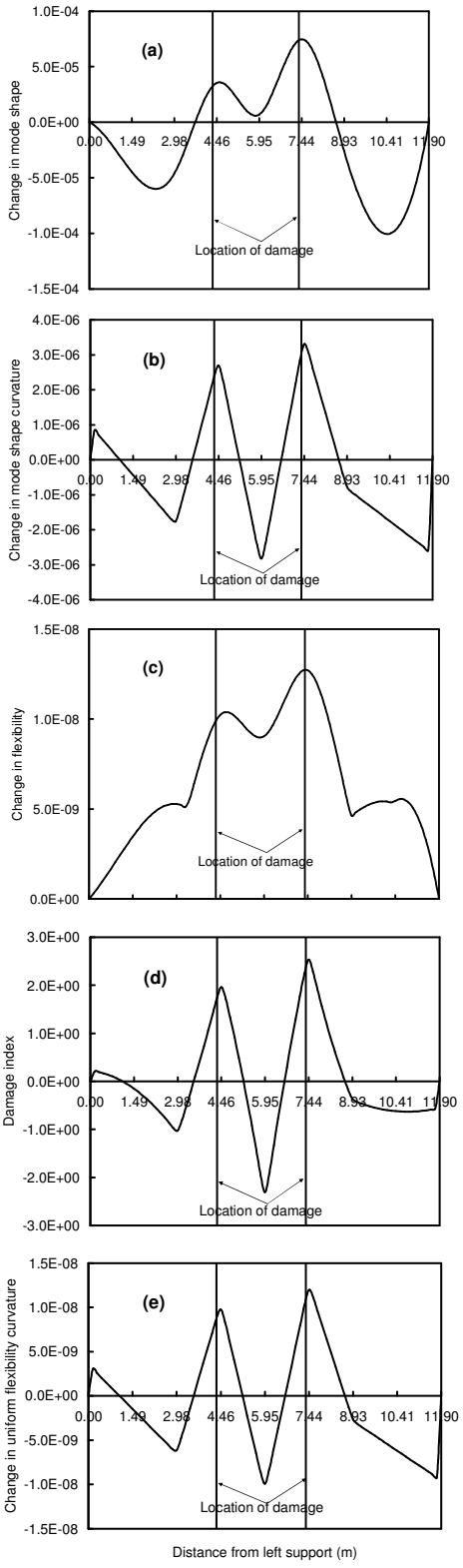

Figure G.1. Localization of damage cases 1a and 1b on the bridge girder

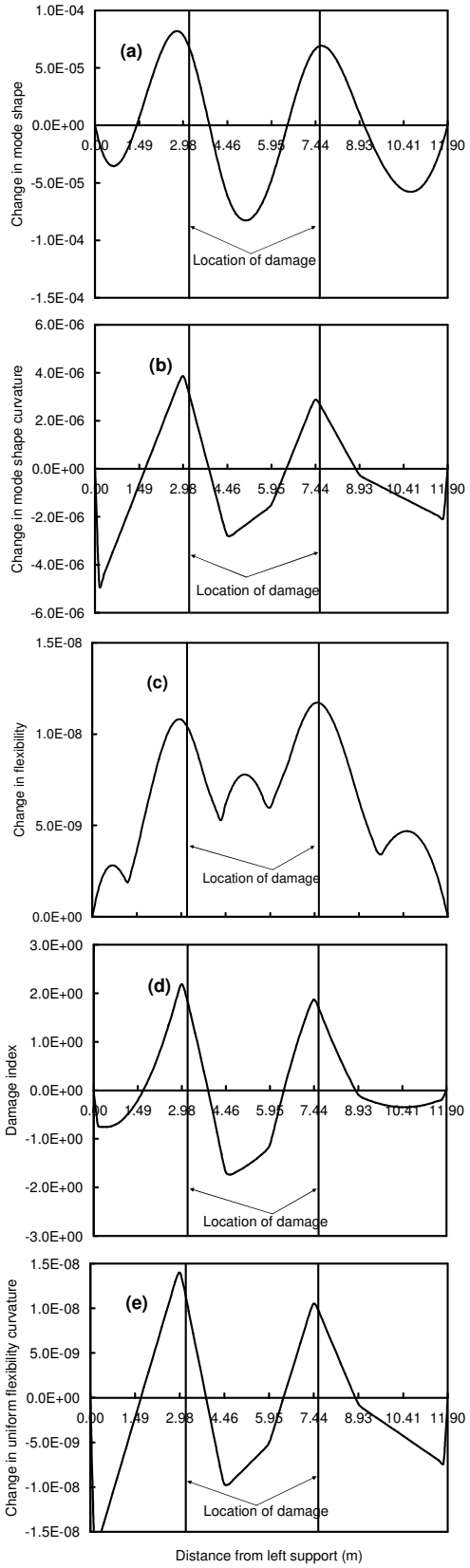

Figure G.2. Localization of damage cases 2a and 2b on the bridge girder

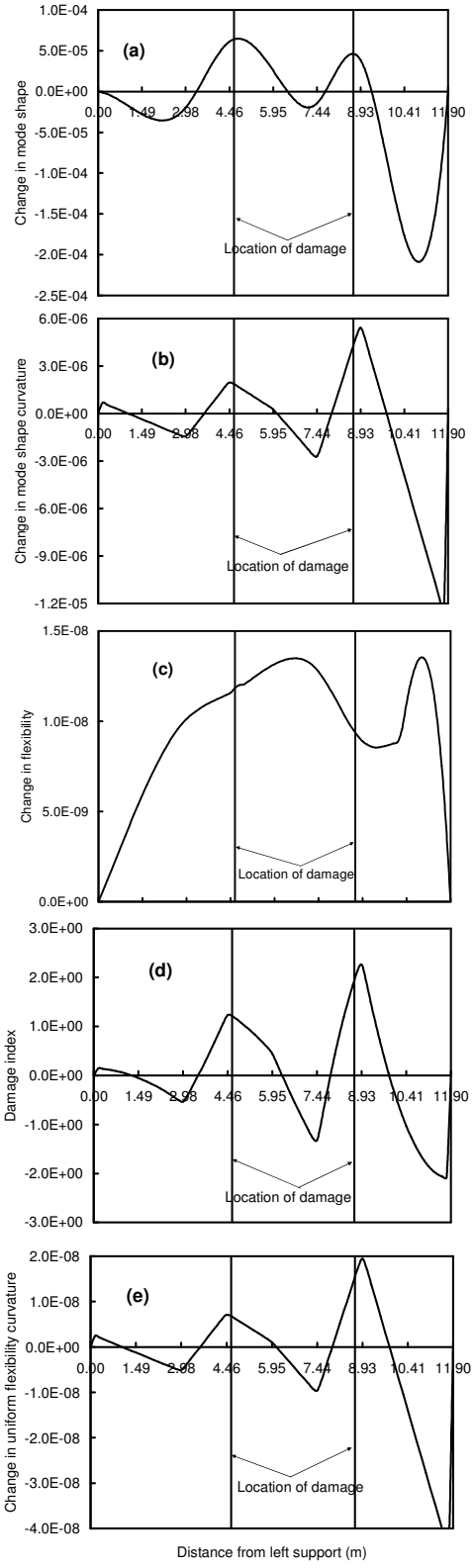

Figure G.3. Localization of damage cases 3a and 3b on the bridge girder

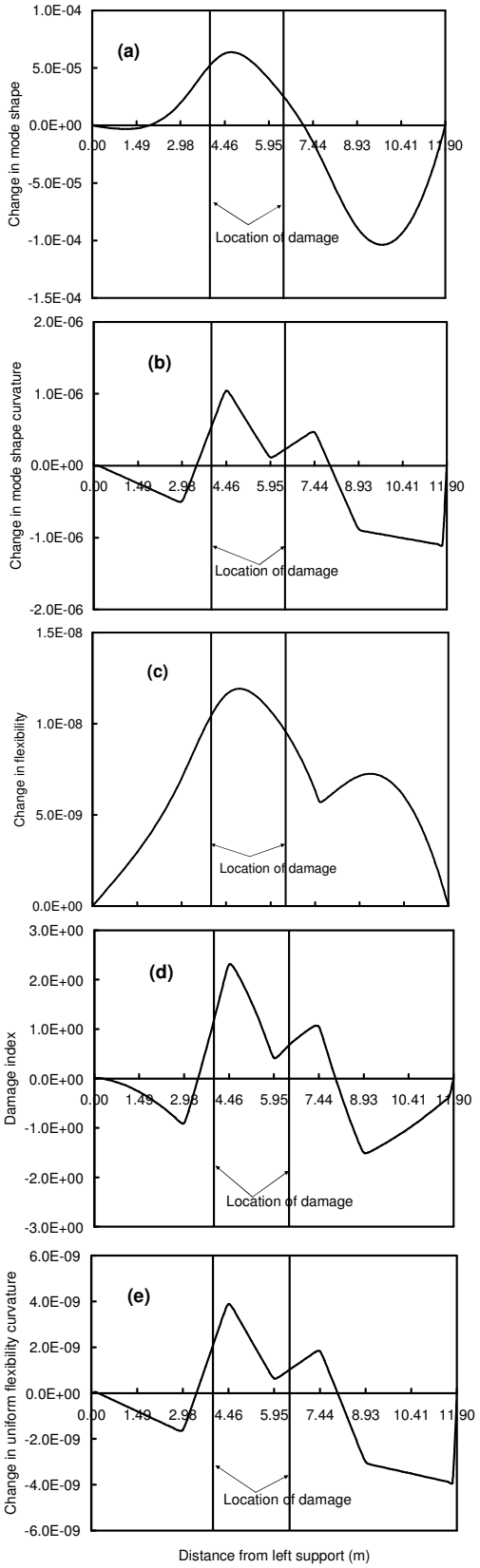

Figure G.4. Localization of damage cases 4a and 4b on the bridge girder

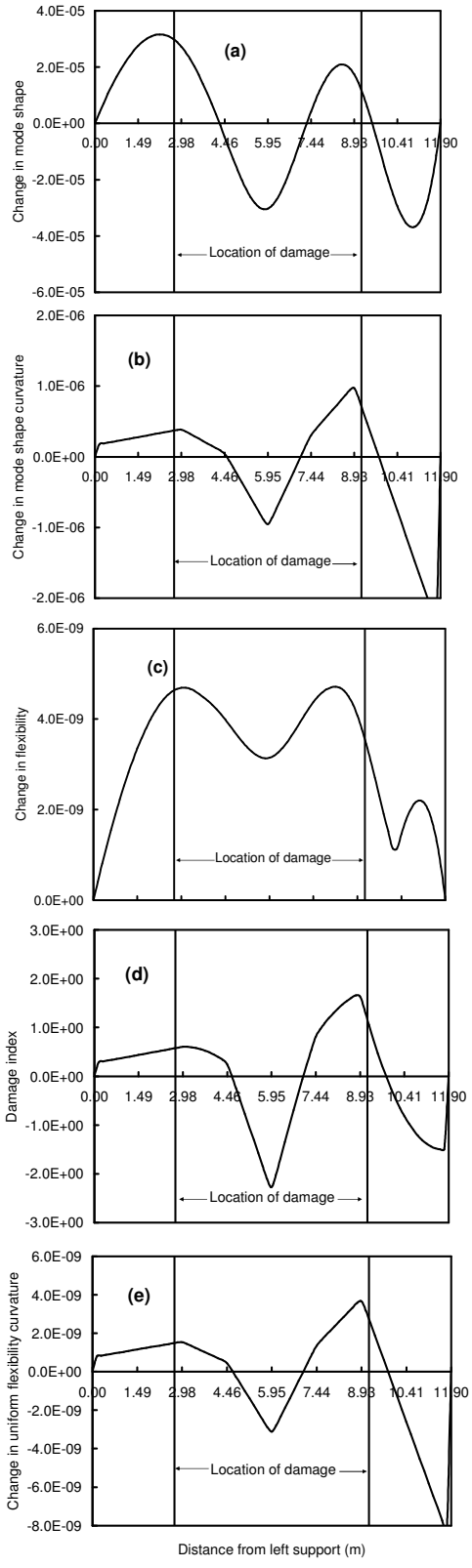

Figure G.5. Localization of damage cases 5a and 5b on the bridge girder

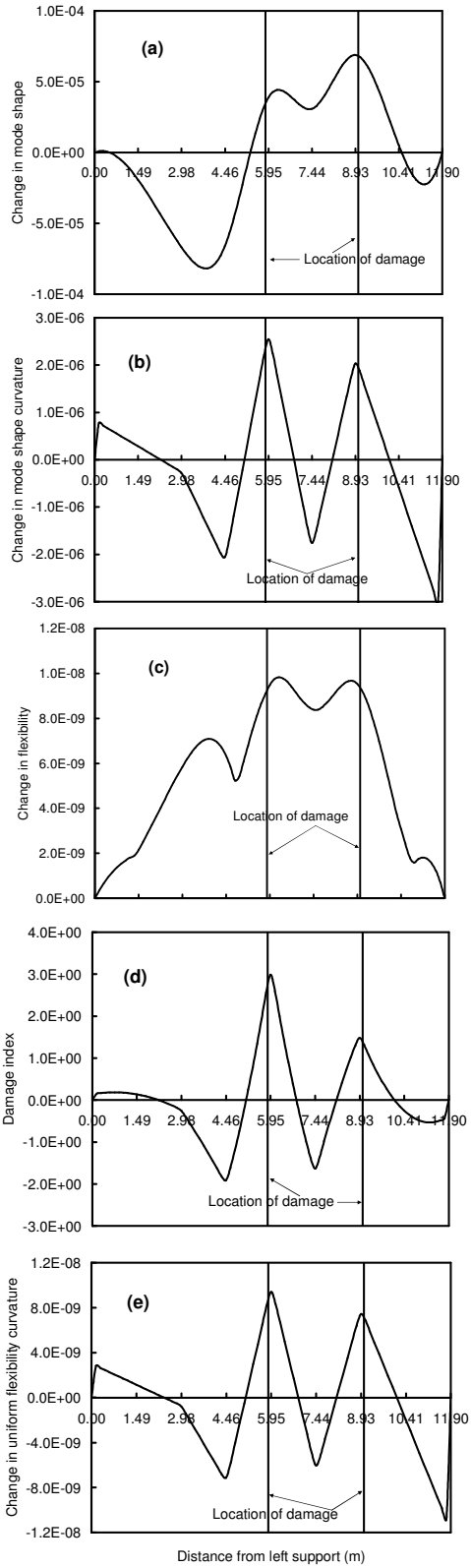

Figure G.6. Localization of damage cases 6a and 6b on the bridge girder

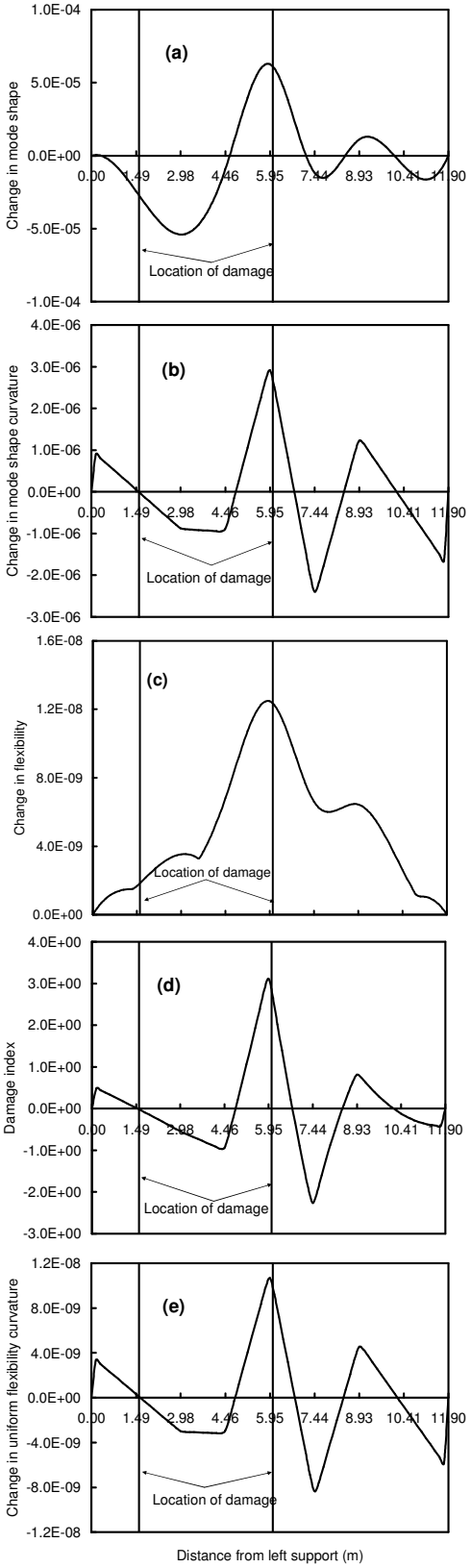

Figure G.7. Localization of damage cases 7a and 7b on the bridge girder

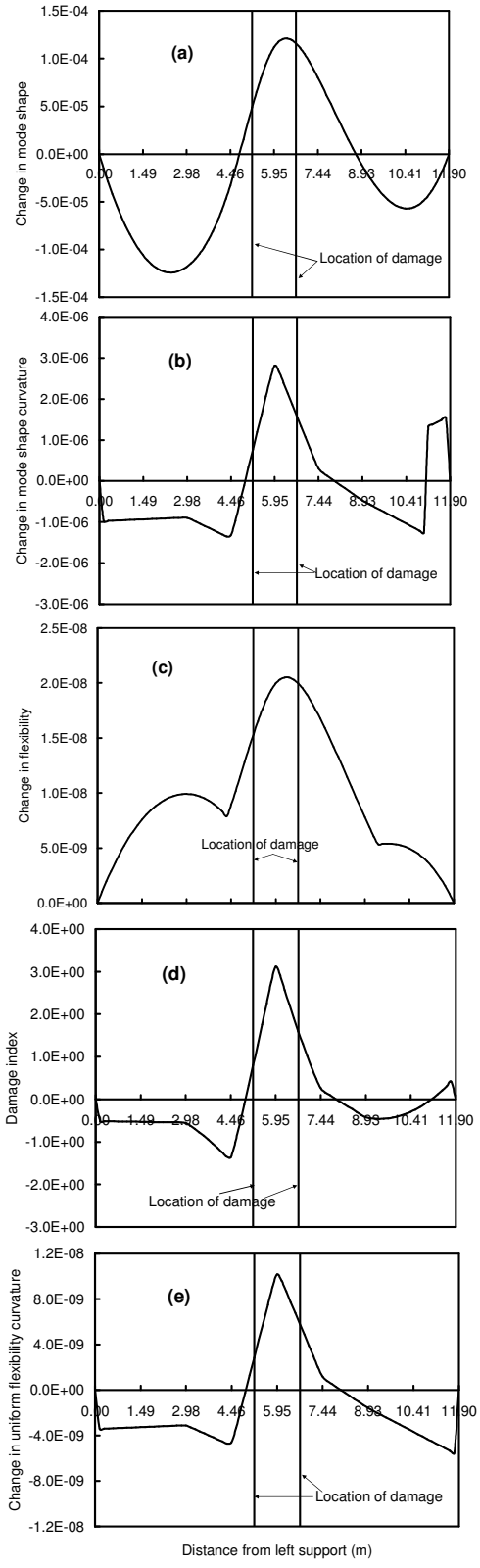

Figure G.8. Localization of damage cases 8a and 8b on the bridge girder

Appendix H Probabilities of damage detection using random vibration without measurement errors

There were 48 sets of 25 tests, 12 sets of 100 tests, and 4 sets of 400 tests in both undamaged and damaged conditions for each damage case. Only the details from the first sets of 25 tests, first sets of 100 tests, and first sets of 400 tests are listed in the tables of this appendix. Tables H27, H28, and H29 summarized the results and calculated the average values of the probabilities of damage detection using 48 sets of 25 tests, 12 sets of 100 tests, and 3 sets of 400 tests, respectively.

Table H1. Statistical results of 25 repeated trials without measurement errors for detecting damage state 1a.

Measurement point	1st	2nd	3rd	4th	5th
S_j	0.00357	0.00248	0.00311	0.00251	0.00338
S_j^*	0.00291	0.00292	0.00233	0.00232	0.00309
$S_{di\mathrm{j}}$	0.00120	0.00109	N/A	0.00104	0.00120
m_{ij}	0.00171	0.00167	N/A	0.00152	0.00157
$m_{ij} / S_{di\mathrm{j}}$	1.417	1.532	N/A	1.466	1.308
$P(D_{ij} \geq 0)$	0.922	0.937	N/A	0.929	0.905

Table H2. Statistical results of 100 repeated trials without measurement errors for detecting damage state 1a.

Measurement point	1st	2nd	3rd	4th	5th
S_j	0.00314	0.00271	0.00283	0.00283	0.00351
S_j^*	0.00335	0.00346	0.00283	0.00322	0.00350
$S_{di\mathrm{j}}$	0.00061	0.00059	N/A	0.00059	0.00064
m_{ij}	0.00171	0.00167	N/A	0.00152	0.00157
$m_{ij} / S_{di\mathrm{j}}$	2.802	2.810	N/A	2.589	2.462
$P(D_{ij} \geq 0)$	0.995	0.995	N/A	0.994	0.993

Table H3. Statistical results of 400 repeated trials without measurement errors for detecting damage state 1a.

Measurement point	1st	2nd	3rd	4th	5th
S_j	0.00327	0.00297	0.00297	0.00317	0.00335
S_j^*	0.00337	0.00322	0.00300	0.00324	0.00340
$S_{di\mathrm{j}}$	0.000316	0.000304	N/A	0.00031	0.000319
m_{ij}	0.00171	0.00167	N/A	0.00152	0.00157
$m_{ij} / S_{di\mathrm{j}}$	1.417	1.532	N/A	1.466	1.308
$P(D_{ij} \geq 0)$	0.9999999	0.9999999	N/A	0.9999999	0.9999990

Table H4. Statistical results of 25 repeated trials without measurement errors for detecting damage state 1b.

Measurement point	1st	2nd	3rd	4th	5th
S_j	0.00357	0.00248	0.00311	0.00251	0.00338
S_j^*	0.00301	0.00237	0.00299	0.00294	0.00258
$S_{di\mathrm{j}}$	0.00127	0.00110	N/A	0.00116	0.00121
m_{ij}	0.00130	0.00129	N/A	0.00115	0.00120
$m_{ij} / S_{di\mathrm{j}}$	1.023	1.169	N/A	0.992	0.990
$P(D_{ij} \geq 0)$	0.922	0.937	N/A	0.929	0.905

Table H5. Statistical results of 100 repeated trials without measurement errors for detecting damage state 1b.

Measurement point	1st	2nd	3rd	4th	5th
S_j	0.00314	0.00271	0.00283	0.00283	0.00351
S_j^*	0.00307	0.00296	0.00318	0.00292	0.00287
$S_{di\mathrm{j}}$	0.000611	0.000585	N/A	0.000589	0.000622
m_{ij}	0.00130	0.00129	N/A	0.00115	0.00120
$m_{ij} / S_{di\mathrm{j}}$	2.128	2.203	N/A	1.954	1.928
$P(D_{ij} \geq 0)$	0.995	0.995	N/A	0.994	0.993

Table H6. Statistical results of 400 repeated trials without measurement errors for detecting damage state 1b.

Measurement point	1st	2nd	3rd	4th	5th
S_j	0.00327	0.00297	0.00297	0.00317	0.00335
S_j^*	0.00342	0.00299	0.00296	0.00300	0.00334
$S_{di\mathrm{j}}$	0.000316	0.000297	N/A	0.000303	0.000316
m_{ij}	0.00130	0.00129	N/A	0.00115	0.00120
$m_{ij} / S_{di\mathrm{j}}$	4.117	4.338	N/A	3.801	3.792
$P(D_{ij} \geq 0)$	0.9999999	0.9999999	N/A	0.9999999	0.9999990

Table H7. Statistical results of 25 repeated trials without measurement errors for detecting damage state 1c.

Measurement point	1st	2nd	3rd	4th	5th
S_j	0.00357	0.00248	0.00311	0.00251	0.00338
S_j^*	0.00344	0.00342	0.00310	0.00387	0.00348
$S_{di\mathrm{j}}$	0.00132	0.00122	N/A	0.00127	0.00131
m_{ij}	0.000684	0.000698	N/A	0.00063	0.00065
$m_{ij} / S_{di\mathrm{j}}$	0.517	0.573	N/A	0.494	0.497
$P(D_{ij} \geq 0)$	0.698	0.716	N/A	0.688	0.691

Table H8. Statistical results of 400 repeated trials without measurement errors for detecting damage state 1c.

Measurement point	1st	2nd	3rd	4th	5th
S_j	0.00327	0.00297	0.00297	0.00317	0.00335
S_j^*	0.00336	0.00306	0.00285	0.00315	0.00333
$S_{di\mathrm{j}}$	0.000312	0.000296	N/A	0.000304	0.000313
m_{ij}	0.000684	0.000698	N/A	0.00063	0.00065
$m_{ij} / S_{di\mathrm{j}}$	2.192	2.357	N/A	2.073	2.073
$P(D_{ij} \geq 0)$	0.986	0.990	N/A	0.980	0.980

Table H9. Statistical results of 25 repeated trials without measurement errors for detecting damage state 1d.

Measurement point	*1st*	*2nd*	*3rd*	*4th*	*5th*
S_j	0.00357	0.00248	0.00311	0.00251	0.00338
S_j^*	0.00268	0.00286	0.00262	0.00268	0.00284
$S_{di\mathrm{j}}$	0.00121	0.00111	N/A	0.00110	0.00120
m_{ij}	0.000441	0.000421	N/A	0.000408	0.000411
m_{ij} / $S_{di\mathrm{j}}$	0.365	0.379	N/A	0.373	0.343
$P(D_{ij} \geq 0)$	0.644	0.648	N/A	0.644	0.633

Table H10. Statistical results of 100 repeated trials without measurement errors for detecting damage state 1d.

Measurement point	*1st*	*2nd*	*3rd*	*4th*	*5th*
S_j	0.00314	0.00271	0.00283	0.00283	0.00351
S_j^*	0.00275	0.00308	0.00288	0.00277	0.00302
$S_{di\mathrm{j}}$	0.00058	0.00058	N/A	0.00057	0.00061
m_{ij}	0.000441	0.000421	N/A	0.000408	0.000411
m_{ij} / $S_{di\mathrm{j}}$	0.759	0.731	N/A	0.722	0.669
$P(D_{ij} \geq 0)$	0.776	0.767	N/A	0.764	0.749

Table H11. Statistical results of 400 repeated trials without measurement errors for detecting damage state 1d.

Measurement point	*1st*	*2nd*	*3rd*	*4th*	*5th*
S_j	0.00327	0.00297	0.00297	0.00317	0.00335
S_j^*	0.00336	0.00306	0.00285	0.00315	0.00333
$S_{di\mathrm{j}}$	0.000312	0.000296	N/A	0.000304	0.000313
m_{ij}	0.000441	0.000421	N/A	0.000408	0.000411
m_{ij} / $S_{di\mathrm{j}}$	1.4143	1.4218	N/A	1.3441	1.3117
$P(D_{ij} \geq 0)$	0.921	0.922	N/A	0.91	0.905

Table H12. Statistical results of 25 repeated trials without measurement errors for detecting damage state 2.

Measurement point	*1st*	*2nd*	*3rd*	*4th*	*5th*
S_j	0.00357	0.00248	0.00311	0.00251	0.00338
S_j^*	0.00342	0.00367	0.00237	0.00249	0.00391
$S_{di\mathrm{j}}$	0.00126	0.001182	N/A	N/A	0.001295
m_{ij}	0.000881	0.000959	N/A	N/A	0.000538
m_{ij} / $S_{di\mathrm{j}}$	0.699	0.812	N/A	N/A	0.416
$P(D_{ij} \geq 0)$	0.758	0.791	N/A	N/A	0.66

Table H13. Statistical results of 100 repeated trials without measurement errors for detecting damage state 2.

Measurement point	*1st*	*2nd*	*3rd*	*4th*	*5th*
S_j	0.00314	0.00271	0.00283	0.00283	0.00351
S_j^*	0.00340	0.00303	0.00298	0.00271	0.00345
$S_{di\mathrm{j}}$	0.000619	0.000578	N/A	N/A	0.000641
m_{ij}	0.000881	0.000959	N/A	N/A	0.000538
m_{ij} / $S_{di\mathrm{j}}$	1.4233	1.6585	N/A	N/A	0.8393
$P(D_{ij} \geq 0)$	0.922	0.952	N/A	N/A	0.7995

Table H14. Statistical results of 400 repeated trials without measurement errors for detecting damage state 2.

Measurement point	*1st*	*2nd*	*3rd*	*4th*	*5th*
S_j	0.00327	0.00297	0.00297	0.00317	0.00335
S_j^*	0.00354	0.00301	0.00283	0.00303	0.00352
$S_{di\mathrm{j}}$	0.000316	0.000294	N/A	N/A	0.000318
m_{ij}	0.000881	0.000959	N/A	N/A	0.000538
m_{ij} / $S_{di\mathrm{j}}$	2.786	3.258	N/A	N/A	1.693
$P(D_{ij} \geq 0)$	0.996	0.9992	N/A	N/A	0.954

Table H15. Statistical results of 25 repeated trials without measurement errors for detecting damage state 3.

Measurement point	*1st*	*2nd*	*3rd*	*4th*	*5th*
S_j	0.003567	0.002476	0.003107	0.002512	0.003376
S_j^*	0.002919	0.003431	0.002614	0.00352	0.003545
$S_{di\mathrm{j}}$	0.001345	0.001294	0.001272	0.001306	N/A
m_{ij}	0.001471	0.001594	0.001454	0.000988	N/A
$m_{ij} / S_{di\mathrm{j}}$	1.094	1.232	1.143	0.756	N/A
$P(D_{ij} \geq 0)$	0.862	0.891	0.873	0.776	N/A

Table H16. Statistical results of 100 repeated trials without measurement errors for detecting damage state 3.

Measurement point	*1st*	*2nd*	*3rd*	*4th*	*5th*
S_j	0.003139	0.002713	0.002832	0.002827	0.003511
S_j^*	0.003515	0.003172	0.002844	0.003106	0.00351
$S_{di\mathrm{j}}$	0.000685	0.000649	0.000638	0.00065	N/A
m_{ij}	0.001471	0.001594	0.001454	0.000988	N/A
$m_{ij} / S_{di\mathrm{j}}$	2.149	2.458	2.277	1.519	N/A
$P(D_{ij} \geq 0)$	0.984	0.992	0.988	0.936	N/A

Table H17. Statistical results of 400 repeated trials without measurement errors for detecting damage state 3.

Measurement point	*1st*	*2nd*	*3rd*	*4th*	*5th*
S_j	0.003267	0.002968	0.00297	0.003172	0.00335
S_j^*	0.00336	0.003092	0.002982	0.003117	0.003386
$S_{di\mathrm{j}}$	0.000334	0.00032	0.000318	0.000326	N/A
m_{ij}	0.001471	0.001594	0.001454	0.000988	N/A
$m_{ij} / S_{di\mathrm{j}}$	4.403	4.977	4.574	3.032	N/A
$P(D_{ij} \geq 0)$	0.99999	1.00000	0.99999	0.99900	N/A

Table H18. Statistical results of 25 repeated trials without measurement errors for detecting damage state 4.

Measurement point	*1st*	*2nd*	*3rd*	*4th*	*5th*
S_j	0.003567	0.002476	0.003107	0.002512	0.003376
S_j^*	0.002919	0.003431	0.002613	0.003521	0.003545
$S_{di\mathrm{j}}$	0.001345	0.001294	0.001272	0.001307	N/A
m_{ij}	0.000328	0.000352	0.000309	0.000197	N/A
$m_{ij} / S_{di\mathrm{j}}$	0.244	0.272	0.243	0.151	N/A
$P(D_{ij} \geq 0)$	0.595	0.606	0.595	0.560	N/A

Table H19. Statistical results of 100 repeated trials without measurement errors for detecting damage state 4.

Measurement point	*1st*	*2nd*	*3rd*	*4th*	*5th*
S_j	0.003139	0.002713	0.002832	0.002827	0.003511
S_j^*	0.003515	0.003171	0.002843	0.003107	0.003512
$S_{di\mathrm{j}}$	0.000685	0.000649	0.000638	0.00065	N/A
m_{ij}	0.001471	0.001594	0.001454	0.000988	N/A
m_{ij} / $S_{di\mathrm{j}}$	0.479	0.542	0.484	0.303	N/A
$P(D_{ij} \geq 0)$	0.684	0.705	0.685	0.618	N/A

Table H20. Statistical results of 400 repeated trials without measurement errors for detecting damage state 4.

Measurement point	*1st*	*2nd*	*3rd*	*4th*	*5th*
S_j	0.003267	0.002968	0.00297	0.003172	0.00335
S_j^*	0.003424	0.003044	0.00298	0.003097	0.003466
$S_{di\mathrm{j}}$	0.000338	0.000321	0.00032	0.000327	N/A
m_{ij}	0.000328	0.000352	0.000309	0.000197	N/A
m_{ij} / $S_{di\mathrm{j}}$	0.971	1.095	0.966	0.602	N/A
$P(D_{ij} \geq 0)$	0.834	0.862	0.833	0.726	N/A

Table H21. Statistical results of 25 repeated trials without measurement errors for detecting damage state 5.

Measurement point	*1st*	*2nd*	*3rd*	*4th*	*5th*
S_j	0.003567	0.002476	0.003107	0.002512	0.003376
S_j^*	0.003072	0.003331	0.003155	0.003656	0.003699
$S_{di\mathrm{j}}$	0.001292	0.001214	N/A	0.001253	0.001337
m_{ij}	0.000877	0.00078	N/A	0.000612	0.000719
m_{ij} / $S_{di\mathrm{j}}$	0.678	0.643	N/A	0.488	0.538
$P(D_{ij} \geq 0)$	0.752	0.739	N/A	0.688	0.705

Table H22. Statistical results of 100 repeated trials without measurement errors for detecting damage state 5.

Measurement point	*1st*	*2nd*	*3rd*	*4th*	*5th*
S_j	0.003139	0.002713	0.002832	0.002827	0.003511
S_j^*	0.00389	0.003081	0.003357	0.003184	0.003306
$S_{di\mathrm{j}}$	0.000665	0.000601	N/A	0.000612	0.000652
m_{ij}	0.000877	0.00078	N/A	0.000612	0.000719
m_{ij} / $S_{di\mathrm{j}}$	1.317	1.298	N/A	1.001	1.102
$P(D_{ij} \geq 0)$	0.906	0.903	N/A	0.841	0.864

Table H23. Statistical results of 400 repeated trials without measurement errors for detecting damage state 5.

Measurement point	*1st*	*2nd*	*3rd*	*4th*	*5th*
S_j	0.003267	0.002968	0.00297	0.003172	0.00335
S_j^*	0.003707	0.003163	0.003222	0.003266	0.003664
$S_{di\mathrm{j}}$	0.00033	0.000308	N/A	0.000316	0.000331
m_{ij}	0.000877	0.00078	N/A	0.000612	0.000719
$m_{ij} / S_{di\mathrm{j}}$	2.655	2.531	N/A	1.937	2.171
$P(D_{ij} \geq 0)$	0.995	0.994	N/A	0.974	0.985

Table H24. Statistical results of 25 repeated trials without measurement errors for detecting damage state 6.

Measurement point	*1st*	*2nd*	*3rd*	*4th*	*5th*
S_j	0.003567	0.002476	0.003107	0.002512	0.003376
S_j^*	0.00306	0.002778	0.003675	0.002882	0.003876
$S_{di\mathrm{j}}$	0.001345	0.001217	N/A	0.001229	0.001408
m_{ij}	0.000447	0.000368	N/A	0.000185	0.000274
$m_{ij} / S_{di\mathrm{j}}$	0.332	0.303	N/A	0.151	0.195
$P(D_{ij} \geq 0)$	0.629	0.618	N/A	0.560	0.575

Table H25. Statistical results of 100 repeated trials without measurement errors for detecting damage state 6.

Measurement point	*1st*	*2nd*	*3rd*	*4th*	*5th*
S_j	0.003139	0.002713	0.002832	0.002827	0.003511
S_j^*	0.003425	0.002997	0.002985	0.003084	0.003386
$S_{di\mathrm{j}}$	0.000621	0.000577	N/A	0.000587	0.000638
m_{ij}	0.000877	0.00078	N/A	0.000612	0.000719
$m_{ij} / S_{di\mathrm{j}}$	0.720	0.639	N/A	0.315	0.430
$P(D_{ij} \geq 0)$	0.764	0.739	N/A	0.625	0.666

Table H26. Statistical results of 400 repeated trials without measurement errors for detecting damage state 6.

Measurement point	*1st*	*2nd*	*3rd*	*4th*	*5th*
S_j	0.003267	0.002968	0.00297	0.003172	0.00335
S_j^*	0.003464	0.003085	0.00294	0.003043	0.003424
$S_{di\mathrm{j}}$	0.000317	0.000299	N/A	0.000303	0.000318
m_{ij}	0.000447	0.000368	N/A	0.000185	0.000274
$m_{ij} / S_{di\mathrm{j}}$	1.411	1.232	N/A	0.610	0.863
$P(D_{ij} \geq 0)$	0.921	0.891	N/A	0.729	0.805

Table H27. Probabilities using 25 repeated trials without measurement errors for detecting all nine damage states.

Damage	1a	1b	1c	1d	2	3	4	5	6
1st 25	0.726	0.523	0.229	0.170	0.396	0.520	0.120	0.270	0.125
2nd 25	0.721	0.515	0.241	0.162	0.410	0.518	0.131	0.262	0.130
3rd 25	0.715	0.519	0.250	0.152	0.394	0.533	0.116	0.269	0.132
4th 25	0.706	0.522	0.252	0.164	0.418	0.519	0.123	0.255	0.116
5th 25	0.724	0.522	0.240	0.151	0.398	0.517	0.130	0.282	0.111
6th 25	0.739	0.518	0.239	0.165	0.395	0.515	0.131	0.258	0.123
7th 25	0.734	0.509	0.227	0.166	0.404	0.537	0.122	0.277	0.117
8th 25	0.714	0.527	0.233	0.173	0.418	0.509	0.121	0.253	0.126
9th 25	0.720	0.528	0.242	0.158	0.387	0.519	0.127	0.279	0.114
10th 25	0.717	0.510	0.236	0.162	0.403	0.516	0.117	0.281	0.118
11th 25	0.722	0.535	0.231	0.159	0.403	0.520	0.124	0.257	0.131
12th 25	0.727	0.526	0.234	0.165	0.387	0.539	0.123	0.266	0.127
13th 25	0.728	0.543	0.244	0.174	0.393	0.514	0.121	0.292	0.132
14th 25	0.726	0.530	0.231	0.165	0.391	0.526	0.123	0.265	0.123
15th 25	0.728	0.533	0.238	0.186	0.406	0.524	0.124	0.262	0.126
16th 25	0.737	0.523	0.228	0.173	0.410	0.515	0.130	0.262	0.122
17th 25	0.737	0.517	0.233	0.171	0.427	0.511	0.117	0.266	0.119
18th 25	0.722	0.535	0.247	0.170	0.402	0.517	0.127	0.266	0.122
19th 25	0.730	0.521	0.237	0.177	0.403	0.514	0.120	0.264	0.111
20th 25	0.728	0.532	0.233	0.178	0.419	0.519	0.121	0.271	0.116
21st 25	0.722	0.520	0.243	0.167	0.404	0.524	0.133	0.273	0.115
22nd 25	0.727	0.513	0.230	0.175	0.403	0.505	0.129	0.286	0.127
23rd 25	0.728	0.523	0.231	0.177	0.402	0.525	0.130	0.266	0.122
24th 25	0.719	0.521	0.242	0.156	0.394	0.515	0.109	0.267	0.107
25th 25	0.735	0.526	0.239	0.179	0.401	0.517	0.121	0.263	0.127
26th 25	0.729	0.513	0.238	0.173	0.407	0.525	0.125	0.248	0.117
27th 25	0.724	0.517	0.243	0.162	0.404	0.515	0.126	0.269	0.127
28th 25	0.723	0.544	0.237	0.166	0.378	0.527	0.119	0.269	0.112
29th 25	0.723	0.535	0.236	0.172	0.378	0.526	0.115	0.265	0.120
30th 25	0.729	0.524	0.240	0.160	0.396	0.526	0.117	0.270	0.114
31st 25	0.722	0.528	0.237	0.179	0.395	0.504	0.120	0.268	0.122
32nd 25	0.733	0.525	0.258	0.154	0.410	0.512	0.127	0.257	0.118
33rd 25	0.725	0.523	0.236	0.178	0.401	0.527	0.120	0.272	0.136
34th 25	0.720	0.517	0.239	0.170	0.404	0.526	0.125	0.278	0.125
35th 25	0.721	0.514	0.237	0.162	0.409	0.520	0.129	0.277	0.121
36th 25	0.716	0.528	0.234	0.160	0.398	0.525	0.126	0.273	0.137
37th 25	0.719	0.514	0.249	0.163	0.400	0.516	0.119	0.261	0.130
38th 25	0.715	0.514	0.235	0.178	0.414	0.539	0.130	0.264	0.113
39th 25	0.723	0.522	0.246	0.167	0.417	0.510	0.112	0.261	0.116
40th 25	0.717	0.511	0.240	0.160	0.414	0.540	0.128	0.263	0.121
41st 25	0.737	0.537	0.251	0.157	0.407	0.519	0.123	0.262	0.099
42nd 25	0.737	0.540	0.240	0.165	0.404	0.517	0.118	0.252	0.109
43rd 25	0.721	0.533	0.234	0.176	0.423	0.523	0.128	0.263	0.114
44th 25	0.720	0.513	0.242	0.162	0.398	0.525	0.111	0.272	0.125
45th 25	0.734	0.523	0.244	0.179	0.389	0.516	0.111	0.280	0.117
46th 25	0.735	0.517	0.239	0.153	0.405	0.518	0.131	0.280	0.116
47th 25	0.735	0.512	0.242	0.161	0.405	0.520	0.126	0.263	0.119
48th 25	0.736	0.526	0.226	0.155	0.402	0.511	0.120	0.255	0.126
Average	**0.726**	**0.523**	**0.239**	**0.167**	**0.403**	**0.520**	**0.123**	**0.267**	**0.121**

Table H28. Probabilities using 100 repeated trials without measurement errors for detecting all nine damage states.

Damage	1a	1b	1c	1d	2	3	4	5	6
1st 100	0.977	0.919	0.575	0.337	0.701	0.904	0.201	0.596	0.237
2nd 100	0.976	0.922	0.585	0.340	0.700	0.902	0.209	0.594	0.241
3rd 100	0.979	0.917	0.578	0.347	0.702	0.901	0.199	0.590	0.222
4th 100	0.978	0.921	0.575	0.347	0.722	0.903	0.201	0.602	0.230
5th 100	0.975	0.916	0.583	0.336	0.704	0.904	0.218	0.605	0.229
6th 100	0.978	0.914	0.573	0.344	0.702	0.898	0.213	0.625	0.249
7th 100	0.978	0.917	0.574	0.347	0.701	0.905	0.215	0.593	0.241
8th 100	0.974	0.917	0.582	0.324	0.691	0.901	0.183	0.596	0.216
9th 100	0.981	0.918	0.580	0.349	0.699	0.902	0.201	0.589	0.249
10th 100	0.979	0.914	0.579	0.342	0.708	0.905	0.207	0.566	0.232
11th 100	0.976	0.915	0.582	0.330	0.703	0.901	0.209	0.599	0.248
12th 100	0.976	0.925	0.578	0.335	0.670	0.905	0.199	0.599	0.224
Average	**0.977**	**0.918**	**0.579**	**0.340**	**0.702**	**0.903**	**0.205**	**0.594**	**0.235**

Table H29. Probabilities using 400 repeated trials without measurement errors for detecting all nine damage states.

Damage	1a	1b	1c	1d	2	3	4	5	6
1st 400	1.0000	0.9998	0.935	0.689	0.949	0.9990	0.435	0.949	0.482
2nd 400	1.0000	0.9998	0.939	0.702	0.947	0.9991	0.442	0.951	0.509
3rd 400	1.0000	0.9998	0.941	0.707	0.948	0.9990	0.432	0.947	0.497
Average	**1.0000**	**0.9998**	**0.938**	**0.699**	**0.948**	**0.9990**	**0.436**	**0.949**	**0.496**

Appendix I Calibration of vibration signal with measurement errors

To produce levels of uncertainty in the numerical results comparable to those found in the experimental data, a white noise random signal was added to the displacement time history obtained from the numerical analysis. An example of this procedure is described next.

As an example, three independent time-domain vibration signals generated by the transient dynamic analysis of finite element model are shown in Fig. I1. After signal processing, three mode shapes of the first mode of the undamaged bridge deck, mode shape-1a, mode shape-1b, and mode shape-1b were produced from vibration-a, vibration-b, and vibration-c, respectively. These mode shapes were defined at five evenly spaced points as shown in Fig. I2. The modal assurance criteria (MAC) between mode shape-1a and mode shape-1b was 0.999857, the MAC between mode shape-1b and mode shape-1c was 0.999913, and the MAC between mode shape-1a and mode shape-1c was 0.999924. The average of these three MAC was 0.99990. However, the average MAC between fundamental mode shapes (10 trials) derived from experimental data was found to be 0.9995. If proper magnitude of random noise is induced to the vibration-1a, vibration-1b and vibration-1c in this study, the average MAC between the mode shape produced by these vibration will reduce to 0.9995.

Three random noises generated by the software Mat Lab are shown in Fig. I3. The root mean squares (rms) of random noise-a, random noise-b, and random noise-c are 3.57×10^{-5}, 3.61×10^{-5}, and 3.57×10^{-5}, respectively. While the *rms* of vibration-a, vibration-b, and vibration-c are 6.84×10^{-5}, 8.22×10^{-5}, and 8.92×10^{-5}.

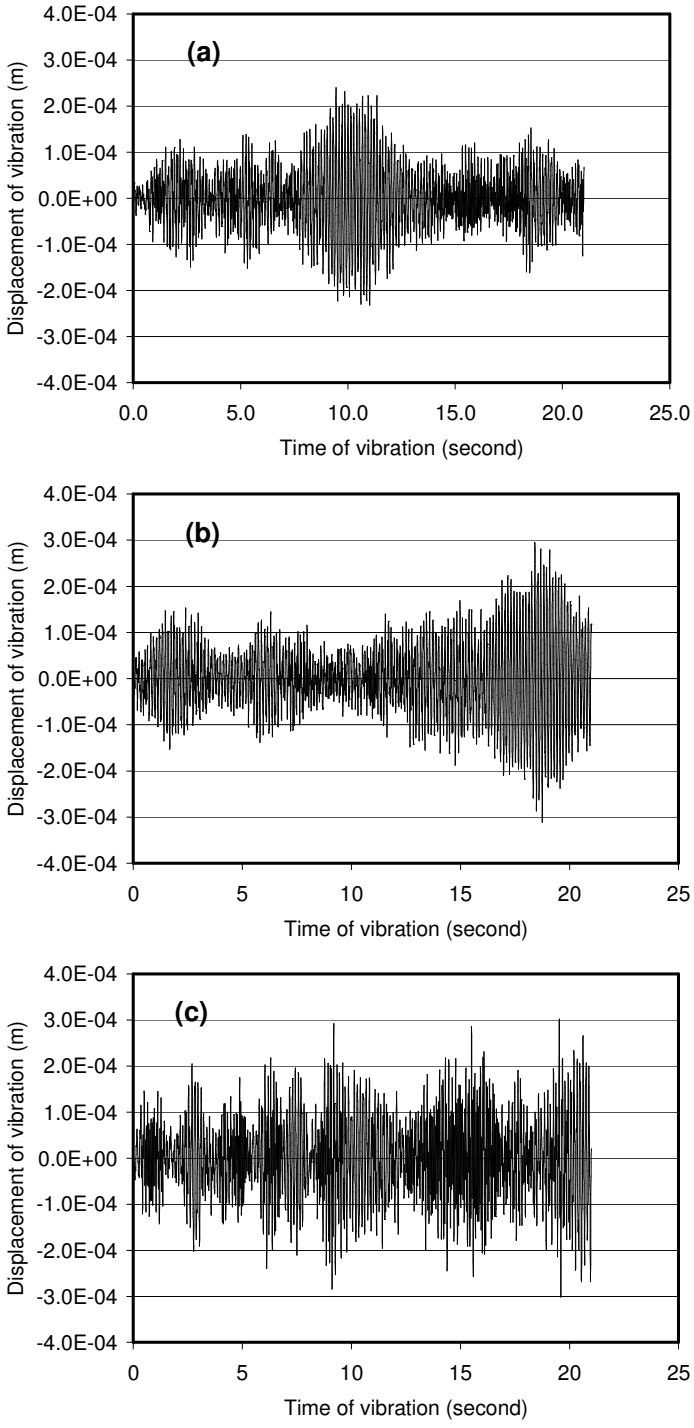

Figure I1 Time-domain signals of vibration generated by the finite element model (a) vibration-a, (b) vibration-b, and (c) vibration-c.

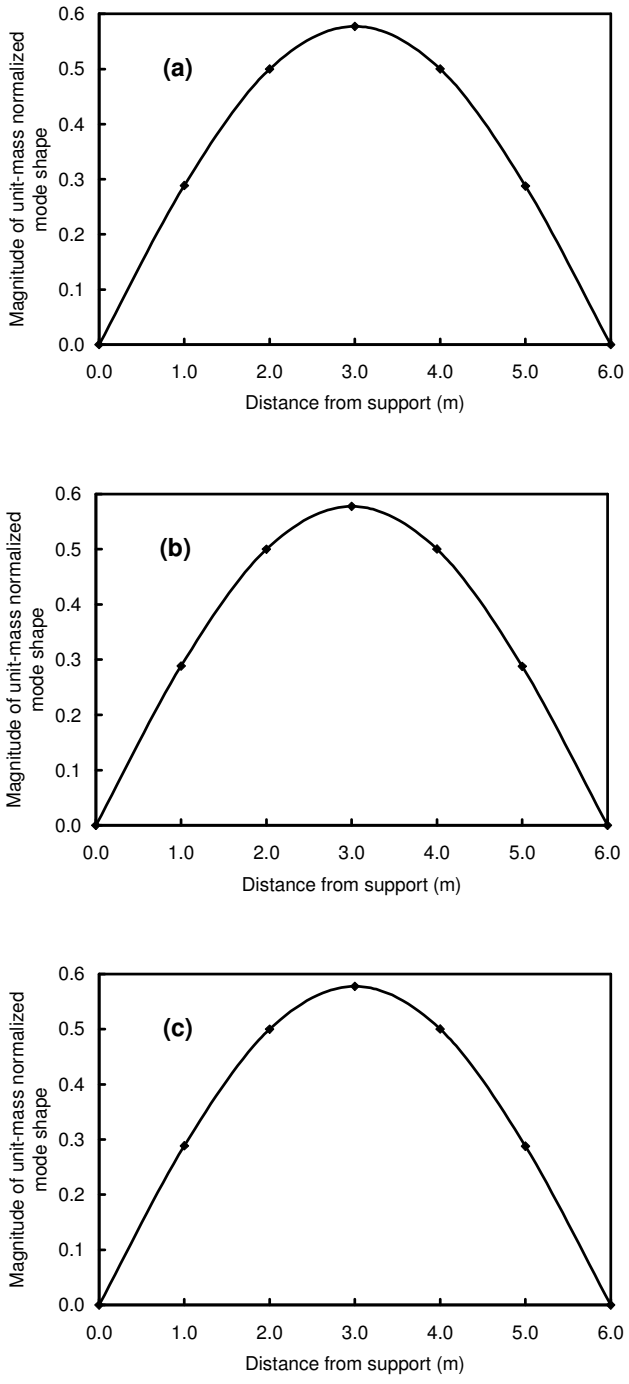

Figure I2 First mode shape produced by processing the vibration signals, (a) mode shape-1a, (b) mode shape-1b, and (c) mode shape-1c.

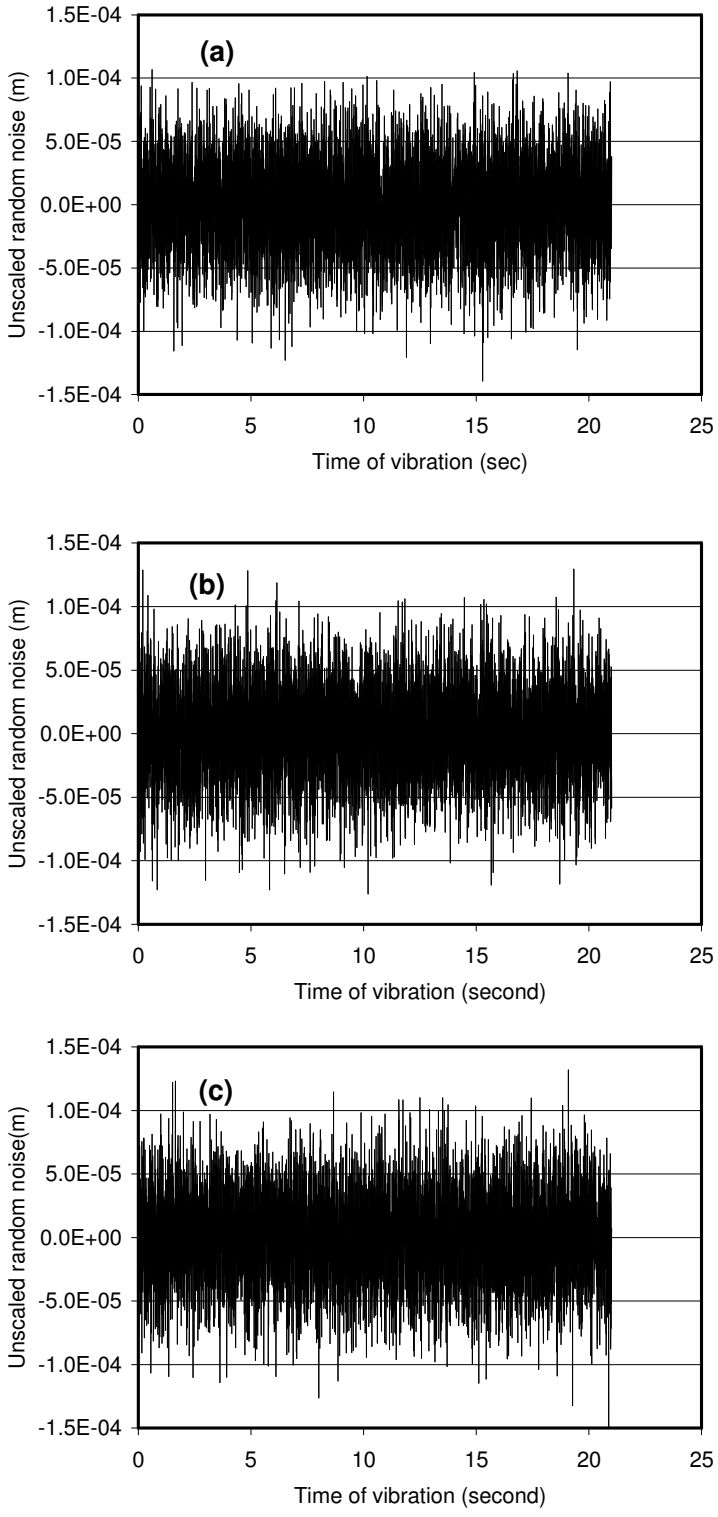

Figure I3 The unscaled random noises, (a) random noise-a, (b) random noise-b, and (c) random noise-c

Now, the three random noises were scaled to make their root mean squares equal to 35% of those of the three vibrations, respectively, i.e., the root mean squares of random noise-a, random-b and random-c became 2.39×10^{-5}, 2.88×10^{-5}, and 3.12×10^{-5}. That means that values of random noise-a, random noise-b, and random noise-c have to be multiplied by 0.671, 0.798, and 0.874. These scale factors were derived from $0.671 \times 3.57 \times 10^{-5} = 2.39 \times 10^{-5}$, $0.798 \times 3.61 \times 10^{-5} = 2.88 \times 10^{-5}$,and $0.874 \times 3.57 \times 10^{-5} = 3.12 \times 10^{-5}$.

Vibration with measurement errors were produced by adding above three scaled random noises to the vibration-a, vibration-b, and vibration-c, respectively. These new vibration signals were shown in Fig. I4. Three new mode shapes new-mode-1a, new-mode-1b, and new-mode-1c were produced by processing these three vibration signals in Fig. I.4. The MAC between new-mode-1a and new-mode-1b was 0.999507, the MAC between new-mode-1b and 1c was 0.999536, and the MAC between new-mode-1a and new-mode-1c was 0.999482. The average MAC between these three new mode shapes was 0.99951, it is very close to 0.99950, the average MAC between fundamental mode shapes (10 trials) derived from experimental data.

It should be noted that the scale factor 35% was obtained after many times of trials and errors.

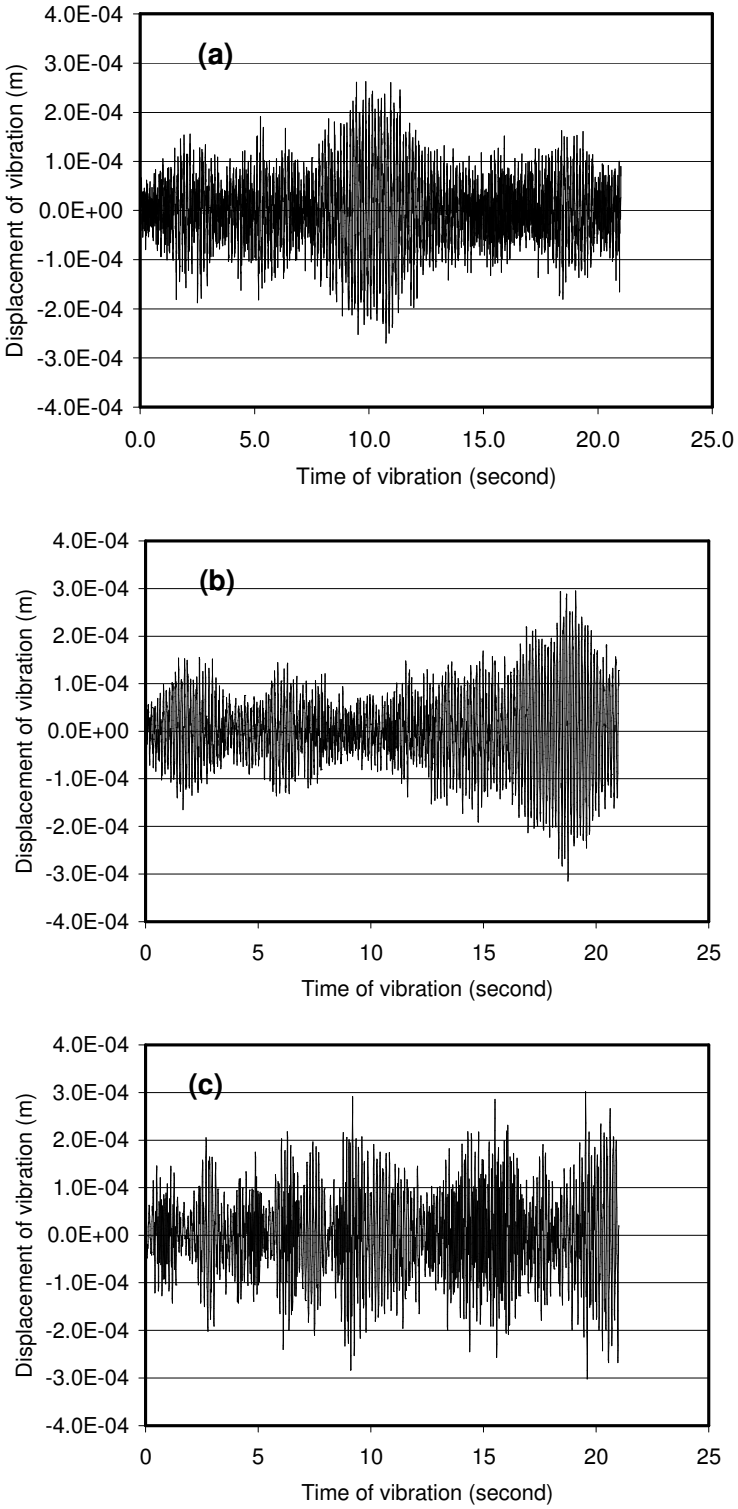

Figure I4 Vibration with random measurement errors, (a) vibration-a, (b) vibration-b, and (c) vibration-c.

Appendix J Probabilities of damage detection using random vibration with measurement errors

There were 48 sets of 25 tests, 12 sets of 100 tests, and 4 sets of 400 tests in both undamaged and damaged conditions for each damage case. Only the details from the first sets of 25 tests, first sets of 100 tests, and first sets of 400 tests are listed in the tables of this appendix. Tables J28, J29, and J30 summarized the results and calculated the average values of the probabilities of damage detection using 48 sets of 25 tests, 12 sets of 100 tests, and 3 sets of 400 tests, respectively.

Table J1. Statistical results of 25 repeated trials with measurement errors for detecting damage state 1a.

Measurement point	*1st*	*2nd*	*3rd*	*4th*	*5th*
S_j	0.005785	0.006166	0.00566	0.005746	0.006089
S_j^*	0.006613	0.007178	0.006788	0.007884	0.00798
$S_{di\mathrm{j}}$	0.002492	0.00259	N/A	0.002633	0.002675
m_{ij}	0.00171	0.00167	N/A	0.00152	0.00157
m_{ij} / $S_{di\mathrm{j}}$	0.685	0.645	N/A	0.577	0.587
$P(D_{ij} \geq 0)$	0.752	0.742	N/A	0.719	0.722

Table J2. Statistical results of 100 repeated trials with measurement errors for detecting damage state 1a.

Measurement point	1st	2nd	3rd	4th	5th
S_j	0.005927	0.006632	0.006218	0.005972	0.006512
S_j^*	0.008375	0.006641	0.007226	0.006856	0.007122
$S_{di\mathrm{j}}$	0.001401	0.001338	N/A	0.001317	0.001356
m_{ij}	0.00171	0.00167	N/A	0.00152	0.00157
$m_{ij} / S_{di\mathrm{j}}$	1.219	1.249	N/A	1.152	1.157
$P(D_{ij} \geq 0)$	0.889	0.894	N/A	0.875	0.875

Table J3. Statistical results of 400 repeated trials with measurement errors for detecting damage state 1a.

Measurement point	1st	2nd	3rd	4th	5th
S_j	0.007235	0.006582	0.006141	0.006775	0.007178
S_j^*	0.007986	0.006813	0.006938	0.007033	0.00789
$S_{di\mathrm{j}}$	0.000711	0.000663	N/A	0.000673	0.000706
m_{ij}	0.00171	0.00167	N/A	0.00152	0.00157
$m_{ij} / S_{di\mathrm{j}}$	2.402	2.522	N/A	2.255	2.221
$P(D_{ij} \geq 0)$	0.992	0.994	N/A	0.988	0.987

Table J4. Statistical results of 25 repeated trials with measurement errors for detecting damage state 1b.

Measurement point	1st	2nd	3rd	4th	5th
S_j	0.005785	0.006166	0.00566	0.005746	0.006089
S_j^*	0.007102	0.006394	0.00593	0.007724	0.007362
$S_{di\mathrm{j}}$	0.002459	0.002417	N/A	0.002529	0.002518
m_{ij}	0.00130	0.00129	N/A	0.00115	0.00120
m_{ij} / $S_{di\mathrm{j}}$	0.529	0.533	N/A	0.455	0.476
$P(D_{ij} \geq 0)$	0.702	0.702	N/A	0.675	0.684

Table J5. Statistical results of 100 repeated trials with measurement errors for detecting damage state 1b.

Measurement point	1st	2nd	3rd	4th	5th
S_j	0.005927	0.006632	0.006218	0.005972	0.006512
S_j^*	0.008315	0.005931	0.00619	0.007344	0.006787
$S_{di\mathrm{j}}$	0.001346	0.00125	N/A	0.001291	0.001286
m_{ij}	0.00130	0.00129	N/A	0.00115	0.00120
m_{ij} / $S_{di\mathrm{j}}$	0.966	1.031	N/A	0.891	0.932
$P(D_{ij} \geq 0)$	0.834	0.849	N/A	0.813	0.824

Table J6. Statistical results of 400 repeated trials with measurement errors for detecting damage state 1b.

Measurement point	1st	2nd	3rd	4th	5th
S_j	0.007235	0.006582	0.006141	0.006775	0.007178
S_j^*	0.008091	0.006714	0.006444	0.006723	0.007324
$S_{di\mathrm{j}}$	0.000702	0.000647	N/A	0.000653	0.000679
m_{ij}	0.00130	0.00129	N/A	0.00115	0.00120
$m_{ij} / S_{di\mathrm{j}}$	1.853	1.991	N/A	1.762	1.765
$P(D_{ij} \geq 0)$	0.968	0.977	N/A	0.961	0.961

Table J7. Statistical results of 25 repeated trials with measurement errors for detecting damage state 1c.

Measurement point	1st	2nd	3rd	4th	5th
S_j	0.005785	0.002476	0.003107	0.002512	0.003376
S_j^*	0.007164	0.006451	0.005136	0.006281	0.008348
$S_{di\mathrm{j}}$	0.002198	0.001831	N/A	0.001809	0.002165
m_{ij}	0.000684	0.000698	N/A	0.00063	0.00065
$m_{ij} / S_{di\mathrm{j}}$	0.311	0.381	N/A	0.348	0.300
$P(D_{ij} \geq 0)$	0.622	0.648	N/A	0.637	0.622

Table J8. Statistical results of 100 repeated trials with measurement errors for detecting damage state 1c.

Measurement point	1st	2nd	3rd	4th	5th
S_j	0.005927	0.006632	0.006218	0.005972	0.006512
S_j^*	0.006761	0.00636	0.006043	0.006908	0.006805
$S_{di\mathrm{j}}$	0.001249	0.001263	N/A	0.001259	0.00128
m_{ij}	0.000684	0.000698	N/A	0.00063	0.00065
$m_{ij} / S_{di\mathrm{j}}$	0.547	0.553	N/A	0.500	0.507
$P(D_{ij} \geq 0)$	0.709	0.709	N/A	0.692	0.695

Table J9. Statistical results of 400 repeated trials with measurement errors for detecting damage state 1c.

Measurement point	1st	2nd	3rd	4th	5th
S_j	0.007235	0.002968	0.00297	0.003172	0.00335
S_j^*	0.007042	0.006796	0.006348	0.006936	0.0074
$S_{di\mathrm{j}}$	0.000615	0.00051		0.000518	0.000536
m_{ij}	0.000684	0.000698	N/A	0.00063	0.00065
$m_{ij} / S_{di\mathrm{j}}$	1.113	1.369		1.216	1.211
$P(D_{ij} \geq 0)$	0.867	0.915		0.889	0.887

Table J10. Statistical results of 25 repeated trials with measurement errors for detecting damage state 1d.

Measurement point	1st	2nd	3rd	4th	5th
S_j	0.005785	0.006166	0.00566	0.005746	0.006089
S_j^*	0.007748	0.00593	0.007452	0.006537	0.005804
$S_{di\mathrm{j}}$	0.002691	0.002536	N/A	0.002556	0.002517
m_{ij}	0.000441	0.000421	N/A	0.000408	0.000411
$m_{ij} / S_{di\mathrm{j}}$	0.164	0.166	N/A	0.160	0.163
$P(D_{ij} \geq 0)$	0.564	0.568	N/A	0.563	0.564

Table J11. Statistical results of 100 repeated trials with measurement errors for detecting damage state 1d.

Measurement point	1st	2nd	3rd	4th	5th
S_j	0.005927	0.006632	0.006218	0.005972	0.006512
S_j^*	0.007687	0.006542	0.007227	0.006258	0.006759
$S_{di\mathrm{j}}$	0.001361	0.001333	N/A	0.001287	0.001338
m_{ij}	0.000441	0.000421	N/A	0.000408	0.000411
$m_{ij} / S_{di\mathrm{j}}$	0.324	0.316	N/A	0.317	0.307
$P(D_{ij} \geq 0)$	0.626	0.625	N/A	0.625	0.621

Table J12. Statistical results of 400 repeated trials with measurement errors for detecting damage state 1d.

Measurement point	1st	2nd	3rd	4th	5th
S_j	0.007235	0.006582	0.006141	0.006775	0.007178
S_j^*	0.007479	0.006645	0.00643	0.006559	0.006834
$S_{di\text{j}}$	0.000684	0.000645	N/A	0.000648	0.000666
m_{ij}	0.000441	0.000421	N/A	0.000408	0.000411
$m_{ij} / S_{di\text{j}}$	0.645	0.653	N/A	0.630	0.617
$P(D_{ij} \geq 0)$	0.740	0.742	N/A	0.736	0.731

Table J13. Statistical results of 25 repeated trials with measurement errors for detecting damage state 2.

Measurement point	1st	2nd	3rd	4th	5th
S_j	0.005785	0.006166	0.00566	0.005746	0.006089
S_j^*	0.006738	0.006724	0.006037	0.006519	0.00934
$S_{di\text{j}}$	0.002428	0.002463	N/A	N/A	0.002777
m_{ij}	0.000881	0.000959	N/A	N/A	0.000538
$m_{ij} / S_{di\text{j}}$	0.363	0.389	N/A	N/A	0.194
$P(D_{ij} \geq 0)$	0.641	0.652	N/A	N/A	0.575

Table J14. Statistical results of 100 repeated trials with measurement errors for detecting damage state 2.

Measurement point	1st	2nd	3rd	4th	5th
S_j	0.005927	0.006632	0.006218	0.005972	0.006512
S_j^*	0.007297	0.006863	0.005574	0.006219	0.008022
$S_{di\mathrm{j}}$	0.001257	0.001268	N/A	N/A	0.001328
m_{ij}	0.000881	0.000959	N/A	N/A	0.000538
$m_{ij} / S_{di\mathrm{j}}$	0.700	0.756	N/A	N/A	0.405
$P(D_{ij} \geq 0)$	0.758	0.776	N/A	N/A	0.657

Table J15. Statistical results of 400 repeated trials with measurement errors for detecting damage state 2.

Measurement point	1st	2nd	3rd	4th	5th
S_j	0.007235	0.006582	0.006141	0.006775	0.007178
S_j^*	0.007159	0.006524	0.006111	0.006702	0.007977
$S_{di\mathrm{j}}$	0.000668	0.000634	N/A	N/A	0.00069
m_{ij}	0.000881	0.000959	N/A	N/A	0.000538
$m_{ij} / S_{di\mathrm{j}}$	1.318	1.512	N/A	N/A	0.780
$P(D_{ij} \geq 0)$	0.905	0.934	N/A	N/A	0.782

Table J16. Statistical results of 25 repeated trials with measurement errors for detecting damage state 3.

Measurement point	1st	2nd	3rd	4th	5th
S_j	0.00579	0.00617	0.00566	0.00575	0.00609
S_j^*	0.00762	0.00764	0.00622	0.00587	0.00732
$S_{di\mathrm{j}}$	0.00270	0.00274	0.00254	0.00252	N/A
m_{ij}	0.001471	0.001594	0.001454	0.000988	N/A
m_{ij} / $S_{di\mathrm{j}}$	0.5448	0.5829	0.5722	0.3927	N/A
$P(D_{ij} \geq 0)$	0.708	0.719	0.716	0.652	N/A

Table J17. Statistical results of 100 repeated trials with measurement errors for detecting damage state 3.

Measurement point	1st	2nd	3rd	4th	5th
S_j	0.00593	0.00663	0.00622	0.00597	0.00651
S_j^*	0.00817	0.00638	0.00602	0.00633	0.00763
$S_{di\mathrm{j}}$	0.00142	0.00136	0.00132	0.00133	N/A
m_{ij}	0.001471	0.001594	0.001454	0.000988	N/A
m_{ij} / $S_{di\mathrm{j}}$	1.034	1.171	1.097	0.744	N/A
$P(D_{ij} \geq 0)$	0.849	0.879	0.864	0.770	N/A

Table J18. Statistical results of 400 repeated trials with measurement errors for detecting damage state 3.

Measurement point	1st	2nd	3rd	4th	5th
S_j	0.00723	0.00658	0.00614	0.00677	0.00718
S_j^*	0.00759	0.00645	0.00613	0.00636	0.00772
$S_{di\mathrm{j}}$	0.000743	0.000700	0.000683	0.000703	N/A
m_{ij}	0.001471	0.001594	0.001454	0.000988	N/A
$m_{ij} / S_{di\mathrm{j}}$	1.979	2.277	2.130	1.406	N/A
$P(D_{ij} \geq 0)$	0.976	0.988	0.983	0.921	N/A

Table J19. Statistical results of 25 repeated trials with measurement errors for detecting damage state 4.

Measurement point	1st	2nd	3rd	4th	5th
S_j	0.00579	0.00617	0.00566	0.00575	0.00609
S_j^*	0.00660	0.00579	0.00681	0.00719	0.00821
$S_{di\mathrm{j}}$	0.00269	0.00265	0.00270	0.00275	0.00289
m_{ij}	0.000328	0.000352	0.000309	0.000197	N/A
$m_{ij} / S_{di\mathrm{j}}$	0.1217	0.1326	0.1143	0.0716	N/A
$P(D_{ij} \geq 0)$	0.548	0.552	0.544	0.528	N/A

Table J20. Statistical results of 100 repeated trials with measurement errors for detecting damage state 4.

Measurement point	1st	2nd	3rd	4th	5th
S_j	0.00593	0.00663	0.00622	0.00597	0.00651
S_j^*	0.00735	0.00681	0.00716	0.00703	0.00736
$S_{di\mathrm{j}}$	0.00136	0.00137	0.00137	0.00135	N/A
m_{ij}	0.001471	0.001594	0.001454	0.000988	N/A
$m_{ij} / S_{di\mathrm{j}}$	0.241	0.257	0.226	0.146	N/A
$P(D_{ij} \geq 0)$	0.595	0.603	0.591	0.56	N/A

Table J21. Statistical results of 400 repeated trials with measurement errors for detecting damage state 4.

Measurement point	1st	2nd	3rd	4th	5th
S_j	0.00723	0.00658	0.00614	0.00677	0.00718
S_j^*	0.00700	0.00678	0.00645	0.00668	0.00745
$S_{di\mathrm{j}}$	0.000722	0.000701	0.000682	0.000703	N/A
m_{ij}	0.000328	0.000352	0.000309	0.000197	N/A
$m_{ij} / S_{di\mathrm{j}}$	0.454	0.502	0.453	0.280	N/A
$P(D_{ij} \geq 0)$	0.674	0.692	0.674	0.61	N/A

Table J22. Statistical results of 25 repeated trials with measurement errors for detecting damage state 5.

Measurement point	1st	2nd	3rd	4th	5th
S_j	0.00579	0.00617	0.00566	0.00575	0.00609
S_j^*	0.00813	0.00646	0.00785	0.00650	0.00711
$S_{di\mathrm{j}}$	0.00278	0.00263	N/A	0.00260	0.00269
m_{ij}	0.000877	0.00078	N/A	0.000612	0.000719
m_{ij} / $S_{di\mathrm{j}}$	0.315	0.296	N/A	0.235	0.267
$P(D_{ij} \geq 0)$	0.624	0.617	N/A	0.593	0.606

Table J23. Statistical results of 100 repeated trials with measurement errors for detecting damage state 5.

Measurement point	1st	2nd	3rd	4th	5th
S_j	0.00593	0.00663	0.00622	0.00597	0.00651
S_j^*	0.00855	0.00714	0.00653	0.00624	0.00733
$S_{di\mathrm{j}}$	0.00138	0.00133	N/A	0.00125	0.00133
m_{ij}	0.000877	0.00078	N/A	0.000612	0.000719
m_{ij} / $S_{di\mathrm{j}}$	0.637	0.588	N/A	0.490	0.540
$P(D_{ij} \geq 0)$	0.737	0.722	N/A	0.688	0.705

Table J24. Statistical results of 400 repeated trials with measurement errors for detecting damage state 5.

Measurement point	1st	2nd	3rd	4th	5th
S_j	0.00723	0.00658	0.00614	0.00677	0.00718
S_j^*	0.00739	0.00629	0.00613	0.00657	0.00761
$S_{di\mathrm{j}}$	0.000675	0.000629	N/A	0.000641	0.00068
m_{ij}	0.000877	0.00078	N/A	0.000612	0.000719
$m_{ij} / S_{di\mathrm{j}}$	1.299	1.241	N/A	0.955	1.058
$P(D_{ij} \geq 0)$	0.903	0.893	N/A	0.828	0.855

Table J25. Statistical results of 25 repeated trials with measurement errors for detecting damage state 6.

Measurement point	1st	2nd	3rd	4th	5th
S_j	0.00579	0.00617	0.00566	0.00575	0.00609
S_j^*	0.00761	0.00658	0.00565	0.00740	0.00752
$S_{di\mathrm{j}}$	0.00249	0.00241	N/A	0.00246	0.00251
m_{ij}	0.000447	0.000368	N/A	0.000185	0.000274
$m_{ij} / S_{di\mathrm{j}}$	0.1793	0.1529	N/A	0.0751	0.1092
$P(D_{ij} \geq 0)$	0.571	0.56	N/A	0.53	0.544

Table J26. Statistical results of 100 repeated trials with measurement errors for detecting damage state 6.

Measurement point	1st	2nd	3rd	4th	5th
S_j	0.00593	0.00663	0.00622	0.00597	0.00651
S_j^*	0.00739	0.00680	0.00648	0.00678	0.00759
$S_{di\mathrm{j}}$	0.00131	0.00131	N/A	0.00127	0.00134
m_{ij}	0.000877	0.00078	N/A	0.000612	0.000719
m_{ij} / $S_{di\mathrm{j}}$	0.3424	0.2819	N/A	0.1453	0.2040
$P(D_{ij} \geq 0)$	0.633	0.61	N/A	0.559	0.579

Table J27. Statistical results of 400 repeated trials with measurement errors for detecting damage state 6.

Measurement point	1st	2nd	3rd	4th	5th
S_j	0.00723	0.00658	0.00614	0.00677	0.00718
S_j^*	0.00749	0.00704	0.00648	0.00694	0.00744
$S_{di\mathrm{j}}$	0.000686	0.000657	N/A	0.000659	0.000683
m_{ij}	0.000447	0.000368	N/A	0.000185	0.000274
m_{ij} / $S_{di\mathrm{j}}$	0.652	0.561	N/A	0.281	0.401
$P(D_{ij} \geq 0)$	0.742	0.712	N/A	0.61	0.655

Table J28. Probabilities using 25 repeated trials with measurement errors for detecting all nine damage states.

Damage	1a	1b	1c	1d	2	3	4	5	6
1st 25	0.290	0.228	0.160	0.102	0.240	0.238	0.087	0.138	0.092
2nd 25	0.302	0.221	0.157	0.106	0.245	0.242	0.095	0.143	0.091
3rd 25	0.285	0.225	0.173	0.103	0.246	0.244	0.084	0.146	0.087
4th 25	0.280	0.228	0.167	0.099	0.221	0.230	0.100	0.136	0.091
5th 25	0.290	0.220	0.159	0.105	0.240	0.239	0.081	0.144	0.095
6th 25	0.295	0.222	0.159	0.105	0.256	0.231	0.086	0.146	0.096
7th 25	0.290	0.226	0.144	0.101	0.255	0.214	0.084	0.123	0.085
8th 25	0.299	0.242	0.150	0.104	0.230	0.238	0.089	0.125	0.092
9th 25	0.285	0.235	0.163	0.100	0.233	0.228	0.089	0.126	0.087
10th 25	0.299	0.234	0.171	0.108	0.246	0.227	0.086	0.151	0.100
11th 25	0.293	0.230	0.162	0.101	0.236	0.246	0.083	0.151	0.092
12th 25	0.286	0.225	0.167	0.110	0.251	0.244	0.078	0.147	0.103
13th 25	0.284	0.239	0.169	0.096	0.260	0.231	0.093	0.148	0.088
14th 25	0.290	0.252	0.175	0.101	0.242	0.238	0.090	0.140	0.086
15th 25	0.291	0.231	0.159	0.093	0.244	0.248	0.086	0.121	0.087
16th 25	0.294	0.215	0.168	0.106	0.241	0.237	0.084	0.144	0.096
17th 25	0.291	0.224	0.161	0.094	0.234	0.244	0.093	0.131	0.102
18th 25	0.288	0.234	0.167	0.099	0.226	0.243	0.095	0.143	0.094
19th 25	0.278	0.220	0.164	0.095	0.242	0.217	0.091	0.141	0.090
20th 25	0.310	0.229	0.163	0.106	0.242	0.244	0.078	0.140	0.099
21st 25	0.286	0.233	0.171	0.109	0.232	0.228	0.092	0.145	0.099
22nd 25	0.299	0.229	0.167	0.107	0.233	0.252	0.084	0.132	0.106
23rd 25	0.289	0.213	0.170	0.107	0.250	0.223	0.081	0.134	0.090
24th 25	0.290	0.219	0.164	0.112	0.241	0.229	0.084	0.144	0.093
25th 25	0.306	0.227	0.175	0.097	0.234	0.256	0.094	0.142	0.099
26th 25	0.288	0.235	0.174	0.097	0.241	0.240	0.078	0.144	0.094
27th 25	0.313	0.235	0.164	0.102	0.244	0.248	0.088	0.134	0.094
28th 25	0.287	0.231	0.159	0.102	0.244	0.237	0.082	0.153	0.089
29th 25	0.283	0.232	0.158	0.101	0.229	0.251	0.086	0.146	0.088
30th 25	0.284	0.222	0.173	0.111	0.242	0.235	0.083	0.127	0.091
31st 25	0.302	0.228	0.178	0.104	0.227	0.256	0.085	0.134	0.095
32nd 25	0.279	0.234	0.172	0.112	0.240	0.236	0.094	0.142	0.100
33rd 25	0.291	0.228	0.170	0.091	0.246	0.241	0.085	0.140	0.087
34th 25	0.284	0.235	0.164	0.098	0.251	0.249	0.088	0.146	0.095
35th 25	0.304	0.233	0.166	0.097	0.232	0.250	0.084	0.128	0.086
36th 25	0.288	0.237	0.162	0.113	0.220	0.232	0.095	0.154	0.098
37th 25	0.275	0.220	0.163	0.095	0.239	0.245	0.095	0.122	0.099
38th 25	0.296	0.219	0.166	0.096	0.247	0.231	0.086	0.126	0.082
39th 25	0.299	0.232	0.171	0.098	0.232	0.230	0.084	0.141	0.093
40th 25	0.298	0.232	0.159	0.102	0.243	0.246	0.088	0.139	0.086
41st 25	0.288	0.243	0.175	0.126	0.230	0.244	0.089	0.142	0.087
42nd 25	0.285	0.226	0.168	0.109	0.246	0.257	0.089	0.143	0.084
43rd 25	0.295	0.229	0.169	0.105	0.261	0.242	0.083	0.140	0.102
44th 25	0.302	0.228	0.158	0.099	0.220	0.234	0.095	0.133	0.101
45th 25	0.302	0.216	0.159	0.103	0.224	0.229	0.086	0.128	0.101
46th 25	0.289	0.226	0.164	0.096	0.251	0.233	0.098	0.130	0.088
47th 25	0.299	0.226	0.153	0.099	0.234	0.237	0.086	0.147	0.096
48th 25	0.292	0.232	0.150	0.105	0.242	0.237	0.084	0.122	0.085
Average	**0.292**	**0.226**	**0.163**	**0.103**	**0.241**	**0.238**	**0.087**	**0.138**	**0.093**

Table J29. Probabilities using 100 repeated trials with measurement errors for detecting all nine damage states.

Damage	1a	1b	1c	1d	2	3	4	5	6
1st 100	0.608	0.474	0.242	0.152	0.386	0.496	0.119	0.258	0.125
2nd 100	0.602	0.492	0.248	0.145	0.357	0.505	0.130	0.263	0.127
3rd 100	0.592	0.462	0.243	0.137	0.390	0.466	0.124	0.259	0.119
4th 100	0.625	0.482	0.240	0.158	0.389	0.505	0.104	0.257	0.136
5th 100	0.600	0.489	0.257	0.165	0.369	0.482	0.125	0.265	0.137
6th 100	0.614	0.482	0.249	0.161	0.371	0.517	0.114	0.245	0.149
7th 100	0.603	0.447	0.255	0.162	0.404	0.476	0.109	0.247	0.118
8th 100	0.604	0.461	0.242	0.172	0.386	0.483	0.114	0.263	0.126
9th 100	0.620	0.478	0.264	0.140	0.374	0.523	0.129	0.260	0.137
10th 100	0.601	0.495	0.263	0.141	0.388	0.500	0.105	0.263	0.127
11th 100	0.627	0.494	0.243	0.151	0.393	0.511	0.120	0.247	0.127
12th 100	0.601	0.486	0.232	0.151	0.393	0.496	0.110	0.277	0.117
Average	**0.608**	**0.478**	**0.248**	**0.153**	**0.383**	**0.497**	**0.117**	**0.259**	**0.129**

Table J30. Probabilities using 400 repeated trials with measurement errors for detecting all nine damage states.

Damage	1a	1b	1c	1d	2	3	4	5	6
1st 400	0.961	0.873	0.625	0.295	0.661	0.873	0.192	0.571	0.211
2nd 400	0.966	0.878	0.619	0.283	0.635	0.865	0.212	0.561	0.236
3rd 400	0.966	0.860	0.622	0.292	0.641	0.857	0.195	0.553	0.237
Average	**0.964**	**0.870**	**0.622**	**0.290**	**0.646**	**0.865**	**0.199**	**0.562**	**0.228**

Appendix K Relationship between the probability of damage detection and β_{MAC}

The relationship between the probabilities of damage detection and the ratio of the standard deviation to the mean of MACs of the change of mode shape β_{MAC} using 25, 100, and 400 trials are listed in Tables K1, K2 and K3, respectively. It should be noted that the listed probabilities of damage detection and β_{MAC} in these tables are the average values for each damage case and number of trials.

Table K1. Relationship between the probability of damage detection and β_{MAC} when 25 trials were used.

Damage	1a	1b	1c	1d	2	3	4	5	6
$\overline{\Delta}_{MAC}$	0.332	0.273	0.265	0.272	0.248	0.273	0.232	0.243	0.304
$\tilde{\Delta}_{MAC}$	0.290	0.273	0.259	0.275	0.263	0.26	0.242	0.248	0.243
β_{MAC}	0.873	0.998	0.98	1.01	1.06	0.954	1.041	1.02	0.797
Probability	0.726	0.523	0.238	0.167	0.403	0.520	0.123	0.267	0.121

Table K2. Relationship between the probability of damage detection and β_{MAC} when 100 trials were used.

Damage	1a	1b	1c	1d	2	3	4	5	6
$\overline{\Delta}_{MAC}$	0.628	0.403	0.289	0.242	0.384	0.700	0.245	0.264	0.22
$\tilde{\Delta}_{MAC}$	0.199	0.289	0.250	0.232	0.286	0.256	0.248	0.232	0.251
β_{MAC}	0.317	0.716	0.864	0.955	0.746	0.365	1.021	0.88	1.139
Probability	0.977	0.918	0.579	0.34	0.702	0.903	0.204	0.594	0.235

Table K3. Relationship between the probability of damage detection and β_{MAC} when 400 trials were used.

Damage	1a	1b	1c	1d	2	3	4	5	6
$\overline{\Delta}_{MAC}$	0.935	0.906	0.686	0.471	0.844	0.925	0.435	0.622	0.239
$\tilde{\Delta}_{MAC}$	0.056	0.081	0.196	0.253	0.139	0.056	0.340	0.244	0.197
β_{MAC}	0.0596	0.089	0.287	0.536	0.164	0.0608	0.781	0.392	0.822
Probability	0.99999	0.9998	0.938	0.699	0.948	0.999	0.436	0.949	0.482